NATIONAL TECHNICAL UNIVERSITY OF ATHENS

School of Civil Engineering

The Structural Department

in cooperation with

The Geotechnical Department

Numerical simulation of the response of Ottawa Sand in the triaxial and torsional shear apparatus

Christina Z. Krachtoudi

Supervisor:

Dr. V.N. Georgiannou, Associate Professor, NTUA

A DISSERTATION SUBMITTED TO THE POSTGRADUATE SCHOOL OF CIVIL ENGINEERING
IN PARTIAL FULFILLMENT OF THE REQUIREMENTS FOR THE DEGREE OF
MASTER OF SCIENCE IN
"ANALYSIS & DESIGN OF EARTHQUAKE RESISTANT STRUCTURES",
NATIONAL TECHNICAL UNIVERSITY OF ATHENS

Athens, 2011

TABLE OF CONTENTS

ABSTRACT

Results from an experimental program on Ottawa sand subjected on generalized monotonic loading are presented. The experimental program was conducted on both solid and hollow cylinder specimens, including isotropic, triaxial compression and torsional loading at various stress levels.

The results are used in an attempt to numerically simulate the behaviour of the sand using Lade's Double Hardening model and evaluate is predictive capabilities. The calibration procedure is thoroughly presented.

The numerical analysis has been based on the Finite Element Method (FEM) and by using the finite element software ICFEP (Imperial College Finite Element Programme).

Comparison between experimental data and model predictions shows good agreement for all practical purposes highlighting the potential of complex elasto-plastic models in predicting soil behaviour.

AKNOWLEDGEMENTS

This work was carried out under the supervision of Dr V.N. Georgiannnou, Associate Professor in the National Technical University of Athens. As part of this thesis was conducted at Imperial College London where I was accepted through the ERASMUS exchange programme, I worked under the supervision of Dr S. Kontoe, lecturer at Imperial College London. I wish to express my gratitude for both their expert advice and assistance and for their continuous support throughout this project.

This thesis would not have been made possible without the valuable help of Maria Konstadinou, PhD student at NTUA, to whom I owe a big thank you for her kindness, patience and assistance for the provision of all the necessary data used throughout this work.

Sincere thanks to all Imperial College geotechnical research team that welcomed me at Imperial College and have been so helpful throughout carrying out this thesis. Specific thanks are due to Loizos Pelecanos and Vassileios Avgerinos for their assistance and patience mostly regarding the use of ICFEP program.

Last but not least, a heartfelt thank to the researchers I shared an office with at Imperial College London, Natàlia Climent Pera and Alexander Khalturin. Thank you for being my friends. Your support was more than valuable.

CHAPTER 1

INTRODUCTION

1.1 GENERAL

The experimental results presented in this thesis and those of respective studies found in international literature show that real soil behaviour is neither ideal, nor simple. On the contrary, the soil behaves in an intense non-linear way, as its strength and stiffness depend on the size of the stresses and deformations. Moreover, the structure of the naturally disposed sands is anisotropic and, as a result, their response is different depending on the type and the direction of the applied loads. It is therefore necessary, in order to simulate the response of a soil material and particularly that of a sand in a realistic way, it is necessary to implement complex elasto-plastic models that can be induced into Finite Element codes (or Finite Differences codes) in a PC so that the results can be extracted numerically.

In this project, an attempt has been made to numerically simulate the behaviour of Ottawa sand using **Lade's Double Hardening model** (1977). The calibration of the model is based on results from drained triaxial and isotropic consolidation tests. The model is used further in an attempt to predict the behaviour of the same sand under torsional shear loading. The numerical analyses have been performed using the Imperial Finite Element Programme (ICFEP) which has been developed by professor Dave M. Potts and is specialized in the analysis of geotechnical problems.

1.2 OUTLINE OF THESIS

In this thesis the numerical simulation of the behaviour of Ottawa sand is attempted. It involves the simulation of triaxial compression and monotonic shearing hollow cylinder tests under drained and undrained loading conditions and for various stress states.

The model used for the numerical simulation is Lade's Double Hardening Model (or Lade's Double Yield Surface Model) which has been developed by Lade in 1977 and simulates the behaviour of cohesionless materials. All numerical analyses presented in this thesis have been conducted by use of the Imperial College Finite Element Programme (ICFEP) which has been specifically developed by Professor D. M. Potts for the analysis of geotechnical problems.

This thesis is divided in **five chapters**:

The remaining part of this chapter introduces the definitions of the stress and strain variables used in this thesis.

Chapter 2 gives a brief review of the theoretical substratum which is necessary to understand the work that has been carried out in this thesis. It is subdivided into three main parts: · The first part gives the basic principles of the elasto-plastic behaviour of the soils and briefly reviews the elasto-plastic models and their evolution through the past 30 years. · The second part focuses on the main theoretical elements of the Finite Element Method. · Finally, the third part is an attempt to describe the laboratory equipment and the experimental procedures followed during the triaxial and hollow cylinder tests used in this thesis.

Chapter 3 presents the numerical simulation of Ottawa Sand using Lade's Double Hardening model. It is subdivided in three parts: · In the first part the model is fully explained and all the respective mathematical equations are given. · In the second part, the analytical procedure followed by Kovacevic (1994) in order to implement the model into ICFEP including all the changes made to avoid numerical problems are presented. · Finally, in the third part, the calibration of Lade's model based on a set of

isotropic consolidation and triaxial tests on Ottawa sand is thoroughly presented in order to obtain the total of the 14 parameters required by the model.

In **Chapter 4** the numerical analysis is presented in three parts. · In the first part, the software use for the analysis (Imperial College Finite element Programme - ICFEP) is introduced and the modeling of triaxial and hollow cylinder tests is explained. · In the second part, the function of Lade's Double Hardening model in the software as well as the mentioned modeling of the tests are successfully verified through the reproduction of Lade's original results for loose and dense Sacramento River sand. An attempt to study the sand's predicted behaviour under torsional loading is then discussed. · In the third part, the calibration of Ottawa sand is evaluated through the comparison of the predicted behaviour with the use of the parameters' values extracted in Chapter 3 and the respective experimental results from triaxial tests. Since the comparison is proved satisfactory, the predictions of the model for torsional loading are evaluated through comparison with experimental results in the cases that these were available – otherwise evaluated based on the reasonably expected behaviour. · The final part of the chapter summarizes the results presented.

Chapter 5 gives a summary of the work carried out in this thesis and the main conclusions reached, as it also gives recommendations for further research.

1.3 DEFINITIONS

Stress is a second order tensor which is defined by six components. *Equation 1.1* gives the effective stress tensor:

$$\sigma' = \begin{bmatrix} \sigma'_x & \tau_{xy} & \tau_{xz} \\ \tau_{yx} & \sigma'_y & \tau_{yz} \\ \tau_{zy} & \tau_{zy} & \sigma'_z \end{bmatrix} \tag{1.1}$$

where $\tau_{xy} = \tau_{yx}$, $\tau_{xz} = \tau_{zx}$ and $\tau_{zy} = \tau_{yz}$.

The stress tensor can be divided into two components, the volumetric component and the deviatoric component:

$$\sigma' = \begin{bmatrix} \sigma'_x & \tau_{xy} & \tau_{xz} \\ \tau_{yx} & \sigma'_y & \tau_{yz} \\ \tau_{zy} & \tau_{zy} & \sigma'_z \end{bmatrix} = \begin{bmatrix} p' & 0 & 0 \\ 0 & p' & 0 \\ 0 & 0 & p' \end{bmatrix} + \begin{bmatrix} \sigma'_x - p' & \tau_{xy} & \tau_{xz} \\ \tau_{yx} & \sigma'_y - p' & \tau_{yz} \\ \tau_{zy} & \tau_{zy} & \sigma'_z - p' \end{bmatrix} \tag{1.2}$$

In the above equation p' is the **mean effective stress**:

$$p' = \frac{1}{3}(\sigma_x' + \sigma_y' + \sigma_z') \tag{1.3}$$

Equation 1.2 can be rewritten as follows:

$$\sigma' = p' \cdot I + s \tag{1.4}$$

where $\boldsymbol{\sigma'}$ is the effective stress tensor, $\boldsymbol{p'}$ is the mean effective stress, $\boldsymbol{s}$ is the deviatoric stress tensor and $\boldsymbol{I}$ is the second-rank identity tensor (the tensor quantities are represented by bold-faced characters).

It is common to represent the state of stress with three stress invariants, the mean effective stress, $\boldsymbol{p'}$, the deviatoric stress, $\boldsymbol{J}$ or $\boldsymbol{q}$ and the Lode's angle, $\boldsymbol{\theta}$. The mean effective stress, $\boldsymbol{p'}$, can be calculated from *Equation 1.3*. The deviatoric stress, $\boldsymbol{J}$ or $\boldsymbol{q}$, and the Lode's angle, $\boldsymbol{\theta}$, are defined as following:

$$J = \left[\frac{1}{2}(s:s)\right]^{\frac{1}{2}} = \left\{\frac{1}{2}\left[(\sigma_x' - p')^2 + (\sigma_y' - p')^2 + (\sigma_z' - p')^2 + 2\tau_{xy}^2 + 2\tau_{yz}^2 + 2\tau_{zx}^2\right]\right\}^{\frac{1}{2}} \tag{1.5}$$

$$q = \sqrt{3} \cdot J \tag{1.6}$$

$$\theta = -\frac{1}{3}\sin^{-1}\left\{\frac{3\sqrt{3}}{2}\cdot\frac{\det(s)}{\left[\left(\frac{1}{2}(s:s)\right)^{\frac{1}{2}}\right]^3}\right\} \tag{1.7}$$

where ***det(s)*** is the determinant of the deviatoric stress tensor ***s***.

These three invariants can be expressed in terms of the principal effective stresses $\boldsymbol{\sigma'_1}$, $\boldsymbol{\sigma'_2}$ and $\boldsymbol{\sigma'_3}$ as following:

$$p' = \frac{1}{3}(\sigma_1' + \sigma_2' + \sigma_3') \tag{1.8}$$

$$J = \frac{1}{\sqrt{6}}\left[(\sigma_1' - \sigma_3')^2 + (\sigma_2' - \sigma_3')^2 + (\sigma_1' - \sigma_2')^2\right]^{\frac{1}{2}} \tag{1.9}$$

or

$$q = \frac{1}{\sqrt{2}}\left[(\sigma_1' - \sigma_3')^2 + (\sigma_2' - \sigma_3')^2 + (\sigma_1' - \sigma_2')^2\right]^{\frac{1}{2}} \tag{1.10}$$

$$\theta = \tan^{-1}\left[\frac{1}{\sqrt{3}}(2b - 1)\right] \tag{1.11}$$

where:

$$b = \frac{\sigma_2' - \sigma_3'}{\sigma_1' - \sigma_3'} \tag{1.12}$$

The above three quantities, ***p', J*** or ***q***, and ***θ***, have a geometrical significance in principal effective stress space. *Figure 1.1a* shows the principal effective stress space with the space diagonal *($\sigma'_1 = \sigma'_2 = \sigma'_3$)* and a deviatoric plane (defined as any plane perpendicular to the space diagonal). *Figure 1.1b* shows the projection of the principal stress space onto the deviatoric plane.

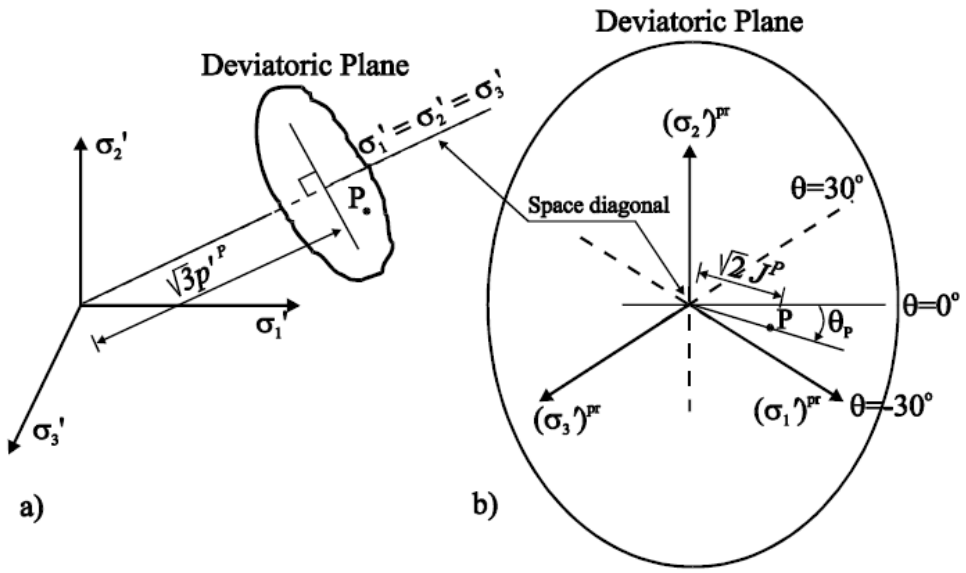

Figure 1.1: a) *Principal stress space and* ***b)*** *deviatoric plane* (After Potts and Zdravkovic-1999)

It can be seen that the mean effective stress, $\boldsymbol{p'}$, is a measure of the distance of the current deviatoric plane from the origin along the space diagonal. The deviatoric stress, $\boldsymbol{q}$ or $\boldsymbol{J}$, is a measure of the distance of the current stress state from the space diagonal in the deviatoric plane. Finally the Lode's angle, $\boldsymbol{\theta}$, defines the orientation of the stress state within the deviatoric plane, and varies between +30° (which corresponds to triaxial extension, $\sigma'_1 = \sigma'_2 \geq \sigma'_3$ and $b = 1$) and -30° (which corresponds to triaxial compression, $\sigma'_1 \geq \sigma'_2 = \sigma'_3$ and $b = 0$).

The three stress invariants, $\boldsymbol{p'}$, $\boldsymbol{J}$ or $\boldsymbol{q}$ and $\boldsymbol{\theta}$ are commonly used in order to define the stress state of a loaded body. However, although they define the overall magnitude of the stress state, they do not provide any information on the direction of the planes on which the principal effective stresses act. This is not necessary if the material considered is isotropic, in which case the material properties are the same in all directions. However, if the material considered is anisotropic (i.e. its properties are directional dependent), then the direction of the principal effective stress planes becomes significant and the use of just the three stress invariants, $\boldsymbol{p'}$, $\boldsymbol{J}$ or $\boldsymbol{q}$ and $\boldsymbol{\theta}$ is not sufficient. This is the reason why these stress invariants have been used extensively in the formulation of isotropic constitutive models, whereas in the case of anisotropic constitutive models the formulation usually involves the calculation of the whole stress tensor.

Strain, like stress, is a second order tensor, defined by six components.

$$\varepsilon = \begin{bmatrix} \varepsilon_x & \frac{1}{2}\gamma_{xy} & \frac{1}{2}\gamma_{xz} \\ \frac{1}{2}\gamma_{yx} & \varepsilon_y & \frac{1}{2}\gamma_{yz} \\ \frac{1}{2}\gamma_{zy} & \frac{1}{2}\gamma_{zy} & \varepsilon_z \end{bmatrix} \tag{1.13}$$

where $\gamma_{xy} = \gamma_{yx}$, $\gamma_{xz} = \gamma_{zx}$ and $\gamma_{zy} = \gamma_{yz}$.

The strain tensor can be divided into two components, the volumetric and deviatoric components:

$$\begin{bmatrix} \varepsilon_x & \frac{1}{2}\gamma_{xy} & \frac{1}{2}\gamma_{xz} \\ \frac{1}{2}\gamma_{yx} & \varepsilon_y & \frac{1}{2}\gamma_{yz} \\ \frac{1}{2}\gamma_{zy} & \frac{1}{2}\gamma_{zy} & \varepsilon_z \end{bmatrix} = \begin{bmatrix} e_v & 0 & 0 \\ 0 & e_v & 0 \\ 0 & 0 & e_v \end{bmatrix} + \begin{bmatrix} \varepsilon_x - e_v & \frac{1}{2}\gamma_{xy} & \frac{1}{2}\gamma_{xz} \\ \frac{1}{2}\gamma_{yx} & \varepsilon_y - e_v & \frac{1}{2}\gamma_{yz} \\ \frac{1}{2}\gamma_{zy} & \frac{1}{2}\gamma_{zy} & \varepsilon_z - e_v \end{bmatrix} \tag{1.14}$$

In the above equation e_v is equal to:

$$e_v = \frac{1}{3}\left(\varepsilon_x + \varepsilon_y + \varepsilon_z\right) = \frac{1}{3}\varepsilon_v \tag{1.15}$$

where ε_v is the volumetric strain.

Equation 1.14 can be rewritten as:

$$\varepsilon = \frac{1}{3}\varepsilon_v \cdot I + e_s \tag{1.16}$$

where $\boldsymbol{\varepsilon}$ is the strain tensor, $\boldsymbol{\varepsilon_v}$ is the volumetric strain and $\boldsymbol{e_s}$ is the deviatoric strain tensor.

The strain invariants corresponding to the previously described stress invariants are the volumetric strain, $\boldsymbol{\varepsilon_v}$, given by *Equation 1.15* and the deviatoric strain $\boldsymbol{E_d}$, if the stress invariant $\boldsymbol{J}$ is chosen, or $\boldsymbol{\varepsilon_s}$, if the stress invariant $\boldsymbol{q}$ is used. These are defined from the following equations:

$$E_d = \left[\frac{1}{2}\left(e_s : e_s\right)\right]^{\frac{1}{2}} = \left\{\frac{1}{2}\left[\left(\varepsilon_x - e_v\right)^2 + \left(\varepsilon_y - e_v\right)^2 + \left(\varepsilon_z - e_v\right)^2 + 2\gamma_{xy}^2 + 2\gamma_{yz}^2 + 2\gamma_{zx}^2\right]\right\}^{\frac{1}{2}} \tag{1.17}$$

$$\varepsilon_s = \frac{1}{\sqrt{3}} E_d \tag{1.18}$$

The above equations are expressed in terms of the principal strains, $\boldsymbol{\varepsilon_1}$, $\boldsymbol{\varepsilon_2}$ and $\boldsymbol{\varepsilon_3}$ as follows:

$$\varepsilon_v = \varepsilon_1 + \varepsilon_2 + \varepsilon_3 \tag{1.19}$$

$$E_d = \frac{2}{\sqrt{6}}\left[\left(\varepsilon_1 - \varepsilon_3\right)^2 + \left(\varepsilon_2 - \varepsilon_3\right)^2 + \left(\varepsilon_1 - \varepsilon_2\right)^2\right]^{\frac{1}{2}} \tag{1.20}$$

or

$$\varepsilon_s = \frac{\sqrt{2}}{3}\left[\left(\varepsilon_1 - \varepsilon_3\right)^2 + \left(\varepsilon_2 - \varepsilon_3\right)^2 + \left(\varepsilon_1 - \varepsilon_2\right)^2\right]^{\frac{1}{2}} \tag{1.21}$$

In triaxial stress space the most commonly adopted stress and strain invariants are the mean effective stress, $\boldsymbol{p'}$, the shear stress, $\boldsymbol{q}$, the volumetric strain, $\boldsymbol{\varepsilon_v}$, and the shear strain, $\boldsymbol{\varepsilon_s}$. In this case of axially symmetric conditions *Equations 1.8, 1.10, 1.19* and *1.21* reduce to:

$$p' = \frac{1}{3}\left(\sigma_\alpha' + 2\sigma_r'\right) \tag{1.22}$$

$$q = \sigma_a' - \sigma_r' \tag{1.23}$$

$$\varepsilon_v = \varepsilon_a + 2\varepsilon_r \tag{1.24}$$

$$\varepsilon_s = \frac{2}{3}\left(\varepsilon_a - \varepsilon_r\right) \tag{1.25}$$

where $\boldsymbol{\sigma'_a}$ and $\boldsymbol{\sigma'_r}$ are the axial and radial effective stresses and $\boldsymbol{\varepsilon_a}$ and $\boldsymbol{\varepsilon_r}$ are the axial and radial strains respectively.

CHAPTER 2

THEORETICAL CONSIDERATIONS

INTRODUCTION

In this chapter, the basic theoretical considerations upon which this thesis is based are presented. First of all the **basic principles of the elasto-plastic models** of the behaviour of soils are presented as well as a short reference to their **evolution through the years**. Secondly, the **triaxial apparatus and test** are explained, as well as the **hollow cylinder apparatus and the monotonic torsional shear test**. Finally, the **basic principles of the finite element analysis** implemented in this project are described in brevity.

2.1 BASIC PRINCIPLES OF ELASTO-PLASTIC BEHAVIOUR OF SOILS

The elasto-plastic theory basically derives from the study of the behaviour of metals (Tresca, 1869, Von Mises, 1913). This theory has been further developed, in order to include the behaviour of soils (Drucker and Prager, 1952).

The basic assumption upon which the elasto-plastic theory is based is that the **total strains** during the loading of a soil element consist of two parts; one **elastic (reversible)** and one **plastic (irreversible):**

$$\{d\varepsilon\} = \{d\varepsilon^e\} + \{d\varepsilon^p\} \tag{2.1}$$

where the indexes ***e*** and ***p*** refer to elastic and plastic strains respectively.

An infinitesimal change of the **elastic strain** is connected to the infinitesimal change in stress with the use of an elastic tensor [D] as following:

$$\{d\sigma\} = [D]\{d\varepsilon^e\} = [D](\{d\varepsilon\} - \{d\varepsilon^p\}) \tag{2.2}$$

The calculation of the infinitesimal change of the **plastic strain** demands the introduction of a **yield surface** which separates the purely elastic behaviour from the elasto-plastic behaviour and works as the boundary of the feasible states. The mathematical expression of the yield surface is described by the following **yield function:**

$$F(\{\sigma\},\{k\}) = 0 \tag{2.3}$$

In order to describe the behaviour of an isotropic material (same properties regardless the direction) three parameters of stresses and strains are required (instead of six that are required to describe the behaviour of an anisotropic material). In this case the *Equation 2.3* is illustrated in *Figure 2.1* in the three dimensional space of mean stresses. Moreover, if assumed that the intermediate mean effective stress $\sigma_2=0$, the yield function takes the shape of the yield curve illustrated in *Figure 2.2.*

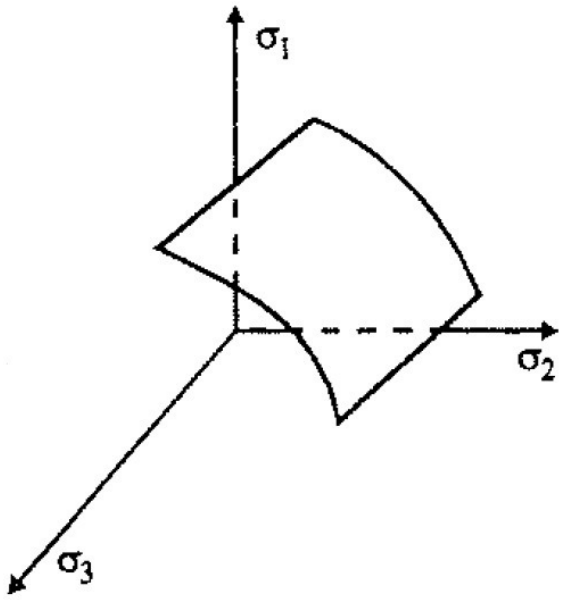

Figure 2.1: *Yield function presentation: Segment of yield surface (3-dimensional space)* (After Potts and Zdravkovic, 1999)

The yield function depends on the **stress state** $\{\sigma\}$ and the vector of the state parameters or the **hardening parameters** $\{k\}$**.** The value of the function defines the behaviour of the soil element: If $F(\{\sigma\},\{k\})<0$, the behaviour is **purely elastic** and if $F(\{\sigma\},\{k\})=0$ the behaviour is **elasto-plastic.** Values that are $F(\{\sigma\},\{k\})>0$ are considered as **non-feasible states** *(Figure 2.2).*

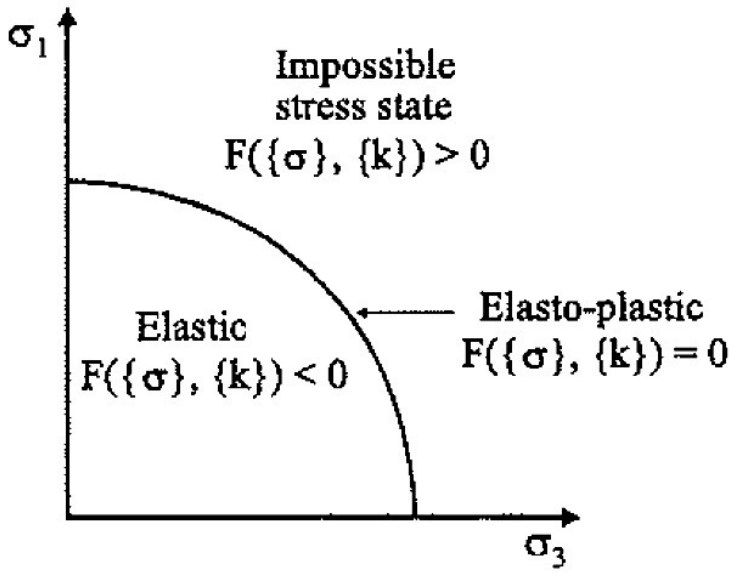

Figure 2.2: *Yield function presentation: Yield curve (2-dimensional space)* (After Potts and Zdravkovic, 1999)

When the stress state of the material reaches the yield surface, plastic strains are developed. The infinitesimal changes of the plastic stains are initially defined by a **flow rule** expressed as following:

$$\{d\varepsilon^{p}\}=\Lambda\left\{\frac{\partial P(\{\sigma\},\{m\})}{\partial\sigma}\right\} \tag{2.4}$$

where:

- $\{d\varepsilon^{p}\}$ is the vector of the change of the plastic strains
- $\partial P(\{\sigma\},\{m\})$ is the **plastic potential function** that defines the direction of the plastic strains and
- Λ is a **scalar multiplier** that defines the real size of the plastic strains.

- the values of the state parameters {m} are of no substantial meaning, as in the potential flow rule only the partial derivatives of the plastic potential are required.

The plastic potential function is mathematically expressed as following:

$$\partial P(\{\sigma\},\{m\}) = 0 \tag{2.5}$$

Equation (2.5) is illustrated in *Figure 2.3* in the three dimensional space of the mean stresses. If assumed that the intermediate mean effective stress $\sigma_2=0$, the plastic potential function takes the shape of the plastic potential curve illustrated in *Figure 2.4*.

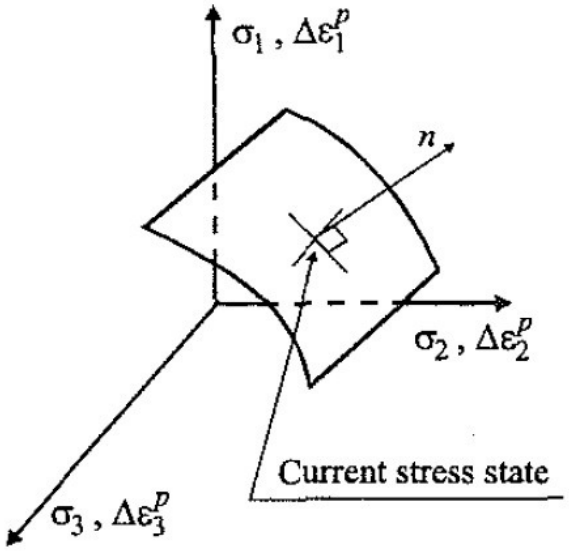

Figure 2.3: *Plastic potential presentation: Segment of the plastic potential surface (3-dimensional space)* (After Potts and Zdravkovic, 1999)

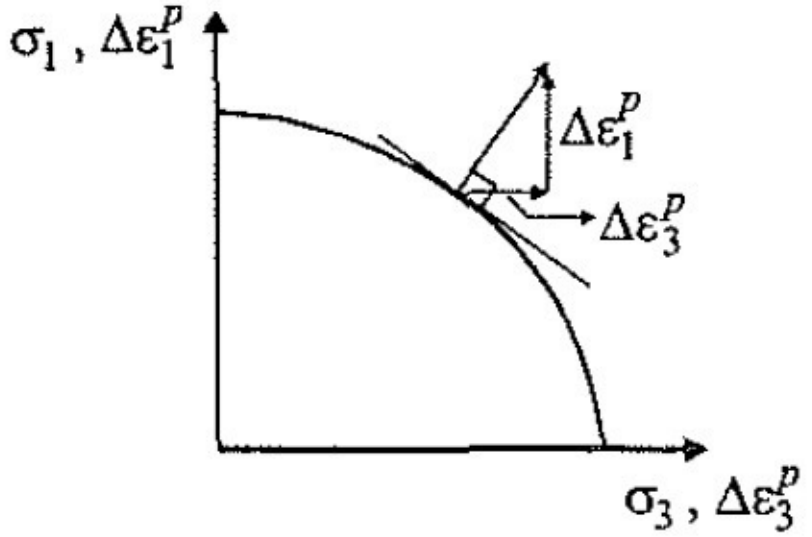

Figure 2.4: *Plastic potential presentation: Plastic potential curve (2-dimensional space)* (After Potts and Zdravkovic, 1999)

The vector {n} that is vertical to the plastic potential surface directed outwards indicates the direction of the plastic strains *(Figure 2.3).* In the case that the plastic potential function is similar to the yield function:

$$P(\{\sigma\},\{m\}) = F(\{\sigma\},\{k\}) \tag{2.6}$$

then the flow rule is characterized as **associated**: the vector of the plastic strains is vertical to the yield surface and the normality rule is applied. If the plastic potential function is different from the yield function:

$$P(\{\sigma\},\{m\}) \neq F(\{\sigma\},\{k\}) \tag{2.7}$$

then the flow rule is characterized as **non-associated.**

Finally, the **hardening/softening rules** define how the hardening parameters $\{k\}$ change with plastic strains, while they allow the quantification of the scalar multiplier *Λ*. The size of the yield surface is also defined by the hardening parameters $\{k\}$. In the case that the material behaves elastically, the yield surface remains unaffected when it comes to its size, shape and position. If the material is **elastic-perfectly plastic** *(Figure 2.5)* the hardening parameters have constant values, there is no need for a hardening rule and the multiplier *Λ* is indefinable (the material deforms infinitely with

the yield stress σ_{yield} remaining constant). If the material shows **softening behaviour** *(Figure 2.6)*, which refers to the reduce of the yield stress with further increase of the plastic strains ε^p, or **hardening behaviour** *(Figure 2.7)*, which refers to the increase of the yield stress with further increase of the plastic strains ε^p, it is necessary to use the hardening/softening rules. These rules derive as functions of either the plastic strains (strain hardening/softening rules) or the plastic work (work hardening/softening rules), where the plastic work is given by the expression:

$$W_p = \Sigma\left(\{\sigma\}^T \cdot \{\Delta\varepsilon^p\}\right) \tag{2.8}$$

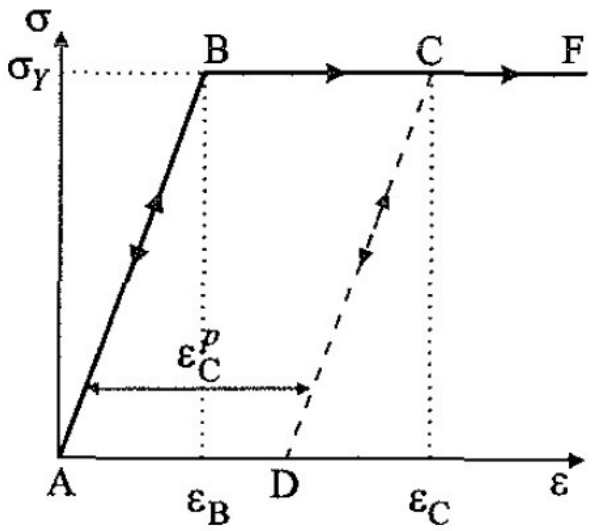

Figure 2.5: *Stress-strain diagram for elastic-perfectly plastic material* (After Potts and Zdravkovic, 1999)

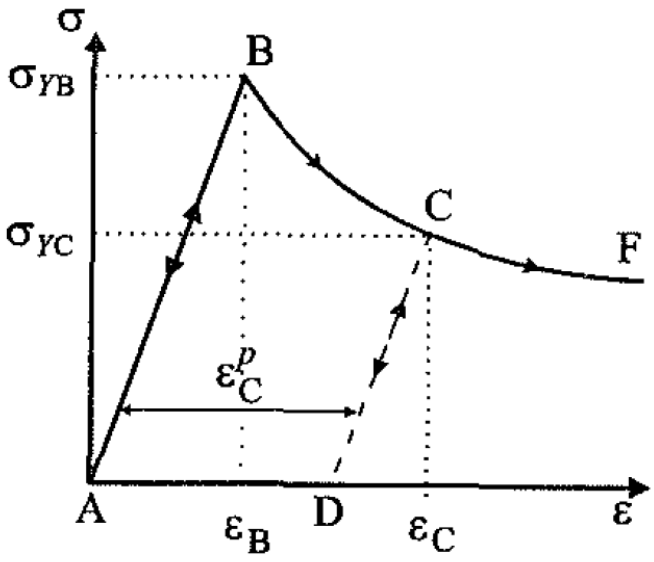

Figure 2.6: *Stress-strain diagram for linear elastic strain softening plastic material* (After Potts and Zdravkovic, 1999)

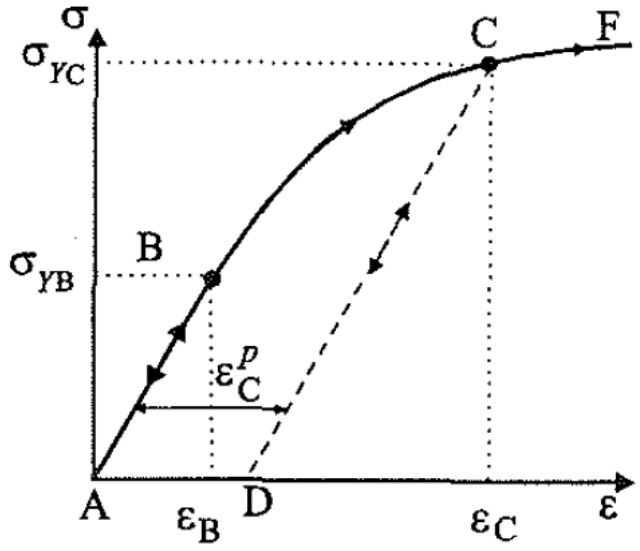

Figure 2.7: *Stress-strain diagram for linear elastic strain hardening plastic material* (After Potts and Zdravkovic, 1999)

If the hardening parameters derive as a function of plastic strains, then the scalar quantity Λ, which, as mentioned already defines the real values of the plastic strains, is given by the expression:

$$\Lambda = \frac{1}{\mathrm{A}} \left\{ \frac{\partial F}{\partial \sigma} \right\}^{\mathrm{T}} \{ d\sigma \} \tag{2.9}$$

where A is the plastic hardening modulus given by the expression:

$$A = -\left\{\frac{\partial F}{\partial k}\right\}^{T}\left[\frac{\partial k}{\partial \varepsilon^{p}}\right]\left\{\frac{\partial P}{\partial \sigma}\right\} \tag{2.10}$$

2.2 THE EVOLUTION OF ELASTO-PLASTIC MODELS

Initially, the elasto-plastic models for soils were simpler: the failure surface, which was similar to the failure surface of the metals, was the yield surface at the same time. The **Mohr–Coulomb** and **Drucker-Prager models** were evolved from the above mentioned making use of the **Mohr-Coulomb failure surface**, which is more representative for the behaviour of soils. In most cases, the soils were assumed to behave elastically-purely plastically.

These models managed to give a rough estimation of the soil behaviour, although they did not predict basic characteristics of the **real soil behaviour** (no prevision for softening/hardening with further loading). The implementation of the softening/hardening law, in combination with the **Critical State Theory** led to the development of the **Critical State elasto-plastic models.**

The first Critical State elasto-plastic model is the **Cam Clay – CC**, presented by Roscoe and Schofield (1963) and Schofield and Wroth (1968). Following, the **Modified Cam Clay – MCC** was presented by Roscoe and Burland (1968). These two models were developed for triaxial loading conditions and are based on the following assumptions:

- A normally consolidated clay sample, when isotropically compressed, follows the Isotropic Compression Line which, when plotted in *v-lnp'* axes, is a straight line (where $v=1+e$, the specific volume of the material):

$$v = v_s - \lambda(\ln p') \tag{2.11}$$

where $\boldsymbol{\lambda}$ is the gradient of the straight line and $\boldsymbol{v_c}$ the specific volume of the consolidation line where *p'=1kPa*. The volume change in the consolidation line is assumed plastic and in the swelling line elastic.

- A soil element subjected to continuous shear is finally led to a Critical State during which it continuously deforms without further change of the applied load or the soil density (as this is expressed by the volume *v*). The Critical State Line is defined in the 3-dimensional space *v-lnp'* as a straight line with gradient λ_{CS} and specific volume value v_{CS} for *p'=1kPa (Figure 2.8).* In the

axes of *q-p'*, the projection of the Critical State Line is the straight line with gradient M_{CS} which passes from the beginning of the axes.

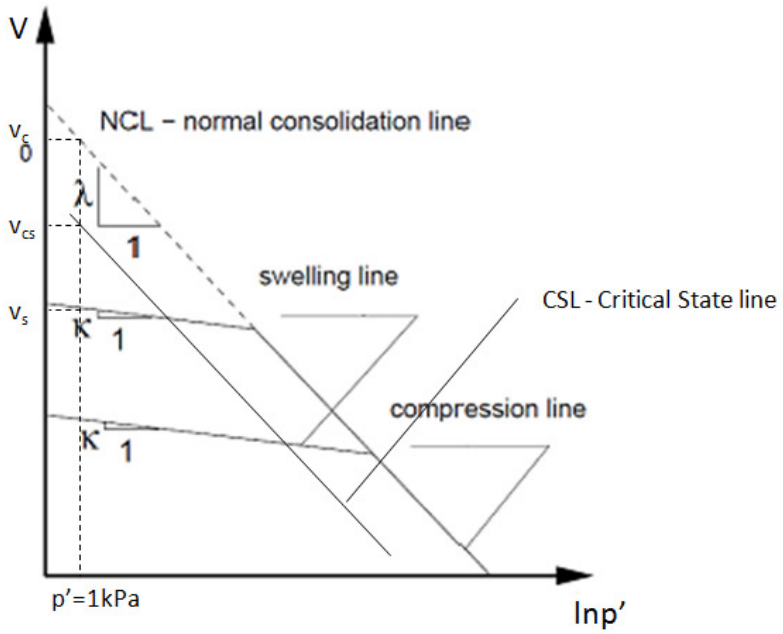

Figure 2.8: *Normal Consolidation Line, Swelling Line, Critical State Line.*

- In the space *v-p'-q* there is a **State Boundary Surface** that separates the feasible and non-feasible states. This means that the stress state of a soil element can either be inside the Boundary Surface (elastic behaviour) or on the Boundary Surface (elasto-plastic behaviour). Above the swelling line and until the Boundary Surface is met, the material behaviour is elastic *(Figure 2.9).* Between the swelling line and the Boundary Surface the yield surface of the Cam-Clay model is defined and is of a logarithmic form *(Figure 2.10)*, as well as the yield surface of the Modified Cam Clay which has an elliptic form *(Figure 2.11).* The mathematical equations of the surfaces are described by Roscoe and Schofield (1963) and Roscoe and Burland (1968). Moreover, the Cam-Clay models implement an isotropic hardening/softening rule controlled by p_o' *(Figures 2.9-2.11),* as well as an associated flow rule.

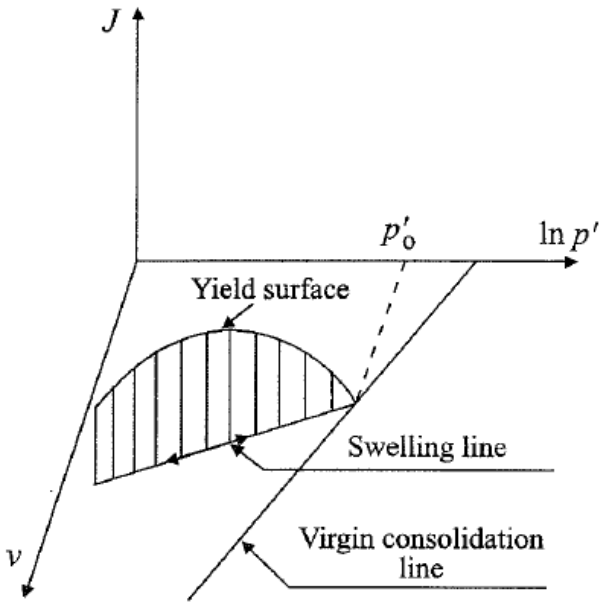

Figure 2.9: *Yield surface presentation: 3-dimensional space v-lnp'-q* (After Potts and Zdravkovic, 1999)

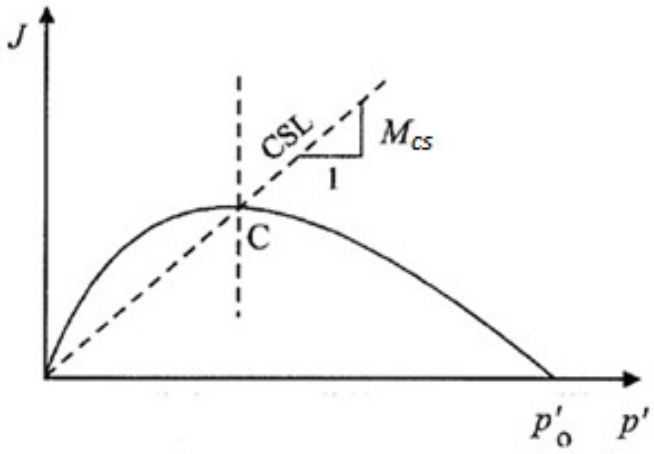

Figure 2.10: *Cam Clay model: Yield surface presentation: 2-dimensional space J-p'* (After Potts and Zdravkovic, 1999)

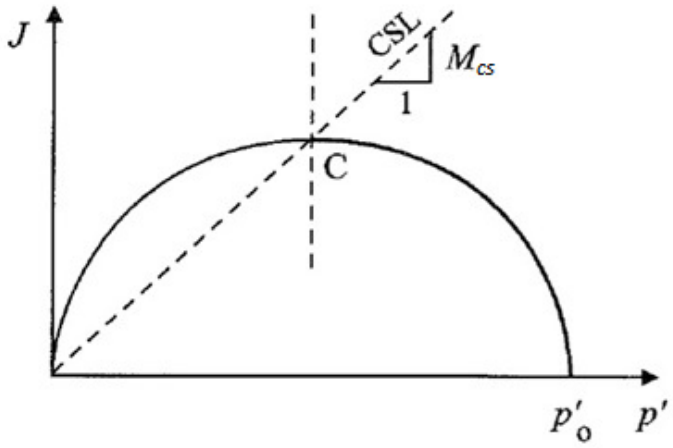

Figure 2.11: *Modified Cam Clay model: Yield surface presentation: 2-dimensional space J-p'* (After Potts and Zdravkovic, 1999)

Between the above described models the most commonly used is the Modified Cam-Clay as it overcame some problems of the Cam-Clay, e.g. the existence of strains for *q=0*. Even so, both models have significant weaknesses, as they cannot sufficiently simulate the behaviour of the overconsolidated clays, the cohesionless materials (sands) and cyclic loading conditions.

These weaknesses of the first Critical State elasto-plastic models led to the modification of their initial design in order to simulate experimental results more sufficiently. A first category of the modified models are the **Cap models**. The first cap model was introduced by Drucker et al. (1957) while those by DiMaggio and Sandler (1971), Baladi and Rohani (1979), McCarron and Chen (1987), Schwer and Murray (2004) are more recent. The cap models utilize a **constant failure surface**. On the other hand, the yield surface has the **form of a cap** and it moves with respect to the plastic volumetric strains, following the rule of isotropic hardening *(Figure 2.12)* and the associated flow rule. In other words, the yield surface keeps its shape and position, but it changes size depending on the plastic deformation *(Figure 2.13).* However, the cap models maintain some of the disadvantages of the initial models, such as the **failure to predict the soil behaviour under cyclic loading and the failure to predict dilative volumetric strains.**

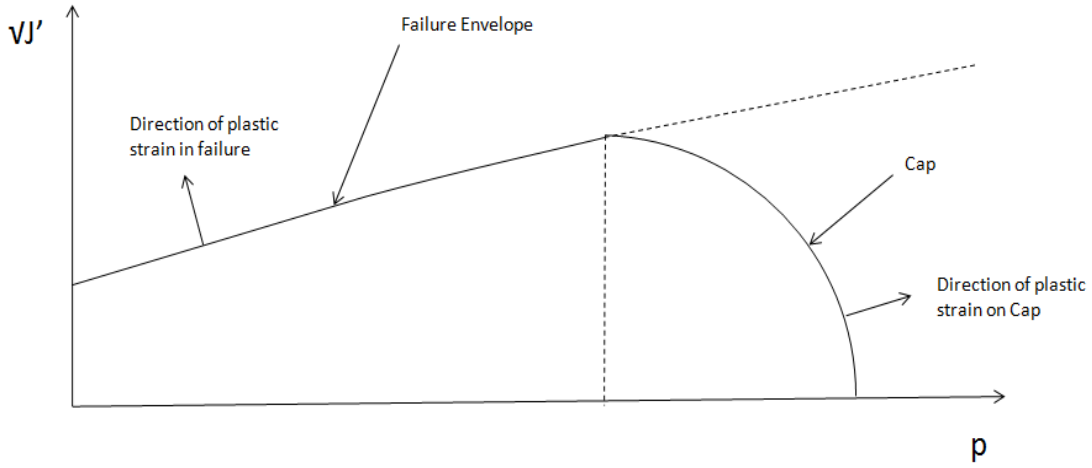

Figure 2.12: *Yield surface of a cap model.* (Figure based on Sandler, 2002)

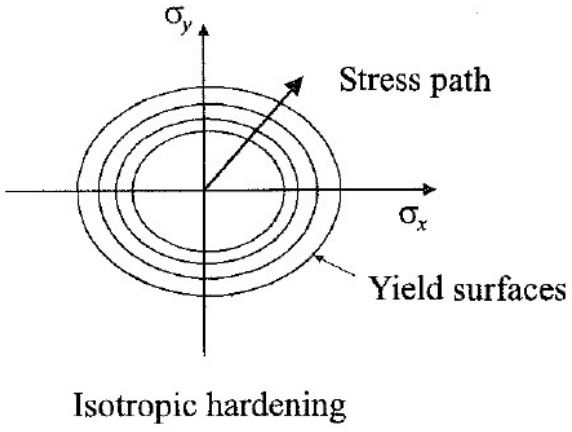

Figure 2.13: *Isotropic hardening law* (After Potts and Zdravkovic, 1999)

Another category of modified elasto-plastic models **includes isotropic models that do not implement a failure surface like the cap models do**. Such are the models of Lade and Duncan (1975), Pender (1978), Lade and Kim (1988), Jefferies (1993), Peric and Ayari (2002) and more. Other models that also do not implement a failure surface utilize an **anisotropic kinematic hardening rule**. This means that the yield surface has the ability to move inside the loading space without changing its shape *(Figure 2.14).* A characteristic example of such a model is the MIT-E1 model, by Kavvadas (1982).

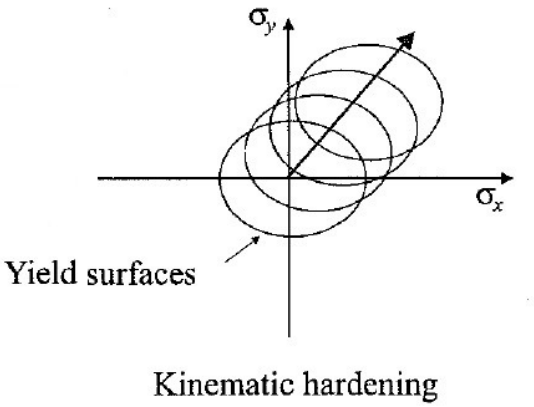

Figure 2.14: *Kinematic hardening law* (After Potts and Zdravkovic, 1999)

Another important category of elasto-plastic models are the **Generalized Plasticity models**. Their main characteristic is the implementation of a non-associated flow rule and the introduction of a plastic potential surface which differs from the yield surface. Typical examples of such models are those of Lade and Duncan (1975), Pastor et al. (1985), Lade (1990) and more. More complicated models which implement two yield surfaces and two plastic potential surfaces are for example Lade's (1977) (see §3.1) and Banerjee et al. (1992) and more.

As mentioned previously, the yield surface in an elasto-plastic model separates the elastic behaviour from the elasto-plastic behaviour, while inside the yield surface only elastic (reversible) strains are possible. In reality though, soils develop a non-reversible behaviour inside the boundaries of the yield surface and, as a result, the elasto-plastic theory is not sufficient to describe this behaviour. An attempt to overcome these weaknesses is made by the introduction of the **Boundary Plasticity Surface** (Dafalias and Popov, 1975, Krieg, 1975, Dafalias and Popov, 1976). The Boundary Plasticity Surface is respectful to the yield surface but it does allow the development of plastic strains inside the surface.

Whittle (1993) and Whittle and Kavvadas (1994) further developed the anisotropic model MIT-E1 of Kavvadas (1982) by embodying the Boundary Plasticity Surface in order to capture the behaviour of overconsolidated clays. The model was named MIT-E3. The Boundary Plasticity Surface that is being utilized has a similar form to the elliptic yield surface of the Modified Cam-Clay model, but in this case it is anisotropic.

There are also the subloading surface models which are place among the general category of Boundary Plasticity Surface models. They were initially proposed by Hashiguchi and Ueno (1977a, 1977b) and Hashiguchi (1980). These models assume that a subloading surface passes from the point that corresponds to the stress state of the soil element. This surface is similar to the external Boundary Surface. The plastic hardening modulus (hence the plastic strains) depend on the ratio of the size of the subloading surface to the size of the Boundary Surface.

The main weakness of the Boundary Plasticity Surface models is the fact that during unloading they predict elastic behaviour. In order to overcome this, **a number of kinematic yield surfaces are introduced inside the Boundary Surface**. Within each one of these surfaces the behaviour of the soil element is elastic, and when it reaches the boundary of the surface it becomes elasto-plastic (with the respectful plastic hardening modulus). The surface moves until it meets the next bigger yield surface. Subsequent loading activated the next yield surface and both of them move until they meet the third one and so on (Figure 2.15). Models that utilize these kinematic yield surfaces are those of Prevost (1977), (1978) and Mroz et al. (1978).

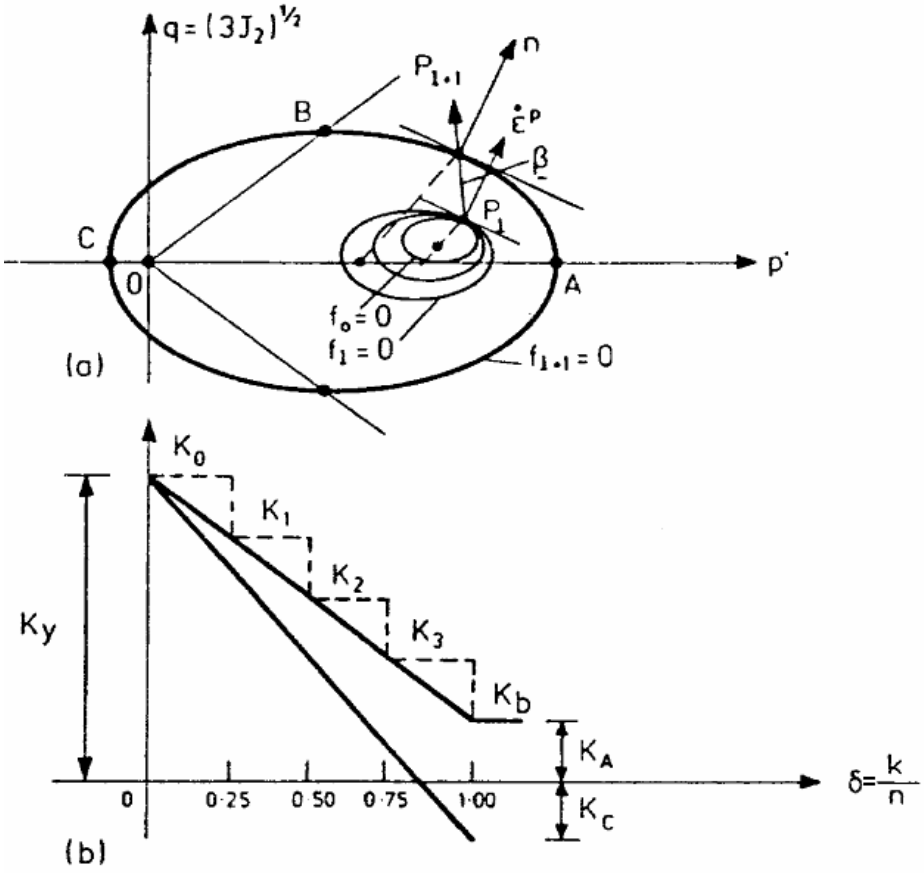

Figure 2.15*: Multi-surface model a) nesting surfaces; b) variation of hardening moduli at conjugate points on nesting surfaces* (redrawn by Mroz and Norris (1982) after Mroz et al. (1978))

Mroz et al. (1979) presented a simplified form of the multiple kinematic yield surfaces model and assumed two yield surfaces in total, one kinematic and one boundary *(Figure 2.17).* Al Tabbaa (1987) and Al Tabbaa and Wood (1989) presented an elasto-plastic model that incorporated the Critical State theory and one kinematic yield in the form of a bubble while their Boundary Surface was the same as the one of the Modified Cam Clay *(Figure 2.17).* Inside the bubble, the stress state of the soil element is considered isotropically elastic. When the stress state reaches the circumference of the kinematic yield surface the material behaviour changes to elasto-plastic. Following the bubble moves with respect to the plastic hardening modulus which depends on the distance between the bubble and the boundary surface. When the stress state hence the bubble reaches the Boundary Surface, the elasto-plastic behaviour of the soil element is then defined by the Boundary Surface. Stallebrass and Taylor (1997) further developed this model by introducing two kinematic yield

surfaces (one containing the other) inside the Boundary Surface of the Modified Cam Clay model. The new yield surface (history surface) *(Figure 2.18)* accommodates the simulation of the loading history of the soil element.

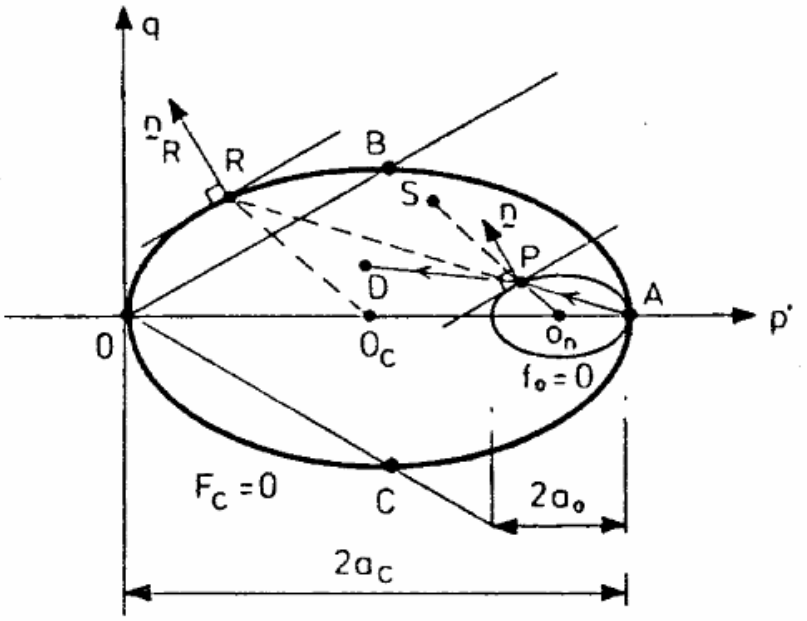

***Figure 2.16**: Two-surface model: kinematic yield surface and bounding surface* (redrawn by Mroz and Norris (1982) after Mroz et al. (1979))

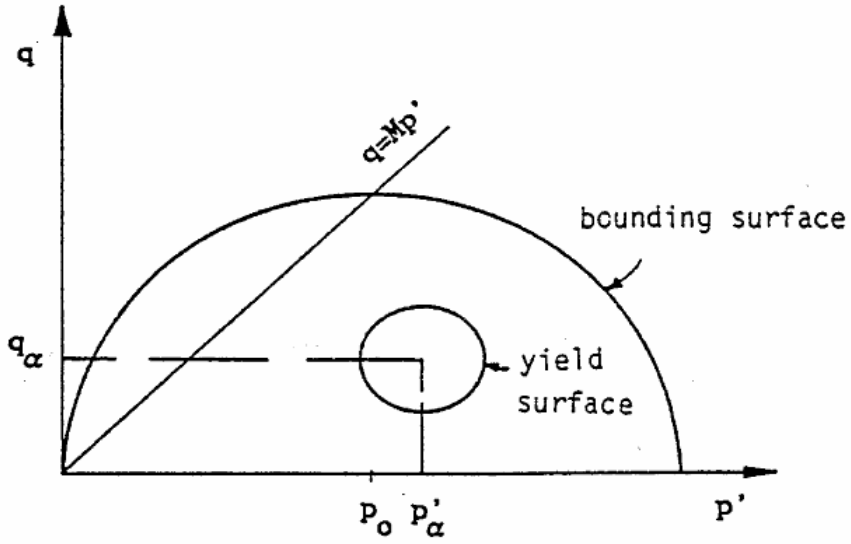

***Figure 2.17**: Two-surface model* (after Al-Tabbaa, 1987)

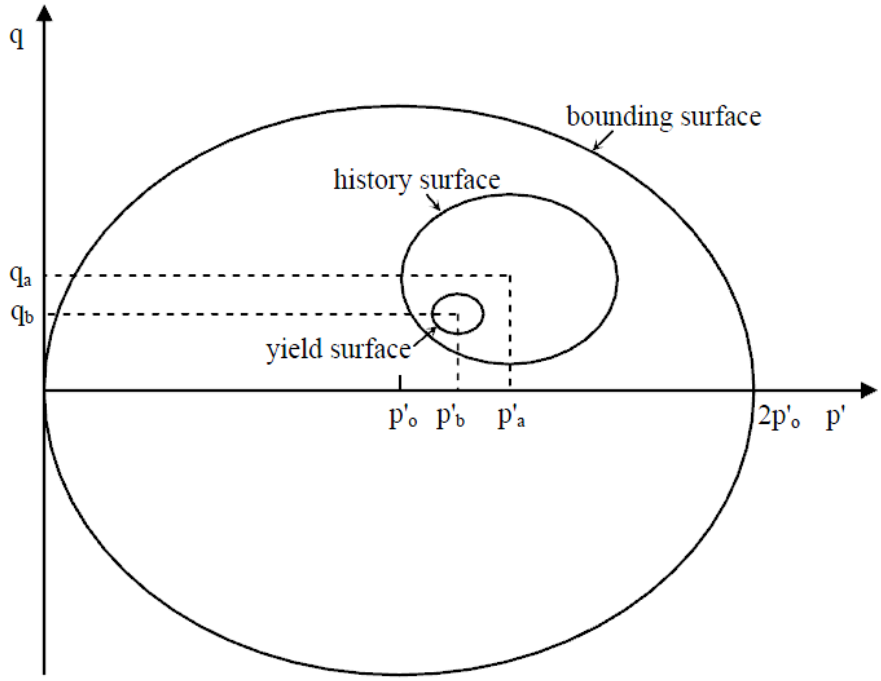

***Figure 2.18**: Three-surface model* (after Stallebrass, 1990)

Furthermore, the elasto-plastic models have been further developed as to incorporate the effect of structure into the soil behaviour. Such models are those of Kavvadas and Amorosi (2000), Rouainia and Wood (2000) and Callisto et al. (2002).

As it derives from the above brief historical reference to the evolution of the elasto-plastic models over the years, they have many different characteristics and their categorization can be hard. Each one provides different advantages and has different weaknesses which need to be taken into consideration with respect to the material that needs to be studied, as well as the loading conditions of the geotechnical problem.

In this thesis, in order to simulate the behaviour of Ottawa Sand, the model implemented was Lade's Double Hardening Model (1977) fully explained in paragraph §3.1. Lade's Double Hardening Model has been proved to successfully capture the behaviour of cohesionless materials under monotonic loading.

2.3 THE FINITE ELEMENT METHOD

The Finite Element Method (FEM) is a numerical technique which provides approximate solutions to a wide range of engineering problems for the past 30 years. The complex issues which are specific to geotechnical engineering and have only recently been resolved are the main cause why FEM has only relatively recently begun to be widely used for the analysis of geotechnical problems.

Numerical analysis can be a very useful tool for geotechnical engineers but its use needs to be very careful and always evaluated by engineering judgment in order to avoid pitfalls. It is therefore essential for geotechnical engineers, no matter what type of analysis they perform, to be able to understand the principles of the method used by the software they use.

The success of FEM, unlike classical methods of analysis (e.g. limit equilibrium, limit analysis, etc.) when analyzing any boundary value problem, is due to the satisfaction of all four basic solution requirements for a complete theoretical solution, namely:

- the equilibrium of forces,
- the compatibility of displacements,
- the material constitutive laws,
- the boundary conditions

In this paragraph the general principles of the Finite Element Method are briefly described, with particular reference to the approach followed in ICFEP and, consequently, to the analyses performed in this thesis.

A more detailed description of the method and its application to geotechnical engineering can be found in the literature, especially in Potts and Zdravkovic (1999) upon which this brief description has been based.

2.3.1 FORMULATION OF THE METHOD

In summary, the basic steps in the FEM are the following:

- element discretisation
- displacement approximation
- formulation of element equations

- assembly of global equilibrium equations
- formulation of the boundary conditions
- solution of global equations

Each one of the above steps is discussed in brevity in the following sections.

2.3.1.1 ELEMENT DISCRETISATION

This is the first step of the analysis and refers to the discretisation of the problem domain into a finite number of discrete regions, connected with each other at their nodes. These are the ***finite elements***. And thus, the ***finite element mesh*** is formed. The elements can be of various shapes. *(Figure 2.19)* The simplest shape of an element for plane strain or axisymmetric analyses is a ***triangular*** or ***quadrilateral*** with straight sides and nodes located at the element corners (Zieckiewicz, 1977). For more complex problems involving non-linear material properties, curved boundaries and/or curved material interfaces higher order elements with mid-side nodes are utilized. For example, additional nodes can be used, usually at the midpoints of the sides, resulting in 6-noded triangular or 8-noded quadrilateral elements.

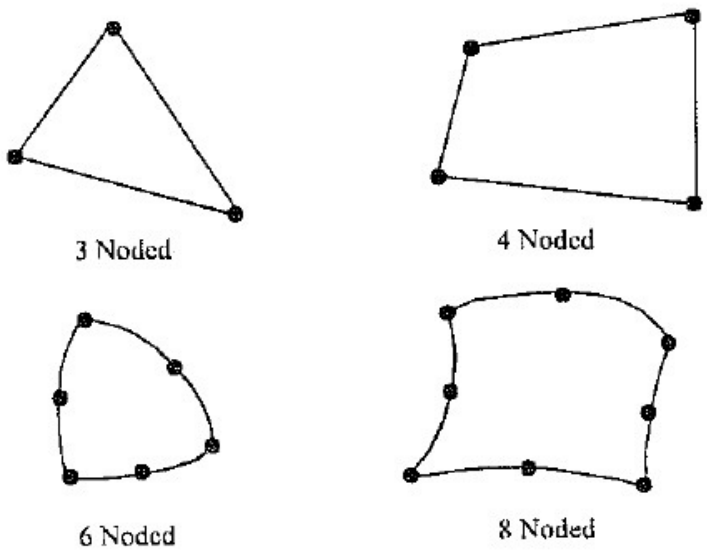

Figure 2.19*: Typical 2-D finite elements* (after Potts and Zdravkovic, 1999)

In the present thesis, all the analyses were performed using one single element representing the soil sample in the triaxial or the hollow cylinder apparatus. The geometry of the specific simulations are thoroughly explained in *§4.1.1* and *§4.1.2*.

2.3.1.2 DISPLACEMENT APPROXIMATION

In the displacement based FEM (the one utilized by ICFEP), the primary unknown quantity is the ***displacement field, d_f,*** which varies over the problem domain. All other quantities are treated as secondary quantities and they are determined once this primary unknown has been calculated. It is assumed that the displacements within each element can be expressed as a function of its nodal displacements through a set of functions called the ***shape functions***. In plain strain and fully axisymmetric analyses the displacement field is characterised by the two global displacements ***u*** and ***v***, in the ***x*** and ***y*** coordinate directions respectively. Over each element the displacement components are assumed to have a simple polynomial form, which, if expressed as a function of the nodal displacements, $\boldsymbol{d_e}$, it is has the following form:

$$d_f = N_d \cdot d_e \tag{2.12}$$

where

$d_f = [u, v]^T$,

$d_e = [u_1, v_1, u_2, v_2, ..., u_n, v_n]^T$ and

N_d is the element displacement interpolation matrix (the matrix of the shape functions)

In the above equation it can be seen that the variation of the unknown displacement field within an element, $\boldsymbol{d_f}$, is expressed as a simple function of the displacements as the nodes, $\boldsymbol{d_e}$. Therefore, the problem of determining the displacement field is reduced to determining the displacements of the nodes. These nodal displacements are often referred to as the ***unknown degrees of freedom.***

It is also understood that the accuracy of the method increases as the size of the elements become smaller, as it depends on the size of the elements and the nature of the displacement approximation. However, this happens at the expense of the computational time required. For the accuracy to increase in this way, the displacement approximation should satisfy certain compatibility conditions. It is clear that the displacement components must vary continuously within each element and

across each element side. This way gaps and overlaps are avoided. This is achieved only if the displacements of one side of the element depend only on the displacements of the nodes situated on that side. Another requirement would be for the element to be able to undergo rigid body motions and constant straining if such is desirable. This is also allowed by a simple polynomial displacement approximation.

By applying the material constitutive law it is possible to calculate the **values of the stresses and strains** within each element. By the definition of strains and assuming a linear elastic material:

$$\varepsilon = \mathrm{B} \cdot d_e \tag{2.13}$$

$$\sigma = D \cdot \varepsilon \tag{2.14}$$

where

B is the element strain-displacement matrix and

D is the constitutive matrix relating the stress vector, $\boldsymbol{\sigma}$, to the strain vector, $\boldsymbol{\varepsilon}$. The constitutive matrix for isotropic linear elastic materials and for plane strain conditions takes the following form:

$$\begin{Bmatrix} \Delta\sigma_x \\ \Delta\sigma_y \\ \Delta\sigma_z \\ \Delta\tau_{xy} \end{Bmatrix} = \frac{E}{(1+\mu)(1-2\mu)} \begin{bmatrix} (1-\mu) & \mu & \mu & 0 \\ \mu & (1-\mu) & \mu & 0 \\ \mu & \mu & (1-\mu) & 0 \\ 0 & 0 & 0 & (1/2-\mu) \end{bmatrix} \begin{Bmatrix} \Delta\varepsilon_x \\ \Delta\varepsilon_y \\ \Delta\varepsilon_z \\ \Delta\gamma_{xy} \end{Bmatrix} \tag{2.15}$$

where

$\boldsymbol{\mu}$ is the Poisson's ratio and

E is the Young's modulus.

2.3.1.3 ELEMENT EQUATIONS

Element equations are those that govern the deformational behaviour of each element. They essentially combine the **compatibility, equilibrium and constitutive behaviour**. For a single element of linear elastic material subjected to an infinitesimal strain, the satisfaction of the above result in the following set of equations:

$$K_e \cdot d_e = R_e \tag{2.16}$$

where

$K_e = \int (B^T \cdot D \cdot B) dV$ is the element stiffness matrix,

d_e is the vector of the corresponding nodal displacements (the primary unknown), and

$R_e = \int [N]^T \{\Delta F\} dV + \int [N]^T \{\Delta T\} dS$ is the vector of the corresponding nodal forces, or the right hand side vector.

2.3.1.4 GLOBAL EQUATIONS

The next stage in the formulation of the finite element equations is the assembly of the separate element equilibrium equations into a set of global equations:

$$K \cdot d = R \tag{2.17}$$

where

K is the global stiffness matrix assembled from the element stiffness matrices, $\boldsymbol{K_e}$**:**

$$K = \sum K_e = \sum \int (B^T \cdot D \cdot B) dV \tag{2.18}$$

d is the vector of the unknown nodal displacements (degrees of freedom) of the finite element mesh and

R is the global right hand side load vector.

2.3.1.5 BOUNDARY CONDITIONS

The final stage the finite element formulation is the application of the boundary conditions. There are two categories of boundary conditions. These are the loading and the displacement conditions which fully define the boundary value problem being analysed.

- Loading boundary conditions affect the right hand side vector, ***R***. These include the effects of body forces, $\boldsymbol{R_b}$, surface tractions, $\boldsymbol{R_s}$, initial stresses, $\boldsymbol{R_i}$, and pore pressure changes, $\boldsymbol{R_f}$, given by the following equations:

$$R = R_b + R_s + R_i + R_f \tag{2.19}$$

$$R_b = \sum \int \left(N_\delta^T \cdot f_b \right) dV \tag{2.20}$$

$$R_s = \sum \int \left(N_\delta^T \cdot f_s \right) dS + F_c \tag{2.21}$$

$$R_i = \sum \int \left(B^T \cdot \sigma_i \right) dV \tag{2.22}$$

$$R_f = \sum \int \left(B^T \cdot \Delta u \cdot m \right) dV \tag{2.23}$$

where

$\boldsymbol{V}$ is the volume of the element,

$\boldsymbol{S}$ is the area of an element over which surface tractions are applied,

$\boldsymbol{f_b}$ is the vector of body forces,

$\boldsymbol{f_s}$ is the vector of applied forces,

$\boldsymbol{F_c}$ is the vector of concentrated nodal loads,

$\boldsymbol{\sigma}$ is the vector of the initial stresses,

$\boldsymbol{\Delta u}$ is the change in pore pressure and

$\boldsymbol{m}$ is a column matrix

- Displacement boundary conditions affect the vector of nodal displacements, d. During the solution process, the equation corresponding to the prescribed degree of freedom (displacement component) must be effectively eliminated. In order to retain any rigid body modes of deformation (e.g. rotations, translations), sufficient displacement conditions must be prescribed in all cases. Unless these conditions are satisfied, the global stiffness matrix will be singular and the equations cannot be solved.

2.3.1.6 NUMERICAL INTEGRATION

In order to evaluate the global stiffness matrix, ***K***, and right hand side load vector, ***R***, in *equation (2.17),* integrations over element volumes, ***V***, and surfaces, ***S***, must be carried out. The explicit evaluation of these element integrals cannot usually be performed, except for some special cases, and therefore a numerical integration scheme is often used. In this process the integral of a function *f(x)* is replaced by a weighted sum of the function $f(x_i)$ evaluated at *m* integration points

$$\int f(x)dx = \sum f(x_i) \cdot w_i \qquad (2.24)$$

where

w_i is the weighting factor that corresponds to integration point ***i***, (i = 1 ,2,.. .,m).

The values of w_i and the location of the integration points depends on the type of integration scheme being used. The number of integration points determines the integration order and the higher the order the more accurate the integration process. However, the computation effort increases substantially with number of integration points. ICFEP employs the Gaussian integration scheme with up to 16 (4x4) integration points (see Nyaoro, 1989).

2.3.1.7 SOLUTION OF GLOBAL EQUATIONS

The solution of the global equations is the last stage in the finite element formulation. After the establishment of the global stiffness matrix and the boundary conditions have been added, in order to get the values for the unknown nodal displacements, ***d***, a large system of simultaneous equations has to be solved. Several mathematical techniques are available.

2.3.3 NON LINEAR ANALYSIS

The previous paragraph gave the basic principles of the Finite Element Method in the simple case of a linear elastic material. As it is already known, this does not apply for the real soil behaviour we usually seek to capture as it is highly non-linear. This paragraph extends the theory previously presented and describes how the finite element method can be adapted to deal with the nonlinear constitutive models used to

describe the real soil behaviour. In the case of non-linear elastic constitutive models the elastic constitutive matrix ***D*** is no longer constant but varies with stress and/or strain. The use of the non-linear constitutive models also involves the incremental application of the boundary conditions. There are various methods to do so, the most popular of which are:

- the tangent stiffness scheme,
- the visco-plastic scheme and
- the **modified Newton-Raphson** scheme

According to Potts and Zdravkovic (1999) "the tangent stiffness and the visco-plastic approaches are sensitive to increment size and can lead to inaccurate predictions, unless many small solution increments are adopted. The modified Newton-Raphson scheme is consistently shown to be both the most robust and most economical." Consequently, the modified Newton-Raphson method has been used throughout this thesis and this is the one briefly presented here.

The incremental application of the boundary conditions requires the solution of the incremental form of the global equilibrium *equation (2.16):*

$$K_i \cdot \Delta d_i = \Delta R_i \tag{2.25}$$

The above equation is solved by the modified Newton-Raphson method by utilising an iterative technique. In the first iteration, an approximate stiffness matrix, K_o, and the incremental vector, ΔR_i are used. It is however expected that the solution will be in error, therefore, the predicted incremental displacements are used to calculate the residual load, ψ^i, as following:

$$\psi^{i} = R - \sum \int (B^T \cdot \sigma) dV \tag{2.26}$$

The above expression is actually a measure of the error in the analysis. Equation (2.17) is then solved again with this residual load forming the right hand side vector:

$$\Delta d_i = \left[K_o\right]^1 \cdot \psi^{j-1} \tag{2.27}$$

where the superscript *j* refers to the iteration number, whereas $\psi^0 = \Delta R$.

The above process is repeated until **convergence** is succeeded and it is illustrated in *Figure 2.20* for a single degree of freedom.

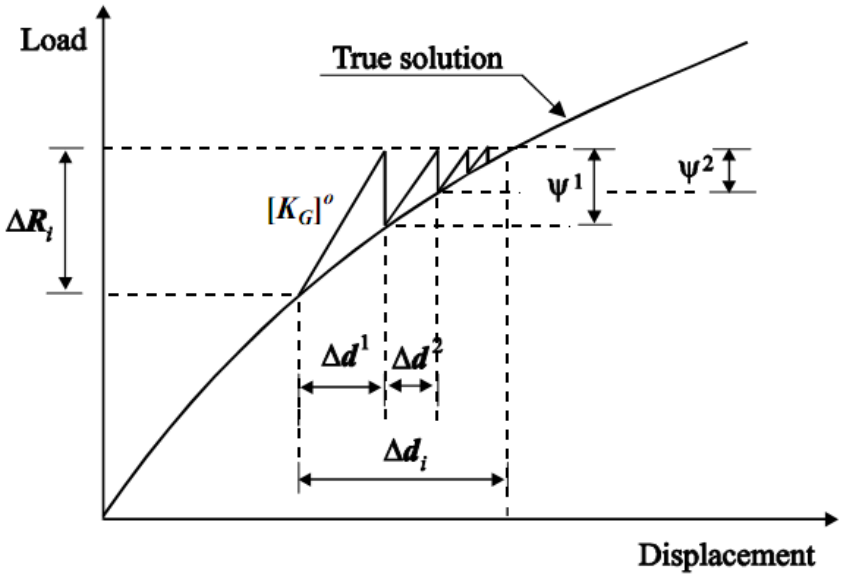

***Figure 2.20**: Application of the modified Newton-Raphson algorithm to the uniaxial loading of a bar of a non-linear material* (after Potts and Zdravkovic, 1999)

In the above figure, the incremental displacements, ***Δd,*** are equal to the sum of the iterative displacements, ***Δd.***

The convergence of the solution can either be determined by checking the changes of the iterative applied loads (residual loads) or the iterative displacements or both. Consequently, a **convergence tolerance** has to be determined. In the analysis reported in this thesis, convergence has been determined by checking the changes of the iterative displacements and the respective tolerance was set to *2%*, which means that the norm of the iterative values of the parameters should be less than *2%* for the solution to converge.

In order to define the stress changes, the modified Newton-Raphson method first determines the residual load vector $\boldsymbol{\psi}^i$. At the end of each iteration, the current estimate of the incremental displacements is used to evaluate the incremental strains, and, finally, the constitutive model is then integrated along the incremental strain paths to obtain an estimate of the stress changes:

$$\Delta\sigma = \int D^{ep}(\varepsilon,\sigma)d\varepsilon \tag{2.28}$$

where D^{ep} is the elasto-plastic stress-strain matrix. These stress changes are added to the initial stresses and are used to evaluate the integral in *equation (2.18).*

It is understood that, since the constitutive behaviour varies over the increment, *equation 2.28* must be integrated in order to obtain the stress changes. This is accomplished by the application of a stress point algorithm which can be approached by different methods. ICFEP uses a **sub-stepping algorithm with a modified Euler integration scheme.**

The procedure starts with the determination of the elastic proportion of the increment. Then the remaining elasto-plastic strain increment is divided into a number of smaller sub-steps (or flow steps). A modified Euler approximation is used for the integration of the constitutive equations over each sub-step. The size of the sub-step can be determined by estimating the error in the numerical integration. The overall stress changes at the end of the iteration are obtained by summing the stress changes from each sub-step. *(Figure 2.21)*

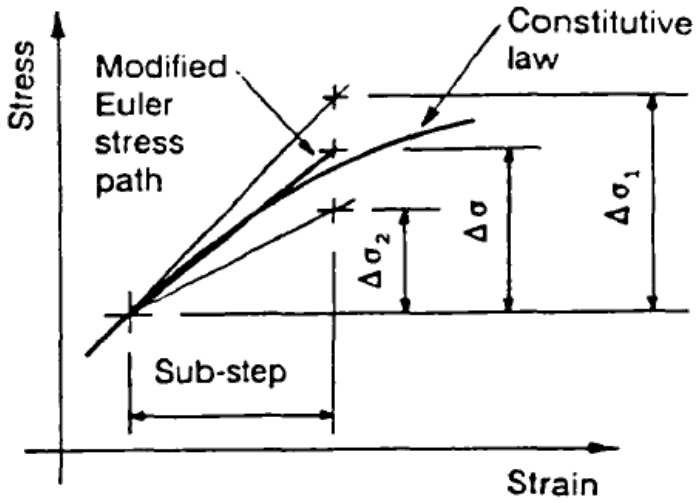

***Figure 2.21**: Modified Euler sub-stepping* (after Kovacevic, 1994)

2.4 LABORATORY TESTS: APPARATUSES & PROCEDURES

To impose any arbitrary stress state on a soil element, one must control simultaneously all six components of stress (σ_x, σ_y, σ_z, τ_{xy}, τ_{yz}, τ_{zy}) that fully define the stress state of the soil element. Unfortunately, there is no experimental device that allows the full control of all six stress components. Conventional triaxial compression, triaxial extension, and simple shear tests allow control of two principal stresses only. The true triaxial test (using a cubical soil specimen) allows control of the three principal stresses (σ_1, σ_2, σ_3), although it does not allow a continuous rotation of the directions of their axes. It is in fact limited to only a sudden 90^o rotation. Consequently, the effects of cross-anisotropy in natural or reconstituted soil cannot be fully investigated with the true triaxial device (Saada, 1988). *Figure 2.22* summarizes all experimental devices of a geotechnical laboratory, the degrees of freedom each one controls and the range of the parameters ***a*** and ***b*** that each one achieves.

The ***b*** parameter represents the relative value of the intermediate mean stress σ_2 to the maximum and minimum mean stresses σ_1 and σ_3. It is equal to

$$b = \frac{\sigma_2 - \sigma_3}{\sigma_1 - \sigma_3} \tag{2.29}$$

The angle ***a*** represents the direction of the maximum mean stress σ_1.

triaxial loading	α=0°	0°<α<90°	α=90°	b=0	0<b<1	b=1	B.E.*
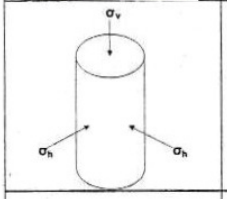	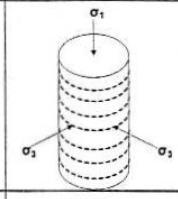		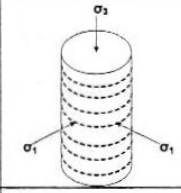	●		●	2
true triaxial loading	α=0°	0°<α <90°	α=90°				
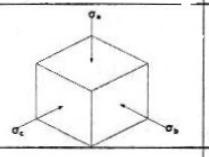	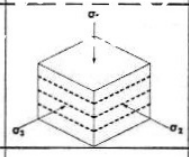		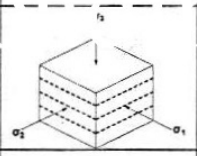	●	●	●	3
plane strain	α=0°	0°<α<90°	α=90°				
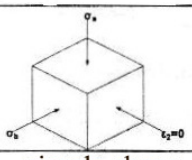	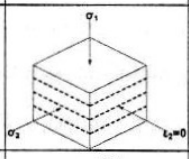		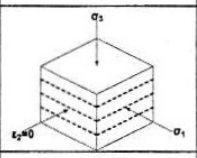		~0.3**		2
simple shear	α=0°	0°<α<90°	α=90°				
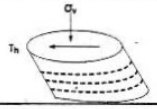		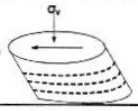			~0.3***		2
trorsional shearing: hollow cylinder specimen	α=0°	0°<α<90°	α=90°				
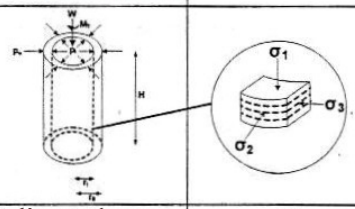				●	● ****	●	3 4
direct shear	α=0°	0°<α<90°	α=90°				
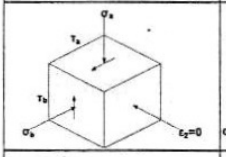	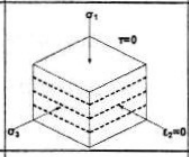	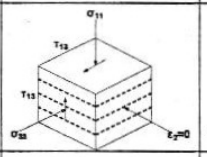	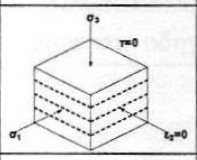	●	●	●	3
direct shear	α=0°	0°<α<90°	α=90°				
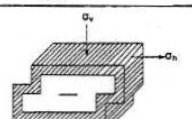		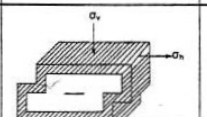			***		2

B.E. – Degrees of Freedom

*** cannot be controlled*

**** cannot be controlled or measured*

***** parameters a and b are connected with the equation $b=\sin^2 a$ when $p_i=p_o$.*

***Figure 2.22**: Experimental apparatuses.* (after Tsomokos, 2004)

In *Figure 2.22* it can be seen that the hollow cylinder apparatus offers a favorable alternative by allowing, within certain range of stresses, the control of the three principal stresses, as well as the continuous rotation of two principal stress directions.

Analytical descriptions of all devices can be found in the literature, presenting the advantages and weaknesses of each device (Saada and Townsend, 1981; Height et al., 1983; Saada, 1988; Tatsuoka, 1988). In this part of the chapter the experimental procedures and their basic features of the respective apparatuses of the tests used in this thesis are briefly presented. These are namely the triaxial apparatus and triaxial testing procedure as well as the hollow cylinder apparatus and the torsional shear testing procedure.

2.4.1 TRIAXIAL TEST

2.4.1.1 TRIAXIAL APPARATUS

The triaxial apparatus or the triaxial cell is perhaps the most commonly used piece of laboratory equipment in a geotechnical laboratory. It is described in detail by Bishop and Henkel (1962) in their standard text book on triaxial testing of soil. Its main advantages are that it is simple to operate and also large strain levels can be achieved. By using specified gauges on the sample, the triaxial apparatus can also be used for the measurement of very small strains (by the order of 0.0001%) and the study of the non-linear characteristics of the soil materials. Its main disadvantages lie on the fact that the direction of the mean effective stress $\boldsymbol{\sigma_1}$ can either be vertical ($\alpha=0^o$, compression) or horizontal ($\alpha=90^o$, extension). The angle α cannot have a value between 0^o and 90^o and the intermediate mean effective stress is always equal to the triaxial cell pressure.

A cross section of a conventional triaxial apparatus is schematically shown in *Figure 2.23*. It incorporates a cylindrical soil sample which has a diameter of 38mm. The sample is enclosed within a thin rubber membrane. The membrane is sealed at the top and bottom platens by rubber O-ring seals. It gives flexibility to radial deformation of the cell pressure sample. It also separates pore pressures generated inside the sample from total radial stresses applied to the outside of the sample.

The sealed sample is placed on a pedestal in a water-filled cell. An all-around cell pressure, σ_c, applies radial total stress, σ_r, to the vertical sides of the sample and a uniform vertical stress to the top rigid platen *(Figure 2.24).* An additional axial force, F_a, is applied to the top platen via a loading frame.

Pore pressure can be measured in the end platens adjacent to the bottom and/or top end of the sample, or by a probe placed at approximately mid-height of the sample.

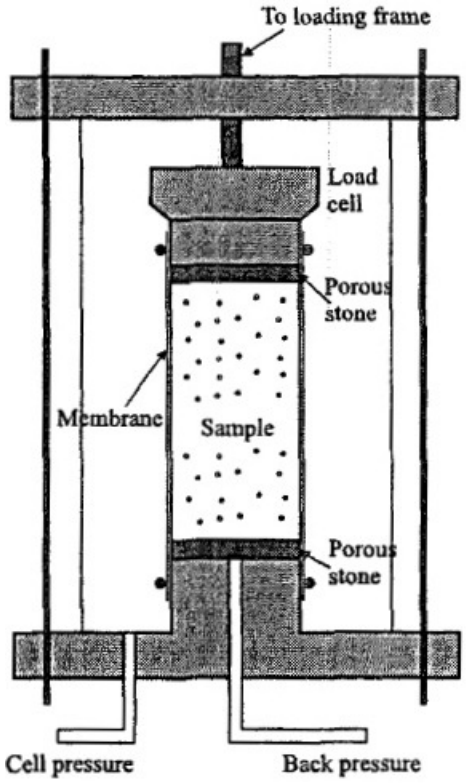

Figure 2.23*: Schematic representation of a conventional triaxial apparatus* (after Potts and Zdravkovic, 1999)

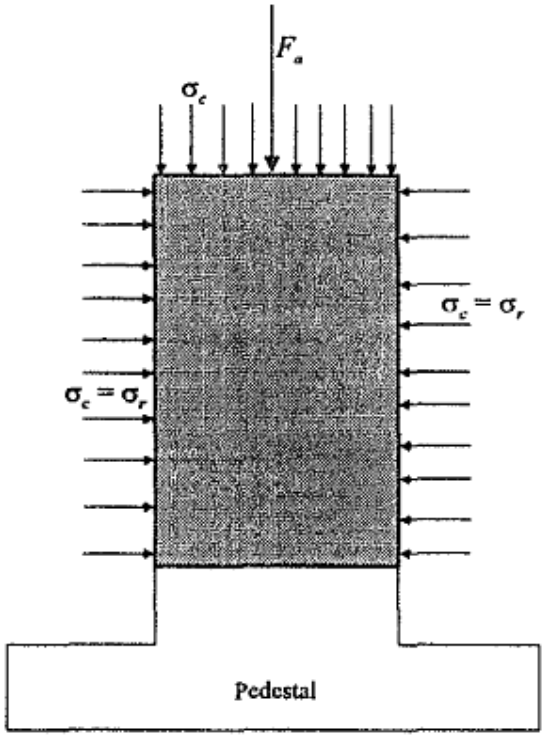

***Figure 2.24**: Stresses applied on a triaxial sample* (after Potts and Zdravkovic, 1999)

It is possible to perform several different tests by making use of the triaxial apparatus, the most common of which are:

- ✓ one-dimensional compression (similar to oedometer conditions)
- ✓ isotropic compression
- ✓ drained of undrained shearing

depending on the stress scenario and the conditions desirable to apply.

2.4.1.2 EXPERIMENTAL PROCEDURE

In this paragraph, the steps of the experimental procedure of the triaxial test are briefly discussed.

1. Before every test the triaxial apparatus is carefully cleaned by the residues of any previous test. This is done by inducing water or air through the pressure supply tubes of the cell and the pore pressure tubes.
2. The porous stone is then placed on the pedestal. The porous stone allows the flow of water and at the same time blocks the leak of the solid grains of the material.

3. Then the impermeable elastic membrane is applied around the pedestal of the sample which is withheld with an O-ring. This way the leak of water or material from the pedestal is prevented. The membrane is of a cylindrical shape with diameter almost equal to the diameter of the pedestal, while its height is a bit longer than the height of the sample (80mm).
4. Next a metallic cell is also applied at the pedestal that will give the sample the shape of a cylinder. The cell is divided into 3 similar parts that are applied at the bottom of the sample and among them with the use of a metallic ring. This ring enables the adjustment of the diameter. The cylinder should be vertically placed and should be as stable as possible.
5. The metallic cell is now externally surrounded by new membranes. These are temporarily placed, as long as the sample preparation takes place and are then removed before the consolidation phase. In order to seal the metallic cell as to not have air and pressure between the 3 parts of the cell, the part of the elastic membrane that protrudes out of the internal of the cell is applied to the external edge around the other membranes.
6. Afterwards, back pressure is applied to the cell. By doing so, the internal membrane is fitted to the cell's paries. The back pressure is applied by the air suction from the space between the membrane and the cell around it. An air pump is used to achieve this. The pump is connected to the cell by a flexible tube applied to a specified exit of the cell.
7. At his point the material to be tested is ready to be induced, the sand namely. The material should have already been weighted by an electronic balance of high accuracy. The sand is weighted with its container and the container is weighted separately. The difference between the two weights gives the net weight of the sand. Usually 140-160gr of soil is required to fill the metallic cell. For this reason a bigger quantity should be prepared and then the surplus material is weighted and deducted. A first estimation of the material quantity is therefore calculated. A second measurement takes place after experiment: The sample is induced in the oven, at a stable temperature of 95^{o}C and is weighted again.

8. The sample is produced either by the dry deposition method (if it contains fine ingredients) or by the water sedimentation method (if standard sand is concerned).
9. By applying the dry deposition method, the sand is directly induced into the metallic cell using a funnel. Small quantity of sand should be allowed to exit and from a small height so that the grains are evenly distributed and in order to obtain a high value pore index (if a loose sample is required). The production of dense samples is achieved by vibration, namely by tipping the cell walls. This causes the re-distribution of the grains and its condensation.
10. After the cylinder is full, a new porous stone is applied at the top of the cell. It should be applied with special care as to not condensate the sample. At the top of the cell a metal ring is also placed, upon which the second O-ring is applied.
11. A top cap is applied at the upper surface of the porous stone. The tube within which the back pressure is applied to the sample abuts to the top cap. The cap is temporarily held in horizontal place and at a steady height with the use of a metallic arm. This arm is placed on a vertical bar placed on the apparatus.
12. The protruding part of the membrane is lifted up and applied to the cap and the porous stone. The O-ring is then applied to the vertical cylindrical surface of the cap.
13. The same back pressure is applied through the cap as to the one applied initially. This way the membrane maintains its surface tightly applied to the sample. Now, the sample has the ability to stand thanks to the membrane and the elastic rings without the help of the metallic rings that can now be removed. This way the sample is standing at a vertical position thanks to the back pressure applied through the cap.
14. In the next step, the diameter and the height of the sample are measured. They are measured in three different points around the sample and the average values are extracted.
15. For at least half an hour the sample is carbonated (channeling of carbon dioxide – CO_2) as to replace the containing air. CO_2 is more easily dissolvable into water than the air. The gas is channeled in through a special hole in the pedestal and channeled out through the cap. Special care should be taken on

this step, as the channeling of gas inside the sample destabilizes the back pressure and if this happens very rapidly the sample may collapse.

16. In the next step the sample is saturated with water. The water is also channeled through a hole in the pedestal. It is channeled out through the cap while a part of it remains inside the sample replacing the CO_2. The water level inside the sample can be seen though the membrane as it fills the sample.

17. Inclinometers are placed in the surface of the sample with the use of powerful glue.

18. At this point the cell can be put into place and filled with water.

19. Since the cell has been filled with water, the confining pressure can be applied. Consequently, the back pressure is no liger needed to keep it in place. Moreover, it is desirable to achieve high pore water pressure (300-400kPa). This way a higher degree of saturation can be achieved, as air and CO_2 are more easily dissolvable into water. During this step it is essential to keep the mean effective stress (that is, the difference between the cell pressure and the pore pressure) steady and not higher than the final consolidation stress that is desirable. That is in order to maintain isotropic conditions. For this reason, the increase takes place in small steps of 50 kPa, which is applied simultaneously at the cell and inside the sample as pore pressure. This control is achieved by the computer to which the apparatus is connected.

20. The degree of saturation is frequently calculated during the pressure increase. That is equal to the change in the pore pressure under undrained conditions divided by the respective change in the cell pressure. For a fully saturated sample this should be equal to 1. In order to continue the experiment it is required to be higher than 0.95. It has been observed that the use of CO_2 provides values of 0.95-0.97.

21. During consolidation the final effective stress is defined by adjusting the difference between the cell pressure and the pore pressure. Once this value has been reached, the sample is let in free drained condition for at least one hour. During this period of time its volume is decreasing symmetrically which is verified by the water flow that occurs. This water quantity is accurately measured.

22. By the end of consolidation it is possible to initiate the shearing of the sample: The piston which lies on the top of the cell is manually lowered as to come almost in contact with the top cap.
23. In the next step, the pressure inside the axial pressure cell becomes equal the cell pressure. Next, it starts to increase in very small steps. Once it has sufficiently overcome the cell pressure, the pedestal, which communicates with the piston, has the tendency to rise. It cannot do so as it is blocked by the piston, it applies and receives force which is measured by the load gauge.
24. At his point the automatic hydraulic pump is connected to the apparatus. With the use of a specified computer programme the pump has the ability to apply axial strain to the sample on a stead slow rate. The programme continuously calculates the rate of the applied axial strain and respectively adjusts the applied axial force. This way the strain rate remains constant and equal to the desirable value that has been set.
25. Depending on whether the experiment is under drained or undrained conditions, the pore pressure valve is open or closed respectively.
26. During the experiment, the measurements of all gauges are frequently recorded:
    - ✓ the applied axial force to the sample,
    - ✓ the cell pressure which remains constant as water is flowing out of the cell, the pore pressure inside the sample,
    - ✓ the increase and the decrease of the water quantity inside it (zero for undrained conditions),
    - ✓ the measurements of the axial strain gauges on the sample and
    - ✓ the axial strain at the pedestal of the sample.
27. All the desirable curves are obtained by the further processing of the above measurements in a specified software programme (e.g. MS Excel)

2.4.2 HOLLOW CYLINDER TEST

2.4.2.1 HOLLOW CYLINDER APPARATUS

As it has already been mentioned, the hollow cylinder apparatus allows full control of both the magnitude and the rotation of principal stresses. That makes it the most suitable device to explore soil anisotropy.

For a cylindrical specimen to be considered hollow, the following geometrical properties should be present:

- ✓ its height should be greater than its external diameter. This ratio should be greater than 2 as for the stress distribution in the center of the specimen not to be influenced by its rigid edges.
- ✓ the thickness if the specimen wall should not be smaller than its internal diameter.

A hollow cylinder apparatus allows the application of four independent loads:

- ✓ the inner cell pressure, p_i,
- ✓ the outer cell pressure, p_o,
- ✓ the vertical load, W, and
- ✓ the torque, M_T

The above combination of loads allows the control of four component stresses, namely the normal stresses σ_z, σ_r, σ_θ, and the torsional shear stress $\tau_{z\theta}$ ($\tau_{rz}= \tau_{r\theta}=0$). This way it is possible to control the magnitude and the direction a of the principal stresses. It is also possible to independently control the parameter b *(equation 2.29).* Thus, it is possible to perform different sets of shear tests, either changing a with a constant value of b or vice versa. This way it is possible to evaluate the effects of each one of the two parameters independently.

In the hollow cylinder device, all strain components are locally measured:

- ✓ the three normal strains, ε_z, ε_r and ε_θ and
- ✓ the torsional shear strain, $\gamma_{z\theta}$
- ✓ ($\gamma_{rz}= \gamma_{r\theta}=0$)

That way the strain state is fully determined and known.

It is understood that the hollow cylinder test is ideal for investigating the anisotropic behaviour of soil. Both stiffness and strength parameters can be estimated from tests performed in this apparatus.

In spite of all the advantages the hollow cylinder test may provide, there are some disadvantages in its use. That is, for example, the difficulty in the specimen

preparation, especially when undisturbed specimens of cohesive soils are required. Specified production procedures of specimens are employed in such cases. Another disadvantage is the phenomenon of the penetration of the surrounding membrane in the void pores of the specimens in the case of granular materials. Especially the influence of the membrane is more important in the hollow cylinder test because the ratio of the surface in contact with the membrane to the total volume of the specimen is five times greater than the respective ratio concerning a bulk cylindrical specimen.

The membrane penetration takes place under drained loading conditions while under undrained conditions membrane compliance takes place. Both phenomena are similar but they affect the hollow cylinder specimens in different ways. With the change in the mean effective stress the membrane penetration affects the measurements in the volume change of the specimen while the membrane compliance depends on the state of the specimen. If the radial pressure decreases (tendency to contract) the membrane draws away from the voids leading to an underestimation of the pore water pressure and overestimation of the strength. The opposite occurs when the specimen shows tendency to dilate.

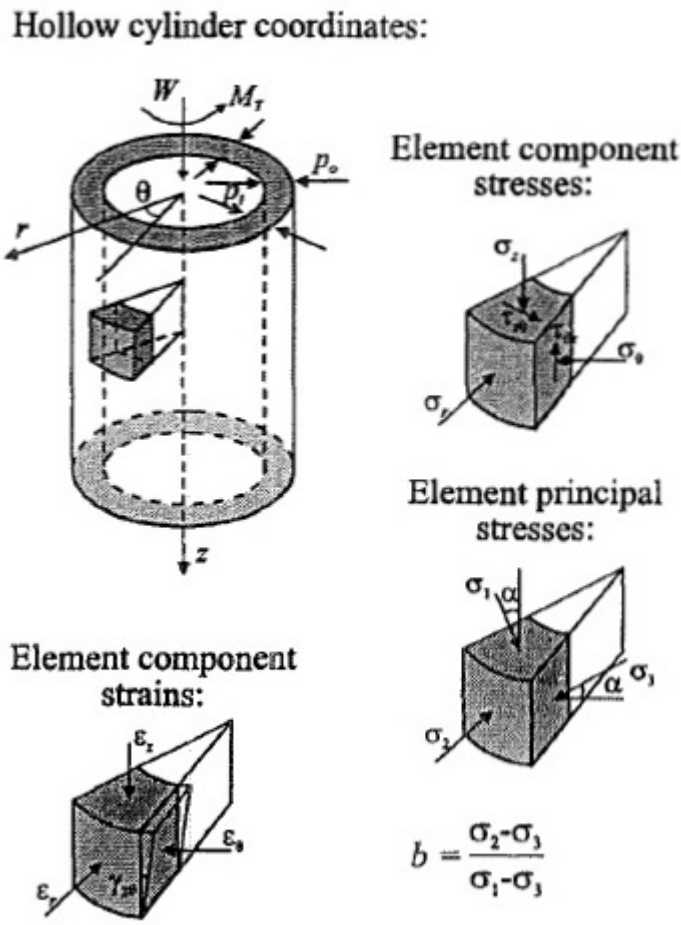

***Figure 2.25**: Schematic representation of the hollow cylinder sample and stresses applied.* (after Potts and Zdravkovic, 1999)

2.4.2.2 EXPERIMENTAL PROCEDURE

In the following, the experimental procedure followed for the performance of the monotonic torsional hollow cylinder tests presented in this thesis is briefly described.

The procedure involving the production, placement, saturation, isotropic consolidation and loading of the specimen consists of the following steps:

1. The thickness of the internal and the external impermeable membranes within which the specimen lies are measured. The internal membrane is the one that is first placed on the cylindrical pedestal of the specimen while it is held into place and dried there by the use of special elastic rings made from caoutchouk (O-rings).

2. The cylindrical pedestal is placed and screwed on the pedestal of the triaxial cell. Next, the pipelines that are utilized for the drainage of the specimen are connected. The external membrane is placed next just like the internal membrane was placed (using two O-rings)
3. The specified metallic matrices are closed up around the external and inside the internal membrane. A back pressure of approximately 20kPa is applied in the space between the external and the matrix through the supply unit. This was the membrane is sucked and set on the walls – having taken the desirable cylindrical shape.
4. The specimen space is next filled with deionized and deaired water. The sand is wetly laid in the same space by utilising a funnel with applied tube of 1.5cm diameter. This way the best possible saturation is secured. The sand deposition is performed by a height that changes continuously in order to maintain the distance from the surface of the sand that has already been deposited and consequently to maintain the incidence energy constant. This way the higher uniformity possible of the specimen is secured as well as the ability to produce similar specimens. The above specimen production method has been proposed by Bishop and Henkel (1957) and it is called "pluviation through water" and is suitable for the production of loose specimens. Denser specimens are possible to produce by depositing the whole quantity or in three sequential layers and equal hits on the external metallic matrix per each layer. The upper surface of the specimen is then made plane and a specified cap with a rigid porous disc are placed on top. Finally, the top drainage line is connected.
5. A back pressure of approximately ***30kPa*** is applied to the specimen through the drainage line and the change in its volume is measured. The back pressure, which is equivalent to a mean effective stress ***p'=30kPa,*** adds strength to the specimen and the metallic matrices can be displaced. After the metallic matrices have been displaced the external diameter and the height of the specimen are measured with an accuracy of 0.01mm. Next, the part of the apparatus which is used to apply the external load is put into place and deaired water is pumped through the specimen from the base to the top. This way the specimen and the drainage lines get fully saturated.

6. The external jacket of the cell is put into place and all bolts are screwed as to seal the chamber. Next, the chamber is filled with water by opening the supply valve.
7. The confining pressure of the cell is then increased as well as the pore water pressure (simultaneously) in order to maintain the mean effective stress of the specimen at 30kPa.
8. In order to check the degree of saturation of the specimen the Skempton parameter B is used (1954). According to this method, if a stress change $\Delta\sigma$ is applied isotropically under undrained loading conditions to a fully saturated soil element, excess pore water pressures are developed $\Delta\sigma = \Delta u$. If the element is not fully saturated then the excess pore water pressure is $\Delta u < \Delta\sigma$. In the experiments conducted the degree of saturation was assumed to be full for values of parameter B higher than 0.97 which were usually achieved after 2-3 hours after the specimen production.
9. The specimen is isotropically consolidated by changing the confining pressure and at the same time increasing, via the balance pressure, the axial stress and maintaining the pore water pressure constant. The final value of the mean effective stress for the experiments presented in this thesis was 100kPa, 200kPa or 300kPa.
10. After the isotropic consolidation a time period of 12 hours leaves the secondary consolidation to take place. This period is the same for all specimens so that they have the same stress history.
11. The torsional loading of the specimen is next. The loading is performed under either under drained or undrained conditions which is defined by whether the drainage valve is open or closed respectively. All loadings are stress controlled. During the monotonic torsional loading the procedure is terminated when at a torque value for which the specimen has demonstrated all its specific characteristics.

CHAPTER 3

NUMERICAL SIMULATION

INTRODUCTION

Lade has developed two elasto-plastic constitutive models that capture the behavior of cohesionless soils or granular materials: a single hardening model, with a single yield surface *(Kim and Lade, 1988; Lade and Kim, 1988a, 1988b)* and a double hardening model, with two intersecting yield surfaces *(Lade, 1977)*. In the first part of this chapter the double hardening model is presented, as it is the main model used for the numerical simulation of Ottawa sand in the present thesis.

In 1994, in his PhD thesis related to the design and analysis of concrete face rock fill dams, Kovacevic implemented Lade's single and double hardening models in ICFEP. It was considered purposeful to present the adaptation of Lade's equations for this implementation, as there were changes that had to be made in order to avoid numerical problems. Any additional options or alterations offered are presented as well, in order to keep full track of the analysis procedure while running the finite element analysis. This composes the second part of this chapter.

In the third part of this chapter, the calibration of Lade's model is thoroughly presented for Loose Ottawa Sand in order to obtain the values of the fourteen parameters required to fully determine the soil behaviour according to the model. A total of 12 drained triaxial compression tests and equal number of isotropic

compression tests have been assessed for this procedure, performed in the National Technical University of Athens.

Finally, it should be noted that in this chapter there has been effort to present both Lade's and Kovacevic different notations for completeness's reasons.

3.1 LADE'S DOUBLE HARDENING MODEL *(LADE, 1977)*

Lade's double hardening model is an extension of a previously developed model *(Lade and Duncan, 1975)* which employed a single yield surface. It involves the employment of curved yield and failure surfaces, the use of work-hardening and work-softening relationships and an added cap-yield surface.

The model is based on the elasto-plastic stress-strain theory for cohesionless soils which is observed in laboratory tests. These tests include isotropic compression and drained triaxial compression tests. All the parameters of the model can derive from these tests.

The theory Lade developed incorporates a yield criterion, a non-associated flow rule and an empirical work-hardening law. This way he managed to encapsulate the characteristics of the behavior of sand as observed in several different laboratory tests, such as cubical triaxial laboratory tests, torsion shear tests and tests performed using various stress paths. Lade predicted the results of such tests with reasonable accuracy. The concepts of elasticity and plasticity which had been developed at the time were taken into consideration, as well as all the essential aspects of the behavior of cohesionless soils observed in experimental investigations: nonlinearity, the influence of σ_2, stress-path dependency, shear-dilatancy effects and coincidence of strain increment and stress axes at high stress levels.

Lade had to make some basic assumptions in order to be able to develop the model, which result to certain limitations:

- while laboratory tests show that proportional loading with increasing stresses does cause some plastic deformation, for proportional loading only elastic strains are predicted

- failure envelopes of sand are assumed straight in the previous theory, while experiments show that most often they are curved in the Mohr diagram
- the gradual change of the behavior characteristics from those typical of dense sand to those typical of loose sand with increasing confining pressure is not accounted for

3.1.1 BASIC BEHAVIOR OF COHESIONLESS SOILS

Lade observed the behavior of three different cohesionless soils in isotropic compression and triaxial compression tests, each one tested at two different densities: Sacramento River Sand *(Dr = 38% & Dr = 100%)*, Crushed Napa Basalt *(Dr = 70% & Dr = 100%)* and Painted Rock Material *(Dr = 70% & Dr = 100%)*. He verified his theory by comparing laboratory measured strains and strains predicted by his theory for a number of laboratory test conditions. He demonstrated that the theory accurately predicts soil behavior in triaxial tests over a range of confining pressures in which the maximum stress ratio decreases (curved failure envelope) and the volume change behavior becomes compressive with increasing confining pressure. He also managed to capture the post-peak behavior for the certain range of confining pressures used in the tests. Finally, he predicted pore pressures in undrained tests and since with his theory handles stress-path dependency, he assumes that most aspects of undrained behavior can be accounted for.

The characteristics of the three soils Lade used to develop his theory vary in terms of composition, grain shape, grain size, and maximum and minimum void ratios.

3.1.1.1 TYPES OF STRAIN

Lade modeled the stress-strain behavior of soils basing on the elasto-plastic theory, according to which the total strain increments $\{d\varepsilon_{ij}\}$, are divided into an elastic component, $\{d\varepsilon^{e}_{ij}\}$, a plastic collapse component, $\{d\varepsilon^{c}_{ij}\}$, and a plastic expansive component, $\{d\varepsilon^{p}_{ij}\}$ so that:

$$\left\{d\varepsilon_{ij}\right\}=\left\{d\varepsilon^{e}_{ij}\right\}+\left\{d\varepsilon^{c}_{ij}\right\}+\left\{d\varepsilon^{p}_{ij}\right\} \tag{3.1a}$$

or, simply

$$\Delta\varepsilon=\Delta\varepsilon^{e}+\Delta\varepsilon^{p}=\Delta\varepsilon^{e}+\left[\Delta\varepsilon^{p1}+\Delta\varepsilon^{p2}\right] \tag{3.1b}$$

Each of these strain components is calculated separately:

- the **elastic strains**, $\Delta\varepsilon^{e}$, are calculated by **Hooke's law**,
- the **plastic collapse strains**, $\Delta\varepsilon^{p1}$, are calculated by a plastic stress-strain theory involving a **cap-type yield surface** and, finally,
- the **plastic expansive strains** are calculated by a stress-strain theory involving a **conical-type yield surface** with apex at the origin of the stress space.

In the following *Figure 3.1* the parts of the total strain are schematically illustrated in a stress difference $(\sigma_1-\sigma_3)$ – axial strain ε_1 and volumetric strain ε_v – axial strain ε_1 diagram for a triaxial compression test concerning Sacramento River Sand of a relative density $Dr=38\%$ and initial void ratio $e=0.87$. The test is for a constant value of confining pressure σ_3.

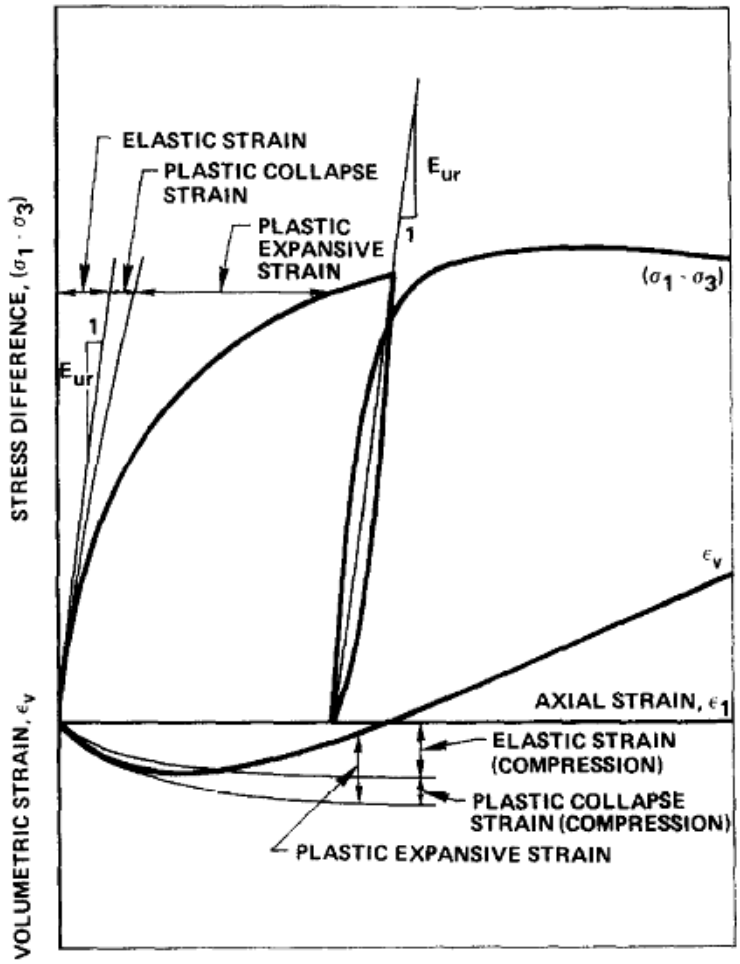

Figure 3.1: *Schematic illustration of elastic, plastic collapse and plastic expansive strain components in drained triaxial compression test.* (After Lade, 1977)

It can be observed that:

- from the very beginning of the loading both elastic (recoverable) and plastic (unrecoverable) deformations occur
- the stress-strain relationship is non-linear
- a decrease of strength follows peak failure
- the volumetric strain is initially compressive with a behavior followed by expansion - in other cases it can be followed by continued compression
- the plastic strains are initially smaller than the elastic strains, but at higher values of stress difference the plastic strains tend to become larger

In the following it is explained how each component of these strains can be calculated.

3.1.1.2 ELASTIC BEHAVIOUR

When referred to elastic strain increments, it is meant those which are recoverable upon unloading. In order to calculate these increments, **Hooke's law** is used. The purely elastic response of the model is described by isotropic elasticity and therefore requires two independent elastic parameters. The elastic modulus used is the one referred to the unloading-reloading cycle:

$$E_{ur} = K_{ur} \cdot p_a \cdot \left(\frac{\sigma_3}{p_a} \right)^n \tag{3.2a}$$

where

- the dimensionless, constant value of the modulus number $\boldsymbol{K_{ur}}$ and the exponent $\boldsymbol{n}$ are dimensionless parameters that can be calculated from triaxial compression tests performed at various confining pressures σ_3,
- $\boldsymbol{p_a}$ is the atmospheric pressure expressed in the same units as E_{ur} and σ_3.

According to Lade, because of the fact that the value of Poisson's ratio has often found to be close to *0.20* for the elastic parts of unloading – reloading stress paths, it is therefore used in all his calculations, as it was also used for the present thesis.

In ICFEP, there are three alternatives for the modeling of Young's modulus *(Kovacevic 1994):*

-The first, coincides with that of Lade's *(1977)*, mentioned above, based on drained triaxial compression tests and refers to the same expression for the initial tangent modulus *(Janbu, 1963),* or the unloading-reloading modulus *(Duncan and Chang, 1970)* that is expressed as a power function of the effective confining pressure, σ'_3:

$$E = M \cdot p_a \cdot (\frac{\sigma'_3}{p_a})^n \tag{3.2b}$$

where

- $\boldsymbol{p_a}$ is the atmospheric pressure expressed in the same units as E and σ'_3,
- $\boldsymbol{M}$ is the modulus number and $\boldsymbol{n}$ is the elastic exponent, both dimensionless and constant at a given initial void ratio

-The second expression is a more generalized one, where the minor principal stress σ'_3 is replaced by the mean effective stress, p':

$$E = M \cdot p_a \cdot \left(\frac{p'}{p_a} \right)^n \tag{3.2c}$$

where

$$p' = \frac{\sigma'_1 + \sigma'_2 + \sigma'_3}{3} = \frac{\sigma'_x + \sigma'_y + \sigma'_z}{3} \tag{3.3}$$

-The third option is of importance if the loading involves many stress reversals. The following expression is after Lade and Nelson *(1987)* and is derived from theoretical considerations based on the principle of conservation of energy. Young's modulus is expressed as following:

$$E = N \cdot p_a \cdot \left[\left(\frac{I_1}{p_a} \right)^2 + R \cdot \left(\frac{J_2}{p_a^2} \right) \right]^\lambda \tag{3.2d}$$

where

- $R = 6 \cdot \frac{1-\upsilon}{1-2\upsilon}$, (3.4)

- $I_1 = \sigma_1' + \sigma_2' + \sigma_3' = \sigma_x' + \sigma_y' + \sigma_z'$, (3.5)

the first invariant of the effective stress tensor $\boldsymbol{I_1}$,

- $$J_2 = J^2 = \frac{1}{6}[(\sigma_1' - \sigma_2')^2 + (\sigma_2' - \sigma_3')^2 + (\sigma_3' - \sigma_1')^2] = \frac{1}{6}[(\sigma_x' - \sigma_y')^2 + (\sigma_y' - \sigma_z')^2 + (\sigma_z' - \sigma_x')^2] + \tau_{xy}^2 + \tau_{yz}^2 + \tau_{zx}^2 \quad (3.6)$$

the second invariant of the deviatoric stress tensor $\boldsymbol{J_2}$,

- the parameter $\boldsymbol{p_a}$ is the atmospheric pressure expressed in the same units as E, I_1 and $(J_2)^{1/2}$ and
- the modulus number, $\boldsymbol{N}$, and the exponent, $\boldsymbol{\lambda}$, are constant, dimensionless parameters.

M, n, N and $\boldsymbol{\lambda}$ are linked between them as follows:

$$M = 3^{2\lambda} \cdot \mathrm{N} \quad (3.7)$$

$$n = 2 \cdot \lambda \quad (3.8)$$

3.1.1.3 PLASTIC COLLAPSE BEHAVIOUR

Plastic collapse strains are generally produced by any increase in mean normal stress and plastic shear strains are associated with the shear stresses acting on the soil skeleton. For a general stress increment (not along the hydrostatic axis) plastic collapse strains and plastic expansive strains occur simultaneously and it is therefore difficult to separate them. Therefore the magnitudes of the plastic collapse strains have to be calculated from an isotropic compression test because it is the only loading condition that does not produce any plastic expansive strains.

During an isotropic compression loading-unloading cycle, part of the strains is recoverable (elastic), and part is irrecoverable (plastic). That is due to the increasing isotropic stresses which cause a partial collapse of the grain structure resulting in a volumetric compression.

Figure 3.2 shows an isotropic compression test for loose Sacramento River Sand (relative density *Dr=38%,* initial void ratio *e=0.87*). The diagram is an isotropic stress σ_3 – volumetric strain ε_v *(%)* diagram with two loading – unloading – reloading cycles. For every cycle it is easy to distinguish the recoverable and the irrecoverable strains. As shown, the recoverable (elastic) strains are successfully calculated from Hooke's law, as mentioned above. Therefore, the plastic collapse strains can be easily calculated if the elastic strains are subtracted from the total strains along such a cycle.

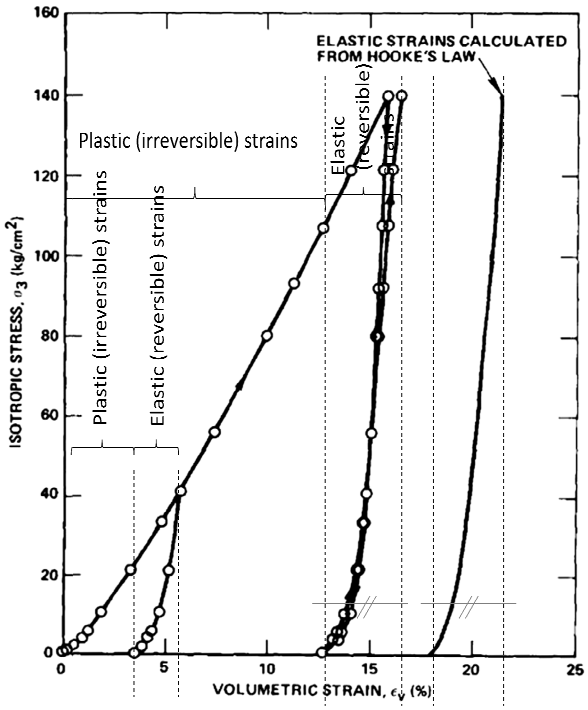

Figure 3.2: *Isotropic compression of loose Sacramento River Sand with primary loading, unloading and reloading branches.* (After Lade, 1977)

YIELD CRITERION

Lade used a yield criterion that forms a cap on the open end of the conical yield surface in order to model the above described behavior *(Figure 3.3).* This collapse yield criterion forms a sphere with center in the origin of the principal stress space and it is used in connection with the conical yield surface. The equation describing the yield cap can be written in terms of first and second stress invariants I_1 and I_2:

$$f_c = I_1^2 + 2 \cdot I_2 \tag{3.9a}$$

or

$$F_2 = I_1^2 + 2 \cdot I_2 - H_2 = 0 \tag{3.9b}$$

where:

$$I_1 = \sigma_1' + \sigma_2' + \sigma_3' = \sigma_x' + \sigma_y' + \sigma_z'$$

(3.10)

$$I_2 = -(\sigma_1' \cdot \sigma_2' + \sigma_2' \cdot \sigma_3' + \sigma_3' \cdot \sigma_1') = \tau_{xy} \cdot \tau_{yx} + \tau_{yz} \cdot \tau_{zy} + \tau_{zx} \cdot \tau_{xz} - (\sigma_x' \cdot \sigma_y' + \sigma_y' \cdot \sigma_z' + \sigma_z' \cdot \sigma_y')$$

(3.11)

H_2 is the work-hardening parameter described in the following relevant paragraph describing the work-hardening law.

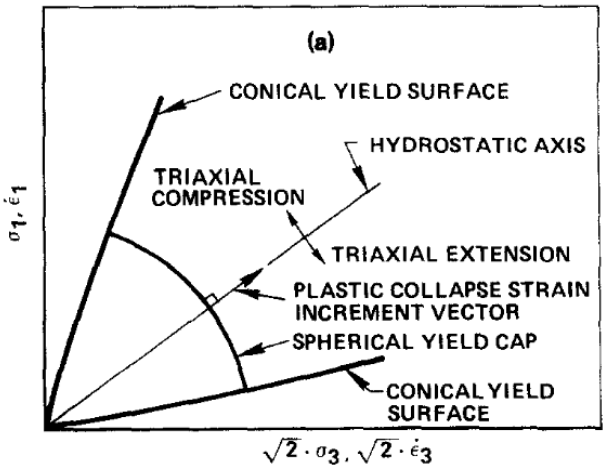

Figure 3.3: *Location of yield cap relative to conical yield surface shown in triaxial plane.* (After Lade, 1977)

As the value increases beyond its current value, the soil work-hardens and collapse strains are produced. It should be noted that yielding according to equations *(3.9a)* or *(3.9b)* does not result in eventual failure as failure is controlled entirely by the conical yield surface.

PLASTIC POTENTIAL AND FLOW RULE

In *Figure 3.3*, the strain increment vector is pointed in the direction outward from the origin and coincides with the hydrostatic axis. This is because during isotropic compression the strains are equal in all three principal directions for an isotropic soil.

In order to fulfill this condition, the plastic potential function, g_c, must be identical to the yield criterion, f_c. According to Lade, the flow rule is then derived from:

$$\Delta\varepsilon_{ij}^{c} = \Delta\lambda_c \cdot \frac{\partial f_c}{\partial \sigma_{ij}} \tag{3.12}$$

where $\Delta\lambda_c$ is a proportionality constant. The derivatives of f_c with respect to the normal stresses become:

$$\frac{\partial f_c}{\partial \sigma_x} = 2 \cdot \sigma_x \tag{3.13}$$

And with respect to the shear stresses:

$$\frac{\partial f_c}{\partial \tau_{yz}} = 2 \cdot \tau_{yz} \tag{3.14}$$

WORK-HARDENING LAW

The above mentioned parameter $\Delta\lambda_c$ (proportionality constant) can be determined from the work-hardening law.

For an isotropic compression test the plastic work can be determined empirically from the following expression:

$$W_c = \int \sigma_3 \cdot d\varepsilon_{\upsilon}^{c} \tag{3.15}$$

where

- $\sigma_3 \cdot d\varepsilon_{\upsilon}^{c}$ is the plastic work done per unit volume during the volumetric strain increment $d\varepsilon_{\upsilon}^{c}$

For isotropic compression f_c is:

$$f_c = 3 \cdot \sigma_3^2 \tag{3.16}$$

If W_c and f_c are plotted on a log-log diagram, the relationship between them can be described with good accuracy by the following expression:

$$W_c = C \cdot p_a \cdot \left(\frac{f_c}{p_a^2} \right)^p \tag{3.17a}$$

or

$$H_2 = p_a \cdot \left(\frac{W_{p2}}{C \cdot p_a} \right)^{\frac{1}{p}} \tag{3.17b}$$

where

- ***C*** is the dimensionless collapse modulus and
- ***p*** the collapse exponent, also dimensionless
- W_{p2} is the accumulated plastic work associated with the cap yield surface

$$W_{p2} = \sum(\Delta W_{p2}) = \sum(\sigma^{\mathrm{T}} \cdot \Delta\varepsilon^{p2}) \tag{3.18}$$

In the diagram the value of C is determined at $f_c/p_a^2=1$ and p is the slope of the adopted straight line.

Figure 3.4 shows the above mentioned diagram for loose Sacramento River Sand.

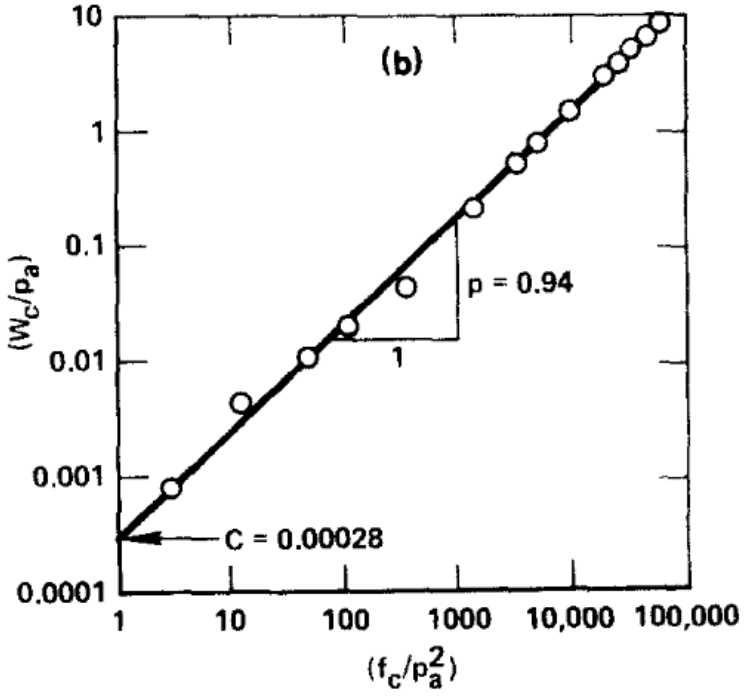

Figure 3.4: *Relation between plastic collapse work, W_c, and the value of f_c for loose Sacramento River Sand.* (After Lade, 1977)

The cap yield surface uses an associated flow rule, F_2=G_2.

The proportionality constant $\Delta\lambda_c$ can now be calculated:

$$\Delta\lambda_c = \frac{dW_c}{2 \cdot f_c} \tag{3.19}$$

3.1.1.4 PLASTIC EXPANSIVE BEHAVIOUR

FAILURE CRITERION

Lade had already suggested a three-dimensional failure criterion with the form of $I_1^3 / I_3 = const$ (Lade and Duncan, 1975). Such a criterion is in better agreement with experimental results than the widely used Mohr-Coulomb. That is, as shown in the following figure *(Figure 3.5),* because it is curved with no corners and this way captures the decrease of the friction angle with increasing magnitude of the mean normal stress.

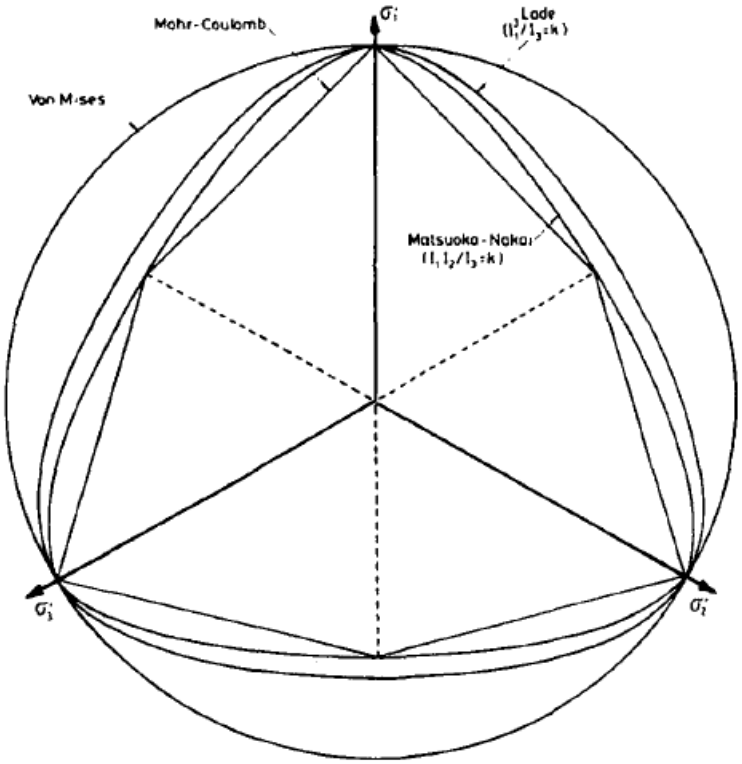

Figure 3.5*: Failure surfaces in the deviatoric plane* (after Gens and Potts, 1988)

Moreover, it takes into account the value of the intermediate principal effective stress, σ_2'. In his double hardening model, Lade *(1977)* extended this three dimensional failure criterion to the following:

$$f_p = \left(\frac{I_1^3}{I_3} - 27 \right) \cdot (\frac{I_1}{p_a})^m \tag{3.20}$$

with

$$f_p = \eta_1^{'} \quad , \quad \text{at failure}$$

where

I_1 is the first stress invariant *(see equation 3.10)* and

$$I_3 = \sigma_1' \cdot \sigma_2' \cdot \sigma_3'$$
$$= \sigma_x' \cdot \sigma_y' \cdot \sigma_z' + \tau_{xy} \cdot \tau_{yz} \cdot \tau_{zx} + \tau_{yx} \cdot \tau_{zy} \cdot \tau_{xz} - (\sigma_x' \cdot \tau_{yz} \cdot \tau_{zy} + \sigma_y' \cdot \tau_{zx} \cdot \tau_{xz} + \sigma_z' \cdot \tau_{xy} \cdot \tau_{yx})$$

(3.21)

is the third stress invariant.

According to Lade, the parameters $\acute{\eta}_1$ and m are dimensionless, constants at a given initial void ratio.

In *Figure 3.6* the above mentioned failure surface is illustrated in the principal stress space. It has the shape of an asymmetric bullet with the pointed apex at the origin of the stress space. The apex angle and the curvature of the surface increase with the increase of the values of $\acute{\eta}_1$ and *m.* For *m=0* the expression of the failure surface becomes $I_1^3 / I_3 = const$ (Lade and Duncan, 1975).

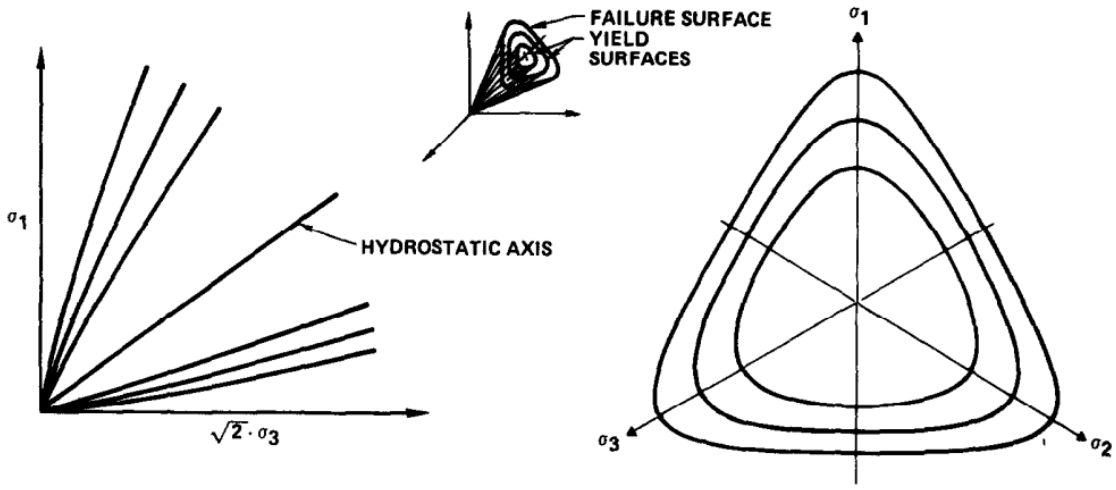

Figure 3.6: *Characteristics of proposed failure and yield surfaces shown in the principal stress space. (a) Traces of failure and yield surfaces in triaxial plane. (b) Traces of yield surfaces in octahedral plane.* (After Lade, 1977)

Lade *(1977)* notes in the developments of his theory that "*the failure surface given in the above equation is always concave towards the hydrostatic axis. However, the real failure surfaces for cohesionless soils open up and become conical at very high values of the mean normal stress (Lee and Seed, 1967). The failure criterion is therefore only valid in the range of mean normal stresses where the failure surface is concave towards the hydrostatic axis. This range of mean normal stresses is dependent on the*

integrity of the soil grains, and only when crushing becomes an important factor in the soil behavior does the real failure surface deviate from that expressed in the above equation. However, for most soils the stresses necessary to produce appreciable crushing are of a magnitude to be found, e.g. at the bottom of very tall earth dams."

In 1984 Lade extended his theory in order to include the effective cohesion and tensile strength which can be sustained by concrete or rock, or compacted clay fill. Ha added a constant stress, $a \cdot p_a$, to the normal effective stresses, σ', before substitution to the failure equation. $a \cdot p_a$ reflects the effect of the tensile strength of the material. a is a dimensionless parameter.

YIELD CRITERION

The boundary between states of stress where only elastic deformations occur and states of stress where both elastic and plastic deformations occur is defined by the yield surface. The yield surface has the same shape as the failure surface. Increasing loading (increasing the value of f_p) causes the symmetrical expansion of the yield surface around the hydrostatic axis. When $f_p=\acute{\eta}_1$, the yield surface reaches its ultimate position which is the failure surface. During unloading or neutral loading, the yield surface maintains its position (the one for the highest value of f_p) and thus the soil hardens isotropically.

PLASTIC POTENTIAL AND FLOW RULE

The plastic potential function associated with the conical yield surface is of the following form (similar to the failure criterion):

$$g_p = G_1 = I_1^3 - \left[27 + \acute{\eta}_2 \cdot \left(\frac{p_a}{I_1}\right)^m\right] \cdot I_3 \qquad (3.22)$$

where

$\acute{\eta}_2$ is a parameter which depends on H_1 and the minimum principal effective stress, σ'_3. Its expression will derive from the following.

Equation (3.22) gives the plastic potential surfaces which are shaped as asymmetrical bullets with their pointed apices at the origin of the stress space. Their traces in

triaxial planes are similar to those of the yield surface shown in *Figure 3.5(a)* but they are more curved, with greater apexes and they cut the yield surfaces while they become asymptotic to the hydrostatic axis at a greater rate than the yield surfaces. Their traces in octahedral planes are the same as those for the yield surfaces shown in *Figure 3.5(b).*

The relation between stress and strain is derived:

$$\Delta\varepsilon_{ij}^{p} = \Delta\lambda_{p} \cdot \frac{\partial g_{p}}{\partial \sigma_{ij}} \tag{3.23}$$

According to the above equation, the strain increments are proportional to the derivatives of the plastic potential. The derivatives of g_p with respect to the normal stresses become:

$$\frac{\partial g_{p}}{\partial \sigma_{x}} = 3 \cdot I_1^2 - \left[27 + \acute{\eta}_2 \cdot \left(\frac{p_a}{I_1} \right)^m \right] \cdot \left(\sigma_y \cdot \sigma_z - \tau_{yz}^2 \right) + \frac{I_3}{I_1} \cdot m \cdot \acute{\eta}_2 \cdot \left(\frac{p_a}{I_1} \right)^m \tag{3.24}$$

And the derivatives of g_p with respect to the shear stresses become:

$$\frac{\partial g_{p}}{\partial \tau_{yz}} = \left[27 + \acute{\eta}_2 \cdot \left(\frac{p_a}{I_1} \right)^m \right] \cdot \left(\sigma_x \cdot \tau_{yz} - \tau_{xy} \cdot \tau_{zx} \right) \tag{3.25}$$

Equations (3.23) and (3.25) show that they model the coupling between shear stresses and normal strains and the coupling between normal stresses and shear strains respectively. This is a significant feature of the stress-strain relations as it is consistent with observed soil behaviour.

The value of $\acute{\eta}_2$ can be determined by the following:

$$v^{p} = \frac{\Delta\varepsilon_3^{p}}{\Delta\varepsilon_1^{p}} \tag{3.26}$$

Substitution of *equations (3.23)* and *(3.25)* to *equation (3.26)* gives:

$$\acute{\eta}_2 = \frac{3\cdot\left(1+\upsilon^p\right)\cdot I_1^2 - 27\cdot\sigma'_3\cdot(\sigma'_1+\upsilon^p\cdot\sigma'_3)}{\left(\frac{p_a}{I_1}\right)^m\cdot\left[\sigma'_3\cdot\left(\sigma'_1+\upsilon^p\cdot\sigma'_3\right)-\frac{m\cdot(1+\upsilon^p)\cdot I_1^2}{f_p\cdot\left(\frac{p_a}{I_1}\right)^m+27}\right]} \tag{3.27}$$

Lade researched the relation between $\acute{\eta}_2$ and f_p or H_1 for loose Sacramento River Sand and came up with the following expression:

$$\acute{\eta}_2 = \rho\cdot \mathrm{H}_1 + R\cdot\left(\frac{\sigma'_3}{p_a}\right)^{1/2} + t \tag{3.28}$$

where

- ***ρ***, ***R*** and ***t*** are dimensionless parameters.
- ***H1*** is the work-hardening (-softening) parameter explained in the following paragraph.

WORK-HARDENING AND –SOFTENING LAW

The work-hardening and –softening law applied by Lade is an isotropic one, which means that the yield surface expands or contracts uniformly. It also implies that the degree of hardening or softening is independent of the stress path. The isotropic hardening hypothesis assumes that the relationship between the total plastic work W_{p1} and the degree of hardening or softening expressed by the value of f_p *(or H_1)* is unique:

$$W_{p1} = F_{p1}(f_p) = F_{p1}(H_1) \tag{3.29}$$

where:

- ***Wp1*** is the accumulated plastic "expansive" work:

$$W_{p1} = \int\left\{\sigma_{ij}\right\}^T\left\{d\varepsilon_{ij}^p\right\} = \sum(\Delta W_{p1}) = \sum(\sigma^{\mathrm{T}}\cdot\Delta\varepsilon^{p1}) \tag{3.30}$$

where

- $(\sigma^T\cdot\Delta\varepsilon^{p1})$ is the plastic work done per unit volume during the strain increment vector $\Delta\varepsilon^{p1}$.

Figure 2.7 shows the variation of the total plastic work with the value of f_p (or H_1) for different values of the confining pressures for drained triaxial tests in Loose Sacramento River Sand.

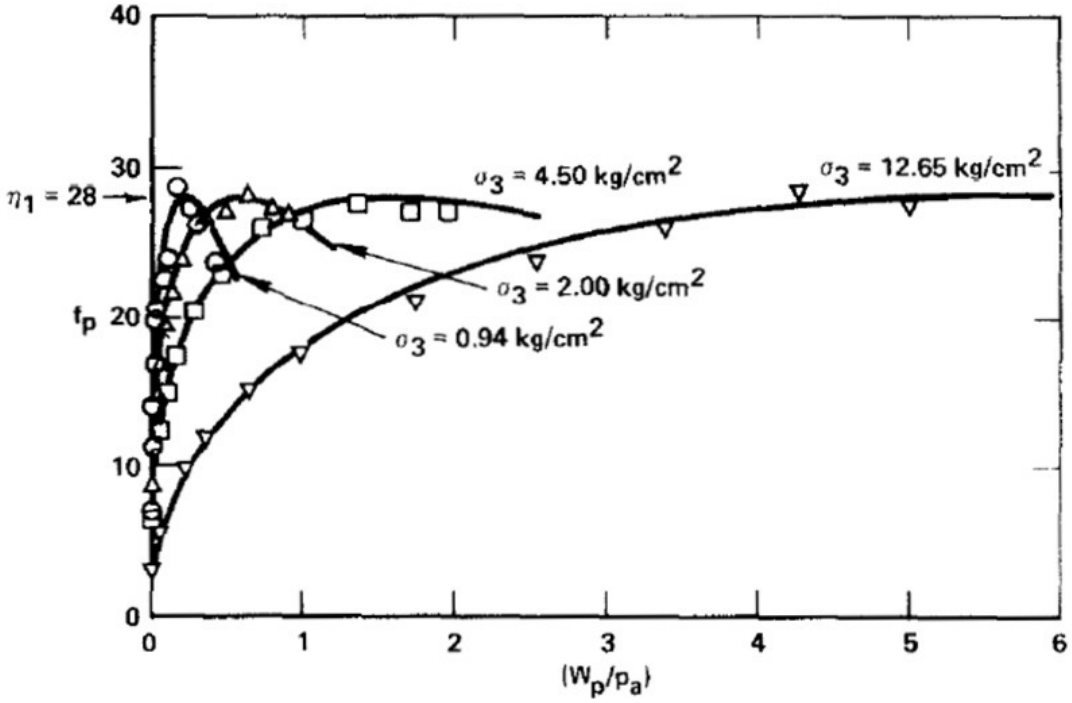

Figure 3.7: *Variation of total plastic work with f_p and σ'_3 for Loose Sacramento River Sand.* (After Lade, 1977)

The work-hardening relationships have vertical tangents at the origin. This is as expected, as at small strain levels the plastic strains produced are very small, even negligible. It can also be seen increasing plastic strain increments are produced with increasing stress levels. The influence of the confining pressure on the amount of plastic work necessary to produce plastic strains at high stress levels is evident in this diagram. The amount of plastic work required to reach the peaks increases with increasing confining pressure. However, all peaks occur where $f_p=\eta_1$.

The relations between W_{p1} and f_p (or H_1) shown in *Figure 3.7* can be approximated by exponential functions for which the following expression is used:

$$H_1 = a \cdot e^{-b \cdot W_{p1}} \cdot \left(\frac{W_{p1}}{p_a}\right)^{1/q}, \qquad q \geq 1 \tag{3.31}$$

The parameters a, b and q depend on the minimum principal effective stress, σ'_3 as following:

$$a = \acute{\eta}_1 \cdot (e \cdot \frac{p_a}{W_{p1p}})^{1/q} \tag{3.32}$$

$$b = \frac{1}{q \cdot W_{p1p}} \tag{3.33}$$

$$q = \alpha + \beta \cdot \frac{\sigma'_3}{p_a}, \qquad q \geq 1 \tag{3.34}$$

where α and β are different from a and b referred to previously.

q is also defined as following:

$$q = \frac{\log\left(\frac{W_{p1p}}{W_{p1,60}}\right) - \left(1 - \frac{W_{p1,60}}{W_{p1p}}\right) \cdot \log e}{\log\left(\frac{\acute{\eta}_1}{H_{1,60}}\right)} \tag{3.35}$$

where $(W_{p1,60}, H_{1,60})$ and $(W_{p1p}, \acute{\eta}_1)$ are two sets of corresponding values on a curve in F*igure 3.7*, and e is the base for natural algorithms. W_{p1p} is the accumulated plastic work associated with the conical yield surface at peak strength. *"Any two points on a curve could in principle be used to determine q, but the best overall curvefit is obtained when the peak point of the curve and the point corresponding to 60% of* $\acute{\eta}_1$ *on the work-hardening part of the curve are used",* according to Lade.

W_{p1p} is also found to depend on the minimum principal effective stress, σ'_3 as following:

$$W_{p1p} = P \cdot p_a \cdot (\frac{\sigma'_3}{p_a})^l \tag{3.36}$$

where ***P*** and ***l*** are dimensionless parameters of the material.

Finally, it is noted that McCarron and Chen *(1988)* simplified the expression for the work-hardening parameter H_1, in the following form:

$$H_1 = \acute{\eta}_1 \cdot [\xi \cdot \exp(1 - \xi)]^{1/q}, \qquad q \geq 1 \tag{3.37}$$

where

$$\xi = \sum \left(\frac{\Delta W_{p1}}{W_{p1p}}\right) \tag{3.38}$$

This, in particular is mentioned because it will be useful for the model's implementation to the finite element program, presented thoroughly in the following.

Overall, it can be seen that in order to fully define the soil behaviour through Lade's double hardening model, a total of fourteen parameters are required (This number increases to fifteen if the material has effective cohesion, which is not the case in the present thesis):

- Three parameters associated with the elastic response of the material:
  - the elastic modulus number ***M***
  - the elastic exponent ***n*** and
  - Poisson's ratio ***υ***
- Three parameters required to define the plastic collapse strain component:
  - the collapse modulus ***C*** and
  - the collapse exponent ***p***
- Nine parameters are required to define the plastic expansive strain increment component
  - the failure constant $\acute{\eta}_1$,
  - the failure exponent ***m***,
  - the plastic potential constant ***ρ,***
  - the plastic potential constant ***R***,
  - the plastic potential constant ***t***,
  - the work-hardening constant ***α***,
  - the work-hardening constant ***β***,
  - the work-hardening constant ***P*** and
  - the work-hardening exponent ***l***

3.2 IMPLEMENTATION OF LADE'S MODEL INTO ICFEP *(KOVACEVIC, 1994)*

Kovacevic, in his PhD thesis *(1994)* related to the design and analysis of concrete face rock fill dams, he implemented Lade's single and double hardening models into ICFEP. It is interesting, form a numerical analysis point of view, to present this implementation. Using the basic equations described previously, Kovacevic obtained the incremental elasto-plastic stress-strain relationships. Their proper implementation into ICFEP was checked against numerous comparisons that were already published in the literature by Lade himself and others.

The incorporation of any elasto-plastic constitutive model into ICFEP requires an incremental stress – incremental strain relationship that has the following form:

$$\Delta\sigma = D^{ep} \cdot \Delta\varepsilon \tag{3.39}$$

where Dep is an elasto-plastic stress-strain matrix. Kovacevic, in order to develop this stress-strain matrix, he applied the procedure described by Lade and Nelson *(1984)* for developing the stress-strain matrix for an elasto-plastic material with multiple yielding surfaces.

Following are the basic concepts and assumptions from classical plasticity theory for the derivation of the incremental elasto-plastic stress-strain relationships *(Duncan et al, 1977)*:

- **Yield function.** The yield function for any hardening/softening material is a function not only of stresses, but also of plastic strains

$$F(\sigma, \varepsilon^p) = 0 \tag{3.40}$$

- **Plastic potential function.** It is expressed as a function of the stresses:

$$G = G(\sigma) \tag{3.41}$$

- The **plastic strain increments** are normal to the plastic potential and they are expressed as:

$$\Delta\varepsilon^p = \lambda \cdot \frac{\partial G}{\partial \sigma} \tag{3.42}$$

  where λ is an arbitrary constant and $\frac{\partial G}{\partial \sigma}$ defines the outward normal to the plastic potential surface.

- **Incremental elastic and plastic strain.** During an incremental change in stress, the total strain increment vector, $\Delta\varepsilon$, is divided into an elastic component, $\Delta\varepsilon^e$, and a plastic component, $\Delta\varepsilon^p$, as equations (3.1a) and (3.1b) indicate.
- **Relationship between stress increment and elastic increment.** The stress increment vector, $\Delta\sigma$, and elastic strain increment vector, $\Delta\varepsilon^e$, are related by means of a symmetric elastic stress-strain matrix, D^e:

$$\Delta\sigma = D^e \cdot \Delta\varepsilon^e \tag{3.43}$$

According to Lade's double hardening model, the plastic flow takes place around the intersection of two isotropically work-hardening yield surfaces. The "consistency condition" requires that:

$$\Delta F_1 = [\frac{\partial F'_1}{\partial \sigma}]^{\mathrm{T}} \cdot \Delta\sigma - \frac{\partial \mathrm{H}_1}{\partial W_{p1}} \cdot \Delta W_{p1} = 0 \tag{3.44a}$$

$$\Delta F_2 = [\frac{\partial F'_2}{\partial \sigma}]^{\mathrm{T}} \cdot \Delta\sigma - \frac{\partial \mathrm{H}_2}{\partial W_{p2}} \cdot \Delta W_{p2} = 0 \tag{3.44b}$$

where $\Delta\sigma$ is the stress change occurring during plastic flow. The subscripts *"1"* and *"2"* denote parameters relevant to each one of the two yield surfaces.

The corresponding plastic strains are given by the two plastic components (plastic collapse and plastic expansive) which because of equations (3.1b) and (3.42) become:

$$\Delta\varepsilon^p = \lambda_1 \cdot \frac{\partial G_1}{\partial \sigma} + \lambda_2 \cdot \frac{\partial G_2}{\partial \sigma} \tag{3.45}$$

According to equations (3.1b) and (3.43):

$$\Delta\sigma = D^e \cdot (\Delta\varepsilon - \lambda_1 \cdot \frac{\partial G_1}{\partial \sigma} - \lambda_2 \cdot \frac{\partial G_2}{\partial \sigma}) \tag{3.46}$$

Substituting for $\Delta\sigma$ from equation (3.46) into equations (3.44a) and (3.44b) gives:

$$\lambda_1 \cdot L_{11} + \lambda_2 \cdot L_{12} = T_1 \tag{3.47}$$

$$\lambda_1 \cdot L_{21} + \lambda_2 \cdot L_{22} = T_2 \tag{3.48}$$

where

$$L_{11} = [\frac{\partial F_1'}{\partial \sigma}]^{\mathrm{T}} \cdot D^e \cdot [\frac{\partial G_1}{\partial \sigma}] + \frac{\partial H_1}{\partial W_{p1}} \cdot \sigma^{\mathrm{T}} \cdot [\frac{\partial G_1}{\partial \sigma}] \tag{3.49}$$

$$L_{22} = [\frac{\partial F_2'}{\partial \sigma}]^{\mathrm{T}} \cdot D^e \cdot [\frac{\partial G_2}{\partial \sigma}] + \frac{\partial H_2}{\partial W_{p2}} \cdot \sigma^{\mathrm{T}} \cdot [\frac{\partial G_2}{\partial \sigma}] \tag{3.50}$$

$$L_{12} = [\frac{\partial F_1'}{\partial \sigma}]^{\mathrm{T}} \cdot D^e \cdot [\frac{\partial G_2}{\partial \sigma}] \tag{3.51}$$

$$L_{21} = [\frac{\partial F_2'}{\partial \sigma}]^{\mathrm{T}} \cdot D^e \cdot [\frac{\partial G_1}{\partial \sigma}] \tag{3.52}$$

$$\mathrm{T}_1 = [\frac{\partial F_1'}{\partial \sigma}]^{\mathrm{T}} \cdot D^e \cdot \Delta\varepsilon \tag{3.53}$$

$$\mathrm{T}_2 = [\frac{\partial F_2'}{\partial \sigma}]^{\mathrm{T}} \cdot D^e \cdot \Delta\varepsilon \tag{3.54}$$

Solution of equations (3.47) and (3.48) gives:

$$\lambda_1 = \frac{L_{22} \cdot T_1 - L_{12} \cdot T_2}{L_{11} \cdot L_{22} - L_{12} \cdot L_{21}} \tag{3.55a}$$

$$\lambda_2 = \frac{L_{11} \cdot T_2 - L_{21} \cdot T_1}{L_{11} \cdot L_{22} - L_{12} \cdot L_{21}} \tag{3.55b}$$

The above equations, if substituted for λ into equation (3.45) and using equation (3.46), the elasto-plastic stress-strain matrix, D^{ep}, for the constitutive law with two yield surfaces is written now in as following:

$$D^{ep} = D^e - \frac{1}{A} \cdot D^e \cdot ([\frac{\partial G_1}{\partial \sigma}] \cdot b_1^T + [\frac{\partial G_2}{\partial \sigma}] \cdot b_2^T) \cdot D^e \tag{3.56}$$

where

$$A = L_{11} \cdot L_{22} - L_{12} \cdot L_{21} \tag{3.57}$$

$$b_1 = L_{22} \cdot [\frac{\partial F_1'}{\partial \sigma}] - L_{12} \cdot [\frac{\partial F_2'}{\partial \sigma}] \tag{3.58a}$$

$$b_2 = L_{11} \cdot [\frac{\partial F_2'}{\partial \sigma}] - L_{21} \cdot [\frac{\partial F_1'}{\partial \sigma}] \tag{3.58b}$$

It is obvious that this matrix is non-symmetrical for non-associative flow on any of the yield surfaces.

The individuals components in equations (3.49)-(3.54) and (3.58a)-(3.58b) have been given by Lade and Nelson *(1984).*

$$\frac{\partial F_1'}{\partial \sigma} = (\frac{\mathrm{I}_1^3}{\mathrm{I}_3} - 27) \cdot \frac{m}{p_a} \cdot \left(\frac{I_1}{p_a}\right)^{m-1} \begin{bmatrix} 1 \\ 1 \\ 1 \\ 0 \\ 0 \\ 0 \end{bmatrix} + \left(\frac{I_1}{p_a}\right)^{m} \cdot \frac{\mathrm{I}_1^2}{\mathrm{I}_3^2} \cdot \begin{bmatrix} 3 \cdot I_3 - (\sigma_y' \cdot \sigma_z' - \tau_{yz}^2) \cdot I_1 \\ 3 \cdot I_3 - (\sigma_z' \cdot \sigma_x' - \tau_{zx}^2) \cdot I_1 \\ 3 \cdot I_3 - (\sigma_x' \cdot \sigma_y' - \tau_{xy}^2) \cdot I_1 \\ 2 \cdot (\sigma_x' \cdot \tau_{yz} - \tau_{xy} \cdot \tau_{zx}) \cdot I_1 \\ 2 \cdot (\sigma_y' \cdot \tau_{zx} - \tau_{yz} \cdot \tau_{xy}) \cdot I_1 \\ 2 \cdot (\sigma_z' \cdot \tau_{xy} - \tau_{zx} \cdot \tau_{yz}) \cdot I_1 \end{bmatrix} \tag{3.59}$$

$$\frac{\partial G_1}{\partial \sigma} = (3 \cdot I_1^2 + \frac{\mathrm{I}_3}{\mathrm{I}_1} \cdot m \cdot \acute{\eta}_2 \cdot (\frac{p_a}{I_1})^m \begin{bmatrix} 1 \\ 1 \\ 1 \\ 0 \\ 0 \\ 0 \end{bmatrix} + 27 + \acute{\eta}_2 \cdot (\frac{p_a}{I_1})^m \cdot \begin{bmatrix} -(\sigma_y' \cdot \sigma_z' - \tau_{yz}^2) \\ -(\sigma_z' \cdot \sigma_x' - \tau_{zx}^2) \\ -(\sigma_x' \cdot \sigma_y' - \tau_{xy}^2) \\ 2 \cdot (\sigma_x' \cdot \tau_{yz} - \tau_{xy} \cdot \tau_{zx}) \\ 2 \cdot (\sigma_y' \cdot \tau_{zx} - \tau_{yz} \cdot \tau_{xy}) \\ 2 \cdot (\sigma_z' \cdot \tau_{xy} - \tau_{zx} \cdot \tau_{yz}) \end{bmatrix} \tag{3.60}$$

$$\frac{\partial H_1}{\partial W_p} = \frac{H_1}{p_a} \cdot (\frac{p_a}{q \cdot W_{p1}}) - b \cdot p_a \tag{3.61}$$

$$\sigma^{\mathrm{T}} \cdot \frac{\partial G_1}{\partial \sigma} = 3 \cdot G_1 + m \cdot \acute{\eta}_2 \cdot (\frac{p_a}{I_1})^m \cdot I_3 \tag{3.62}$$

$$\frac{\partial F_2'}{\partial \sigma} = \frac{\partial G_2}{\partial \sigma} = 2 \cdot [\sigma_x', \sigma_y', \sigma_z', 2 \cdot \tau_{yz}, 2 \cdot \tau_{zx}, 2 \cdot \tau_{xy}]^T \tag{3.63}$$

$$\frac{\partial H_2}{\partial W_p} = \frac{p_a}{C \cdot p} \cdot (\frac{H_2}{p_a^2})^{1-p} \tag{3.64}$$

$$\sigma^{T} \cdot [\frac{\partial G_2}{\partial \sigma}] = 2 \cdot G_2 \tag{3.65}$$

Kovacevic tried to implement Lade's double hardening model based on the above equations by Lade and Nelson *(1984).* However, he discovered that this procedure resulted in failure to satisfy the "consistency condition". This occurred when the conical yield surface, F_1, was active. He noted that the above mentioned equation (3.31) that defines the work-hardening law employed with the conical yield surface

$$H_1 = a \cdot \exp(-b \cdot W_{p1}) \cdot (\frac{W_{p1}}{p_a})^{\frac{1}{q}}, \quad q \geq 1 \tag{3.31}$$

indicates that the hardening parameter H_1 is not only dependent on the plastic work history but also on the stresses. 'Namely, the parameters *a, b* and *q* are not "strictly" constants because they are dependent on the minimum principal effective stress σ'_3, as it is evident from equations (3.32), (3.33) and (3.35).

Kovacevic rewrote the conical yield function, F_1, as following:

$$\frac{\partial F_1}{\partial \sigma} = equation(4.74) - \frac{\partial H_1}{\partial a} \cdot [\frac{\partial a}{\partial \sigma}] - \frac{\partial H_1}{\partial b} \cdot [\frac{\partial b}{\partial \sigma}] - \frac{\partial H_1}{\partial q} \cdot [\frac{\partial q}{\partial \sigma}] \tag{3.66a}$$

or

$$\frac{\partial F_1}{\partial \sigma} = equation(4.74) - \frac{\partial H_1}{\partial q} \cdot [\frac{\partial q}{\partial \sigma}] \tag{3.66b}$$

He used the work-hardening law as expressed by equation (3.37) instead of (3.31):

$$H_1 = \acute{\eta}_1 \cdot [\xi \cdot \exp(1-\xi)]^{1/q}, \qquad q \geq 1 \tag{3.37}$$

where

$$q = \alpha + \beta \cdot \frac{\sigma'_3}{p_a}, \qquad q \geq 1 \tag{3.35}$$

The minimum effective stress, σ'_3, is expressed in terms of stress invariants as (Nayak and Zienkiewicz, 1972):

$$\sigma'_3 = p' + \frac{2}{\sqrt{3}} \cdot J \cdot \sin(\theta - \frac{2\pi}{3}) \tag{3.67}$$

where

$$p' = \frac{\sigma'_1 + \sigma'_2 + \sigma'_3}{3} = \frac{\sigma'_x + \sigma'_y + \sigma'_z}{3} \tag{3.7}$$

J is given by the equation

$$\begin{aligned} J_2 = J^2 &= \frac{1}{6}[(\sigma_1' - \sigma_2')^2 + (\sigma_2' - \sigma_3')^2 + (\sigma_3' - \sigma_1')^2] \\ &= \frac{1}{6}[(\sigma_x' - \sigma_y')^2 + (\sigma_y' - \sigma_z')^2 + (\sigma_z' - \sigma_x')^2] + \tau_{xy}^2 + \tau_{yz}^2 + \tau_{zx}^2 \end{aligned} \tag{3.6}$$

$$\theta = \frac{1}{3} \cdot \sin^{-1}(-\frac{3\sqrt{3}}{2} \cdot \frac{|s|}{J^3}), \qquad -\frac{\pi}{6} \le \theta \le \frac{\pi}{6} \tag{3.68}$$

where

$$s = \begin{bmatrix} s_x & \tau_{xy} & \tau_{zx} \\ \tau_{xy} & s_y & \tau_{yz} \\ \tau_{zx} & \tau_{yz} & s_z \end{bmatrix} \tag{3.69}$$

and

$$|s| = \det s = s_x \cdot s_y \cdot s_z + 2 \cdot \tau_{xy} \cdot \tau_{yz} \cdot \tau_{zx} - s_x \cdot \tau_{yz}^2 - s_y \cdot \tau_{zx}^2 - s_z \cdot \tau_{xy}^2 \tag{3.70}$$

Using the chain rule it is showed that

$$-\frac{\partial H_1}{\partial q} \cdot [\frac{\partial q}{\partial \sigma}] = \frac{\mathrm{H}_1}{q^2} \cdot \frac{\beta}{q_a} \cdot \ln[\xi \cdot \exp(1 - \xi)] \cdot [\frac{\partial \sigma_3'}{\partial \sigma}] \tag{3.71}$$

and from Nayaoro *(1989):*

$$\frac{\partial \sigma_3'}{\partial \sigma} = A \cdot \underline{X} + B \cdot \underline{Y} + C \cdot \underline{Z} \tag{3.72}$$

where

$$A = \frac{1}{3} \tag{3.73}$$

$$B = -\frac{1}{2J^2} \cdot [3C \cdot |s| - \frac{2}{\sqrt{3}} \cdot J \cdot \sin(\theta + \frac{2\pi}{3}) \tag{3.74}$$

$$C = -\frac{1}{2J^2} \cdot \frac{\cos(\theta + \frac{2\pi}{3})}{\cos 3\theta} \tag{3.75}$$

$$\underline{X} = [1,1,1,0,0,0]^T \tag{3.76}$$

$$\underline{Y} = [s_x, s_y, s_z, 2 \cdot \tau_{xy}, 2 \cdot \tau_{yz}, 2 \cdot \tau_{zx}]^T \tag{3.77}$$

$$\underline{Z} = \begin{bmatrix} \frac{2 \cdot s_y \cdot s_z - s_x \cdot s_y - s_z \cdot s_x - 2 \cdot \tau_{yz}^2 + \tau_{xy}^2 + \tau_{zx}^2}{3} \\ \frac{2 \cdot s_z \cdot s_x - s_y \cdot s_z - s_x \cdot s_y - 2 \cdot \tau_{zx}^2 + \tau_{yz}^2 + \tau_{xy}^2}{3} \\ \frac{2 \cdot s_x \cdot s_y - s_z \cdot s_x - s_y \cdot s_z - 2 \cdot \tau_{xy}^2 + \tau_{zx}^2 + \tau_{yz}^2}{3} \\ 2 \cdot (\tau_{zx} \cdot \tau_{yz} - \tau_{xy} \cdot s_z) \\ 2 \cdot (\tau_{xy} \cdot \tau_{zx} - \tau_{yz} \cdot s_z) \\ 2 \cdot (\tau_{yz} \cdot \tau_{xy} - \tau_{zx} \cdot s_z) \end{bmatrix} \tag{3.78}$$

According to Nayaoro *(1989),* equations (3.74) and (3.75) indicate singularities when $\theta = \pm\frac{\pi}{6}$. Investigation to the trend of the coefficients *B* and *C* when θ approaches $\pm\frac{\pi}{6}$ leads to:

- if $\theta = -\frac{\pi}{6}$ then: $\left\{ \begin{array}{l} C = \frac{1}{3J^2}, \\ B = -\frac{1}{2J^2} \cdot [3C \cdot |s| - \frac{2}{\sqrt{3}} \cdot J \cdot \sin(\theta + \frac{2\pi}{3}) \end{array} \right\}$ (3.79)

- if $\theta = +\frac{\pi}{6}$ then: $\left\{ \begin{array}{l} C = 0, \\ B = \frac{1}{\sqrt{3}} \cdot J \cdot \sin(\theta + \frac{2\pi}{3}) \end{array} \right\}$ (3.80)

In the same manner, in deriving the derivatives if the plastic potential function G_1 :

$$G_1 = I_1 - \left[27 + \acute{\eta}_2 \cdot \left(\frac{p_a}{I_1} \right)^m \right] \cdot I_3 \tag{3.22}$$

Lade and Nelson assumed that the parameter $\acute{\eta}_2$ is constant. However, according to equation (3.28):

$$\acute{\eta}_2 = \rho \cdot \mathrm{H}_1 + R \cdot \left(\frac{\sigma_3'}{p_a} \right)^{\frac{1}{2}} + t \tag{3.28}$$

it is evident that $\acute{\eta}_2$ depends on the minimum principal effective stress, σ_3'. The derivatives of the plastic potential function, G_1, are now written as following:

$$\frac{\partial G_1}{\partial \sigma} = equation(2.60) + \frac{\partial G_1}{\partial \acute{\eta}_2} \cdot [\frac{\partial \acute{\eta}_2}{\partial \sigma}] \tag{3.81}$$

Applying the chain rule and using the work-hardening rule *(3.37)* the additional term in equation *(3.71)* can now be written:

$$\frac{\partial G_1}{\partial \acute{\eta}_2} \cdot \frac{\partial \acute{\eta}_2}{\partial \sigma} = \frac{\partial G_1}{\partial \acute{\eta}_2} \cdot \left(\frac{\partial \acute{\eta}_2}{\partial \mathrm{H}_1} \cdot \frac{\partial \mathrm{H}_1}{\partial q} \cdot \frac{\partial q}{\partial \sigma_3'} + \frac{\partial \acute{\eta}_2}{\partial \sigma_3'} \right) \cdot \frac{\partial \sigma_3'}{\partial \sigma} \tag{3.82}$$

where

$$\frac{\partial G_1}{\partial \acute{\eta}_2} = -\left(\frac{p_a}{I_1} \right)^m \cdot I_3 \tag{3.83}$$

$$\frac{\partial \acute{\eta}_2}{\partial \mathrm{H}_1} = \rho \tag{3.84}$$

$$\frac{\partial \mathrm{H}_1}{\partial q} = -\frac{\mathrm{H}_1}{q^2} \cdot \ln[\xi \cdot \exp(1-\xi)] \tag{3.85}$$

$$\frac{\partial q}{\partial \sigma_3'} = \frac{\beta}{p_a} \tag{3.86}$$

$$\frac{\partial \acute{\eta}_2}{\partial \sigma_3'} = \frac{1}{2} \cdot R \cdot \left(p_a \cdot \sigma_3\right)^{\frac{1}{2}} \tag{3.87}$$

and

$\frac{\partial \sigma_3'}{\partial \sigma}$ is given by equations (3.72)-(3.78)

Finally, if the work-hardening law given by equation (3.37) is written in a simpler form, equation (3.61) is written as following:

$$\frac{\partial \mathrm{H}_1}{\partial W_{p1}} = \frac{\partial \mathrm{H}_1}{\partial \xi} \cdot \frac{\partial \xi}{\partial W_{p1}} = \frac{H_1}{q} \cdot \left(\frac{1}{\xi} - 1\right) \cdot \frac{1}{W_{p1p}} \tag{3.88}$$

where

$$W_{p1p} = P \cdot p_a \cdot (\frac{\sigma'_3}{p_a})^l \tag{3.89}$$

Kovacevic implemented all the above changes. With regards to ξ, Kovacevic states: "*For low values of ξ, the model response to shearing is essentially elastic and the conical yield surface expands rapidly. To eliminate numerical difficulties, McCarron and Chen (1988) suggested that the minimum initial value of should be 0.001. For the majority of applications this value is quite appropriate. However, it has been found that in some cases a higher value of should be adopted. The problem is connected with the 'condition of irreversibility' and will be further discussed in the next chapter. In order to avoid the possible difficulties with numerical instabilities of this kind, the initial value of is included as an additional model parameter.*"

3.3 DETERMINATION OF LADE'S DOUBLE HARDENING MODEL PARAMETERS FOR LOOSE OTTAWA SAND

In this part of the chapter, the determination of the 14 above mentioned parameters for Lade's double hardening model is analytically presented for loose Ottawa silica sand. The model parameters are derived from laboratory test data performed in the National Technical University of Athens.

Lade *(1977, 1981, 1988a)* describes the method followed to evaluate the model's parameters. Kovacevic (1994) followed the same method to evaluate the parameters for Roadford rockfill and sand waste fill and all has been taken into consideration for the present calibration.

Generally, the double hardening model parameters can be derived from the results of one isotropic compression test and at least two conventional drained triaxial compression tests. In the present thesis, one set of 12 isotropic compression and 12 corresponding drained triaxial compression tests were used. All samples were isotropically compressed to *600kPa*, including one intermediate unloading-reloading cycle. After having been compressed to *600kPa*, each one of the samples was unloaded back to a mean effective stress of *50kPa*, *100kPa, 150kPa*…etc to *600kPa* with a step of *50kPa*. *(Figure 3.7)* Following, the drained triaxial tests were initiated from each one of these mean effective stresses by increasing the maximum effective stress σ_1' and holding the minimum effective stress σ_3' stable. Two unloading-reloading cycles were performed before the samples reached failure *(Figures 3.8, 3.9).*

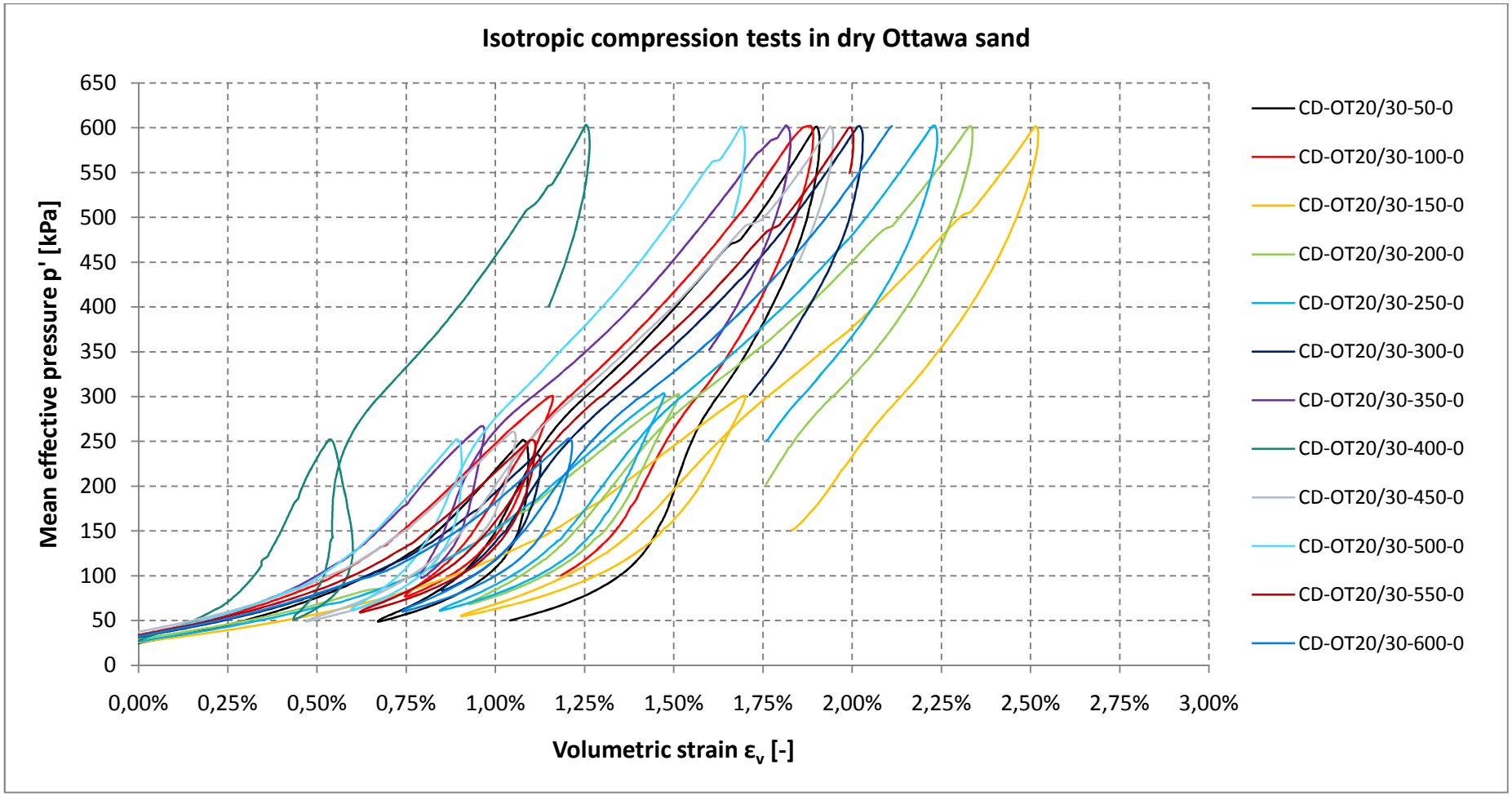

Figure 3.7: *Mean effective stress – volumetric strain diagram for the isotropic compression tests on Ottawa sand used to determine the parameters of Lade's double Hardening Model.*

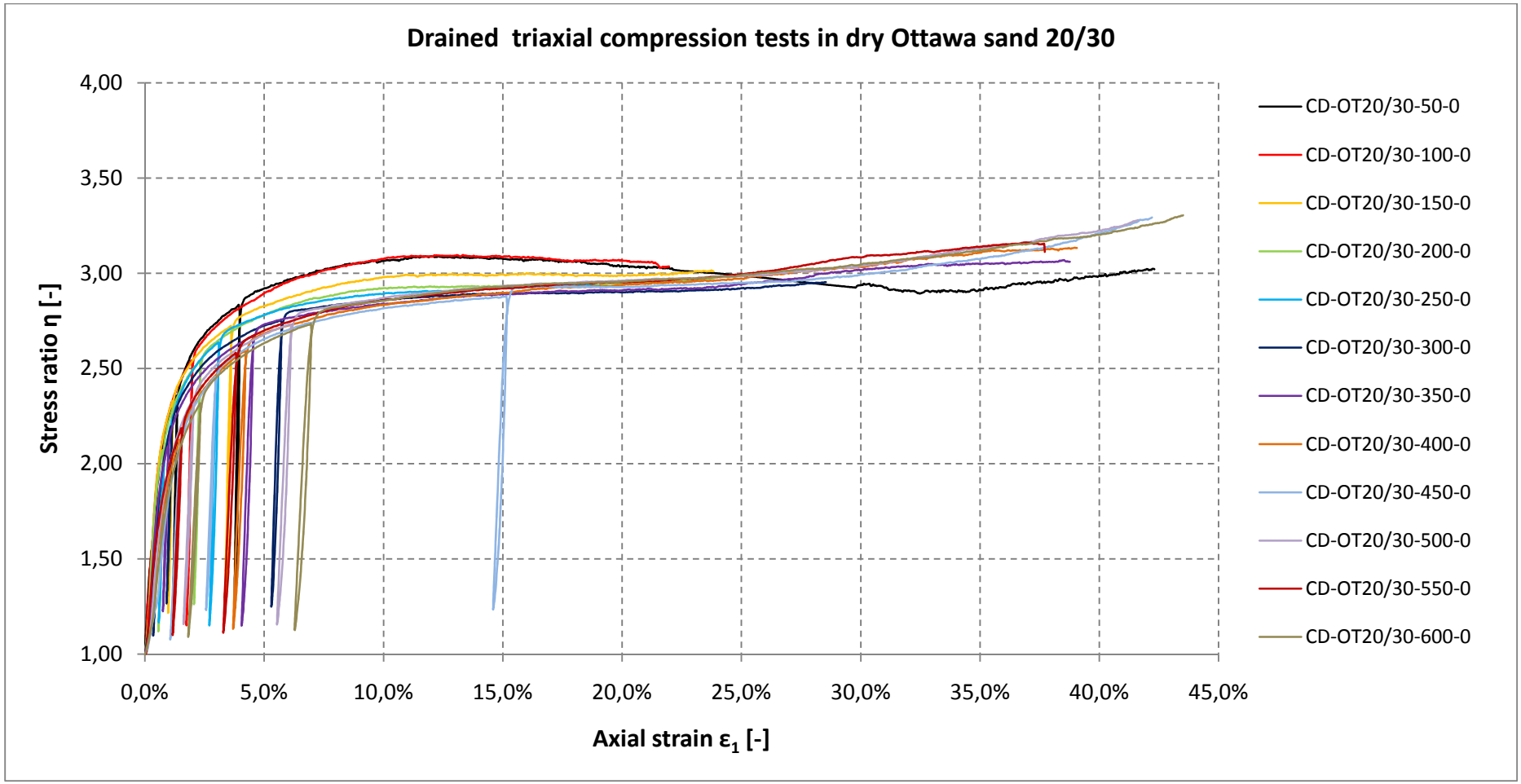

Figure 3.8: *Stress ratio ($\eta=\sigma_1'/\sigma_3'$) – axial strain diagram for the drained triaxial compression tests on Ottawa sand used to determine the parameters of Lade's Double Hardening Model.*

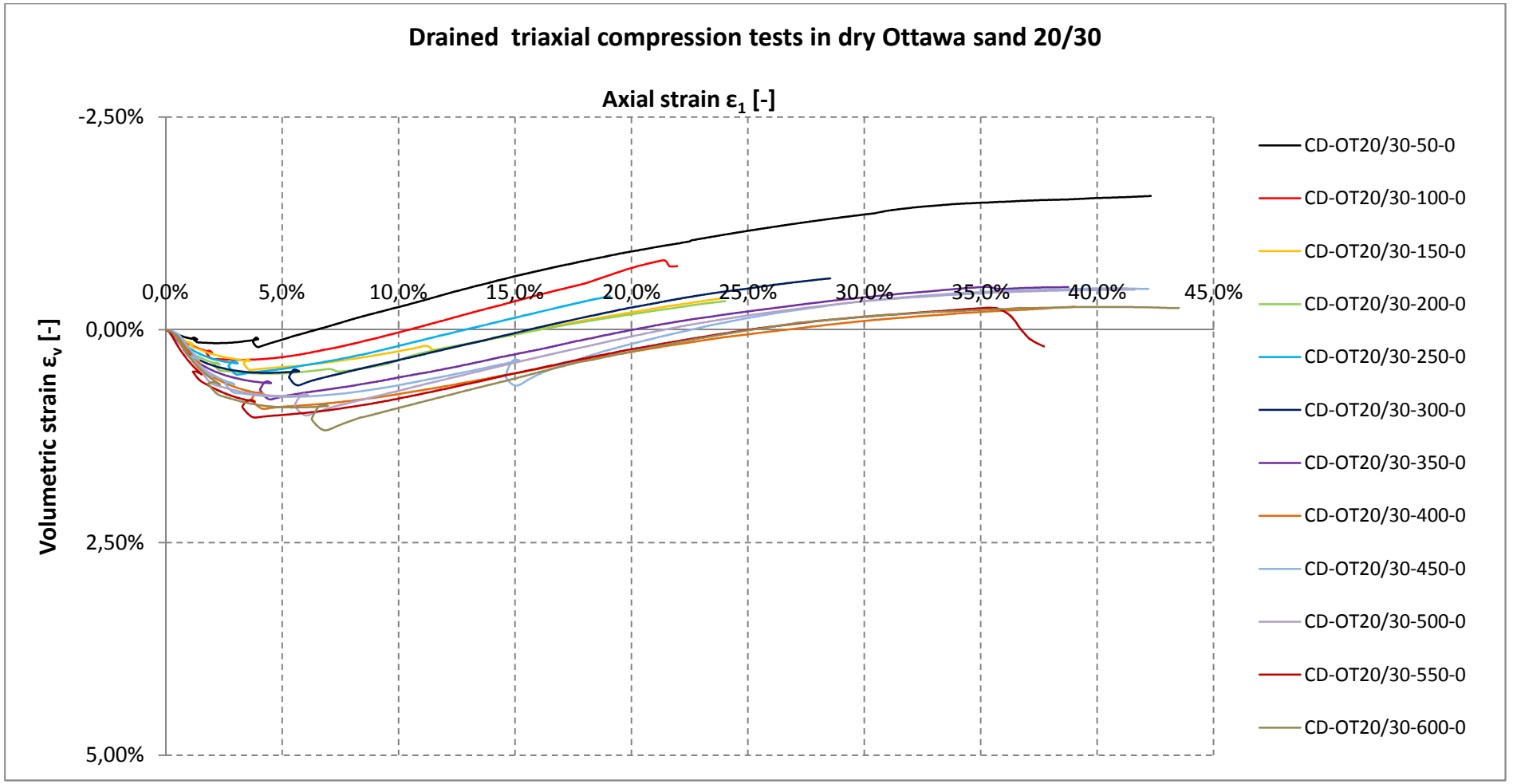

Figure 3.9: *Volumetric strain (ε_v) – axial strain (ε_1) diagram for the drained triaxial compression tests on Ottawa sand used to determine the parameters of Lade's double Hardening Model.*

3.3.1 ELASTIC PARAMETERS

3.3.1.1 POISSON'S RATIO

Lade *(1977)* states that "*the value of Poisson's ratio has often been found to be close to* ***0.20*** *for the elastic parts of unloading-reloading stress paths [5]-[7]"*. Kovacevic states the same about most granular materials and used the same value. This value is therefore used in the following calculations.

3.3.1.2 ELASTIC MODULUS NUMBER & ELASTIC EXPONENT

The pressure dependent Young's modulus, $\boldsymbol{E_{ur}}$, is initially defined by the unloading-reloading cycles during the drained triaxial tests. It was preferred to calculate the secant modulus, exactly the way Lade does as shown in *Figure 3.1,* based on the conventional expression:

$$E_{ur} = \frac{\Delta\sigma'}{\Delta\varepsilon} \tag{3.90}$$

Figure 3.10 shows the calculation of Young's modulus for the drained triaxial test under the confining pressure of *50kPa*. The same procedure was followed for all *12* tests and the results are shown in *Table 3.1*.

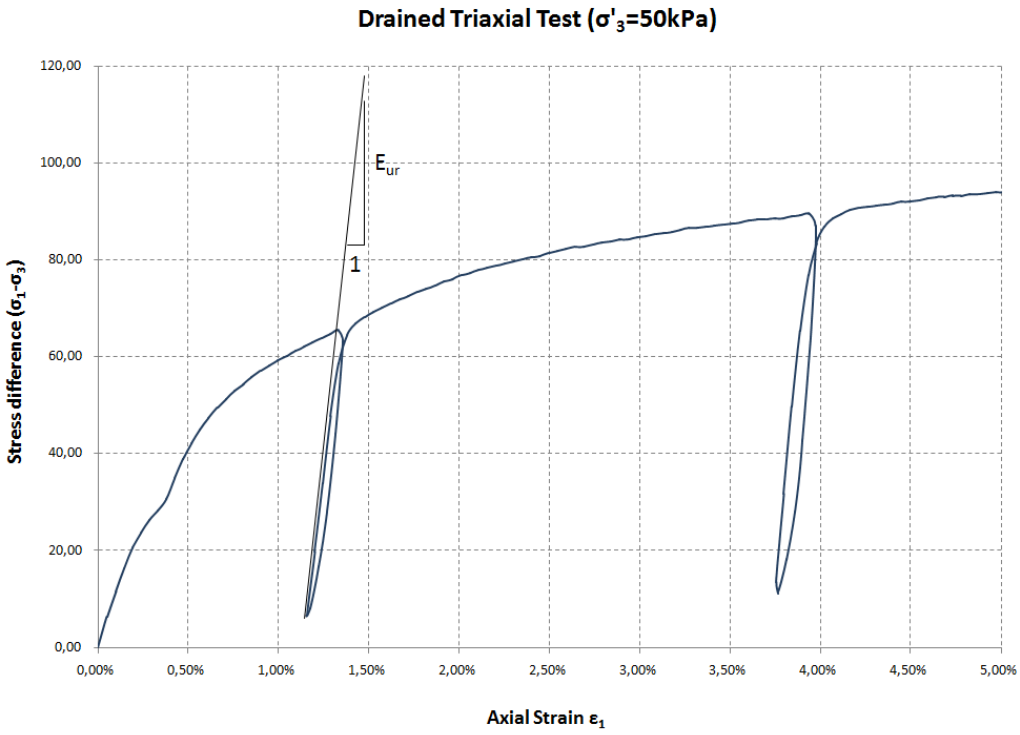

Figure 3.10: *Calculation of secant Young's modulus in the stress difference (σ_1'-σ_3') – axial strain diagram for the drained triaxial compression test of confining pressure of 50kPa.*

Next, the quantities of $\frac{E_i}{p_a}$ and $\frac{\sigma_3'}{p_a}$ are calculated next for each test. The value of the atmospheric pressure p_a used in the calculations was considered equal to *101.325kPa*. The results are shown in the following *Table 3.1* for all *12* tests:

Test No.	E_{ur} [kPa]	E_{ur}/p_a	σ'_3 [kPa]	σ'_3/p_a
CD-OT20/30-50-0	32650,00	322,23	48,16	0,4753
CD-OT20/30-100-0	125209,09	1235,72	98,92	0,9763
CD-OT20/30-150-0	84152,63	830,52	143,18	1,4131
CD-OT20/30-200-0	136050,00	1342,71	200,57	1,9795
CD-OT20/30-250-0	143078,57	1412,08	249,01	2,4575
CD-OT20/30-300-0	255100,00	2517,64	299,89	2,9597
CD-OT20/30-350-0	301080,00	2971,43	349,64	3,4507
CD-OT20/30-400-0	129990,32	1282,90	398,92	3,9370
CD-OT20/30-450-0	127108,57	1254,46	448,26	4,4240
CD-OT20/30-500-0	150430,77	1484,64	501,17	4,9462
CD-OT20/30-550-0	160191,89	1580,97	547,66	5,4050
CD-OT20/30-600-0	144588,24	1426,97	602,89	5,9501

Table 3.1: *Secant Young's modulus for the different confining pressures of the 12 drained triaxial compression tests.*

In *Figure 3.11*, the above quantities are plotted in a log-log scale diagram. The value of the elastic modulus number ***M*** is determined as the intercept between the fitted straight line and the vertical line corresponding to $\frac{\sigma_3'}{p_a}=1$, while the elastic exponent ***n*** is the slope of the adopted straight line.

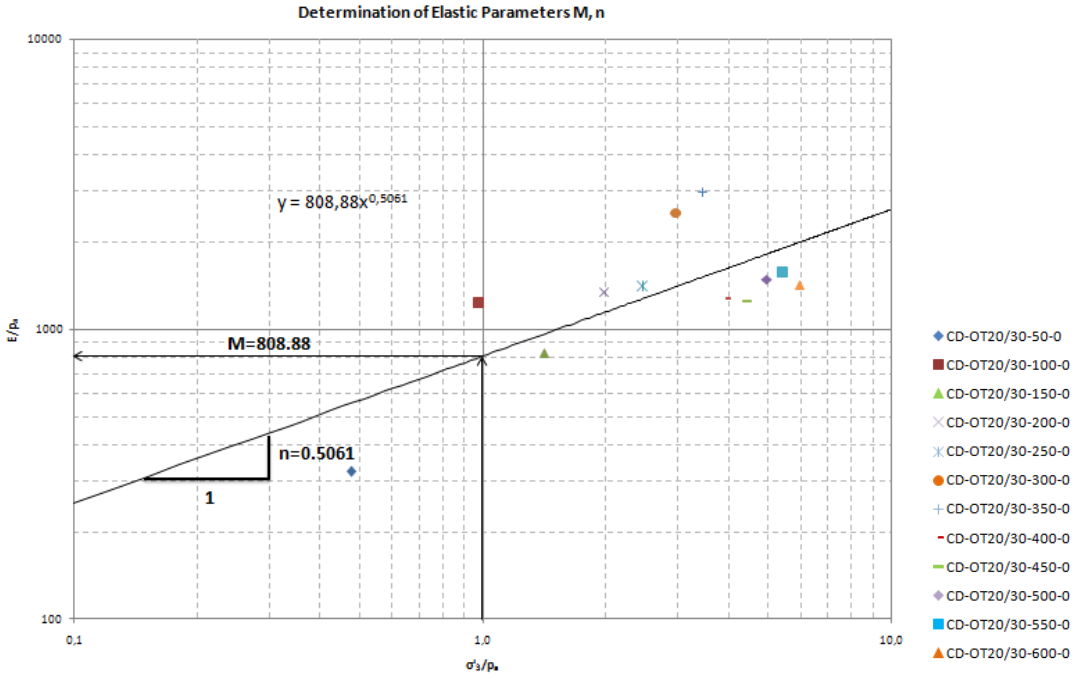

Figure 3.11: *Determination of Double Hardening model's elastic parameters* ***M*** *and* ***n*** *for loose Ottawa fine sand.*

It can be seen that the adopted strain line links the data in the following rule:

$$\left(\frac{E_i}{p_a}\right)=M\cdot\left(\frac{\sigma_3'}{p_a}\right)^n \Rightarrow \left(\frac{E_i}{p_a}\right)=808.88\cdot\left(\frac{\sigma_3'}{p_a}\right)^{0.5061} \Rightarrow \begin{Bmatrix} M=808.88 \\ n=0.5061 \end{Bmatrix} \quad (3.91)$$

3.3.2 FAILURE PARAMETERS

As described in the previous, the failure criterion is expressed by equation *(3.20):*

$$\acute{\eta}_1=\left(\frac{I_1^3}{I_3}-27\right)\cdot\left(\frac{I_1}{p_a}\right)^m \quad (3.20)$$

For each drained triaxial test, the point of failure is determined. That is indicated in a stress-strain diagram, approximately when the stress difference starts becoming

constant for further increasing values of axial strain. *Figure 3.12* shows this point for the drained triaxial test at the confining pressure of *50kPa.* The same procedure was applied for all *12* tests in order to determine all failure points.

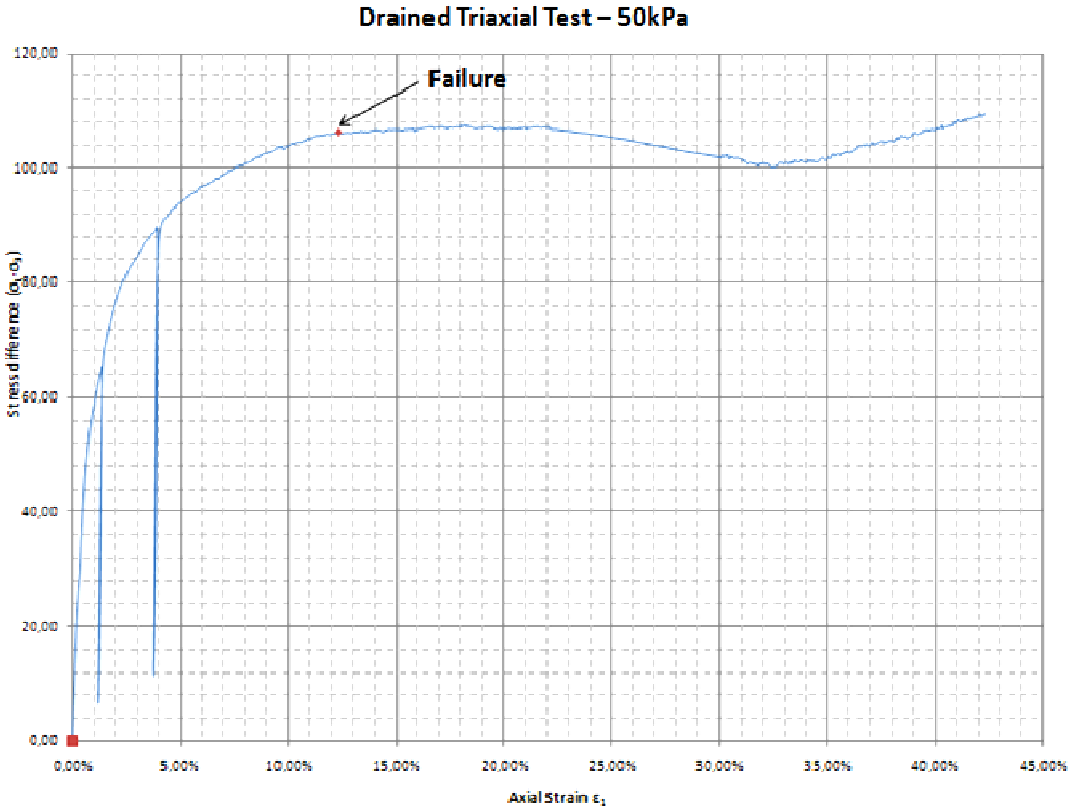

Figure 3.12: *Approximate determination of the point of failure for the drained triaxial test at the confining pressure of 50kPa. Stress difference (σ_1'-σ'_3) – axial strain (ε_1) diagram.*

Once the point of failure is determined, the quantities of first and third stress invariants I_1 and I_3 are calculated for these points, for each test, according to equations *(3.10)* and *(3.21). Table 3.2* shows these points and quantities needed to determine the failure parameters.

Test No.	σ'_1(at failure)	$\sigma'_2=\sigma'_3$(at failure)	I_1	I_3	I_1^3/I_3-27	p_a/I_1
CD-OT20/30-50-0	157,15	50,83	258,80	406006,1	15,69539	0,3915123
CD-OT20/30-100-0	311,50	100,89	513,27	3170559	15,64906	0,1974096
CD-OT20/30-150-0	431,41	144,18	719,78	8968539	14,57889	0,1407727
CD-OT20/30-200-0	603,18	207,66	1018,50	26009991	13,61981	0,0994849
CD-OT20/30-250-0	726,96	250,99	1228,94	45796001	13,529	0,082449
CD-OT20/30-300-0	870,74	301,44	1473,63	79121860	13,44511	0,0687589
CD-OT20/30-350-0	1021,26	351,75	1724,75	1,26E+08	13,60563	0,0587476
CD-OT20/30-400-0	1190,55	402,72	1995,98	1,93E+08	14,18342	0,0507645
CD-OT20/30-450-0	1319,68	450,25	2220,18	2,68E+08	13,90618	0,0456382
CD-OT20/30-500-0	1482,73	501,58	2485,89	3,73E+08	14,18156	0,0407601
CD-OT20/30-550-0	1626,48	551,15	2728,78	4,94E+08	14,12622	0,037132
CD-OT20/30-600-0	1784,53	605,93	2996,40	6,55E+08	14,06047	0,0338156

Table 3.2: *First and third stress invariants I_1 and I_3 at failure. Calculation of* $\left(\frac{I_1^3}{I_3}-27\right)$ *and* $\left(\frac{p_a}{I_1}\right)$ *for all tests.*

$\left(\frac{I_1^3}{I_3}-27\right)$ is then plotted against $\left(\frac{p_a}{I_1}\right)$ on a log-log diagram shown in *Figure 3.13*.

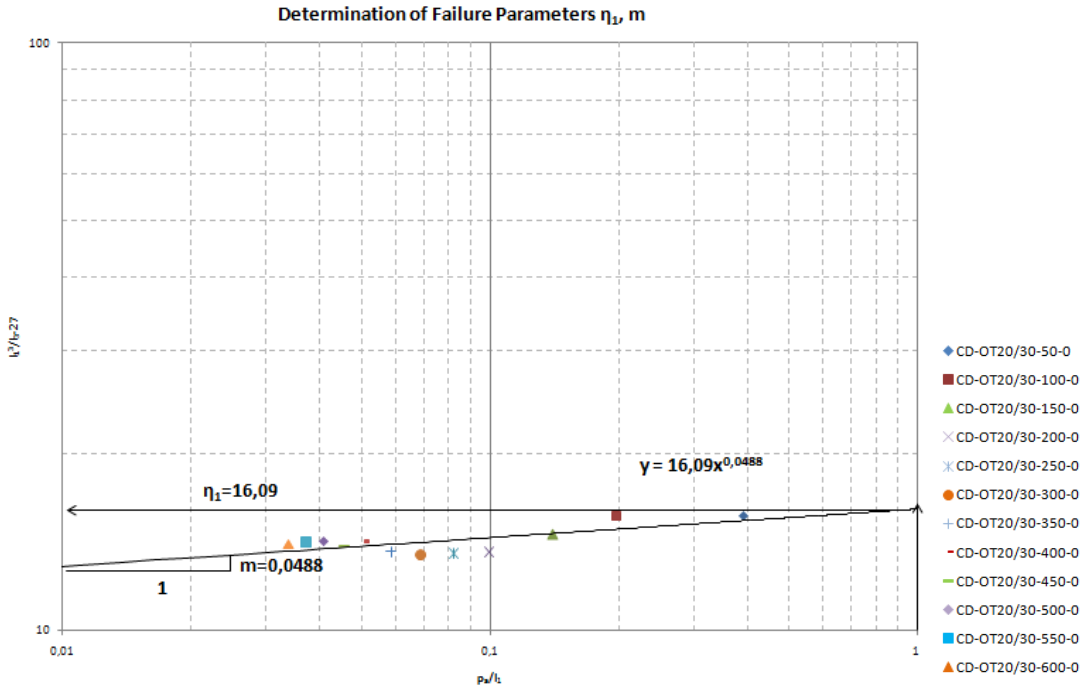

Figure 3.13: *Determination of Double hardening model's failure parameters* $\boldsymbol{\eta_1}$ *and* $\boldsymbol{m}$ *for loose Ottawa sand.*

It can be seen that the adopted strain line links the data in the following rule:

$$\eta_1 = \left(\frac{\mathrm{I}_1^3}{\mathrm{I}_3} - 27\right) \cdot \left(\frac{\mathrm{I}_1}{p_a}\right)^m \Rightarrow 16.09 = \left(\frac{\mathrm{I}_1^3}{\mathrm{I}_3} - 27\right) \cdot \left(\frac{\mathrm{I}_1}{p_a}\right)^{0.0488} \Rightarrow \begin{Bmatrix} \eta_1 = 16.09 \\ m = 0.0488 \end{Bmatrix} \quad (3.92)$$

3.3.3 PLASTIC COLLAPSE PARAMETERS

As it has already been mentioned in the previous, the plastic collapse parameters (the plastic collapse modulus, ***C***, and the collapse exponent, ***p***) are the parameters associated with the conical yield surface. Their determination, as it has also been explained already, requires the experimental data from at least one isotropic compression test. Since there were *12* such tests available, performed before each one of the drained triaxial tests they all have been used. Each one was used individually to determine one set of the parameters and then the values of all *12* were combined to extract the average value for each parameter. In the following the procedure presented in order to determine one set of values for ***C*** and ***p*** is for the sample of the confining pressure of *50kPa*. The same procedure was followed for all *12* tests.

In *Figure 3.14* the isotropic compression test is plotted on a mean effective stress *p'* – volumetric strain diagram ε_v *(%).*It can be seen that there is an intermediate loading-unloading cycle: starting from the point of *(49.19kPa, 0.29%)*, reaching a local peak of *(251.63kPa, 1.08%)* and getting back to approximately the initial stress *(48.87kPa≈49.19kPa, 0.67%).* The ***elastic (reversible)*** and ***plastic (irreversible) strains*** can easily be separated, and, as mentioned before, because this is an isotropic compression test, the plastic strains produced are exclusively "collapse" strains, for in isotropic compression plastic "expansive" strains do not occur at all.

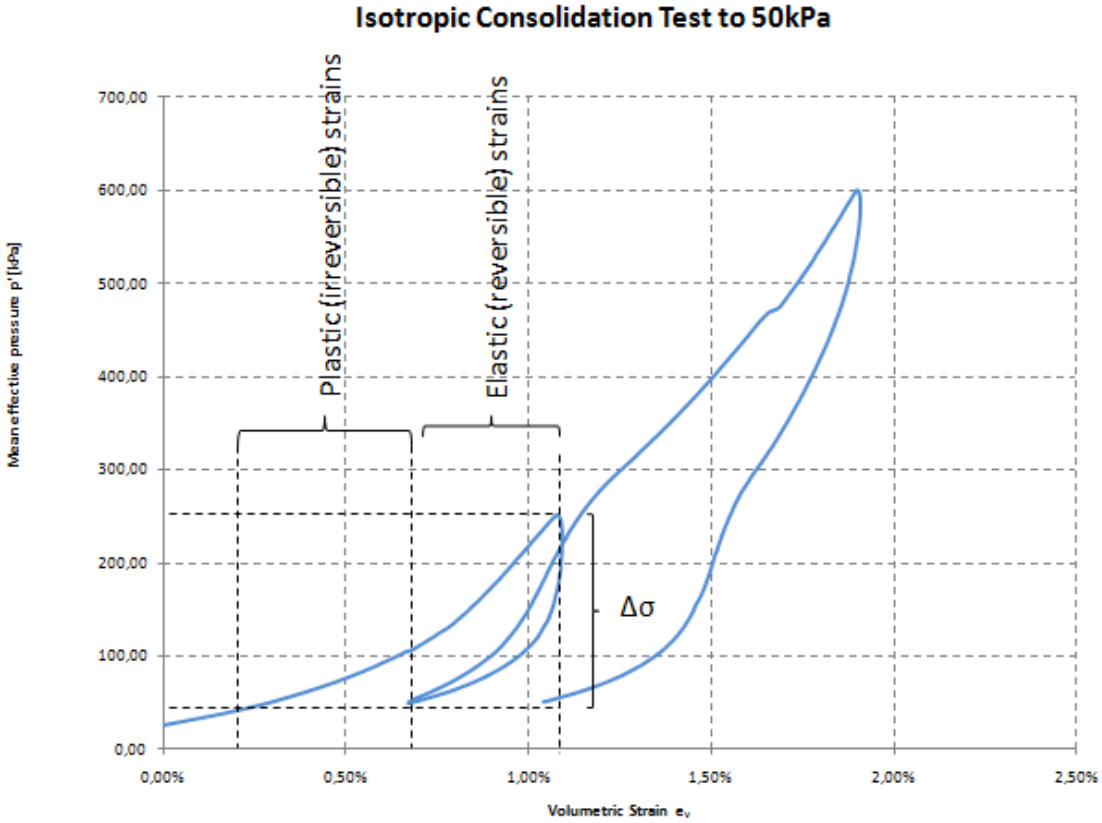

Figure 3.14: *Separation of elastic (recoverable) and plastic collapse (irrecoverable) strains during a loading-unloading cycle in an isotropic compression test. Mean effective stress p'-volumetric strain ε_v(%) diagram.*

Table 3.3 summarizes the strains occurring in the loading-unloading cycle.

	p' [kPa]	IΔp'I	ε_v	IΔε_vI	Type of strains
	49,19		0,29%		
Loading		202,44		0,79%	**Total**
	251,63		1,08%		
Unloading		202,76		0,41%	**Elastic (recoverable)**
	48,87		0,67%		

Table 3.3: *Summary of types of strains occurring during a loading-unloading cycle for isotropic compression test.*

So, according to equation *(3.1b)* and taking into consideration that $\Delta\varepsilon^{p1} = 0$ (non occurring plastic expansive strains), the plastic collapse strains are calculated as following:

$$\Delta\varepsilon = \Delta\varepsilon^{e} + \left[\Delta\varepsilon^{p1} + \Delta\varepsilon^{p2}\right] \qquad (3.1b)$$

and since $\Delta\varepsilon^{p1}=0$:

$$\Rightarrow \Delta\varepsilon = \Delta\varepsilon^{e} + \Delta\varepsilon^{p2}$$
$$\Rightarrow \Delta\varepsilon^{p2} = \Delta\varepsilon - \Delta\varepsilon^{e}$$
$$\Rightarrow \Delta\varepsilon^{p2} = 0.79\% - 0.41\%$$
$$\Rightarrow \Delta\varepsilon^{p2} = 0.38\%$$

It has to be assumed that the elastic strains occur first, and then follow the plastic strains. This way the range of these strains is finally determined. Elastic strains occur from *0.29%* to *0.70% (0.29%+0.41%)* and plastic strains occur from *0.70%* to *1.08% (0.70%+0.38%)*. It was necessary to determine this range in order to calculate the accumulated plastic collapse work produced during these strain increments. According to equation *(3.18):*

$$W_{p2} = \sum(\Delta W_{p2}) = \sum(\sigma^{\mathrm{T}} \cdot \Delta\varepsilon^{p2}) \tag{3.18}$$

and because for an isotropic compression test $\sigma_1' = \sigma_2' = \sigma_3'$, it is:

$$W_{p2} = 3 \cdot \sum(\sigma_3' \cdot \Delta\varepsilon^{p2}) \tag{3.93}$$

The above quantity and the work-hardening parameter H_2 calculated by the expression

$$H_2 = 3 \cdot \sigma_3'^{2} \tag{3.94}$$

are calculated for four points evenly distributed (approximately) along the loading part of the cycle and for the range for which the plastic strains occur. The results are shown in *Table 3.4*:

σ'_3	$H_2=3\sigma'^2_3$	H_2/p_a^2	$Wp_2=3\Sigma(\sigma'_3*\Delta\varepsilon_3^{p2})$	Wp_2/p_a	$(Wp_2/p_a)*10^{-3}$
110,82	36842,88474	3,588561575	0,032092478	0,000316728	0,316728131
150,78	68199,7542	6,642775643	0,570170927	0,00562715	5,62714954
200,78	120940,2346	11,77979091	1,214019123	0,011981437	11,98143719
251,63	189959,0099	18,50234064	2,023323318	0,019968649	19,96864859

Table 3.4: *Calculation of* Wp_2/p_a *and* H_2/p_a^2 *along the range of the occurring plastic (collapse) strains during the intermediate loading-unloading cycle of the isotropic compression test.*

Finally, $\left[\left(\frac{W_{p2}}{p_a}\right)\cdot 10^{-3}\right]$ is plotted against $\left(\frac{H_2}{p_a^2}\right)$ on a log-log diagram as shown in *Figure 3.15*.

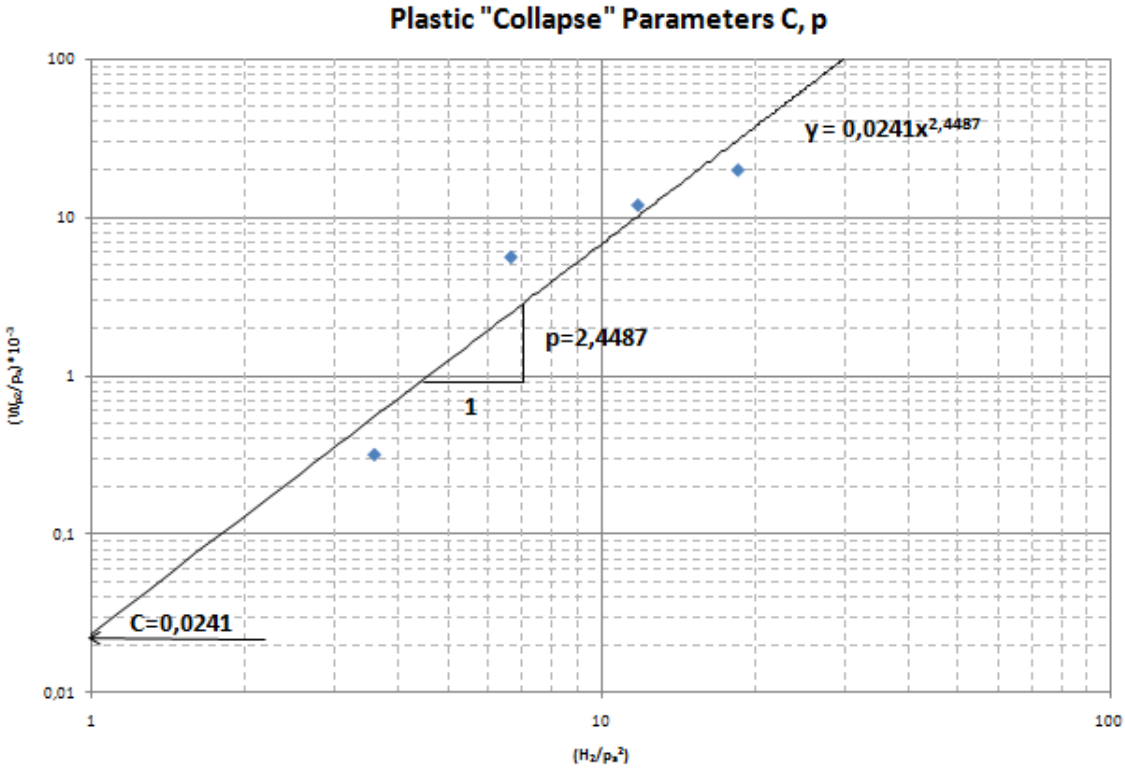

Figure 3.15: *Double hardening model's plastic collapse parameters* ***C*** *and* ***p*** *for loose Ottawa sand – Isotropic compression test.*

It can be seen that the adopted strain line links the data in the following rule:

$$\frac{W_{p2}}{p_a} = C_1 \cdot \left(\frac{H_2}{p_a^2}\right)^{p_1} \Rightarrow = \frac{W_{p2}}{p_a} = 0.0241 \cdot \left(\frac{H_2}{p_a^2}\right)^{2.4487} \Rightarrow \begin{Bmatrix} C_1 = 0.0241 \\ p_1 = 2.4487 \end{Bmatrix} \quad (3.95)$$

The same procedure is followed for all 12 isotropic compression tests. The results are shown in *Table 3.4*, as well as the final parameters used, extracted as an average from all *12* tests.

Plastic "Collapse" Parameters – Isotropic Compression tests								
Test No.	**σ'_3**	**$H_2=3\sigma'^2_3$**	**H_2/p_a^2**	**$Wp_2=3\Sigma(\sigma'_3*\Delta\varepsilon_3^{p2})$**	**(Wp_2/p_a)**	**$(Wp_2/p_a)*10^{(-3)}$**	**C_i**	**p_i**
50kPa	110,82	36842,88	3,5886	0,0321	0,0003	0,3167	0,0241	2,4487
	150,78	68199,75	6,6428	0,5702	0,0056	5,6271		
	200,78	120940,23	11,7798	1,2140	0,0120	11,9814		
	251,63	189959,01	18,5023	2,0233	0,0200	19,9686		
100kPa	164,36	81045,59	7,8940	0,0346	0,0003	0,3417	0,0004	3,5405
	209,60	131793,96	12,8370	0,7291	0,0072	7,1959		
	255,44	195748,78	19,0663	1,5753	0,0155	15,5468		
	300,84	271519,53	26,4465	2,7063	0,0267	26,7092		
150kPa	186,58	104436,29	10,1723	0,0363	0,0004	0,3580	0,00002	4,4818
	224,75	151542,41	14,7605	0,8396	0,0083	8,2865		
	263,47	208243,00	20,2832	1,7844	0,0176	17,6111		
	300,94	271697,36	26,4638	2,9170	0,0288	28,7888		
200kPa	185,74	103494,14	10,0805	0,0376	0,0004	0,3707	0,00003	4,3433
	224,59	151326,72	14,7395	0,8102	0,0080	7,9963		
	264,45	209805,37	20,4354	1,7425	0,0172	17,1970		
	302,77	274999,94	26,7855	2,8988	0,0286	28,6094		
250kPa	178,15	95209,60	9,2736	0,0411	0,0004	0,4059	0,0001	3,894
	220,13	145377,59	14,1600	0,8109	0,0080	8,0035		
	260,27	203222,98	19,7943	1,6607	0,0164	16,3893		
	303,79	276862,36	26,9669	2,8377	0,0280	28,0057		
300kPa	118,28	41972,96	4,0882	0,0509	0,0005	0,5019	0,0192	2,6269
	156,46	73442,01	7,1534	0,6588	0,0065	6,5019		
	195,18	114286,28	11,1317	1,2788	0,0126	12,6210		
	235,70	166657,81	16,2328	2,0037	0,0198	19,7746		
350kPa	119,09	42546,93	4,1441	0,0272	0,0003	0,2683	0,0091	2,7087
	169,01	85690,61	8,3464	0,6301	0,0062	6,2184		
	217,36	141736,76	13,8054	1,2816	0,0126	12,6483		
	267,10	214030,44	20,8469	2,2573	0,0223	22,2775		
400kPa	50,73	7721,09	0,7520	0,0105	0,0001	0,1040	0,2342	1,5694
	118,42	42067,03	4,0974	0,4696	0,0046	4,6343		
	184,87	102527,59	9,9864	0,8810	0,0087	8,6952		
	252,09	190649,33	18,5696	1,5428	0,0152	15,2260		
450kPa	130,38	50993,31	4,9668	0,0417	0,0004	0,4112	0,0071	2,8236
	172,72	89499,19	8,7174	0,6691	0,0066	6,6034		
	217,88	142410,51	13,8710	1,3634	0,0135	13,4559		
	260,02	202824,18	19,7554	2,2104	0,0218	21,8147		
500kPa	100,99	30599,06	2,9804	0,0305	0,0003	0,3006	0,0401	2,2514
	150,15	67632,36	6,5875	0,5918	0,0058	5,8402		
	202,35	122838,39	11,9647	1,2076	0,0119	11,9177		
	252,36	191058,22	18,6094	1,9650	0,0194	19,3930		
550kPa	124,97	46853,25	4,5636	0,0405	0,0004	0,3995	0,0089	2,811
	167,05	83715,10	8,1540	0,6776	0,0067	6,6872		
	207,38	129021,88	12,5670	1,3140	0,0130	12,9687		
	251,47	189717,52	18,4788	2,1643	0,0214	21,3601		
600kPa	135,25	54874,85	5,3449	0,0528	0,0005	0,5214	0,006	2,9239

	175,19	92077,24	8,9685	0,7185	0,0071	7,0911		
	212,54	135524,86	13,2004	1,3504	0,0133	13,3272		
	253,32	192507,75	18,7506	2,1669	0,0214	21,3858		
							C=0,0291	**p=3,0353**

Table 3.4: *Double hardening model's plastic collapse parameters* ***C*** *and* ***p*** *for loose Ottawa sand – all isotropic compression tests.*

Finally, it is:

$$\begin{Bmatrix} C = 0{,}0291 \\ p = 3{,}0353 \end{Bmatrix} \tag{3.96}$$

3.3.4 PLASTIC EXPANSIVE PARAMETERS

In order to calculate the plastic expansive parameters, the plastic expansive work W_{p1} needs to be calculated for each one of the drained triaxial tests. Therefore, the plastic expansive strains $\Delta\varepsilon^{p1}$ need to be defined. According to equation (3.1b), they can be calculated if the elastic strains and the plastic collapse strains are deducted from the total strains:

$$\Delta\varepsilon = \Delta\varepsilon^{e} + \Delta\varepsilon^{p} = \Delta\varepsilon^{e} + \left[\Delta\varepsilon^{p1} + \Delta\varepsilon^{p2}\right] \tag{3.1b}$$

$$\Rightarrow \Delta\varepsilon^{p1} = \Delta\varepsilon - [\Delta\varepsilon^{e} + \Delta\varepsilon^{p2}] \tag{3.97}$$

- The ***total strains*** refer to the strains from the beginning of the loading till failure. The points of failure were determined in *§3.3.3* and therefore the total strains that correspond to these points are the total strains and are known for each test.
- The ***elastic strains*** can easily be calculated since the elastic modulus E_{ur} has already been determined for each test. *(Table 3.1)*
- The ***plastic collapse strains*** have been determined in the previous paragraph for each isotropic compression test. In order to correspond them to the triaxial tests, the bulk modulus is calculated for each one of the loading-unloading cycles of the isotropic compression tests used in the previous paragraph. Then, according to the equation (3.98) that links the bulk modulus with the Young's modulus and Poisson's ratio, the modulus corresponding to the plastic collapse strains E_c for the triaxial tests is determined.

$$E = 3 \cdot K \cdot (1 - 2 \cdot v) \tag{3.98}$$

As a result, the plastic collapse strains can finally be determined. *Table 3.5* summarizes the values of the bulk and the corresponding collapse modulus for each test.

Test No.	K [kPa]	E_c [kPa]
CD-OT20/30-50-0	38400,5	69120,89
CD-OT20/30-100-0	36613,1	65903,58
CD-OT20/30-150-0	29689,95	53441,91
CD-OT20/30-200-0	30467,88	54842,18
CD-OT20/30-250-0	32875,73	59176,31
CD-OT20/30-300-0	31975,06	57555,1
CD-OT20/30-350-0	39332,83	70799,1
CD-OT20/30-400-0	82842,42	149116,4
CD-OT20/30-450-0	35052,5	63094,51
CD-OT20/30-500-0	40646,35	73163,43
CD-OT20/30-550-0	33250,19	59850,34
CD-OT20/30-600-0	32204,51	57968,11

Table 3.5: *Bulk modulus K for the isotropic compression's loading-unloading cycles and the corresponding modulus according to equation (3.98)*

Figure (3.16) shows schematically the full determination of all types of strains for the drained triaxial experiment at the confining pressure of 250kPa. The same procedure is followed for all 12 tests.

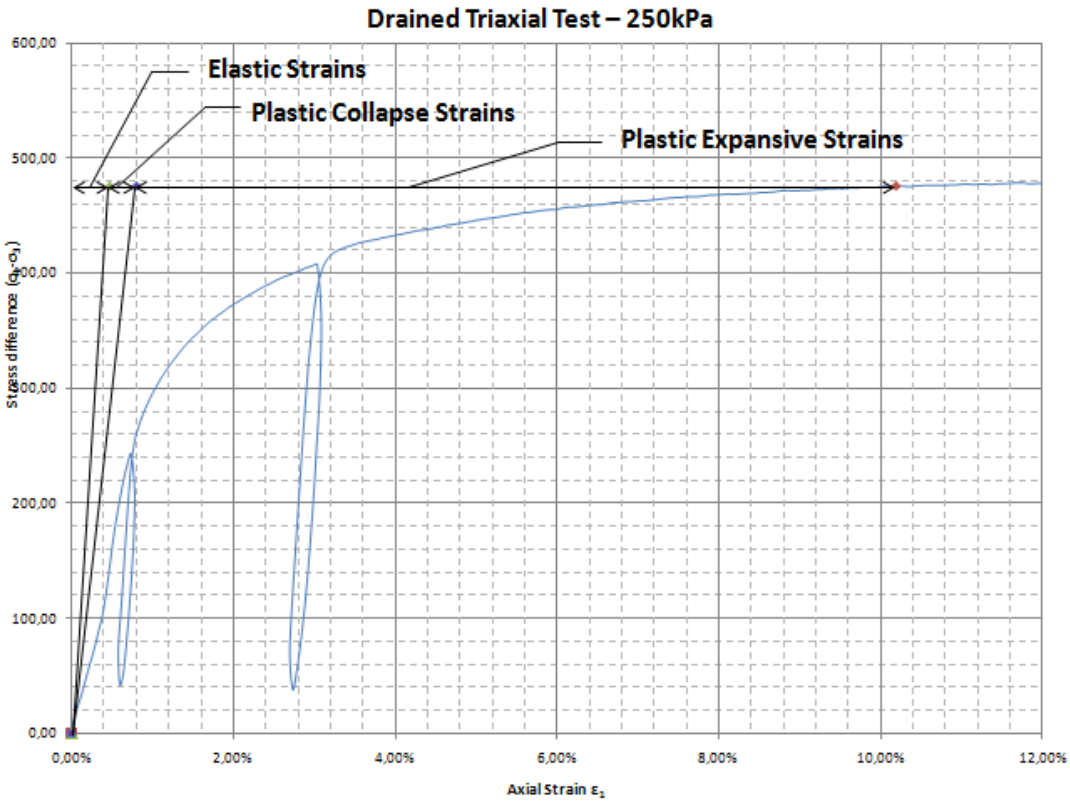

Figure 3.16: *Full determination of the types of strains occurring during the drained triaxial test at the confining pressure of 250kPa.*

Now that the types of strains have full been determined, the plastic expansive strains are determined for each test according to equation *(3.97).*The corresponding plastic expansive work can easily be calculated according to equation (3.30):

$$W_{p1} = \sum(\sigma^{T} \cdot \Delta\varepsilon^{p1}) \tag{3.30}$$

The variation of the plastic expansive work with the work hardening parameter $H_1 = \left(\frac{I_1^3}{I_3} - 27\right) \cdot \left(\frac{I_1}{p_a}\right)^m$ and with the confining pressure σ_3' is shown in *Figure 3.17.*

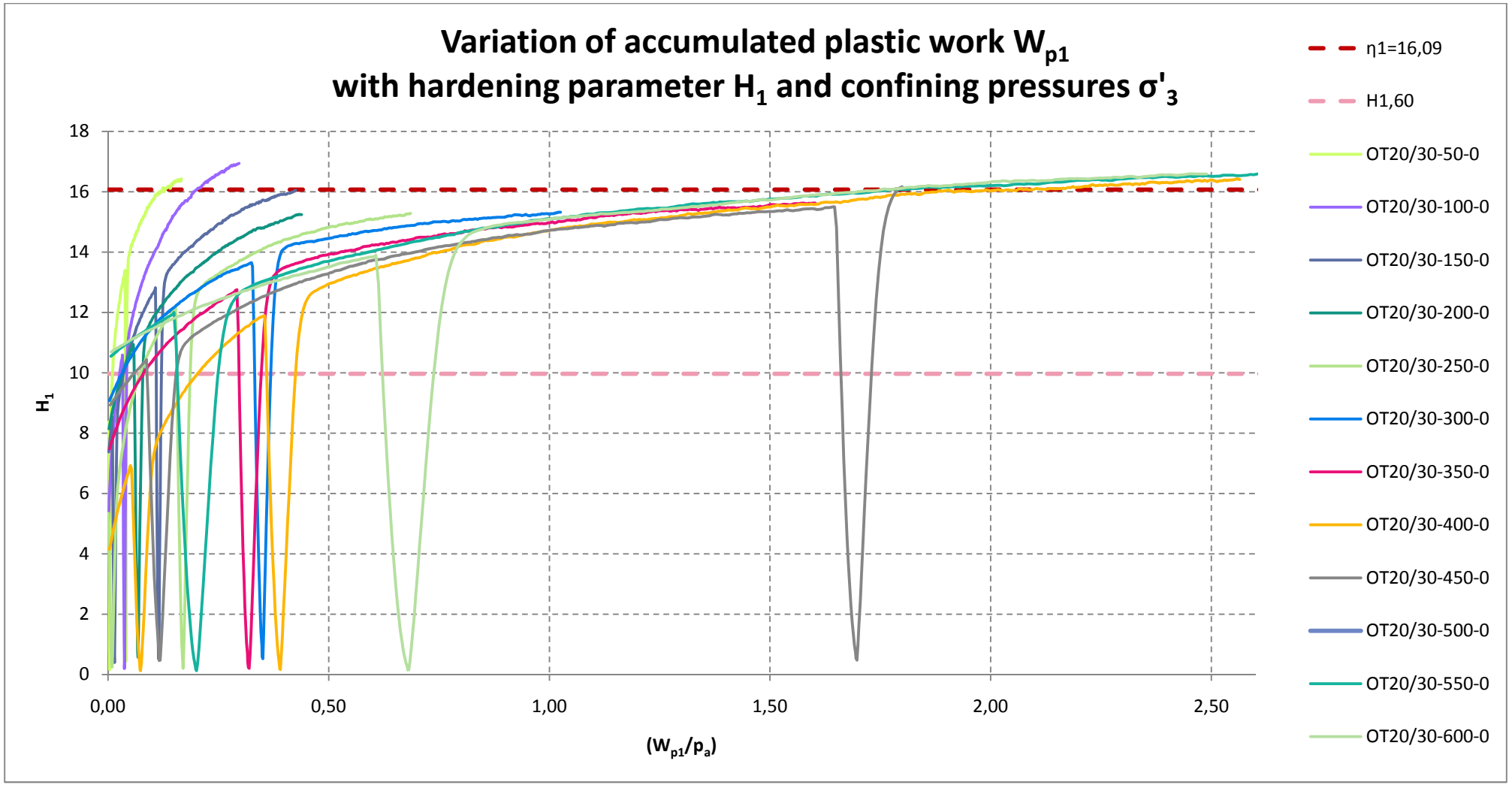

Figure 3.17: *Variation of the plastic expansive work W_{p1} with the work hardening parameter H_1 and with the confining pressure σ_3'.*

From *Figure 3.17* it can be seen that all of Lade's observations on the respective graph for Sacramento River sand *(Figure 3.6)* are verified in this graph for Loose Ottawa sand:

- ✓ the work-hardening relationships have vertical tangents at the origin
- ✓ increasing plastic strain increments are produced with increasing stress levels
- ✓ the amount of plastic work required to reach the peaks increases with increasing confining pressure
- ✓ all peaks occur approximately where $\boldsymbol{f_p=\eta_1=16,09}$

For a particular value of σ_3', the parameter q is defined according to equation *(3.34):*

$$q = \frac{\log\left(\frac{W_{p1p}}{W_{p1,60}}\right) - \left(1 - \frac{W_{p1,60}}{W_{p1p}}\right) \cdot \log e}{\log\left(\frac{\acute{\eta}_1}{H_{1,60}}\right)} \tag{3.34}$$

where $(W_{p1,60},\ H_{1,60})$ and $(W_{p1p},\ \acute{\eta}_1)$ are two sets of corresponding values on each curve in F*igure 3.17*, and e is the base for natural algorithms. These two points correspond to the peak point and the point at 60% of $\acute{\eta}_1$ of the curves.

The following *Table (3.6)* shows the calculated values of W_{p1p}, $\acute{\eta}_1$, $W_{p1,60}$, $H_{1,60}$, and, finally, *q,* for each different confining pressure.

Test No.	W_{p1p}	η'_1	$H_{1,60}$	$W_{p1,60}$	q
CD-OT20/30-50-0	16,84	16,43	9,86	0,990310602	3,703916681
CD-OT20/30-100-0	30,09	16,94	10,16	4,304035316	2,129242429
CD-OT20/30-150-0	43,03	16,04	9,63	2,997970665	3,393824031
CD-OT20/30-200-0	44,44	15,24	9,15	1,560609999	4,667281726
CD-OT20/30-250-0	69,45	15,28	9,17	5,670137688	3,106728869
CD-OT20/30-300-0	103,91	15,32	9,19	0,676102515	7,911632011
CD-OT20/30-350-0	162,42	15,62	9,37	5,729089553	4,658882472
CD-OT20/30-400-0	259,86	16,40	9,84	19,88633793	3,223508272
CD-OT20/30-450-0	182,33	16,17	9,70	4,514360534	5,33125114
CD-OT20/30-500-0	251,19	16,17	9,70	9,290728978	4,569458533
CD-OT20/30-550-0	263,89	16,58	9,95	0,652877016	9,796653051
CD-OT20/30-600-0	252,24	16,59	9,95	0,707125866	9,552621379

Table 3.6: *Calculated values of W_{p1p}, $\acute{\eta}_1$, $W_{p1,60}$, $H_{1,60}$, and q, for each different confining pressure.*

According to equation *(3.35),* the parameter q varies with confining pressure σ_3' :

$$q = \alpha + \beta \cdot \frac{\sigma'_3}{p_a}, \qquad q \geq 1 \tag{3.35}$$

α and β are evaluated as shown in the following *Figure (3.18):*

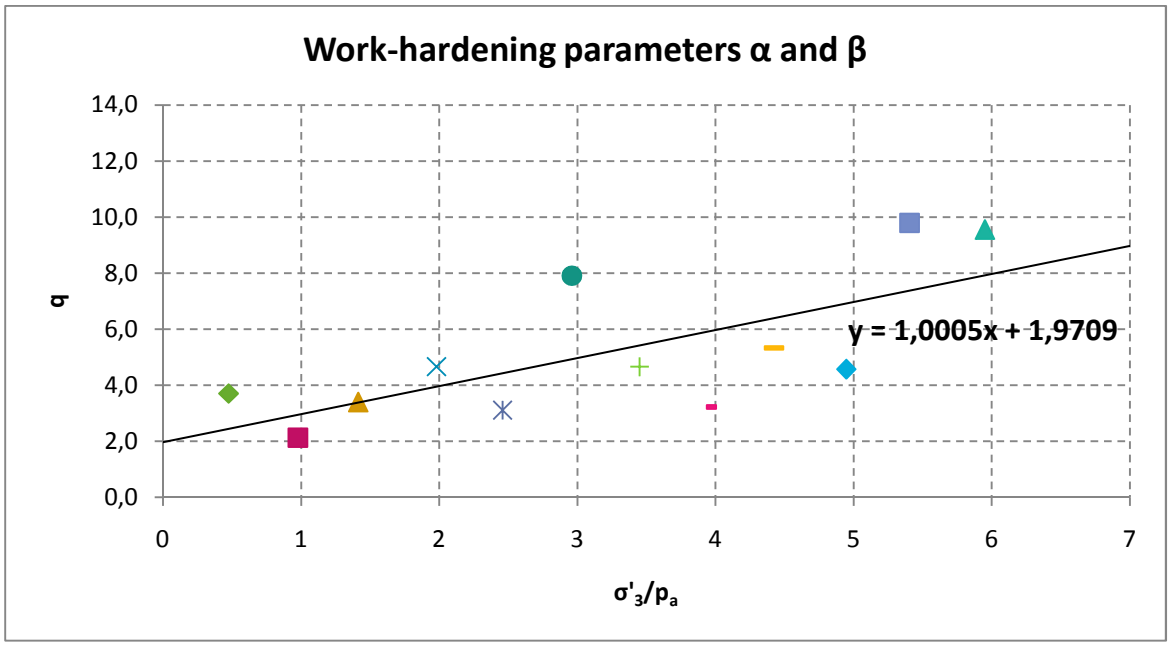

Figure 3.18: *Determination of work-hardening parameters* ***α*** *and* ***β*** *for Loose Ottawa sand.*

It can be seen that:

$$q = \alpha + \beta \cdot \frac{\sigma'_3}{p_a} \Rightarrow q = 1.9709 + 1.0005 \cdot \frac{\sigma'_3}{p_a} \Rightarrow \begin{Bmatrix} \alpha = 1.9709 \\ \beta = 1.0005 \end{Bmatrix} \tag{3.99}$$

The total plastic work associated with the conical yield surface at the point of failure W_{p1p} is also dependent on the confining pressure σ_3', according to equation *(3.36):*

$$W_{p1p} = P \cdot p_a \cdot (\frac{\sigma'_3}{p_a})^l \tag{3.36}$$

In order to evaluate the values of parameters P and l , $\frac{W_{p1p}}{p_a}$ is plotted against $\frac{\sigma'_3}{p_a}$ for each confining pressure *(Figure 3.19).*

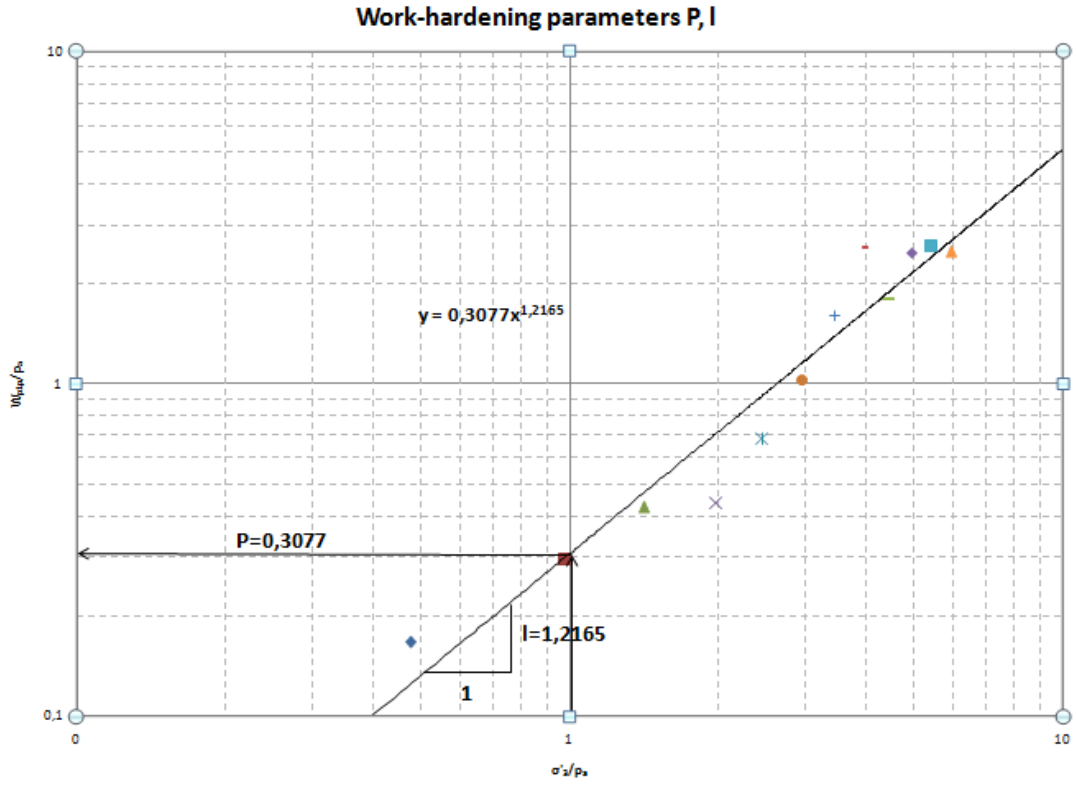

Figure 3.19: *Determination of work-hardening parameters* ***p*** *and* ***l*** *for Loose Ottawa sand.*

It can be seen that:

$$\frac{W_{p1p}}{p_a} = P \cdot \left(\frac{\sigma_3'}{p_a}\right)^l \Rightarrow \frac{W_{p1p}}{p_a} = 0{,}3077 \cdot \left(\frac{\sigma_3'}{p_a}\right)^{1.2165} \Rightarrow \begin{Bmatrix} P = 0.3077 \\ l = 1.2165 \end{Bmatrix} \tag{3.100}$$

Having calculated the values of α, and β, q is re-determined according to equation (3.34) for each value of the confining pressure σ_3':

$$q = \alpha + \beta \cdot \frac{\sigma'_3}{p_a}, \qquad q \geq 1 \tag{3.34}$$

For each of these values of q, a and b (≠α, β) are also calculated according to equations (3.32) and (3.33):

$$a = \acute{\eta}_1 \cdot (e \cdot \frac{p_a}{W_{p1p}})^{1/q} \tag{3.32}$$

$$b = \frac{1}{q \cdot W_{p1p}} \tag{3.33}$$

The results are shown in the following *Table 3.7:*

Test No.	a	b	q=f(α,β) ≥1
CD-OT20/30-50-0	36,99143702	0,021402319	2,446439896
CD-OT20/30-100-0	45,38207469	0,015510362	2,947652628
CD-OT20/30-150-0	27,00975662	0,006205688	3,384683272
CD-OT20/30-200-0	21,47758849	0,002994605	3,951361732
CD-OT20/30-250-0	22,8140406	0,003457873	4,429666395
CD-OT20/30-300-0	17,9344803	0,001082978	4,932064027
CD-OT20/30-350-0	18,58619173	0,001525855	5,423303849
CD-OT20/30-400-0	18,85687291	0,001878468	5,909902813
CD-OT20/30-450-0	17,24519525	0,000985587	6,397094226
CD-OT20/30-500-0	16,93512119	0,001003953	6,919536417
CD-OT20/30-550-0	16,2982843	0,000420372	7,378586454
CD-OT20/30-600-0	16,10537196	0,000383555	7,923936714

Table 3.7: *Calculated values of a, b and q, for each different confining pressure according to equations (3.32)-(3.34).*

Now that the above values have been determined, the relation between H_1 and W_{p1} expressed in equation *(3.31)* is used to produce the prediction lines corresponding to the diagram of *Figure 3.17.*

$$H_1 = a \cdot e^{-b \cdot W_{p1}} \cdot (\frac{W_{p1}}{p_a})^{1/q}, \qquad q \geq 1 \tag{3.31}$$

All the lines, predictions and actual, are presented in the following two graphs *(Figures 3.20-3.21).* The first graph presents the lines for the tests at the confining pressures of *50kPa-300kPa* and the second for the tests at the confining pressures of *350kPa-600kPa*. They are presented separately for clarity reasons.

It can be seen that the expression in *equation (3.31)* reasonably models the observed sand behaviour for all different values of confining pressure σ_3*'=50-600kPa*.

However, it should be noted that in all cases the unloading-reloading cycles are ignored, for they are not simulated.

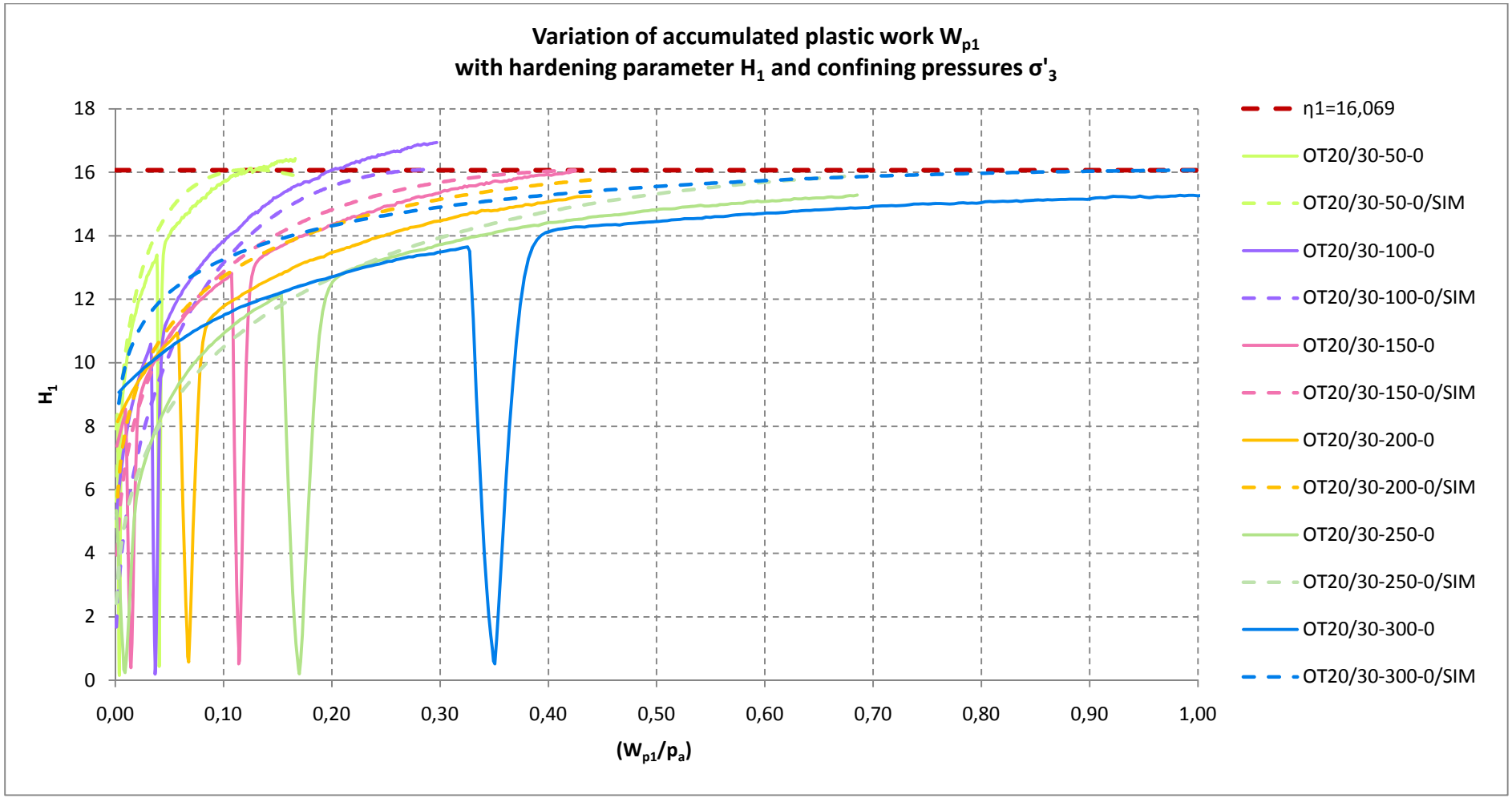

Figure 3.20: *Variation of the plastic expansive work W_{p1} with the work hardening parameter H_1 and with the confining pressure σ_3'-Observations and predictions for the confining pressures 50-300kPa. Unloading - reloading cycles to be ignored.*

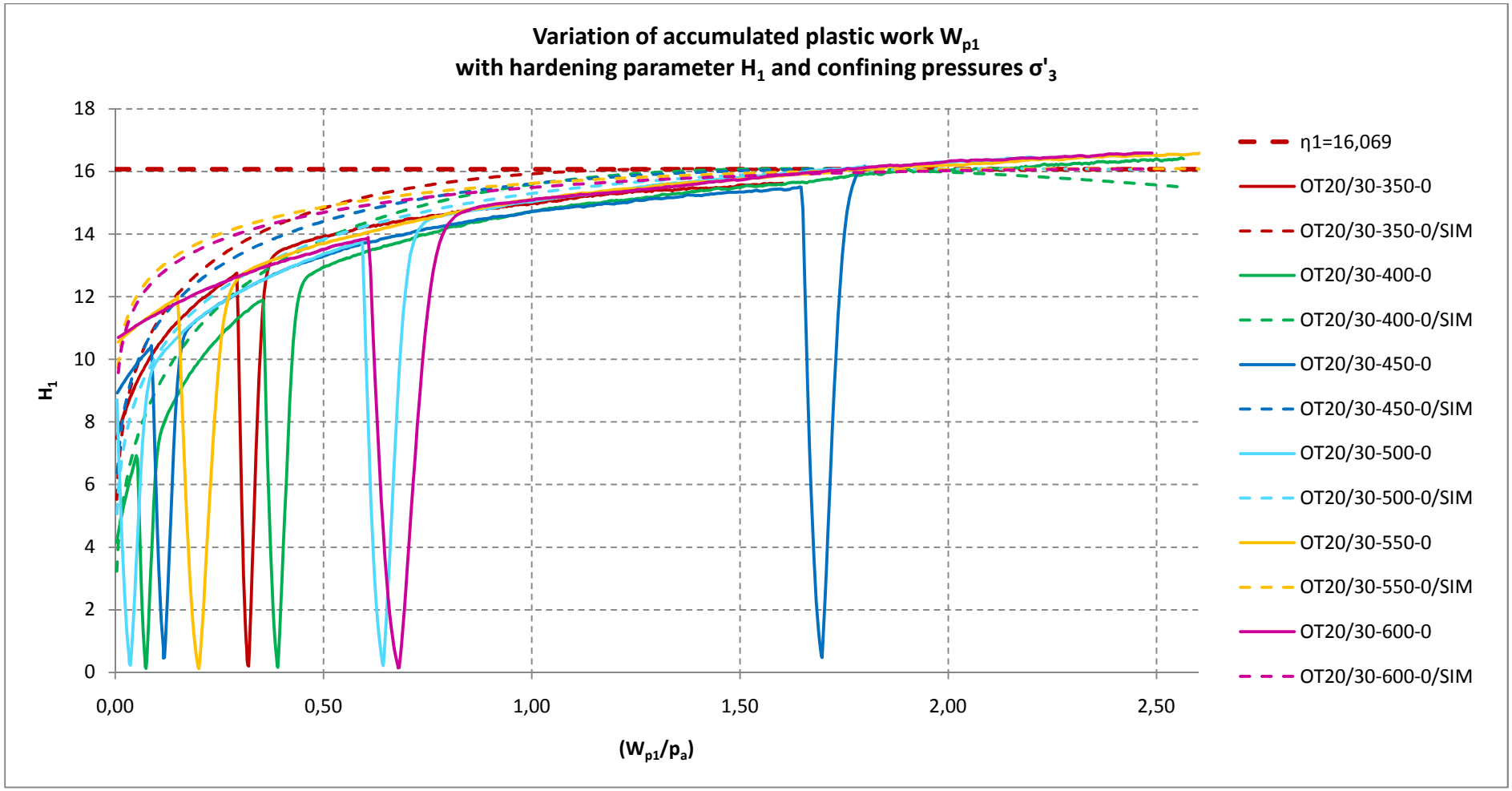

Figure 3.21: *Variation of the plastic expansive work W_{p1} with the work hardening parameter H_1 and with the confining pressure σ_3'-Observations and predictions for the confining pressures 350-600kPa. Unloading - reloading cycles to be ignored*

Finally, the value $\acute{\eta}_2$ of the non-associative flow rule *(equation 3.22)* can be calculated by the following expression (equation 3.27):

$$\acute{\eta}_2 = \frac{3\cdot\left(1+\upsilon^p\right)\cdot I_1^2 - 27\cdot\sigma'_3\cdot(\sigma'_1+\upsilon^p\cdot\sigma'_3)}{\left(\frac{p_a}{I_1}\right)^m\cdot\left[\sigma'_3\cdot\left(\sigma'_1+\upsilon^p\cdot\sigma'_3\right)-\frac{m\cdot(1+\upsilon^p)\cdot I_1^2}{f_p\cdot\left(\frac{p_a}{I_1}\right)^m+27}\right]} \tag{3.27}$$

where υ^p is a function of the plastic "expansive" strain increments determined by subtracting the elastic and plastic "collapse" strain increments from the total ones, as before:

$$\upsilon^p = -\left(\frac{\Delta\varepsilon_3^{p1}}{\Delta\varepsilon_1^{p1}}\right) \tag{3.101}$$

so, $\acute{\eta}_2$ is calculated along the plastic collapse increments of each drained triaxial test. Its variation with H_1 is shown in *Figure 3.22* for all the triaxial tests.

It can be seen that the variation appears to be indifferent of the confining pressure, σ_3', therefore the value of R in equation *(3.28)* is zero. Regarding the values of ρ and t, it can be seen that:

$$\acute{\eta}_2 = \rho\cdot \mathrm{H}_1 + R\cdot\left(\frac{\sigma'_3}{p_a}\right)^{1/2} + t \Rightarrow \acute{\eta}_2 = 0.4216\cdot \mathrm{H}_1 - 0.7607 \Rightarrow \begin{Bmatrix}\rho = 0{,}4216\\ t = -0{,}7607\end{Bmatrix} \tag{3.102}$$

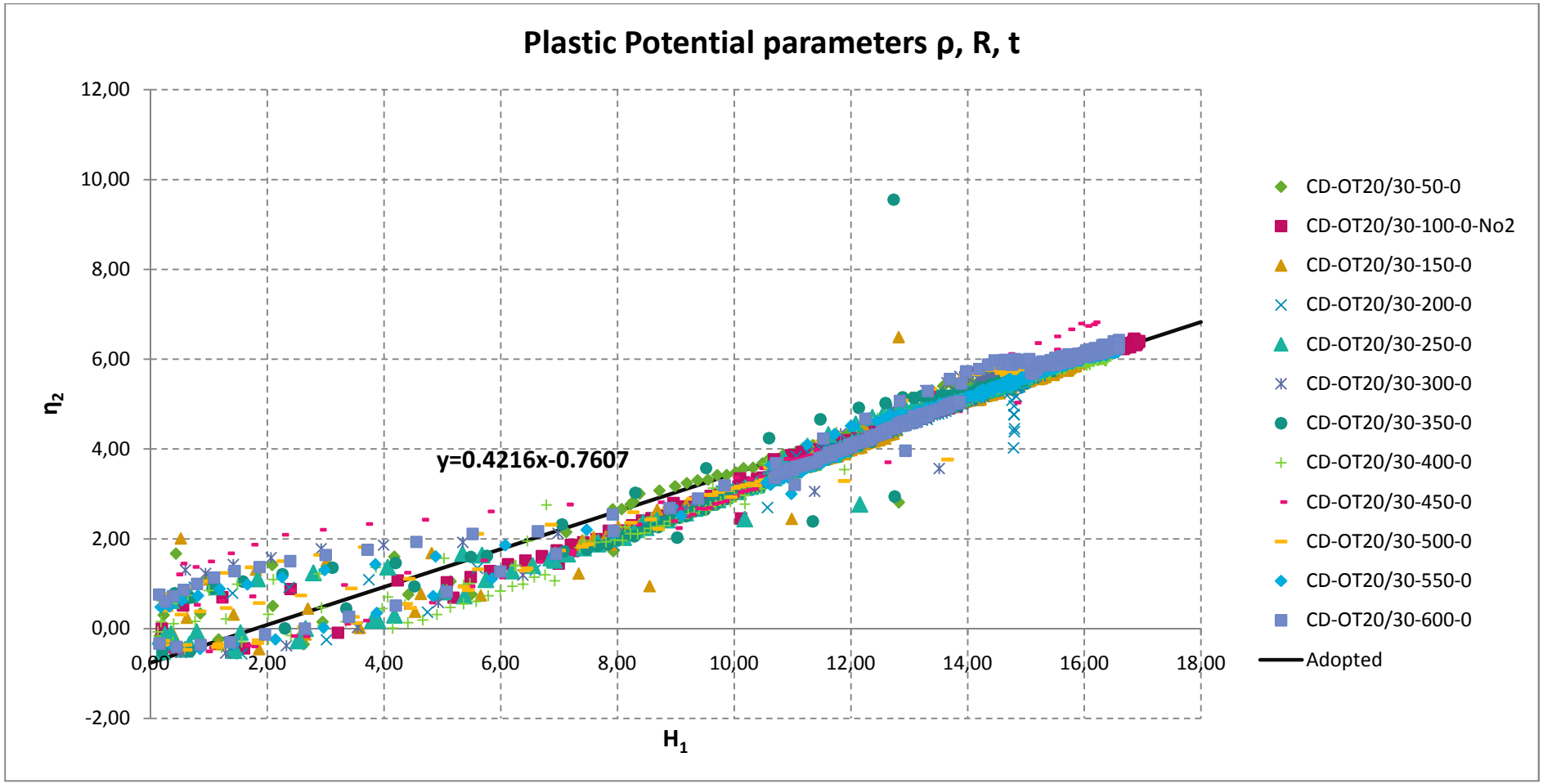

Figure 3.22: *Variation of $\acute{\eta}_2$ with the work hardening parameter H_1 and with the confining pressure σ_3'- Determination of plastic potential parameters ρ, R αvδ t for loose Ottawa sand.*

In *Figure 3.22*, it is evident that the data for the plastic potential surface are well above the adopted line at lower stress levels. This indicates the plastic expansive volumetric strains from the beginning of the triaxial tests. According to Kovacevic (1994) and according to what has been explained in §3.2, these strains are very small, and, in order to neglect most of them, the value of the parameter ξ=0,001 is adopted. The condition of irreversibility $\sigma^{T} \cdot \Delta\varepsilon^{p1} \geq 0$ requires that (Lade, 1988a):

$$\acute{\eta}_2 \leq \frac{3}{3-m} \cdot H_1 \tag{3.103}$$

where *m* is the exponent in the failure criterion and H_1 is given by equation (3.37):

$$H_1 = \acute{\eta}_1 \cdot [\xi \cdot \exp(1-\xi)]^{1/q}, \qquad q \geq 1 \tag{3.37}$$

where

$$\xi = \sum \left(\frac{\Delta W_{p1}}{W_{p1p}}\right) \tag{3.38}$$

By substituting the equations expressing each separate value of equation (3.103), the final inequality becomes:

$$\begin{aligned} &\rho \cdot \mathrm{H}_1 + t \leq \frac{3}{3-m} \cdot H_1 \\ &\Rightarrow \rho \cdot \left[\acute{\eta}_1 \cdot \left(\xi \cdot e^{(1-\xi)}\right)^{\frac{1}{q}}\right] + t \leq \frac{3}{3-m} \cdot \left[\acute{\eta}_1 \cdot \left(\xi \cdot e^{(1-\xi)}\right)^{\frac{1}{q}}\right] \\ &\Rightarrow \rho \cdot \left[\acute{\eta}_1 \cdot \left(\xi \cdot e^{(1-\xi)}\right)^{\frac{1}{\alpha+\beta\cdot\left(\frac{\sigma_3'}{p_a}\right)}}\right] + t \leq \frac{3}{3-m} \cdot \left[\acute{\eta}_1 \cdot \left(\xi \cdot e^{(1-\xi)}\right)^{\frac{1}{\alpha+\beta\cdot\left(\frac{\sigma_3'}{p_a}\right)}}\right] \end{aligned} \tag{3.104}$$

It was calculated that for the following values:

- *ρ=0.4216*
- *t=-0.076*
- $\acute{\eta}_1$*=16.09*
- *α=1.9709*
- *β=1.0005* and
- *ξ=0.001*

and any value of σ_3' the condition is satisfied. The results are shown in the following *Table 3.8:*

Test No.	$\rho \cdot \left[\acute{\eta}_1 \cdot \left(\xi \cdot e^{(1-\xi)} \right)^{\frac{1}{\alpha+\beta \cdot \left(\frac{\sigma_3'}{p_a} \right)}} \right] + t$	$\frac{3}{3-m} \cdot \left[\acute{\eta}_1 \cdot \left(\xi \cdot e^{(1-\xi)} \right)^{\frac{1}{\alpha+\beta \cdot \left(\frac{\sigma_3'}{p_a} \right)}} \right]$	(1) ≤ (2)
	(1)	***(2)***	
CD-OT20/30-50-0	-0,154673677	1,461337235	✓
CD-OT20/30-100-0	0,153091368	2,167631291	✓
CD-OT20/30-150-0	0,423034527	2,807977213	✓
CD-OT20/30-200-0	0,759792706	3,606818445	✓
CD-OT20/30-250-0	1,026232127	4,238852971	✓
CD-OT20/30-300-0	1,286301435	4,855776627	✓
CD-OT20/30-350-0	1,520935194	5,412363319	✓
CD-OT20/30-400-0	1,735072636	5,920329656	✓
CD-OT20/30-450-0	1,932530921	6,388730514	✓
CD-OT20/30-500-0	2,127057227	6,850176275	✓
CD-OT20/30-550-0	2,284619591	7,223937986	✓
CD-OT20/30-600-0	2,457168309	7,633249592	✓

Table 3.8: *Satisfaction of the condition of irreversibility for each one of the drained triaxial tests used for the present calibration.*

3.3.5 SUMMARY OF LADE'S DOUBLE HARDENING MODEL PARAMETERS

Through the procedure described above the complexity of the determination of the 14 parameters is evident. The parameters are not independent from each other. Many's the times where the user defining the parameters intervenes personally in order to chose some specific points in the diagrams or make assumptions which can affect the reliability of the method. There has been effort to adopt the most reasonable assumptions and choices guided by the literature and the knowledge of soil mechanics and the laboratory testing in specific.

Table 3.9 shows the summary of the values of the 14 parameters calculated in the previous to fully determine loose Ottawa sand according to Lade's Double Hardening model:

LADE'S DOUBLE HARDENING MODEL PARAMETERS FOR LOOSE OTTAWA SAND (Dr=14,60%)		
Strain Component	**Parameter**	**Value**
Elastic	Young's modulus coefficient, **M**	**808,88**
	Young's modulus exponent, **λ (n)**	**0,5061**
Plastic Expansive	Poisson's Ratio, **ν**	**0,20**
	Yield constant, η_1	**16,09**
	Yield exponent, **m**	**0,0488**
	Plastic potential constant, **R**	**0,00**
	Plastic potential constant, **S (ρ)**	**0,4216**
	Plastc potental constant, **t**	**-0,7607**
	Work hardening constant, **α**	**1,9709**
	Work hardening constant, **β**	**1,0005**
	Work hardening constant, **P**	**0,3077**
	Work hardening constant, **l**	**1,2165**
Plastic Collapse	Collapse Modulus, **C**	**0,0291**
	Collapse exponent, **p**	**3,0353**

Table 3.9: *Lade's Double Hardening Model parameters for loose Ottawa sand.*

CHAPTER 4

FINITE ELEMENT ANALYSIS

INTRODUCTION

In this chapter, the results of the finite element analysis based on the numerical simulation described in chapter 3 are presented. The predictive capabilities of Lade's Double Hardening model are evaluated through comparison with experimental results of tests on Ottawa Sand.

The numerical analyses were undertaken using the **Imperial College Finite Element Program, ICFEP** (GCG, 1993). The investigation was primarily focused on the prediction of the stress-strain behaviour of the drained triaxial tests used for the calibration described in chapter 3. The fourteen parameters derived from the calibration were input in ICFEP utilising Lade's Double Hardening Model to describe the non-linear material properties. Once the prediction of the drained triaxial tests was verified, a series of predictions were extracted in order to evaluate the further prediction capabilities of the model. These included the predictions concerning mainly hollow cylinder tests, both under drained and undrained loading conditions. In the cases that experimental results were available, the comparison was base upon them. Otherwise, the predicted behaviour was theoretically evaluated.

In the **first part** of the chapter, the simulation of the triaxial and the hollow cylinder test to ICFEP is explained.

In the **second part**, the capability of the above mentioned simulation, as well as the reliability of the program are verified. In order to achieve so, the behaviour of Sacramento River Sand as described by Lade (1977) is successfully reproduced. The fourteen parameters calculated by Lade (1977) are input into ICFEP and the drained triaxial tests Lade used are successfully reproduced, for both loose and dense Sacramento River Sand.

In the **third part**, the 12 drained triaxial tests of Ottawa Sand used to calculate the values of the 14 parameters of the model are simulated and the results are compared with the respective experimental results in order to evaluate and verify these values.

In the **final part**, the predictions of the hollow cylinder tests for both Sacramento River Sand and Ottawa Sand are presented, under drained and undrained loading conditions. The results are compared with experimental results whenever available, otherwise also theoretically evaluated.

4.1 ICFEP (IMPERIAL COLLEGE FINITE ELEMENT PROGRAM)

ICFEP stands for the Imperial College Finite Element Program. It has been developed by professor David M. Potts and is designed to specifically analyze geotechnical problems. ICFEP uses the **displacement based Finite Element Method** which has been described briefly in *§2.3*. It is used for **two-dimensional problems** (plain stress and strain), **axi-symmetric geometry problems**, as well as **fully three-dimensional problems**. The material behaviour can be assumed **linear or non-linear**. The program also handles **geometrical non-linearities**. Moreover, there is the possibility to study **large displacements and strains**. Last but not least, the program can deal with rapid stiffness changes and can also deal effectively with non-symmetric stiffness matrices.

In the current project, plane strain and full axi-symmetric problems (geometry, soil properties and boundary conditions all axi-symmetric) as well as fully three dimensional conditions have been considered.

ICFEP is a computational program written in **FORTRAN language**. The program consists of four self-inclusive software modules that run sequentially. Each one of the

software modules consists of the main program written in FORTRAN language and the respective commands to the computer. The user interacts with ICFEP through a **specifically modified input file** which is substantially a text file that includes all the commands, also specifically modified as to be recognizable by the program *(Appendixes II & III).*

The first software module processes and checks the correctness of the commands given by the user in the input file. Next the commands enable the other three software modules. The mesh of the geotechnical problem is generated and resolved through the use of the appropriate simulations. In the input file the type of the analysis to be performed is determined: plane stress conditions, plain strain conditions, axi-symmetric stress conditions, pseudo-static stress conditions with the implementation of Fourier series or fully three-dimensional stress conditions.

4.1.1 TRIAXIAL TEST SIMULATION IN ICFEP

For the current project, the triaxial test is simulated through a **single element 2-D analysis**. The sample is simulated by a 2-D regular quadrilateral block of unary dimensions that is assumed to rotate around its one side as to create a cylinder. This is determined as **axi-symmetric type of analysis**.

The material of which the element is comprised is the real material which is being simulated, described by a series of **linear** and **non-linear material properties**. The linear material properties refer to Young's Modulus $\boldsymbol{E}$ and Poisson's ratio $\boldsymbol{\nu}$, while the non-linear material properties refer to the parameters of the elasto-plastic model to be used for the numerical analysis (**Lade's Double Hardening Model** namely).

With respect to the **boundary conditions** of the single element, the side around which the rotation takes place is restricted with zero prescribed displacements on the horizontal direction. The base of the element is restricted with zero prescribed displacements in the vertical direction.

The **initial compressive stresses** $\boldsymbol{\sigma_1}$ and $\boldsymbol{\sigma_3}$ are applied uniformly along the top and the side of the single element, so they are input in *kPa* units. The consolidation process that takes place before the shearing is not simulated separately. The initial

stresses given in the specific file "called" by the program are those that correspond to the end of the consolidation and are: $\sigma_1 = \sigma_3$.

The triaxial test is set as a **strain-controlled** procedure, therefore the vertical displacements increase incrementally and the lateral strains are free to develop. The values of the vertical stresses developed are defined by the program. *Figure 4.1* illustrates the above simulation and *Appendix II* gives an example of the respective input file.

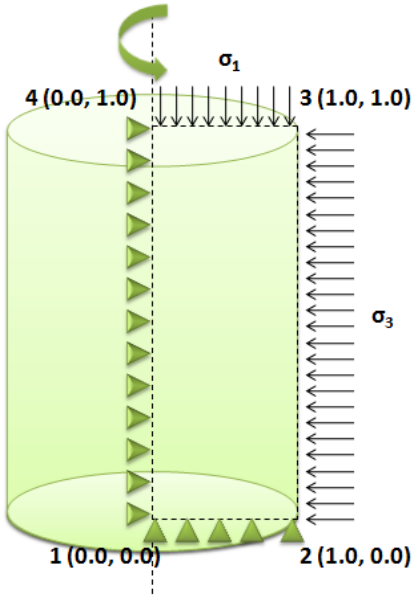

Figure 4.1: *Simulation of triaxial test sample as a plain single element which is rotated around the axis (axi-symmetric simulation) in ICFEP.*

4.1.2 HOLLOW CYLINDER TEST SIMULATION IN ICFEP

As regards the stress condition of the sample inside the hollow cylinder torsional shear apparatus, is has been assumed as a **fully three-dimensional single element**, based on the following assumptions:

For the sake of simplicity, it has been assumed that the loading conditions of the hollow cylinder sample can be simulated by a **cube** (with the material properties of the simulated soil) of unary dimensions upon which the vertical, stresses $\boldsymbol{\sigma_z}$, the lateral stresses $\boldsymbol{\sigma_r}$ and $\boldsymbol{\sigma_\theta}$, as well as the shear stresses $\boldsymbol{\tau}$ are applied. *Figure 4.2* illustrates the simulation and the positive directions for the stresses and rotations around the axes are shown. In order to create the cube in ICFEP, its one face is initially determined in

the two-dimensions. Its vertexes are numbered anti-clockwise. One additional vertex is also defined in the third dimension and the rest of the vertexes are automatically defined (mesh extended on the third dimension) so, finally, the cube is fully defined in the 3-dimensional space. Therefore, the cube consists of **6 regular quadrilateral isoparametric elements**.

With respect to the **boundary conditions** of the single 3-D element, the base of the element is restricted with zero vertical prescribed displacements.

Since the hollow cylinder sample has been defined in the three dimensional space, the **two phases** of the actual experiment performed in the laboratory are simulated.

The **first phase** incorporates the **initial stresses** and the **consolidation procedure**. At this stage the **linear** and **the non-linear properties** of the material are defined in the input file. The linear material properties refer to Young's Modulus ***E*** and Poisson's ratio ***v***, while the non-linear material properties refer to the parameters of the elasto-plastic model to be used for the numerical analysis (**Lade's Double Hardening Model** namely). In terms of procedure, the first phase includes, in summary, the following steps:

- The **initial stresses** that define the initial stress condition of the sample are defined in a separate file. This filed is "called" by the program. Compressive stresses are negative.
- The **linear (elastic) material properties** of the material are defined ***(E, v).***
- The **elasto-plastic model** to be used for the numerical analysis is selected and the values of its parameters are defined.
- The **loads** are applied in sequential increments to the cube in a manner that the consolidation line of the sample is followed. The loads applied are equally distributed in the four top apexes of the cube. For example, if 10kPa need to be applied in one increment, 2.5kPa are applied in each apex. The whole procedure is repeated until the load reaches the desired value.

The **second phase** of the simulation is initiated from the point where the first phase has stopped and it incorporates the **shearing**. It involves the torsional loading of the sample until failure. The steps described above are all similar for the second phase too and the loads are applied incrementally as well. In this case

however, the load increments are much smaller, so that the loading takes place in a relatively slower pace, in order for the model to be realistically applied and consequently produce realistic values for the examined gauges (stresses and strains). The process continues until the cube fails.

Appendix III gives an example of the respective input file.

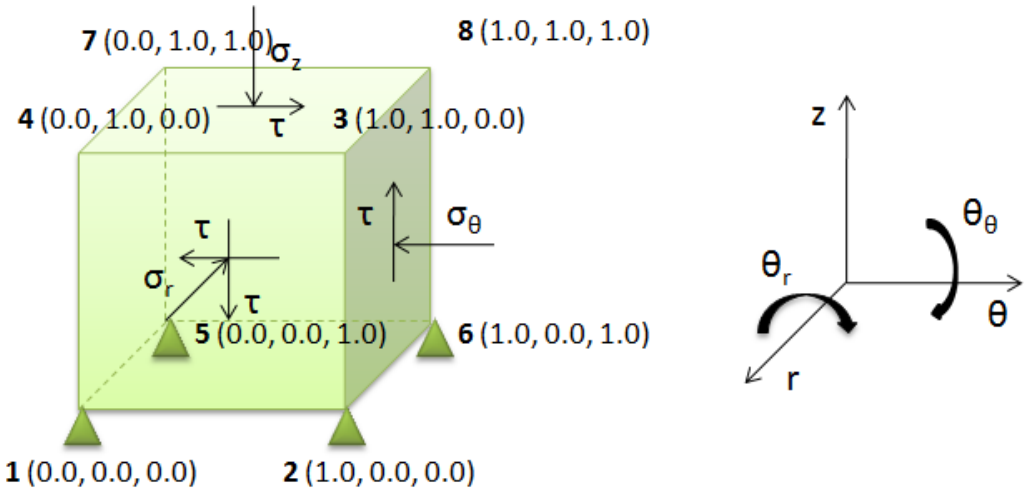

Figure 4.2: *(a) Simulation of hollow cylinder sample as a cube of unary dimensions in ICFEP. (b) Positive directions for the applied stresses and rotations around the axes in ICFEP.*

4.2 NUMERICAL ANALYSIS OF SACRAMENTO RIVER SAND

4.2.1 REPRODUCTION OF DRAINED TRIAXIAL TESTS IN ICFEP – SOFTWARE VERIFICATION

In order to present a verification of the finite element program used in this dissertation and also affirm that the model implemented is properly working, there has been an effort to reproduce the original drained triaxial tests that Lade presents in his paper *(1977)* for **dense** and **loose Sacramento River Sand** as shown in *Figure 4.3(a & b)* respectively.

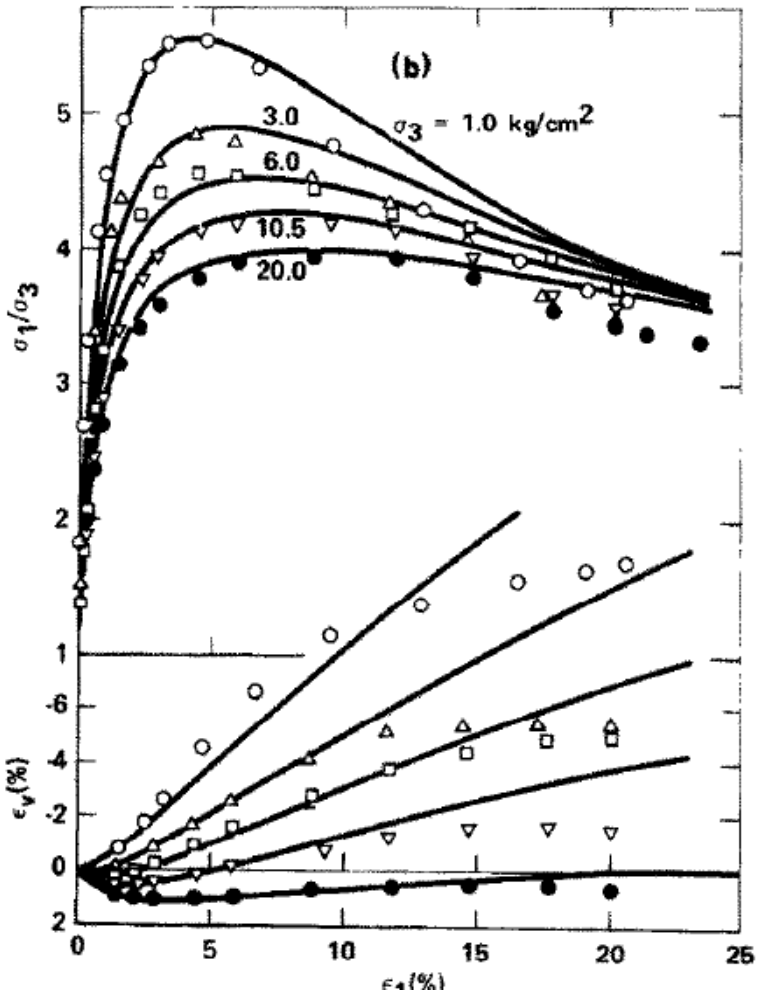

Figure 4.3a: *Comparison between measured and predicted stress-strain and volume change behavior for dense Sacramento River Sand in drained triaxial compression tests. (After Lade, 1977)*

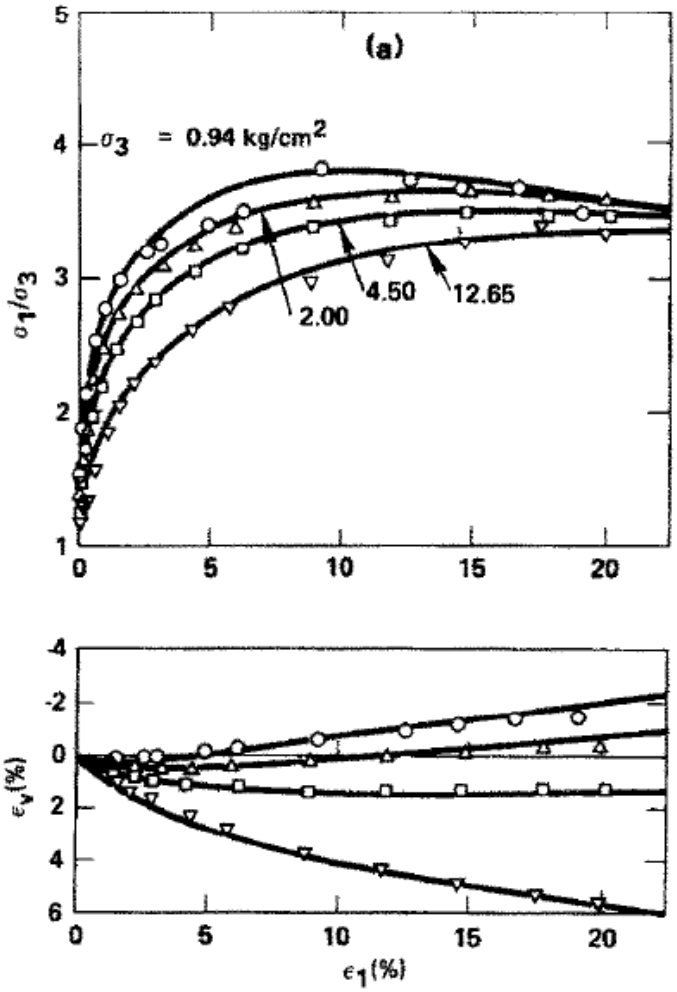

Figure 4.3b: *Comparison between measured and predicted stress-strain and volume change behavior for loose Sacramento River Sand in drained triaxial compression tests. (After Lade, 1977)*

From these figures, one can see clearly the effect of the confining pressure and relative density on the behaviour of drained sand.

For all levels of confining pressure, the results on dense specimens *(Dr=100%) (Figure 4.3a)* show that the mean stress ratio increases to a peak and then drops with increasing axial strain until a steady state is observed. The increase in the mean stress ratios are associated with a slight initial volumetric contraction, followed by a gradually increasing rate of volume expansion (dilation). As the confining pressure increases, dilation is gradually decreased.

Figure 4.3b shows the behaviour of samples with an initial relative density of *Dr=38%.* Although some of the samples do display a dilative behaviour for the range

of the pressure used by Lade, the maximum stress ratios are significantly less in comparison to those observed at a relative density of *100%*. The volumetric strains are contractive at the two levels of confining pressures of $4.50kg/cm^2$ and $12.65kg/cm^2$, while for the other two confining pressures $(0.94/cm^2$ *and* $2.00kg/cm^2)$ the sand shows dilative behaviour at large axial strain levels.

Overall, the effect of the void ratio and the level of effective confining pressure interaction are observed if comparing *Figures 4.3a and 4.3b*: The loose sand sheared at a very low confining pressure behaves nearly like the dense sand at high effective confining pressure.

As it can be seen, there are *4 drained triaxial tests for the loose* and *5 drained triaxial tests for the dense Sacramento River sand*. Lade used a different unit system, so, having taken into consideration that:

$$1\frac{kg}{cm^2} = 98.039kPa \tag{4.1}$$

It can be calculated that Lade's experiments were made in the confining pressures shown in *Table 4.1:*

Material	Confining pressure σ_3 [kg/cm^2]	Confining pressure σ_3 [kPa]	Test No
Loose Sacramento River Sand	0,94	92,184	SACR-92
	2,00	196,136	SACR-196
	4,50	441,306	SACR-441
	12,65	1240,561	SACR-1241
Dense Sacramento River Sand	1,00	98,068	SACR-98
	3,00	294,204	SACR-294
	6,00	588,408	SACR-588
	10,50	1029,715	SACR-1029
	20,00	1961,361	SACR-1961

Table 4.1: *Summary of drained triaxial tests simulated in ICFEP in order to reproduce Lade's results for Sacramento River Sand (1977).*

Lade managed to capture the above described behaviour with success while implementing the double hardening model (1977).

Table 4.2 shows the parameters derived from Lade's original calibration for Sacramento River Sand. These parameters were input in ICFEP in order to simulate the above drained triaxial experiments.

LADE'S DOUBLE HARDENING MODEL PARAMETERS FOR SACRAMENTO RIVER SAND			
Strain Component	**Parameter**	**Loose**	**Dense**
General	Relative density, **Dr (%)**	**38**	**100**
	Void Ratio, **e**	**0,87**	**0,61**
Elastic	Young's modulus coefficient, **M**	**960**	**1680**
	Young's modulus exponent, **λ (n)**	**0,57**	**0,57**
Plastic Expansive	Poisson's Ratio, **ν**	**0,20**	**0,20**
	Yield constant, η_1	**28**	**80**
	Yield exponent, **m**	**0,093**	**0,23**
	Plastic potential constant, **R**	**-1,00**	**-2,95**
	Plastic potential constant, **S (ρ)**	**0,43**	**0,44**
	Plastc potental constant, **t**	**0,00**	**8,45**
	Work hardening constant, **α**	**3,00**	**3,00**
	Work hardening constant, **β**	**-0,076**	**0,060**
	Work hardening constant, **P**	**0,24**	**0,12**
	Work hardening constant, **I**	**1,25**	**1,16**
Plastic Collapse	Collapse Modulus, **C**	**0,00028**	**0,00023**
	Collapse exponent, **p**	**0,94**	**0,86**

Table 4.2: *Summary of Lade's Double Hardening Model parameters for Sacramento River Sand (after Lade, 1977).*

The results from ICFEP plotted against the originals are shown below *(Figures 4.4 a & b)*. It can be seen that ICFEP accurately reproduced Lade's predictions for both dense and loose Sacramento River Sand, as far as stress-strain curves and volumetric strain – axial strain curves are concerned.

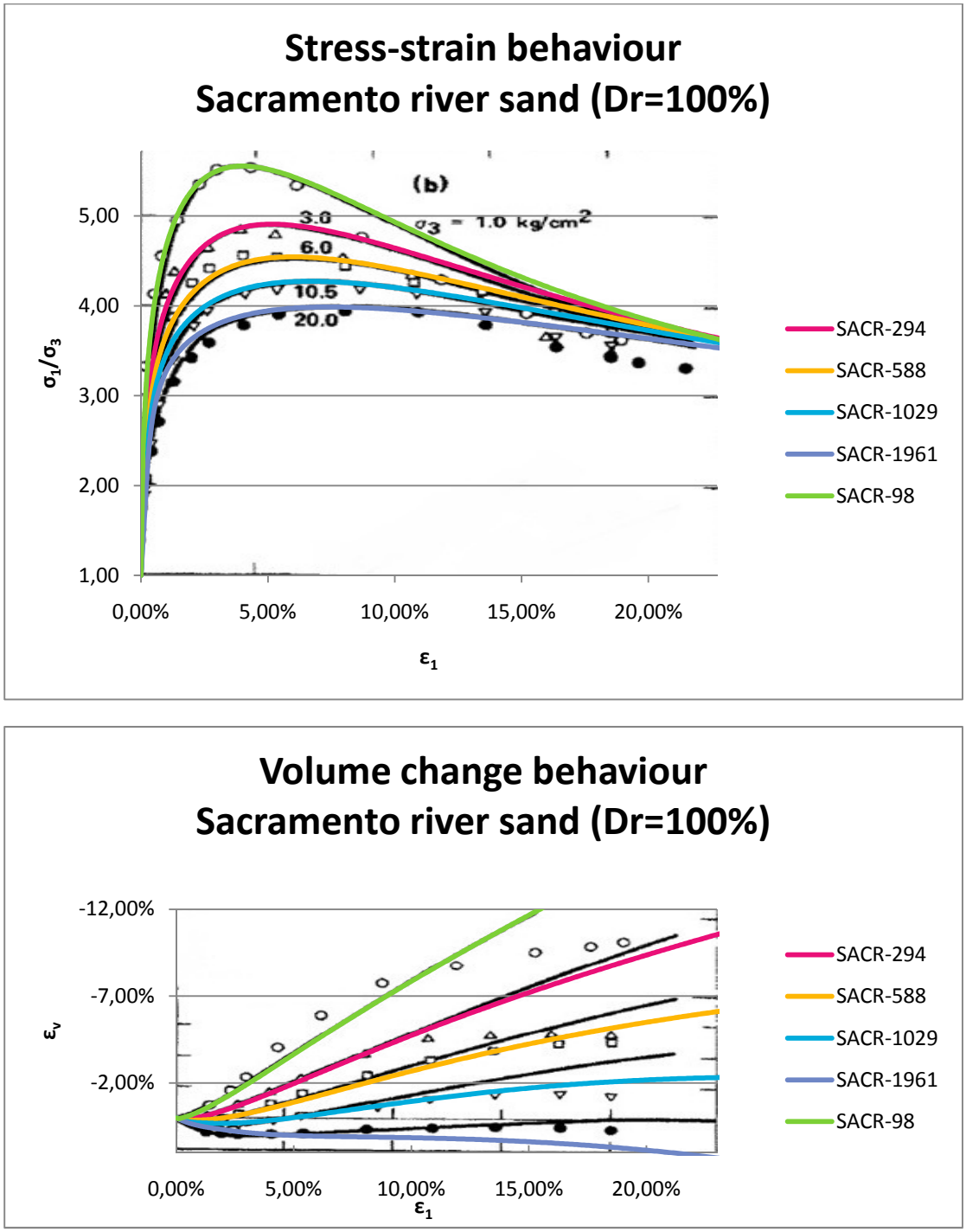

Figure 4.4a: *Comparison between reproduced by ICFEP and predicted by Lade (1977) stress-strain and volume change behavior for dense Sacramento River Sand in drained triaxial compression tests. (After Lade, 1977)*

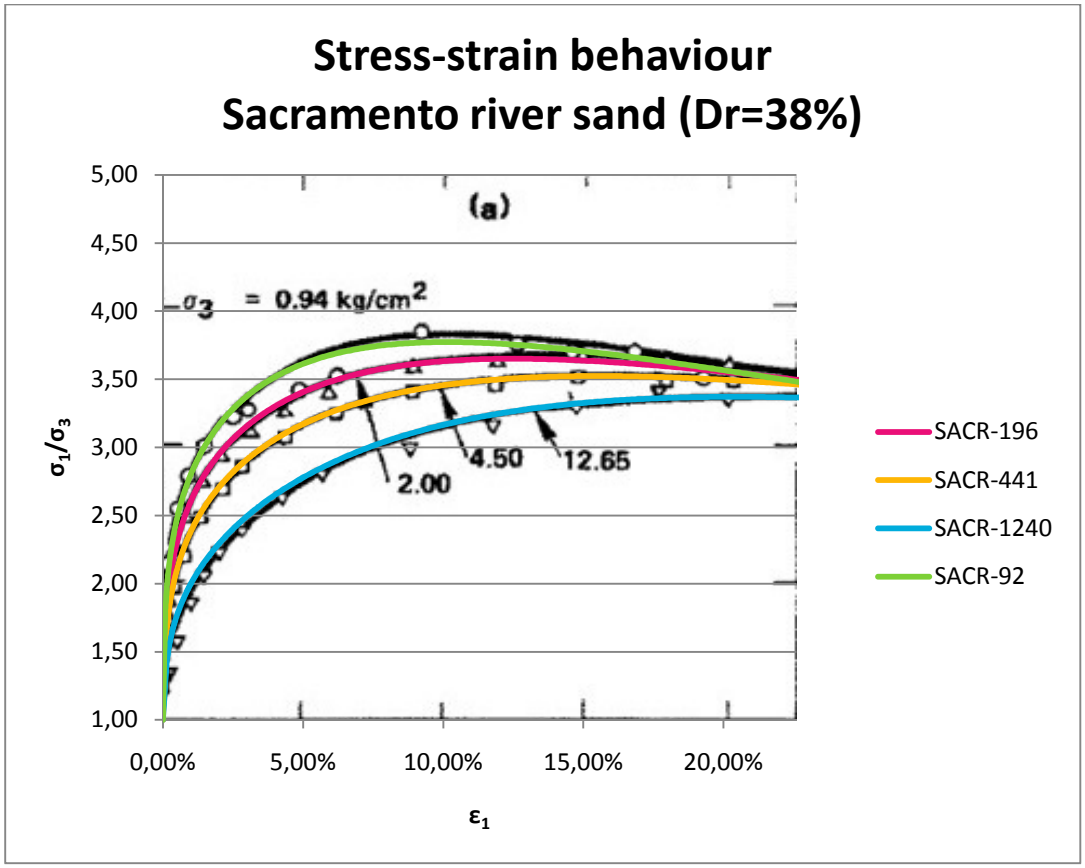

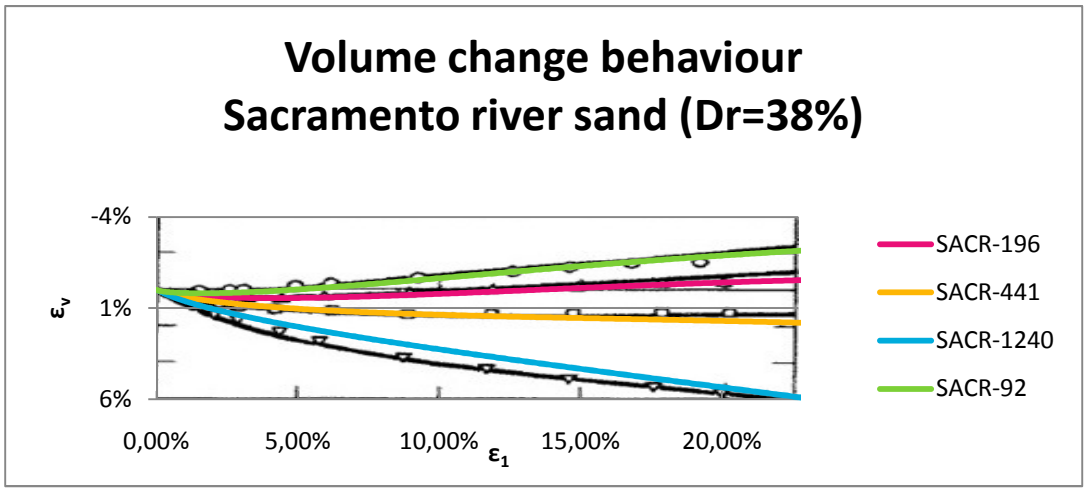

Figure 4.4b: *Comparison between reproduced by ICFEP and predicted by Lade (1977) stress-strain and volume change behavior for loose Sacramento River Sand in drained triaxial compression tests. (After Lade, 1977)*

It is reasonably concluded that the implementation of the model in ICFEP successfully works and it can therefore trustworthily be used for this project's analyses.

4.2.2 MONOTONIC BEHAVIOUR SIMULATION OF SACRAMENTO RIVER SAND (LOOSE & DENSE) UNDER TORSIONAL LOADING

Since Lade's parameters for Sacramento River sand have been verified, as well as the accordance with ICFEP, it was considered purposeful to present a set of torsional tests' simulation using these parameters. The simulation of the hollow cylinder test follows the procedure described in *§4.1.2*.

The tests simulated were divided in **two sets for each density** (total of four sets), each set including three different initial mean effective stresses. The first set includes *3* monotonic hollow cylinder torsional shearing tests under **drained** loading conditions, setting off from the mean effective stresses of: ***100kPa, 200kPa*** and ***300kPa*** *(Figures 4.5-4.7).* The second set is a similar set under **undrained** loading conditions. Again, 3 tests setting off from *3* different mean effective stresses: ***100kPa, 200kPa*** and ***300kPa*** *(Figures 4.8-4.9).* The results are shown below where the simulation is presented through a series of diagrams including: effective stress paths (for both drained and undrained tests), stress-strain curves (for both drained and undrained tests) and volumetric strain-shear strain curves for the drained tests.

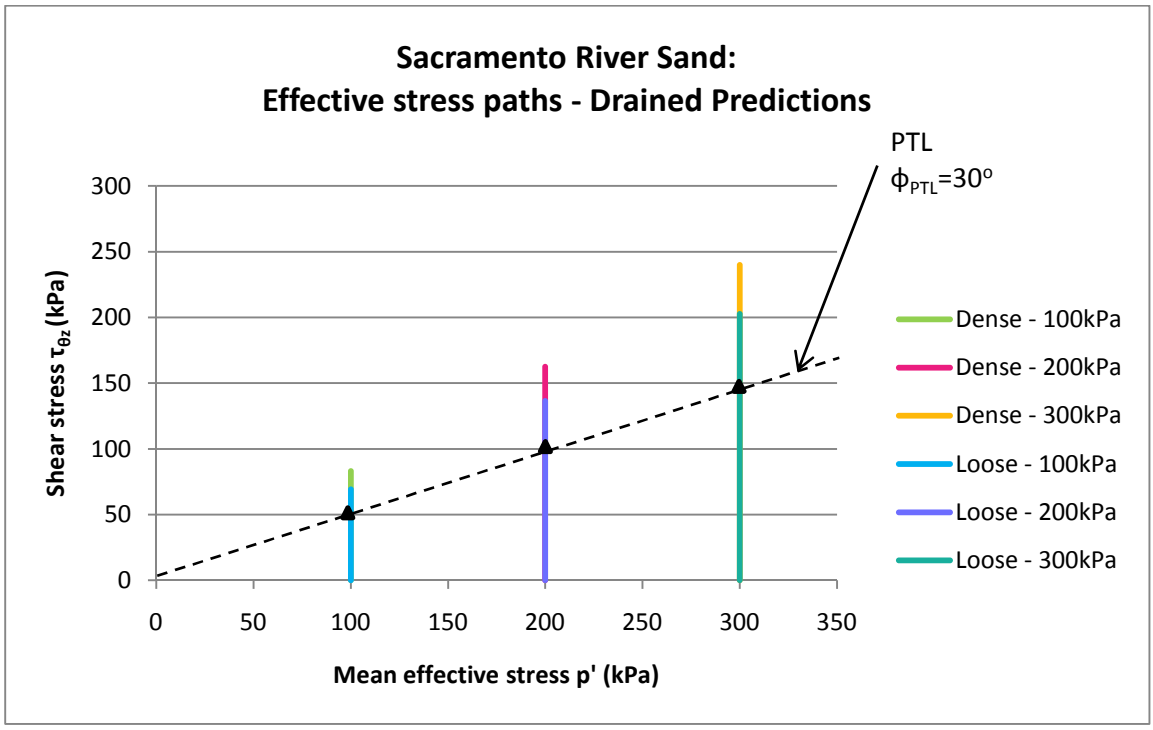

Figure 4.5: *Predicted effective stress paths (ICFEP) for loose and dense Sacramento River Sand based on Lade's Parameters (1977).* ***Drained*** *torsional shear tests.*

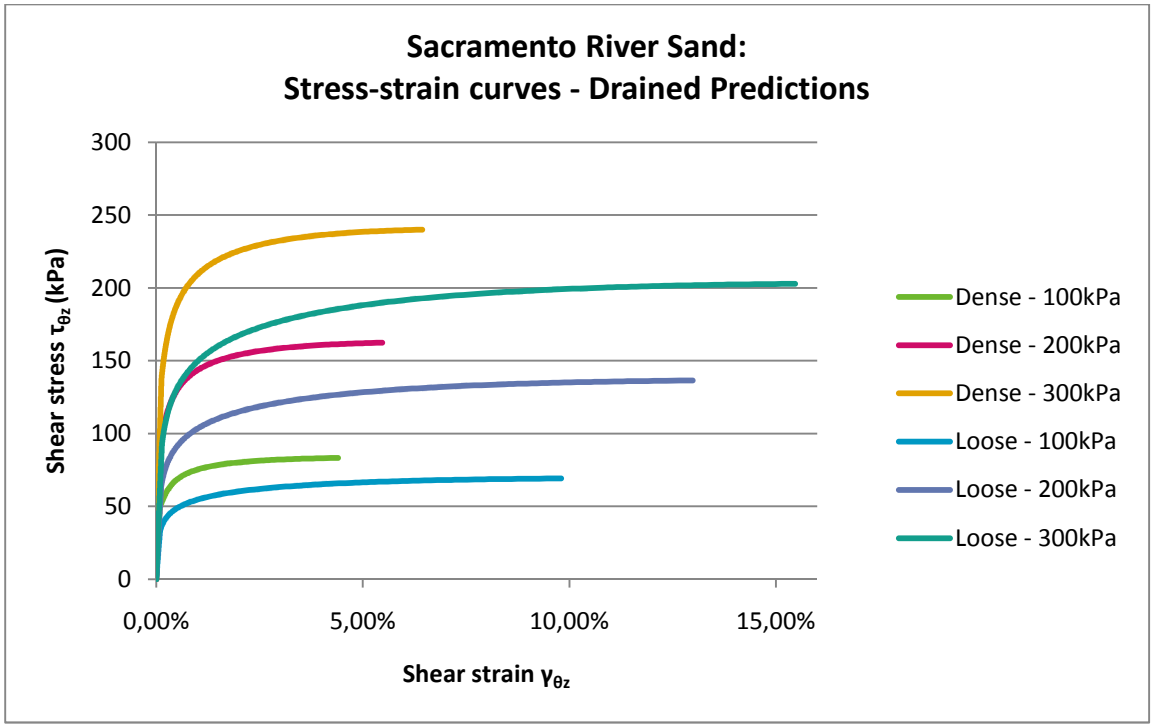

Figure 4.6: *Predicted shear stress – shear strain curves (ICFEP) for loose and dense Sacramento River Sand based on Lade's Parameters (1977).* ***Drained*** *torsional shear tests.*

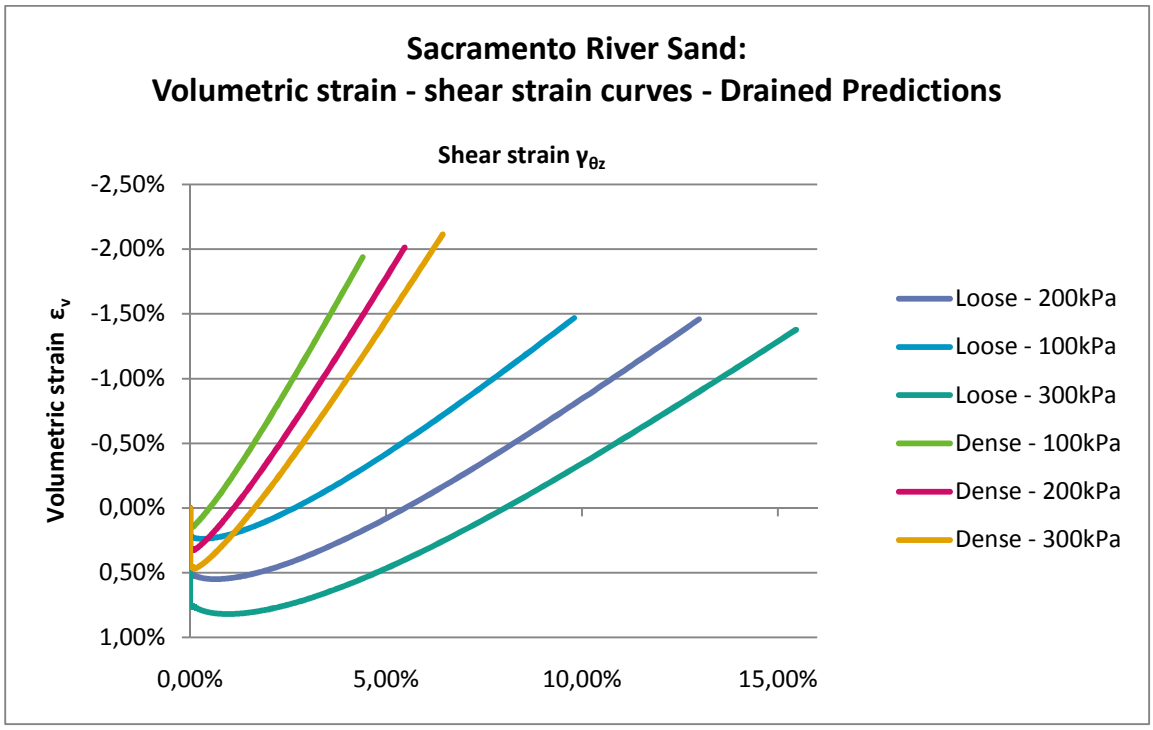

Figure 4.7: *Predicted volumetric strains – shear strain curves (ICFEP) for loose and dense Sacramento River Sand based on Lade's Parameters (1977).* ***Drained*** *torsional shear tests.*

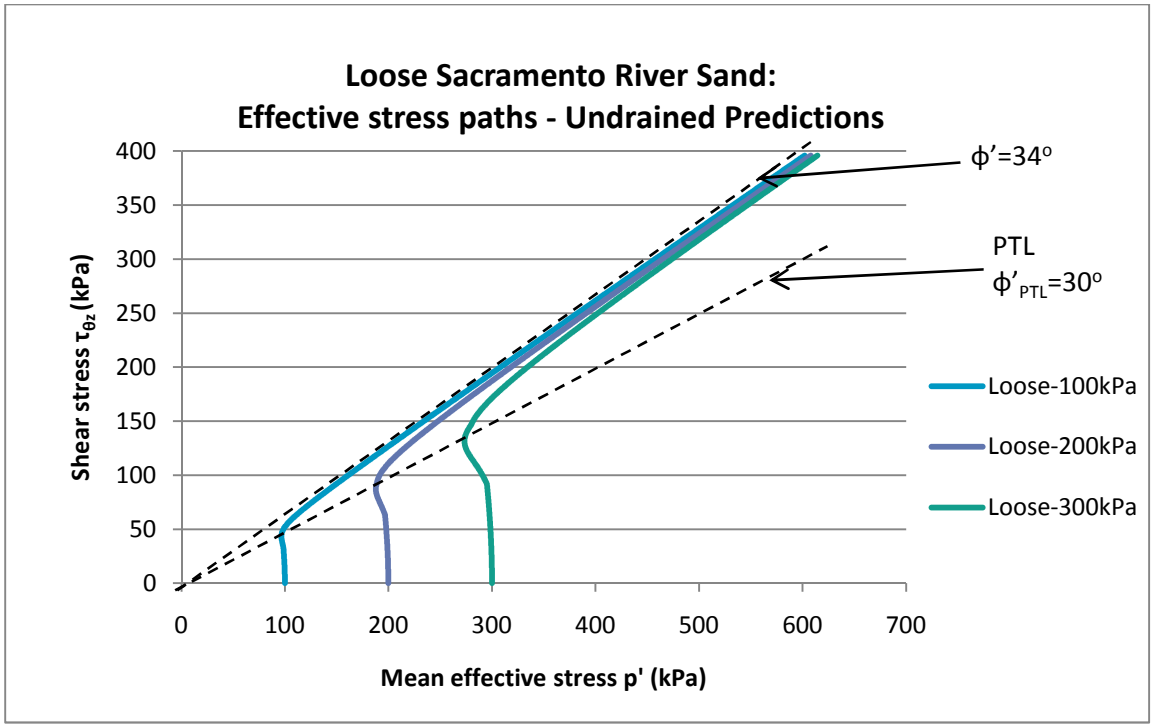

Figure 4.8: *Predicted effective stress paths (ICFEP) for loose Sacramento River Sand based on Lade's Parameters (1977).* ***Undrained*** *torsional shear tests.*

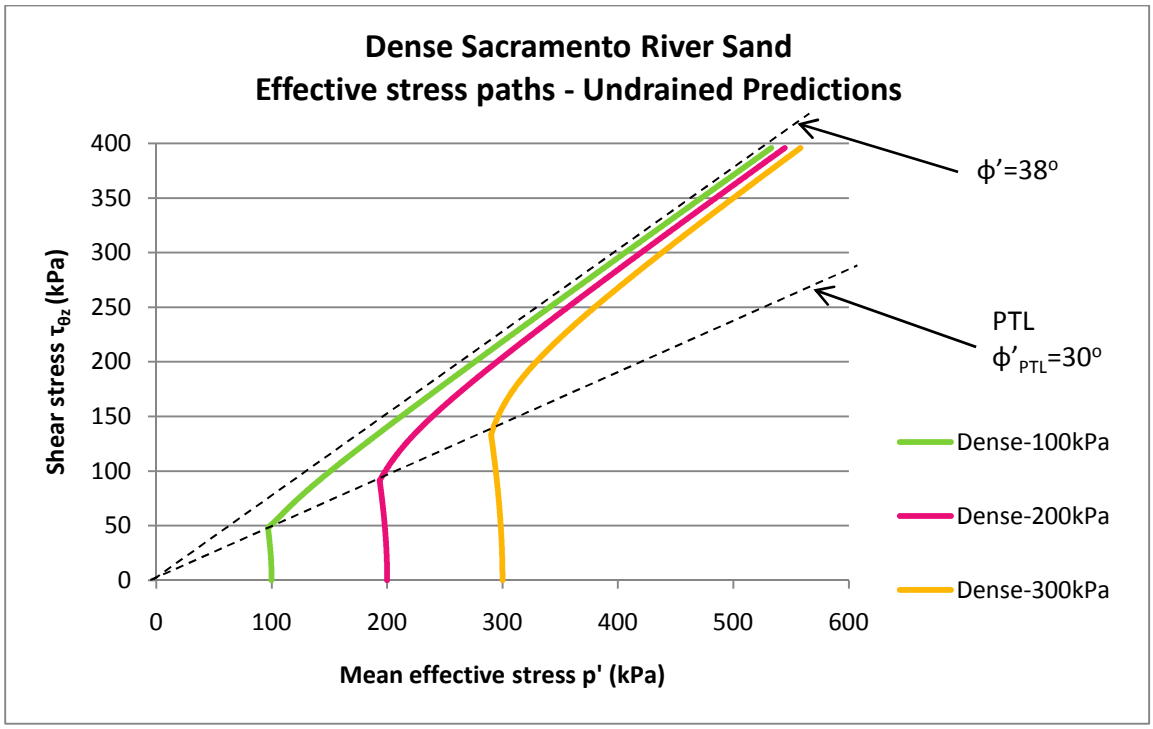

Figure 4.9: *Predicted effective stress paths (ICFEP) for dense Sacramento River Sand based on Lade's Parameters (1977).* ***Undrained*** *torsional shear tests.*

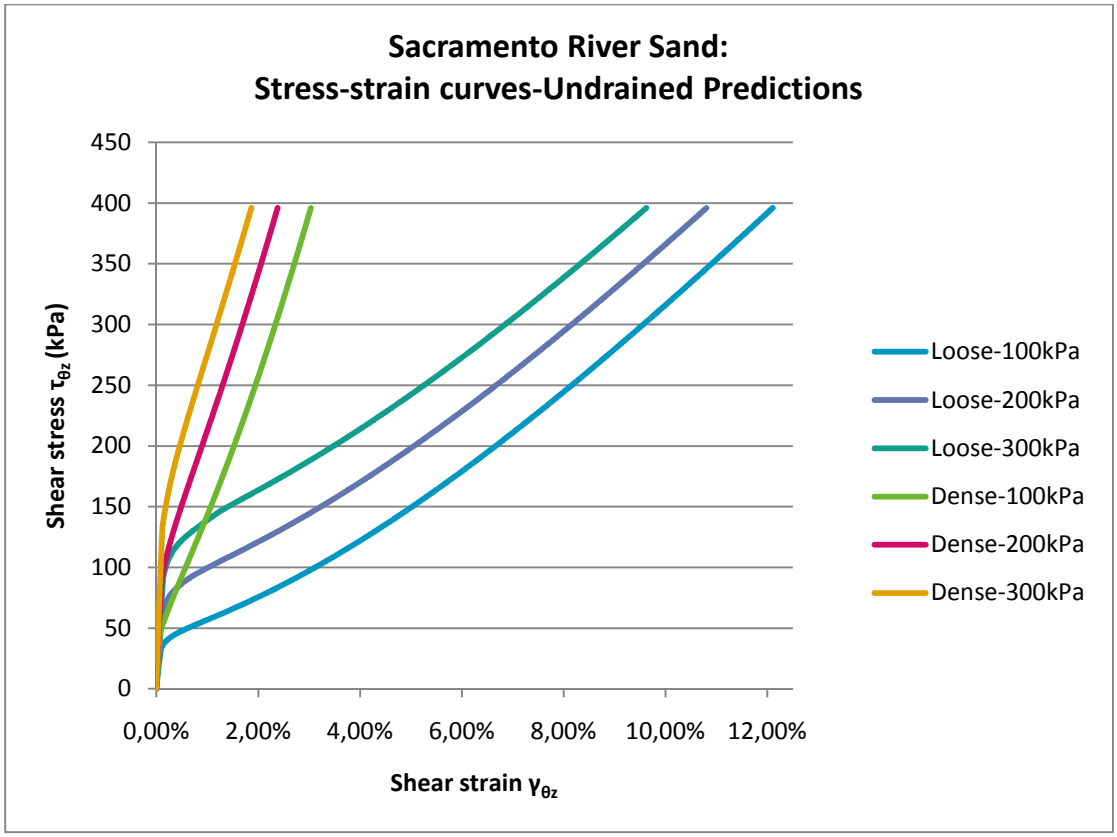

Figure 4.10: *Predicted effective stress paths (ICFEP) for dense Sacramento River Sand based on Lade's Parameters (1977). Undrained torsional shear tests.*

From the above presented diagrams the following observations are derived:

- In *Figure 4.5,* the effective stress paths are illustrated for both dense and loose specimens. As expected, the mean effective stress p' remains constant during the drained torsional loading of isotropically consolidated specimens.
- In *Figure 4.5,* the triangles marked on the drained stress paths correspond to the change from contraction to dilation defined from the volumetric against shear stress curves. The triangles are in the same straight line which passes from the origin of the stress space, and actually define the Phase Transformation Line (PTL). As it can also be seen from *Figures 4.8 and 4.9* which show the effective stress paths for the undrained tests' simulations, the PTL is uniquely defined for one type of sand ($\varphi_{PTL}=30^{o}$) , independently from its relative density or the loading conditions (drained/undrained). As far as the undrained stress paths are concerned, the PTL is defined as the line which connects the phase transformation points and the origin of the stress space. The phase transformation points are defined as the points at which the

effective stress path has a vertical tangent (Ibsen and Lade, 1997). For the Sacramento River sand, in this simulation, it was found to be at 30^{o}, as it rationally derives agreeably from all stress paths diagrams. this value is also close to the values found in the literature for typical sands (Georgiannou, 2010).

- In *Figures 4.5 and 4.6* it is evident that the dense specimens reach much higher shear stress levels than the loose ones, which is also in agreement with what is expected.
- Inspection of *Figures 4.6* and *4.7* shows that for both densities the Sacramento River Sand shows similar behaviour: An initial contractive phase during which the shear stress, $\tau_{\theta z}$, steadily increases to a peak value. The contractive phase is halted by each effective stress path reaching the point of phase transformation. During subsequent loading the shear stress remains nearly constant for all effective stresses and densities. The main difference between the dense and loose specimens is that the peak value is reached much more rapidly (for lower levels of shear strains) than the corresponding loose ones. That is depicted at the slopes of the volumetric curves after the phase transformation points which illustrate the rate of the excess pore pressure decrease. This rate is however the same between specimens of the same density and for different initial stress levels (parallel volumetric curves).
- *Figures 4.8* and *4.9* show the effective stress paths for the undrained simulations. They are shown in separate diagrams for clarity. It is clear however, that the tendency to contract is much less evident for the denser specimens, as it is anticipated. Although it seems that an even denser specimen would be required in order to eliminate it. Overall, the behaviour of the Sacramento River sand indicates no presence of brittleness under undrained loading conditions.
- The failure envelope determined form the undrained tests is also plotted in *Figures 4.8* and *4.9*. The friction angle is defined at 38^{o} for the dense and at 34^{o} for the loose specimens, indicating a reasonable difference, with the higher value corresponding to the denser specimen, that is, the one with the higher strength.

- Finally, *Figure 4.10* shows the stress-strain curves for the undrained simulations for both dense and loose specimens. As it can be shown, their behaviour is again similar, in the sense that shear stress continuously increases; in a higher rate until the phase transformation point and then at al lower rate. Both rates are higher for the denser specimen. The difference between the rates for the denser specimen is less intense, in accordance with the respective stress path.

Overall, the behaviour of loose and dense Sacramento River sand is reasonably predicted. It would have been desirable and of great interest to compare the predicted results with experimental results but unfortunately they were not available.

4.3 NUMERICAL ANALYSIS OF LOOSE OTTAWA SAND

In this part of the chapter the results from ICFEP concerning Loose Ottawa Sand are presented. In the cases that experimental results were available, the respective comparison is presented and commented on. In all other cases that experimental results were not available the predictions are commented on based on the expected behaviour.

4.3.1 DRAINED TRIAXIAL TESTS

First of all, in order to evaluate the calibration performed in chapter *3*, the 12 drained triaxial tests used for this calibration are simulated and compared to the experimental results. The results include stress-strain diagrams, as well as the respective volumetric strain-axial strain diagrams. They were plotted individually for each separate test for clarity reasons and are presented below *(Figures 4.11-4.17).* Again, the unloading – reloading cycles are to be ignored, as they are not simulated in this project.

It can be seen that ICFEP generally predicts the Loose Ottawa Sand behaviour with satisfying accuracy. More specifically:

1. With regards to the **stress-strain diagrams**:
   - In terms of the value of the **yield stress**, that is in very good agreement with the experimental results for all 12 tests.

- In terms of **stiffness** (as interpreted by the gradient of the stress-strain curve in the small strains area), that is in good agreement with the experimental results for the tests at the confining pressures of *50kPa*, *100kPa*, *150kPa* and *200kPa*. However, for the confining pressures of *350kPa* to *600kPa*, the material behaviour in the small strains appears relatively stiffer than reality and this divergence intensifies as the confining pressures grow higher. That can easily be justified since the model re-calculates the elastic modulus according to the *equation (2.2b),* explained in *Chapter 2*:

$$E = M \cdot p_a \cdot (\frac{\sigma'_3}{p_a})^n \qquad (2.2b)$$

  which, for non negative values of n (as it is the case here), is an increasing function between the elastic modulus E and the confining pressure σ_3'. Therefore, as the confining pressure σ_3' increases, the elastic modulus E increases as well, and as this is the parameter that defines the stiffness of the material behaviour in the early strains, it is rational to become stiffer. This stiffness though, seems to be in accordance with the unloading-reloading cycles (gradient of the curves) of these tests by which the elastic modulus was calculated in the first place, according to Lade's suggestions (1977) and as explained in *§3.3.1.2*. Perhaps this is not a very good assumption as it seems to cause slight divergences for the high confining pressures. Overall, the accordance is considered satisfying for all practical purposes.
- There is a small divergence at the intermediate strains at the tests of *50kPa* and *100kPa*, but eventually the predicted and the real curves are found in good agreement for the larger strains. The agreement of the stress ratio-strain curves is excellent for the tests at the confining pressures of *150kPa* and *200kPa* and nearly excellent for tests at the confining pressures of *250kPa* and *300kPa* at all strain levels.
- The softening part of the curve of the *50kPa* test is also accurately predicted, as well as the slightly hardening part of the rest of the tests.

2. With regards to the **volumetric behaviour**:

- The initial slope of the volumetric curve, which expresses the initial dilatant behaviour of the material, is captured very well for the tests at the confining

pressures of *50kPa* to *200kPa* and well enough for the tests at the confining pressures of *250kPa* to *350kPa.*

- For the same tests (*50kPa to 350 kPa*) the phase transformation point to which the material behaviour starts to become compressive is captured very well, as well as the slope of the volumetric curve after this point.
- Small divergences begin to occur from the confining pressures of *400kPa* and higher. These regard the phase transformation point which seems to occur for lower volumetric strains. It is of question though, of what significance are the unloading-reloading cycles that take place and are not simulated and whether they influence these divergences. Their influence is obvious as to the original volumetric curve and seems more intense for the higher confining pressure tests, as they are of greater extent in terms of stresses. For it is a fact that the slope of the volumetric curve is finally (after the phase transformation point) gradually successfully captured for these tests as well.

It is at this point important to note that, as it is evident from the isotropic consolidation tests performed prior to the drained triaxial tests upon which the calibration was based *(Figure 2.7),* the way all specimens were loaded to 600kPa before reaching the final pressures of *50, 100, …, 600kPa* results in a different value of overconsolidation ratio (OCR) for each sample. The different values of the OCR for each sample are shown in *Table 4.3*:

Test No.	Maximum stress (during the isotropic compression test)	Initial stress (at the beginning of the drained triaxial test)	OCR
CD-OT20/30-50-0	601,27	48,69	12,35
CD-OT20/30-100-0	602,17	100,21	6,01
CD-OT20/30-150-0	601,72	150,22	4,01
CD-OT20/30-200-0	601,61	201,81	2,98
CD-OT20/30-250-0	602,50	250,39	2,41
CD-OT20/30-300-0	601,80	301,32	2,00
CD-OT20/30-350-0	602,67	351,52	1,71
CD-OT20/30-400-0	603,22	401,68	1,50
CD-OT20/30-450-0	601,28	450,25	1,34
CD-OT20/30-500-0	601,35	500,78	1,20
CD-OT20/30-550-0	600,41	549,26	1,09
CD-OT20/30-600-0	601,90	603,83	1,00

Table 4.3 *Summary of the resulted overconsolidation ratios (OCR) for the 12 experimental tests performed on loose Ottawa sand.*

This can also be the cause of why the experimental results of the higher confining pressures show a less stiff behaviour, unlike the model predictions. It would be expected for the specimens under higher confining pressures to show a stiffer behaviour, although they don't, and this could be due to their lower OCR in comparison to the specimens under lower confining pressures which have higher OCRs.

Although (as it can be seen analytically in *Appendix I*) the overconsolidation ratio (OCR) is in fact an input parameter in ICFEP, and thus its influence should normally be overcome, it is of question whether it would be preferable to calibrate Lade's Model with a different experimental program, as the one Lade used for Sacramento River Sand, that is, with the same value of OCR for all samples and even more preferably normally consolidated samples (OCR=1.0).

Taking into consideration all the above observations and considerations, it has been assumed that the results of the drained triaxial tests **are generally in satisfying accordance with the experimental results for all practical purposes.** The torsional tests that are simulated in the following paragraphs concern mainly values of mean effective stress *p'* of *100kPa, 200kPa* and *300kPa*, for which, as it has already been shown, the accordance was excellent; for it was decided that the prediction capabilities of the model are adequate.

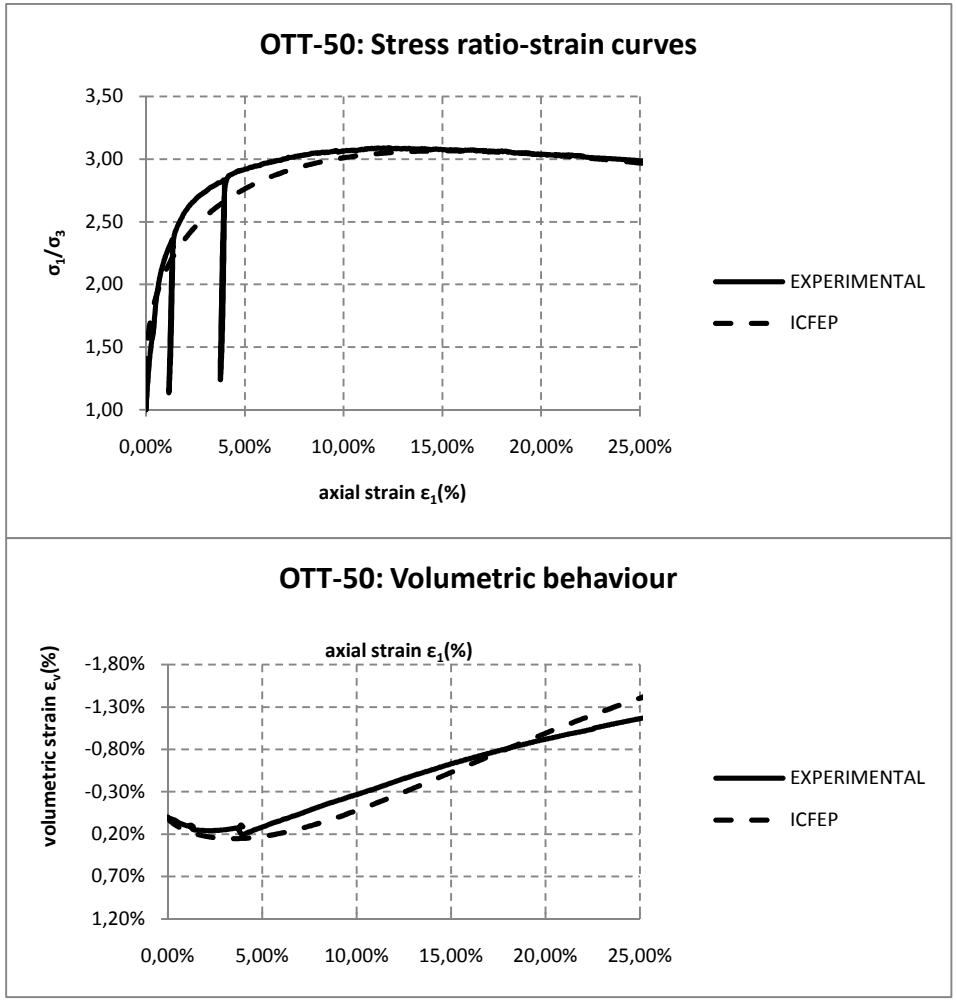

Figure 4.11: *Comparison between predicted behaviour (ICFEP) and the respective experimental results. Stress ratio-strain and volume change behavior for Loose Ottawa Sand: Drained triaxial compression test – confining pressure:* ***50kPa****.*

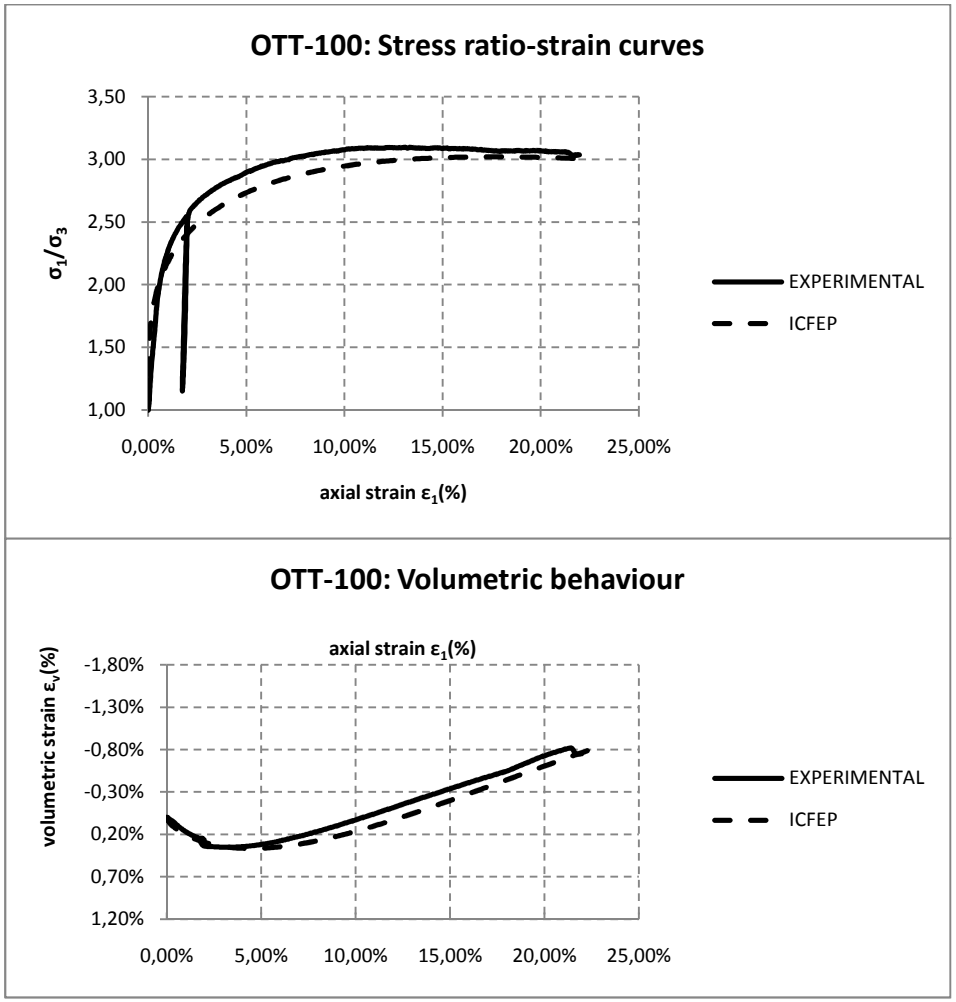

Figure 4.12: *Comparison between predicted behaviour (ICFEP) and the respective experimental results. Stress ratio-strain and volume change behavior for Loose Ottawa Sand: Drained triaxial compression test – confining pressure:* ***100kPa****.*

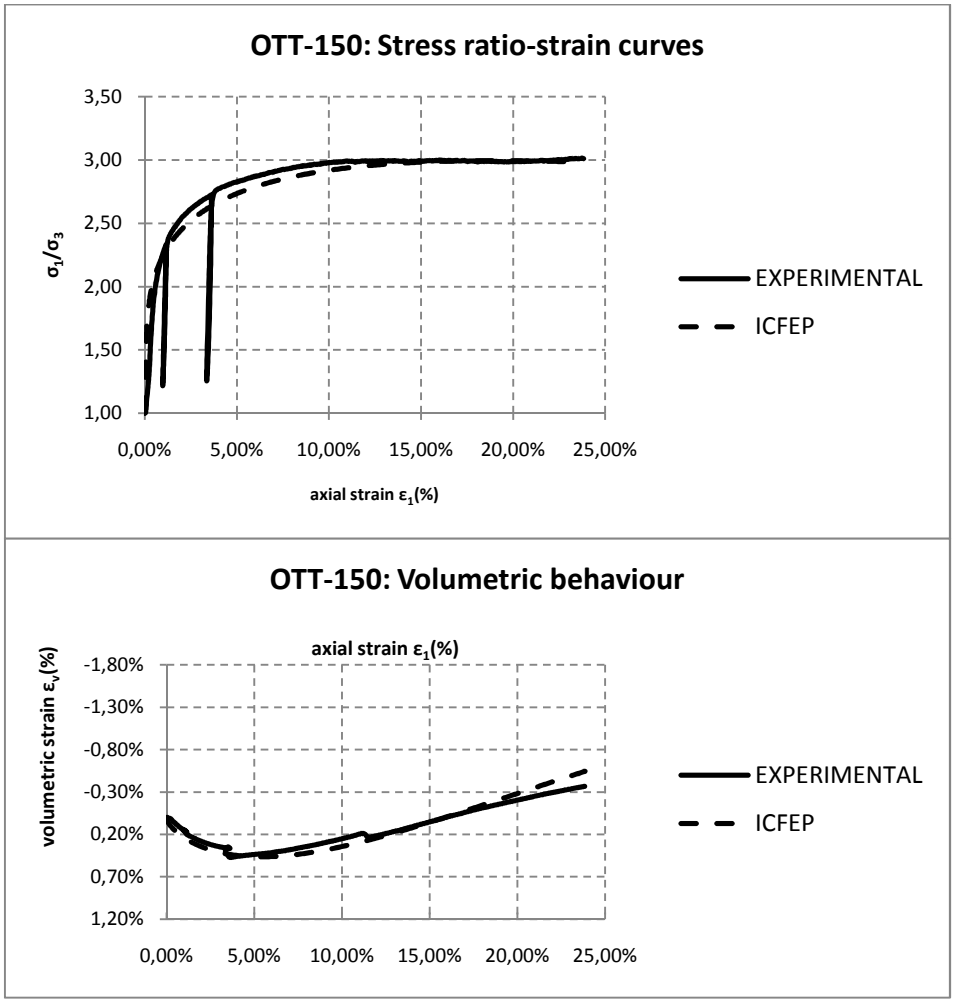

Figure 4.13: *Comparison between predicted behaviour (ICFEP) and the respective experimental results. Stress ratio-strain and volume change behavior for Loose Ottawa Sand: Drained triaxial compression test – confining pressure:* ***150kPa****.*

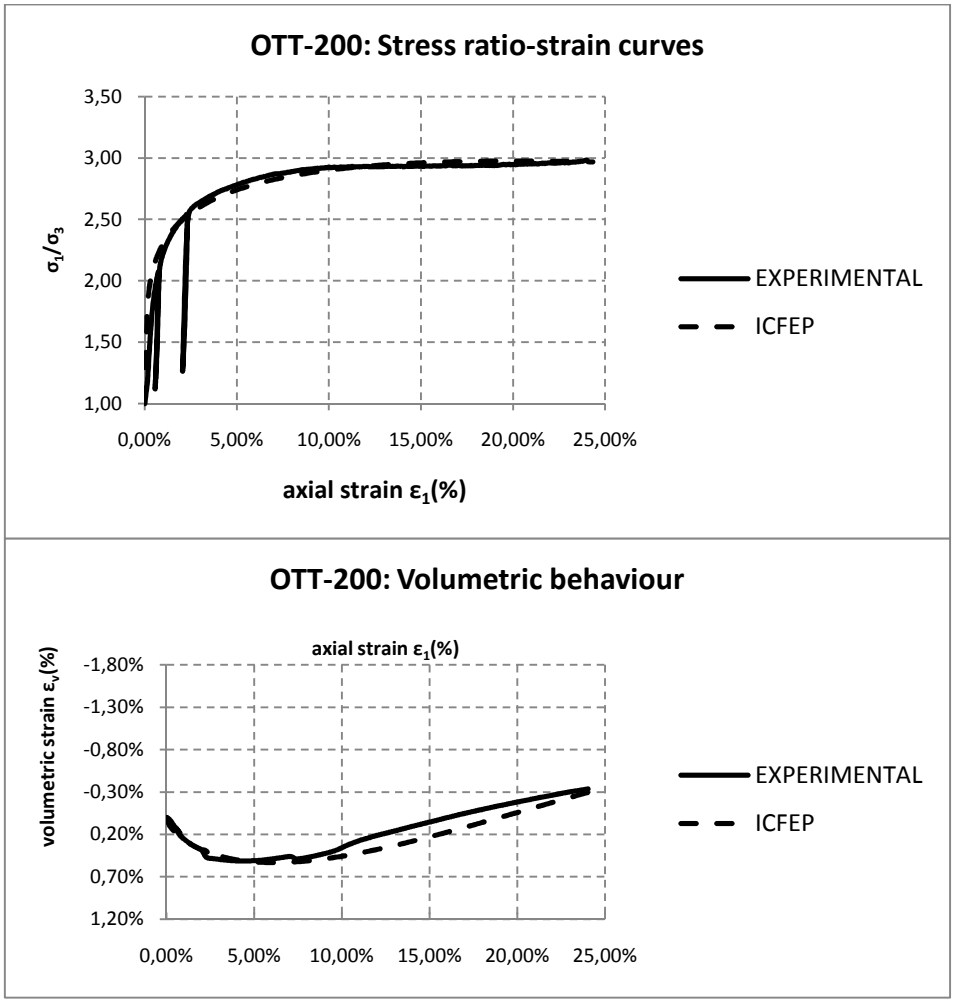

Figure 4.14: *Comparison between predicted behaviour (ICFEP) and the respective experimental results. Stress ratio-strain and volume change behavior for Loose Ottawa Sand: Drained triaxial compression test – confining pressure:* ***200kPa****.*

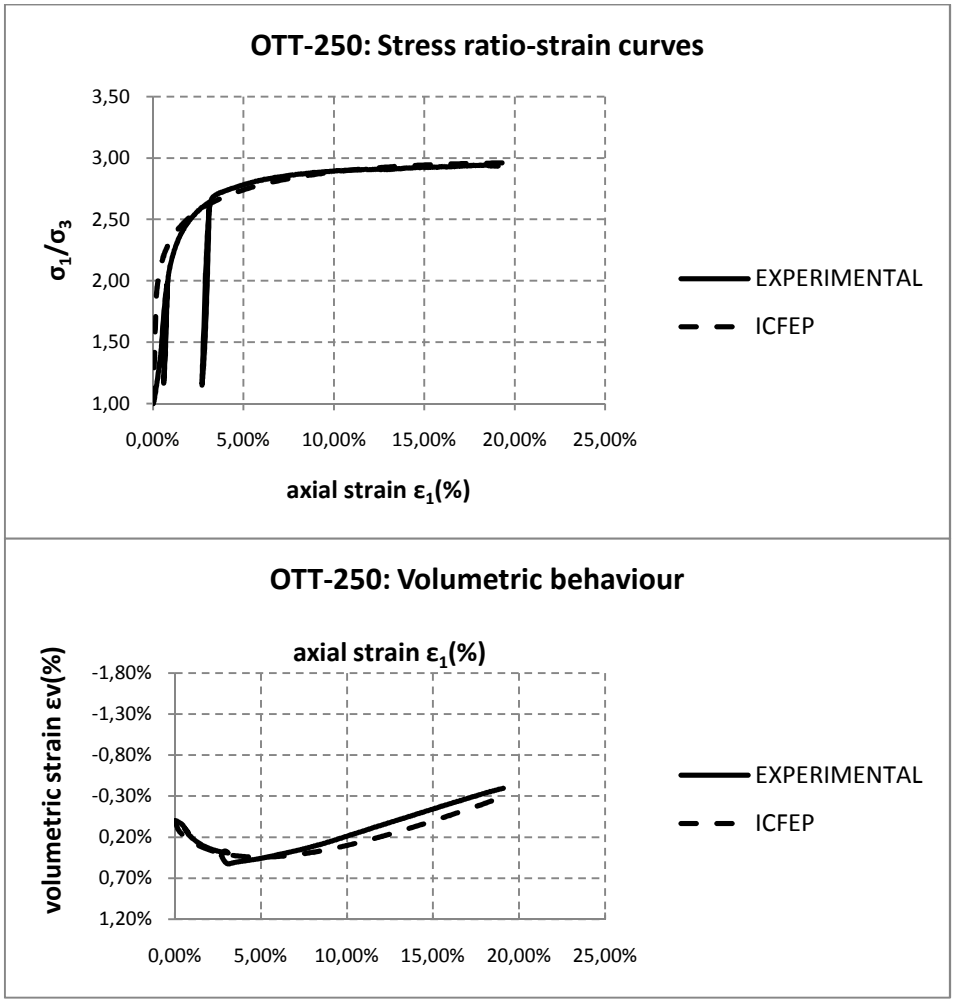

Figure 4.15: *Comparison between predicted behaviour (ICFEP) and the respective experimental results. Stress ratio-strain and volume change behavior for Loose Ottawa Sand: Drained triaxial compression test – confining pressure:* ***250kPa****.*

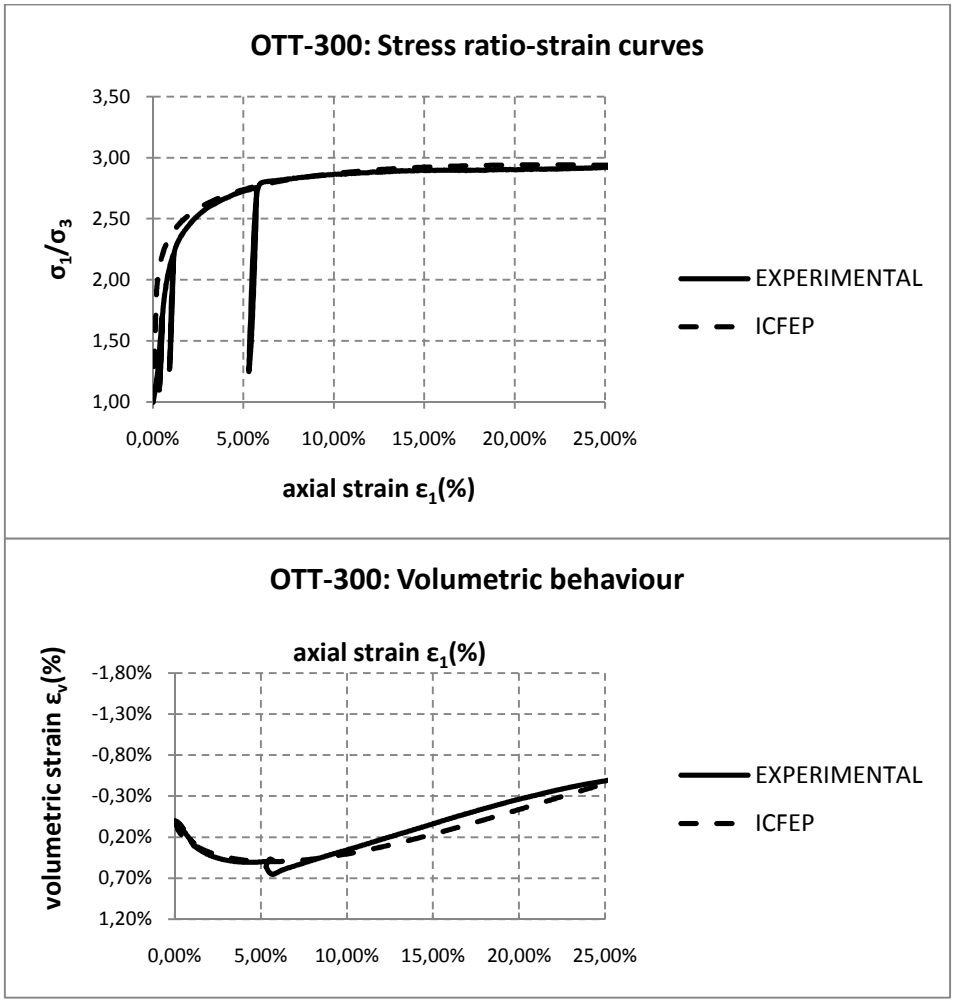

Figure 4.16: *Comparison between predicted behaviour (ICFEP) and the respective experimental results. Stress ratio-strain and volume change behavior for Loose Ottawa Sand: Drained triaxial compression test – confining pressure:* ***300kPa****.*

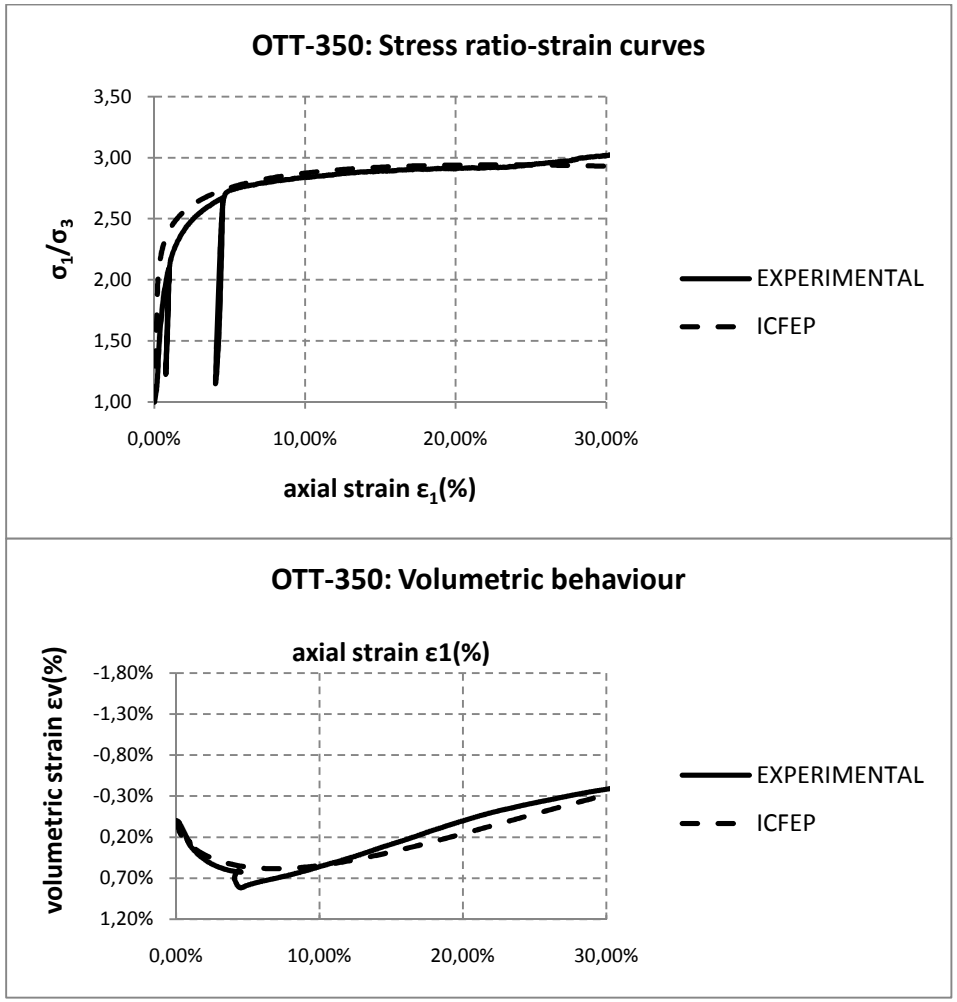

Figure 4.17: *Comparison between predicted behaviour (ICFEP) and the respective experimental results. Stress ratio-strain and volume change behavior for Loose Ottawa Sand: Drained triaxial compression test – confining pressure:* ***350kPa****.*

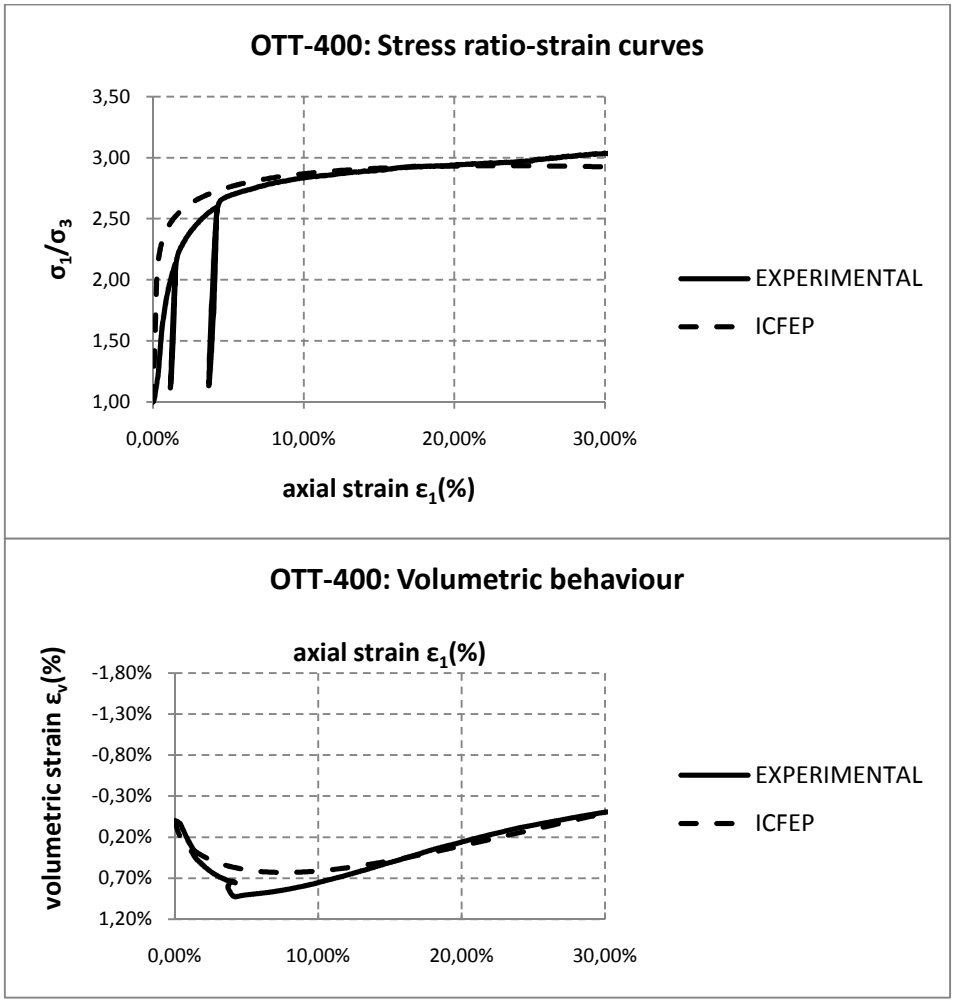

Figure 4.18: *Comparison between predicted behaviour (ICFEP) and the respective experimental results. Stress ratio-strain and volume change behavior for Loose Ottawa Sand: Drained triaxial compression test – confining pressure:* ***400kPa****.*

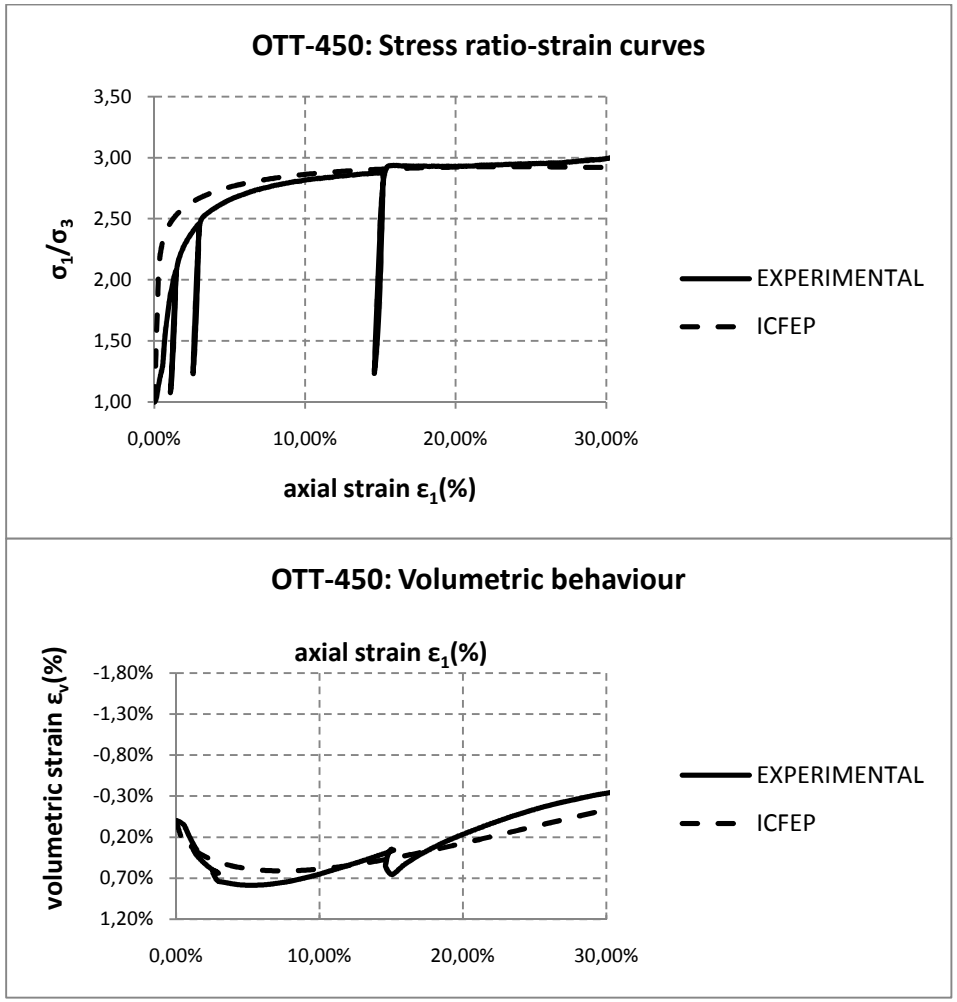

Figure 4.19: *Comparison between predicted behaviour (ICFEP) and the respective experimental results. Stress ratio-strain and volume change behavior for Loose Ottawa Sand: Drained triaxial compression test – confining pressure:* ***450kPa****.*

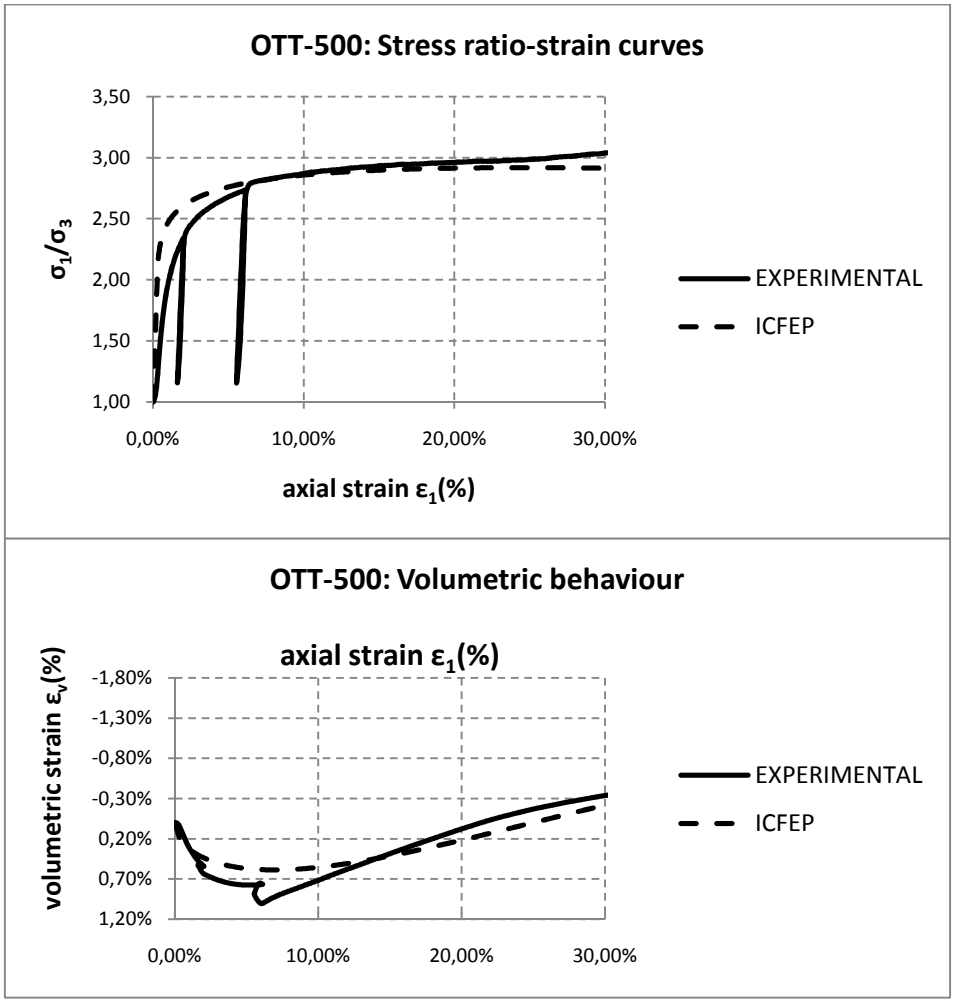

Figure 4.20: *Comparison between predicted behaviour (ICFEP) and the respective experimental results. Stress ratio-strain and volume change behavior for Loose Ottawa Sand: Drained triaxial compression test – confining pressure:* ***500kPa****.*

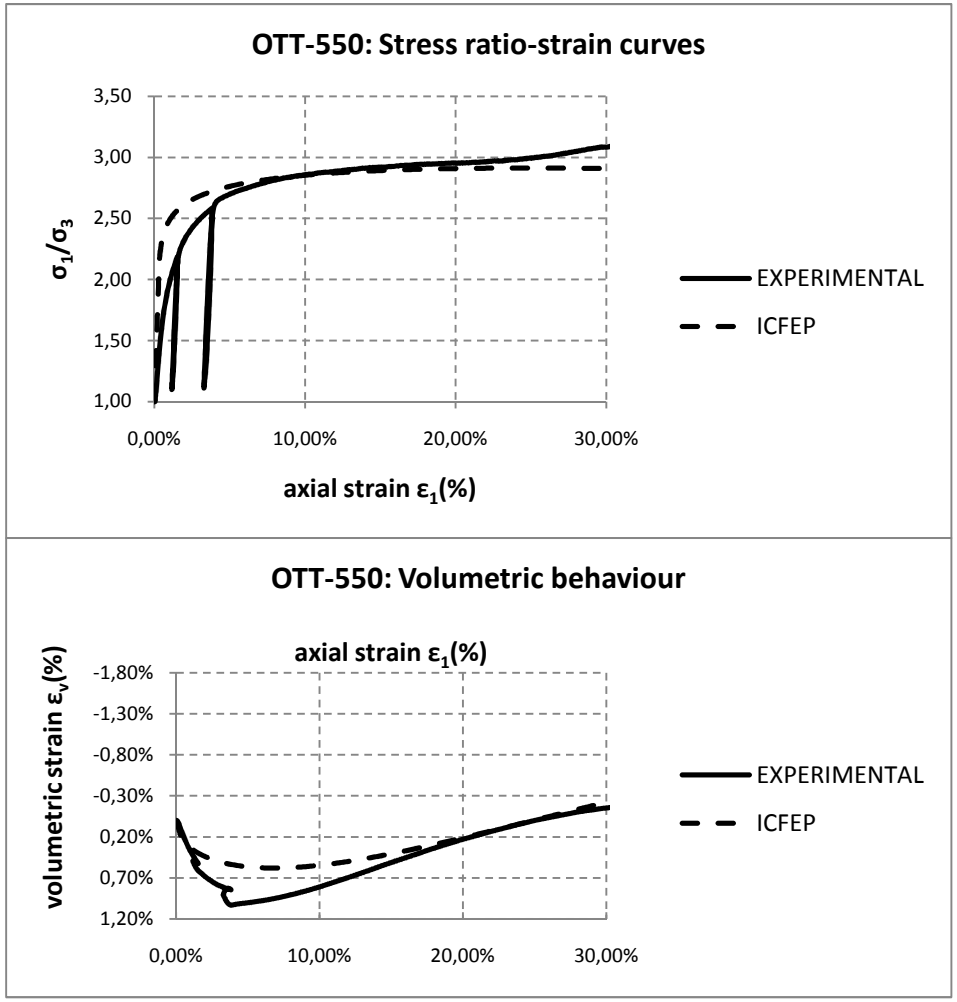

Figure 4.21: *Comparison between predicted behaviour (ICFEP) and the respective experimental results. Stress ratio-strain and volume change behavior for Loose Ottawa Sand: Drained triaxial compression test – confining pressure:* ***550kPa****.*

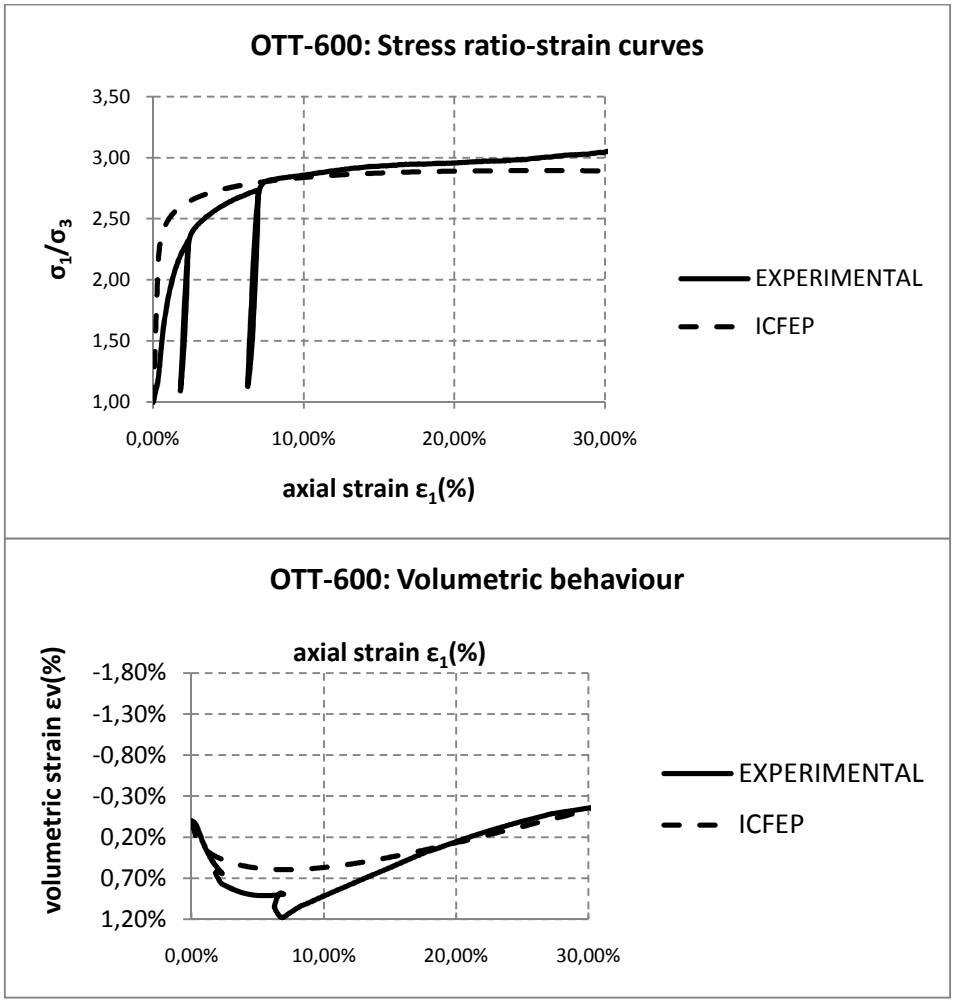

Figure 4.22: *Comparison between predicted behaviour (ICFEP) and the respective experimental results. Stress ratio-strain and volume change behavior for Loose Ottawa Sand: Drained triaxial compression test – confining pressure:* ***600kPa****.*

4.3.2 SIMULATION OF TORSIONAL SHEAR TESTS IN THE HOLLOW CYLINDER APPARATUS

Since Lade's parameters have been satisfyingly verified for the behaviour of loose Ottawa sand for the drained triaxial tests, a similar set of predictions as the ones presented for Sacramento River sand were set up to capture the behaviour of the soil under torsional shear and are presented in this paragraph:

The tests simulated were divided in **two sets,** each one for three different initial mean effective stresses. The first set includes 3 monotonic hollow cylinder torsional shearing tests under **drained** loading conditions, initiated from the mean effective stresses of ***100kPa, 200kPa*** and ***300kPa*** *(Figures 4.23-4.25).* The second set is a similar set under **undrained** loading conditions. Again, 3 tests initiated from 3 different mean effective stresses: ***100kPa, 200kPa*** and ***300kPa*** *(Figures 4.26-4.27).* The results are shown below. The simulation is again presented through a series of diagrams including: effective stress paths (for both drained and undrained tests), stress-strain curves (for both drained and undrained tests) and volumetric strain-shear strain curves for the drained tests.

The simulation of the hollow cylinder test follows the procedure described analytically in *§4.1.2*.

The main purpose was to compare the predictions with experimental results as to effectively evaluate the model's predictive capabilities for the torsional behaviour. Unfortunately, experimental results were not available for torsional shearing tests under **drained** conditions. That would have been of great interest, as it has been shown in the past, for studies conducted on the behaviour of Ham River sand and Fontainebleau sand that the model is in better accordance with experimental results under drained conditions *(Tsomokos, 2005).* However, the results shown can be useful for such a comparison in the future. In the present project, the results for the torsional shearing tests under drained conditions are evaluated based upon the expected behaviour.

On the other hand, experimental results were available for the torsional shearing tests under **undrained** conditions and have been used to make comparisons *(Figures 4.26-4.27).*

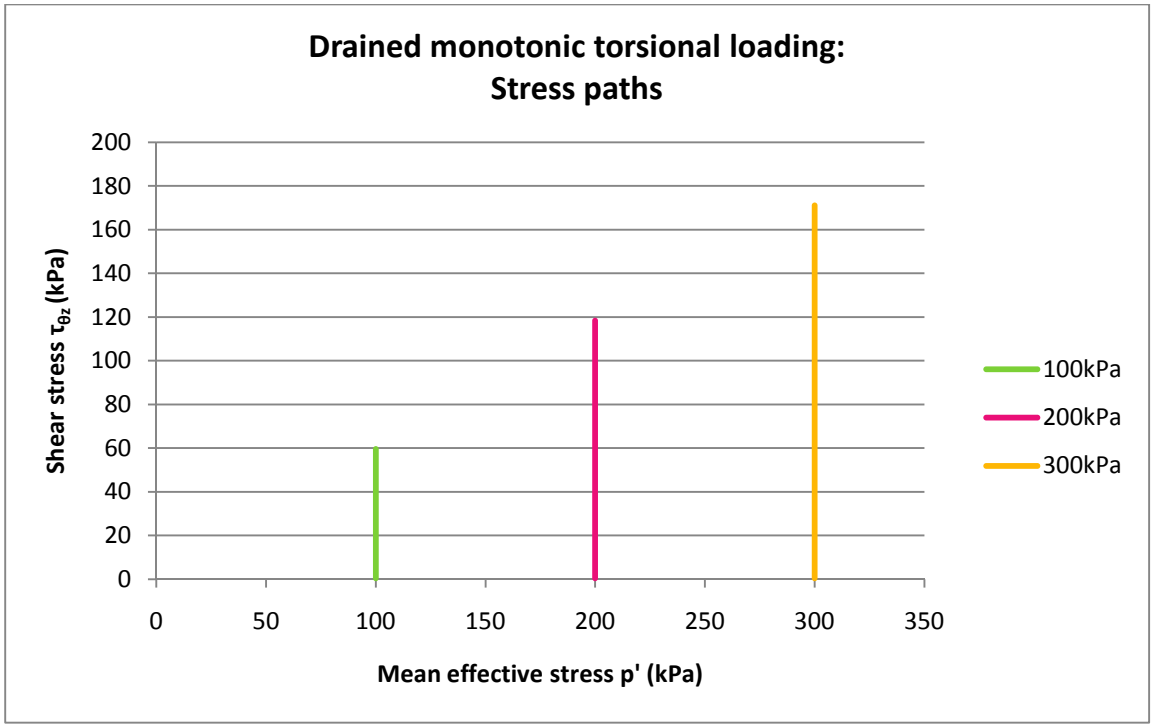

Figure 4.23: *Predicted effective stress paths (ICFEP) for loose Ottawa sand, based on the parameters derived from drained triaxial tests (Table 2.9).* ***Drained*** *torsional shear tests.*

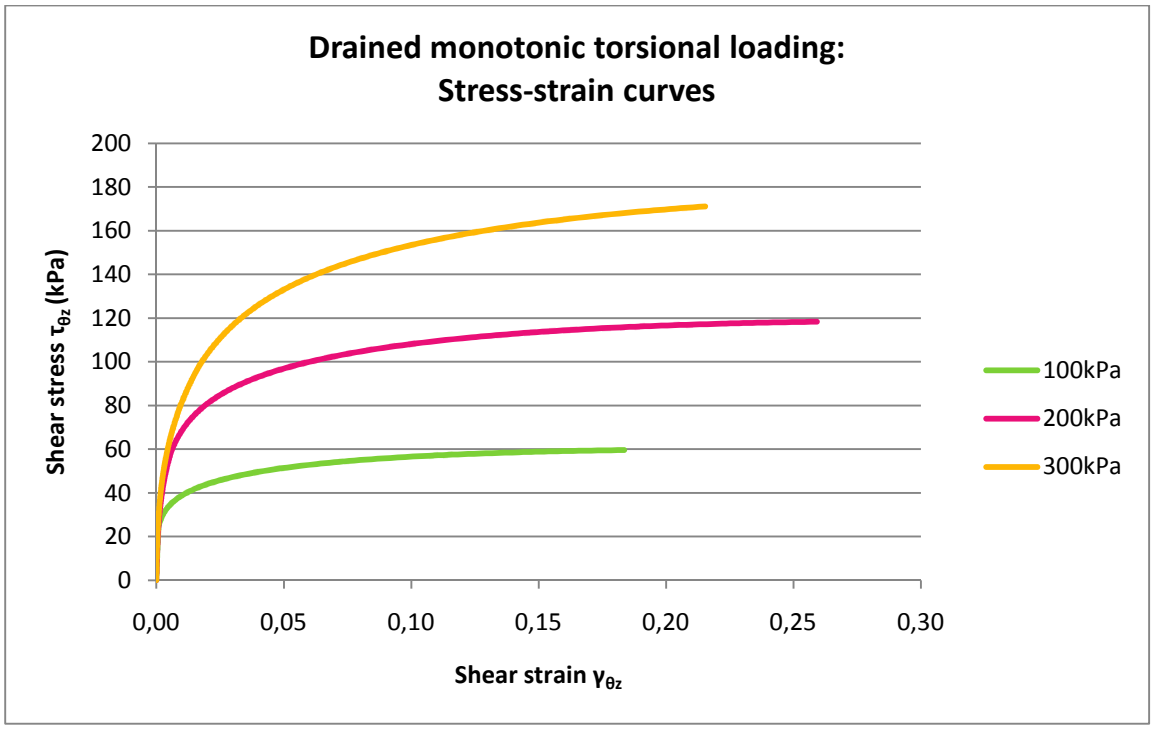

Figure 4.24: *Predicted shear stress – shear strain curves (ICFEP) for loose Ottawa sand based on the parameters derived from drained triaxial tests (Table 2.9).* ***Drained*** *torsional shear tests.*

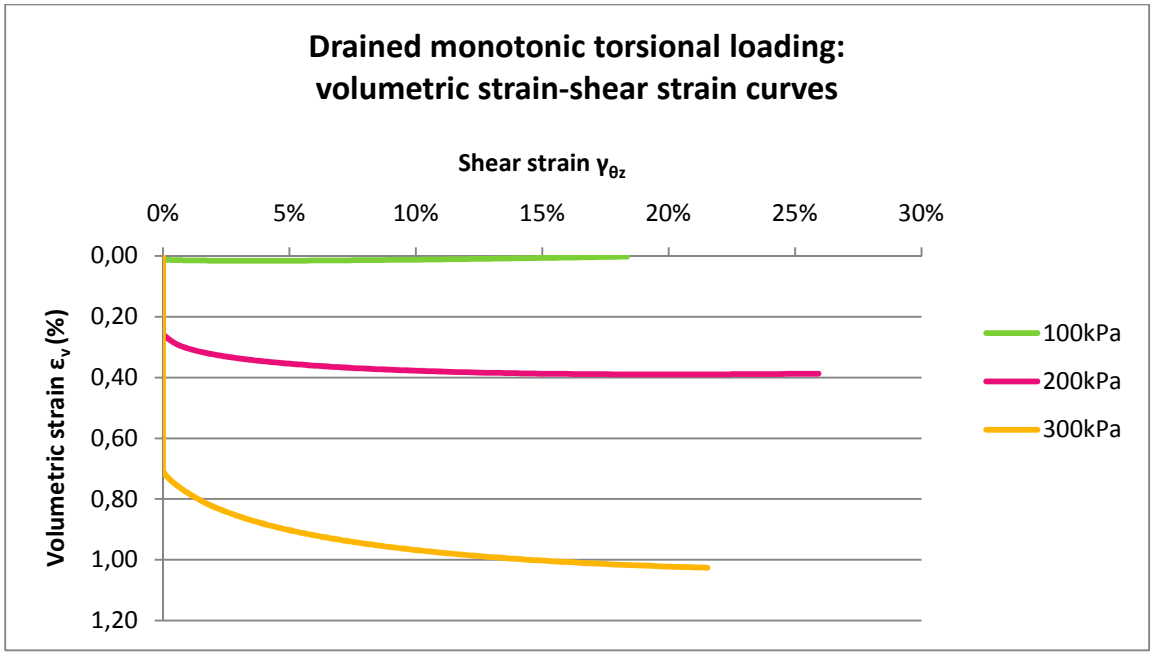

Figure 4.25: *Predicted volumetric strains – shear strain curves (ICFEP) for loose Ottawa sand based on the parameters derived from drained triaxial tests (Table 2.9).* ***Drained*** *torsional shear tests.*

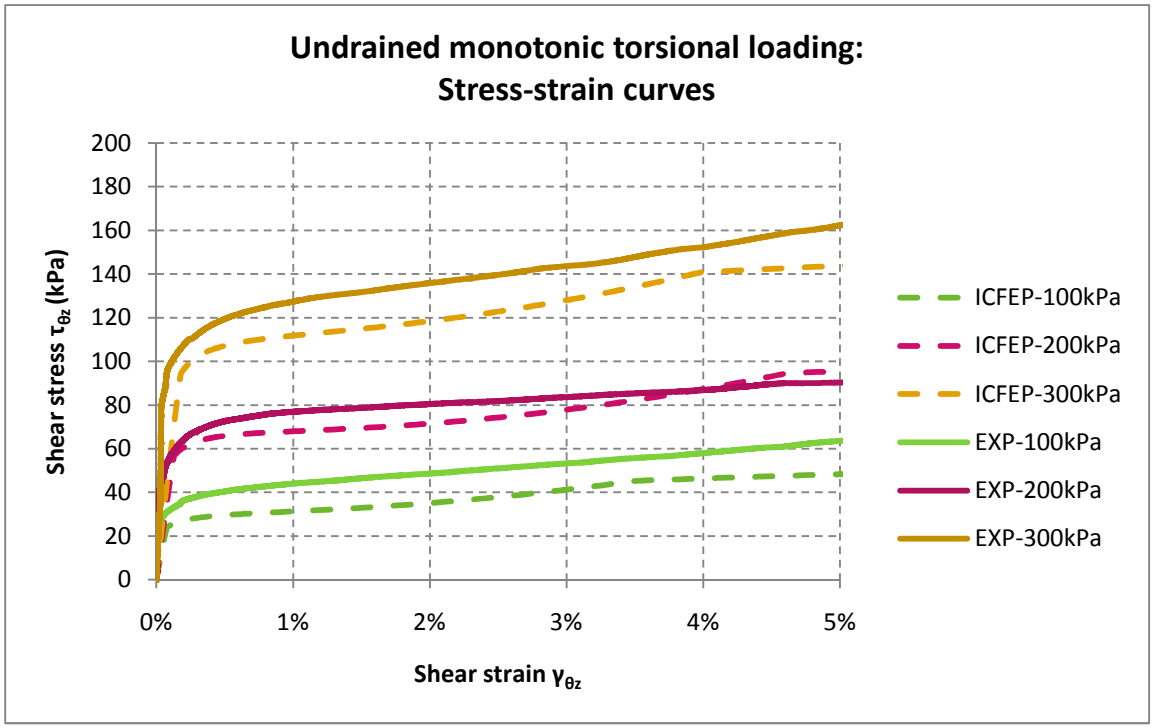

Figure 4.26: *Predicted shear stress – shear strain curves (ICFEP) for loose Ottawa sand based on the parameters derived from drained triaxial tests (Table 2.9).* ***Drained*** *torsional shear tests. Comparison with respective experimental results.*

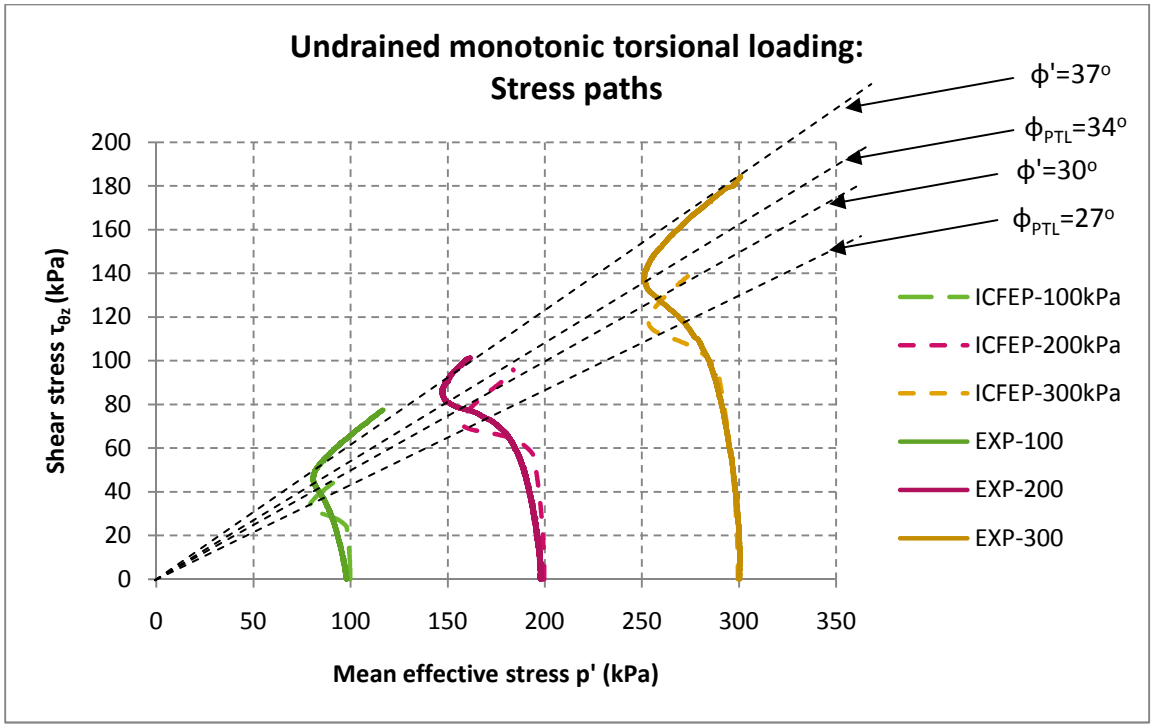

Figure 4.27: *Predicted stress paths (ICFEP) for loose Ottawa sand based on the parameters derived from drained triaxial tests (Table 2.9).* ***Drained*** *torsional shear tests. Comparison with respective experimental results.*

From the above presented diagrams the following observations are derived:

- In *Figure 4.23,* the effective stress paths are illustrated for loose specimens. As expected, the mean effective stress *p'* remains constant during the drained torsional loading of isotropically consolidated specimens.
- Inspection of *Figure 4.24* shows behaviour in accordance with what is expected: In this shear stress – shear strain diagram, the shear stresses are ascending at a gradually decreasing rate for all initial mean effective stresses. The ascending rate decreases at smaller strains (earlier), as lower the initial mean effective stress. All shear stresses seem to become stable under further subsequent loading. Moreover, the higher the initial effective stress, the higher the shear stress reached. All curves are approximately parallel, showing a uniform behaviour for the material at all initial mean effective stresses.
- With respect to the volumetric behaviour illustrated in *Figure 4.25* on a volumetric strain – shear stress diagram, it is evident that the specimens initiated at *200kPa* and *300kPa* show a continuous contractive behaviour. On the other hand, the specimen initiated at the mean effective stress of 100kPa

shows an initial contractive phase which very smoothly turns into a slight dilation, creating a vague transformation point. This dominant contractive behaviour is rational as the specimens simulated are very loose. As the slopes of the volumetric curves illustrate the rate of the excess pore pressure decrease, it can be seen that this rate is higher the higher the initial mean effective stress.

With respect to the comparison with the experimental results shown in *Figures 4.26-4.27,* it should be clarified, at this point, that although the relative density of all *3* simulated specimens corresponds to the average relative density of the 12 specimens used for the calibration of the model (*Dr=14.60%)*, the relative densities of the available experimental results are slightly different, that being: for the specimen initiated at *100kPa*, *Dr=25.54%,* for the one initiated at *200kPa, Dr=15.84%* and, finally for the one initiated at *300kPa*, *Dr=27.08%.* That explains, as it will be shown, the fact that the accordance of the specimen of the *200kPa* is generally, better that the other two, as its relative density is closer to the one simulated. All specimens were isotropically consolidated to the respective initiative mean effective stress.

- *Figure 4.26* shows the stress-strain curves for the undrained simulations for the same loose specimens and it is compared to the respective experimental results. Predictions are marked with broken lines and experimental with solid lines. The accordance is overall satisfying, as the model seems to capture the stress-strain behaviour quite well. For the specimen initiated at *200kPa*, the curves nearly coincide, which is expected, as the relative densities of the real specimen and the simulated one are practically the same. For the other two specimens, the general behaviour is successfully captured, with the real specimens showing slightly higher shear stresses, which is also expected, as their relative densities are slightly higher than the ones simulated. The shear stress seems to increase rapidly in the range of the small strains, reaches a smooth transient peak value and then increases at a very low rate.
- *Figure 4.27* shows the effective stress paths for the undrained simulations and the respective experimental results. Predictions are marked with broken lines and experimental with solid lines. It seems that the predictions show the same

contraction tendency with the real specimens with no indication of brittleness. However, this tendency is expressed at lower shear stress levels for all specimens. This results in lower values of the slopes of the respective phase transformation line (PTL) and the failure envelope. The initial slope of the stress path is relatively better in agreement with the real behaviour the higher the initial mean effective stress.

At this point and due to the above mentioned differences as far as the relative densities are concerned, it was considered purposeful to normalize the above results with respect to the relative densities. To achieve this, the shear stresses appearing in *figures 4.26-4.27* are divided by the factor ***f(e)***, defined by the following expression:

$$f(e) = \frac{(2.17 - e)^2}{1 + e} \tag{4.2}$$

where

e is the porosity index of the respective specimen. The following *Table 4.4* shows the values of *e* for each one of the specimens as well as the modeled specimen and the respective values of *f(e)* calculated according to the above equation.

Specimen	e	f(e)
model	0,707	1,253877563
100kPa	0,680714	1,319661043
200kPa	0,70398	1,261291001
300kPa	0,677002	1,329183285

Table 4.4 *Porosity indexes and respective values of f(e) factor calculated for the normalization of the results with respect to relative densities.*

In *Figures 4.28* and *4.29* the normalized results are shown. As expected, the regularization amplifies the issues caused due to the difference in relative densities and the good accordance of the results is better shown, especially as far as the stress-strain diagram is concerned. As for the stress path diagram, it can be seen that the difference between the angles of the normalized Phase Transformation Lines between the experimental and the predicted curves is smaller ($25^o/21^o$ versus $34^o/27^o$), as it also is for the failure lines ($28^o/24^o$ versus $37^o/30^o$).

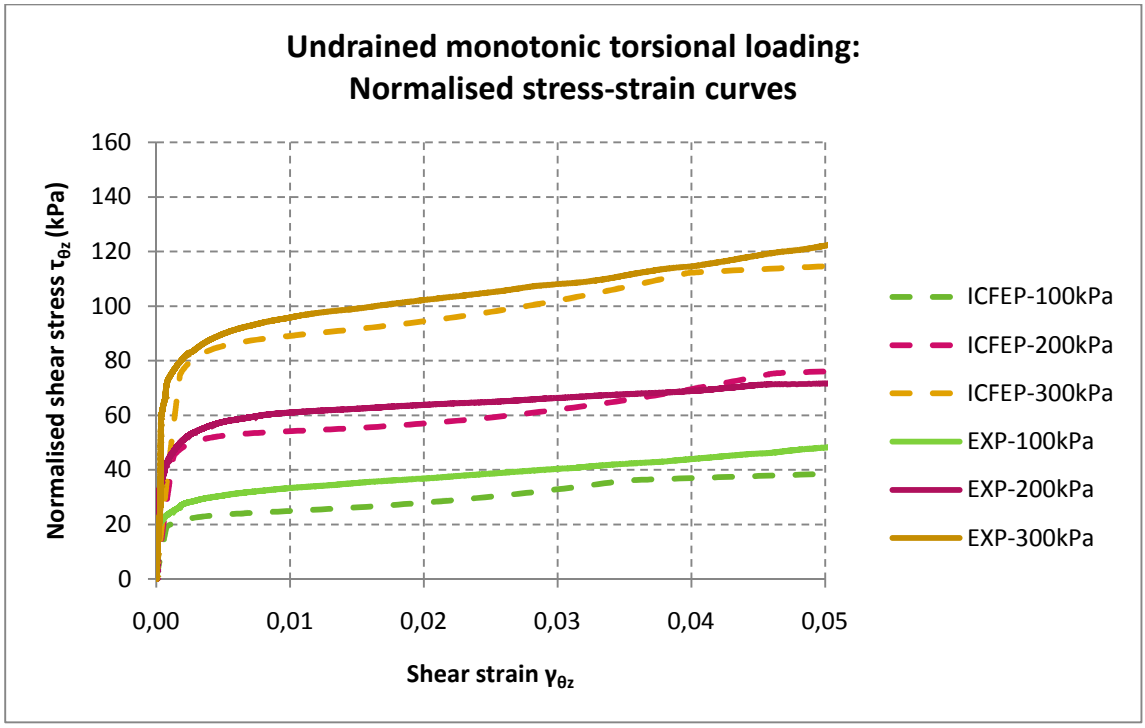

Figure 4.28: *Predicted shear stress – shear strain curves (ICFEP) for loose Ottawa sand based on the parameters derived from drained triaxial tests (Table 2.9).* ***Drained*** *torsional shear tests. Comparison with respective experimental results. All results normalized with respect to relative densities.*

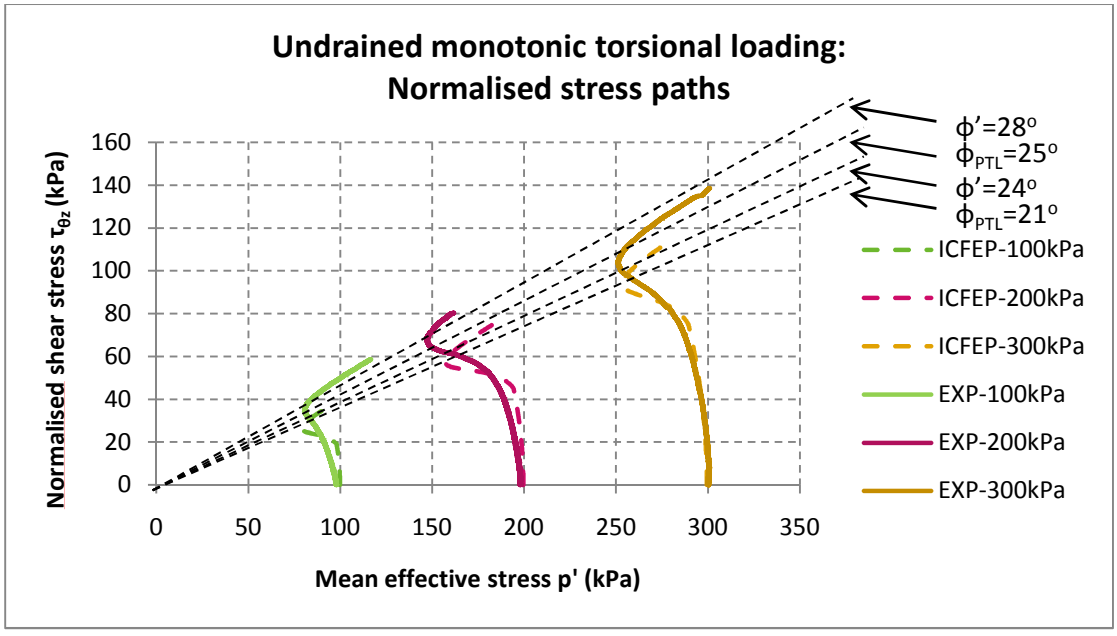

Figure 4.29: *Predicted stress paths (ICFEP) for loose Ottawa sand based on the parameters derived from drained triaxial tests (Table 2.9).* ***Drained*** *torsional shear tests. Comparison with respective experimental results. All results normalized with respect to relative densities.*

Overall, the behaviour of loose Ottawa sand is reasonably predicted with regards to the drained behaviour. It is vital though, for comparisons with experimental results to take place and evaluate the behaviour better.

With respect to the undrained behaviour, Lade's model gives satisfying predictions regarding the shear stress-shear strain behaviour, although it doesn't work as well predicting the stress paths. The general weakness to predict the undrained behaviour may be related to the fact that the model was initially implemented (and therefore calibrated) basing on data regarding drained behaviour.

CHAPTER 5

CONCLUSIONS

SUMMARY – SUGGESTIONS FOR FURTHER RESEARCH

Lade's double hardening model has been presented, along with the model's implementation to the Imperial College Finite Element Programme (ICFEP). The model has been calibrated in order to determine the 14 parameters required for Ottawa sand, based upon a set of 12 drained triaxial tests performed in the National Technical University of Athens (NTUA). The calibration process has been thoroughly presented and can be useful for simulating other granular materials as well as different relative densities of the same material in the future.

The software and the simulation methods used have been verified with respect to their ability to accurately predict the behaviour of loose and dense Sacramento River sand in drained triaxial tests the results of which were found in the literature and have been successfully reproduced. The sand's behaviour under torsional shear loading has been predicted and commented upon, based on the expected behaviour. The predictions were characterized as reasonable, although comparison with actual experimental data is recommended to verify these observations.

The model has also been evaluated as to its ability to predict the drained behaviour of loose Ottawa sand with respect to the experiments used for its calibration and based on the parameters derived from it. The accordance has been satisfactory for all

practical purposes, although certain weaknesses concerning the experimental program have been identified and lead to the suggestion of a more sophisticated one in the future.

Having taken these weaknesses into account, the prediction of behaviour of the loose Ottawa sand under torsional loading has also been evaluated. The lack of experimental results under drained conditions left the evaluation restricted to an evaluation based upon the expected behaviour – that being satisfying.

Finally, the predicted torsional behaviour of loose Ottawa sand under undrained conditions is compared with respective experimental results. The model seems to capture the shear stress – shear strain behaviour in a good way, although shows weaknesses when it comes to the stress paths. That is partially explained by the fact that the model is originally calibrated based on results concerning drained behaviour.

Overall, Lade's double Hardening model shows a lot of potential as to its effectiveness in capturing the behaviour of granular materials under generalized monotonic loading. This is verified by several examples from the literature. It does require though, a well planned, sophisticated experimental programme upon which the calibrations are based, and the final results compared with.

REFERENCES

1. AL-TABBAA A. (1987), “Permeability and stress-strain response of speswhite kaolin”, *PhD thesis, Cambridge University*
2. AL-TABBAA, A.; WOOD, D.M. (1989), “An experimentally based 'bubble' model for clay”. *Numerical models in geomechanics NUMOG III (eds. S. Pietruszczak and G.N. Pande) Elsevier Applied Science, pp.* 91-99
3. BALADI, G.Y.; ROHANI, B. (1979), "Elastic-plastic model for saturated sand," *ASCE, Journal of the Geotechnical Engineering Division* 105(4), 465-480
4. BISHOP, A.W.; HENKEL, D.J., (1962), “The Measurement of Soil Properties in the Triaxial Test”, *2nd Edition, Edward Arnold (Publishers) LTD., London*
5. CALLADINE C.R. (1973), “Overconsolidated clay: A microstructural view”. *Proc. Symp. Role of Plasticity in Soil Mechanics (Edited by A.C. Palmer). p. 144. Cambridge University*
6. CALLISTO, M.; FERREIRA, W.; MORENO, P.; GOULART, MDC; PETRUCIO, M. (2002), “Aplicação de um protocolo de avaliação rápida da diversidade de hábitats em atividades de ensino e pesquisa” (MG-RJ). *Acta Limnologica Brasiliensia, vol.* 14, *no.* 1, *p.* 91-98
7. DAKOULAS, P.; YUANHUI, S. (1992), “Fine Ottawa Sand: Experimental Behavior and Theoretical Predictions”, *Journal of Geotechnical Engineering, Vol. 118, No. 12*
8. DAFALIAS, Y. F.; POPOV, E. P. (1976), ‘‘Plastic internal variables formalism of cyclic plasticity.’’ *J. Appl. Mech.,* 43, 645–651
9. DIMAGGIO, F. L.; SANDLER, I. S. (1971), ‘‘Material model for granular soils.’’ *J. Eng. Mech. Div.,* 97(3), 935–950
10. DRUCKER, D. C.; GIBSON, R. E.; HENKEL, D. J. (1957), ‘‘Soil mechanics and work-hardening theories of plasticity.’’ *Trans. Am. Soc. Civ. Eng.,*122, 338–346
11. DRUCKER, D. C.; PRAGER, W. (1952), “Soil mechanics and plastic analysis for limit design”. *Quarterly of Applied Mathematics, vol.* 10*, no.* 2*, pp.* 157–165
12. DUNCAN J. M.; CHANG C.-Y. (1970) “Non linear analysis of stress and strain in soils”. *ASCE: J. Soil Mech. Found. Div.* 96, 1629

13. GENS, A.; POTTS, D. M. (1988), “Critical state models in computational geomechanics”. *Eng. Comput.,* 5, 178–197
14. GEORGIANNOU, V.N.; (2010), “Behavioural Patterns of Fine Sands”, *Geotechnical Engineering Journal of the SEAGS & AGSSEA* Vol. 41 No.3 September 2010 ISSN 0046-5828
15. GEORGIANNOU, V.N.; TSOMOKOS, A.; STAVROU, K. (2008), “Monotonic and cyclic behaviour of sand under torsional loading”, *Géotechnique* 58, *No*. 2, 113-124
16. GRAMMATIKOPOULOU, A. (2004), "Development, implementation and application of kinematic hardening models for overconsolidated clays". *University of London*
17. HASHIGUCHI, K. (1980), ‘‘Constitutive equations of elastoplastic materials with elastic-plastic translation.’’ *J. Appl. Mech., 47,* 266–272
18. HASHIGUCHI, K.; UENO, M. (1977), “Elastoplastic constitutive laws of granular materials, Constitutive Equations of Soils” *Proc. 9th Int. conf. Soil Mech Found. Eng., Spec. Session 9, Tokyo, JSSMFE,* 73-82
19. HOBULEC I. (1968), “Elastic behaviour of cohesionless soil”. *ASCE: J. Soil Mech. Found Div.* 94, 1215
20. INEL, S.; LADE, P.V. (1997), “Rotational Kinematic Hardening Model for Sand, Part II. Characteristic Work Hardening Law and Predictions,” *Computers and Geotechnics*, *Elsevier, Vol* 21, *No.* 3, *pp.* 217-234
21. JANBU, N., (1963), “Soil compressibility as determined by oedometer and triaxial tests”. *European Conference on Soil Mechanics and Foundations Engineering, Wiesbaden, Germany, Vol.* 1
22. KAVVADAS, M.; AMOROSI, A. (2000), ‘‘A constitutive model for structured soils.’’ *Geotechnique, 50(3),* 263–273
23. KIM, ,M. K.; LADE, P. V. (1988), “Single hardening constitutive model for frictional materials - I. Plastic Potential Function”, *Computers and Geotechnics, vol.* 5
24. KOVACEVIC, N. (1994). “Numerical analysis of rockfill dams, cut sloped and road embankments”. *PhD Thesis, Imperial College, University of London.*
25. KRIEG, R. D. (1975), ‘‘A practical two surface plasticity theory.’’ *J. Appl.Mech.*, 47, 641–646

26. LADE, P.V. (1977), “Elasto-plastic stress-strain theory for cohesionless soil with curved yield surfaces”, *Ind. J. Solids Structures*, *Vol.* 13*, pp.* 1019-1035
27. LADE, P.V. (1981), "Elasto-plastic stress-strain model for sand", *Limit equilibrium, plasticity and generalized stress-strain analysis in geotechnical engineering, ASCE, (eds. Yong and Ko), pp.*628-648
28. LADE, P.V. (1988a), "Double hardening constitutive model for soils, parameter determination and predictions for two sands", *Constitutive Equations for Granular Non-cohesive Soils, (eds. Saada and Bianchini), Balkema, pp.*367-382
29. LADE, P.V. (1990), “Single Hardening Model with Application to NC Clay”. *J. Geotech. Engrg., ASCE,* 116 (3): 394-414
30. LADE, P. V.; DUNCAN, J. M. (1975), “Elasto-plastic stress-strain theory for cohesionless soil”, *J. Geotech. Eng. Div., ASCE*
31. LADE, P. V.; KIM, M. K. (1988a), “Single hardening constitutive model for frictional materials - II. Yield criterion and plastic work contour”, *Computers and Geotechnics, vol.* 6
32. LADE, P. V.; KIM, M. K. (1988b), “Single hardening constitutive model for frictional materials - III. Comparisons with experimental data”, *Computers and Geotechnics, vol.* 6
33. LADE, P.V.; NELSON, R.B. (1984), "Incrementalization Procedure for Elasto-Plastic Constitutive Law with Multiple, Intersecting Yield Surfaces," *International Journal for Numerical and Analytical Methods in Geomechanics*, *Wiley, Vol.* 8, *No.* 4, *July-August* 1984, *pp.* 311-323
34. LADE, P.V.; NELSON, R.B. (1987), “Modelling the elastic behaviour of granular materials” *Int. J. Numer. Anal. Methods Geomech.,* 11, 521-542
35. LEE, K.L.; SEED, H.B. (1967), "Drained Strength Characteristics of Sands," *Journal of the Soil Mechanics and Foundations Division* 93(SM6)
36. McCARRON, W. O.; CHEN, W. F. (1987), ‘‘A capped plasticity model applied to Boston blue clay.’’ *Can. Geotech. J.,* 24(4), 630–644
37. McCARRON W.; CHEN W. (1987). “Application of a bounding surface model to Boston blue clay”. *Comput. Struct.,* 26(6): 887-897
38. MRÓZ, Z.; NORRIS, V. (1982), “Elastoplastic and viscoplastic constitutive models for soil with application to cyclic loading”. *Soil mechanics-transient*

and cyclic loads. In G. Pande and O. Zienkiewicz (Eds.), Soil Mechanics - Transient and Cyclic Loads. Constitutive Relations and Numerical Treatment., pp. 173. 218. *John Wiley and Sons*

39. MRÓZ, Z.; NORRIS, S.; ZIENKIEWICS, O. C. (1978), ‘‘An anisotropic critical state model for soils and its application to cyclic loading.’’ *Int. J. Numer. Analyt. Meth. Geomech.,* 2, 203–221
40. PASTOR, M.; ZIENKIEWICZ, O.C.; AND LEUNG; K.H. (1985), “Simple model for transient soil loading in earthquake analysis. II Non-associative models for sands”, *International Journal forNumerical and Analytical Methods in Geomechanics*, 9(5), 477-498
41. PENDER, M. J. (1978), “A Unified Model for Soil Stress-Strain Behaviours”. *Proc. 10th ICSMFE :* 213-222
42. PERIC, D.; AYARI, M.A. (2002), “On the analytical solutions for the three-invariant Cam clay model”. *International Journal of Plasticity*, 18:8:1061-1082
43. POTTS, D. M.; ZDRAVKOVIC, L. (1999), “Finite element analysis in geotechnical engineering”, *Thomas Telford, London.*
44. PREVOST, J. H. (1978), ‘‘Plasticity theory for soils stress-strain behavior,’’ *J. Eng. Mech. Div.,* 104(5), 1177–1194
45. REGIER, K. (1997), “The stress-Dilatancy of Sands: Pressure and Density Dependencies in both Monotonic and Cyclic Loading Regimes”, *MSc Thesis, University of Calgary, Alberta*
46. ROSCOE, K.H.; BURLAND, J.B. (1968), “On the generalised stress-strain behaviour of 'wet' clay, in Engineering plasticity” *eds. J. Heyman and F.A. Leckie Cambridge University Press, pp.* 535-609
47. ROSCOE, K.H.; SCHOFIELD, A. N. (1963), “Mechanical behaviour of an idealised 'wet' clay”. *Proc. 2nd Eur. Conf. SMFE, Wiesbaden 1, pp.*47-54
48. ROUAINIA, M.; MUIR-WOOD, D. (2000), ‘‘A kinematic hardening model for natural clays with loss of structure.’’ *Geotechnique,* 50(2), 153–164
49. SAADA, A.S. (1988), “State of the art: Hollow cylinder torsional devices: their advantages and limitations. Advance triaxial testing of soil and rock”. *ASTM STP 977, R.T. Donaghe , R.c. Chaney, and M.L. Silver, eds., American Society for Testing and Materials, Philadelphia, pa., pp.*766-795

50. SAADA, A.S.; TOWNSEND, F.C. (1980), "State of the art: Laboratory strength testing of soils, Laboratory Shear Strength of Soil". *ASTM STP* 740, *R.N.Yong and F.C. Townsend, eds., American Society for Testing and Materials, Philadelphia, pa., pp.*7-77
51. SCHOFIELD, A. N.; WROTH, C. P. (1968), "Critical State Soil Mechanics", *McGraw-Hill, pp.* 310
52. SCHWER, L.E.; MURRAY, Y.D. (1994), "A three-invariant Smooth Cap Model with mixed Hardening", *International Journal for numerical and Analytical Methods in Geomechanics, Volume* 18, *pp.* 657-688
53. SKEMPTON, A. W. (1954), "The pore-pressure coefficients *A* and B". *Giotechnique* 4, *No.* 4, 143-147
54. STALLEBRASS, S. E.; TAYLOR, R. N. (1997), "Prediction of ground movements in overconsolidated clay". *Géotechnique* 47, *No.* 2, 235–253
55. STALLEBRASS, S. E. (1990), "Modelling the efects of recent stress history on the behaviour of overconsolidated soils". *Ph.D. thesis, City University, London*
56. TADESSE, S. (2000), "Behaviour of saturated sand under different triaxial loading and liquefaction", *PhD Thesis, Norwegian University of Science and Technology*
57. TATSUOKA,F. (1988), "Some recent developments in triaxial testing system for cohesionless soils", SOA report, ASTM STP No.977, pp.7-67
58. TRESCA, H. (1864), "Mémoire sur l'écoulement des corps solides soumis à de fortes pressions". *C.R. Acad. Sci. Paris, vol.* 59*, p.* 754
59. TSOMOKOS, A. (2005), "Experimental study of the behaviour of a soil element under monotonic and cyclic torsional shear". *PhD Thesis, Geotechnical Division N.T.U.A.*
60. VON MISES, R. (1913), "Mechanik der festen Körper im plastisch deformablen Zustand". *Göttin. Nachr. Math. Phys., vol. 1, pp.* 582–592
61. WHITTLE, A. J. (1993), ''Evaluation of a constitutive model for overconsolidated clays.'' *Geotechnique, 43(2),* 289–314
62. WHITTLE, A. J.; KAVVADAS, M. J. (1994), ''Formulation of MIT-E3 constitutive model for overconsolidated clays.'' *J. Geotech. Eng.,*120(1), 173–198

APPENDIX I

ICFEP MANUAL – LADE'S DOUBLE HARDENING MODEL

MODEL 14: Lade's Double Yield Surface Model

PARAMETERS

	P1	=	14.0	Model number	
	P2	=	p_a	Atmospheric pressure	(>0)
Elastic parameters	P3	=	YSW	Young's modulus switch (see Note 6)	(0≤ ≤2)
	P4	=	M	Young's modulus coefficient	(>0)
	P5	=	λ	Young's modulus exponent	(≥0)
	P6	=	μ	Poisson's ratio	(0≤ ≤1/2)
Deviatoric yield surface	P7	=	η_1	Yield constant	(>0)
	P8	=	m	Yield exponent	(≥0)
	P9	=	R	Plastic potential constant	(0≤)
	P10	=	S	Plastic potential constant	(>0)
	P11	=	t	Plastic potential constant	
	P12	=	α	Work hardening parameter	(>0)
	P13	=	β	Work hardening parameter	
	P14	=	P	Work hardening parameter	(>0)
	P15	=	l	Work hardening parameter	(>0)
Spherical yield surface	P16	=	C	Work hardening parameter	(>0)
	P17	=	p	Work hardening exponent	(>0)
	P18	=	a_{in}	Parameter controlling cohesion and tension	(≥0)
	P19	=	OCRS	OCR switch (see Note 3)	(0≤ ≤3)
	P20	=	OCR	OCR value (see Note 3)	(≥0)
Optional	P21	=	E_{min}	Minimum value of Young's modulus	(≥0)
	P22	=	q_{min}	Minimum value of q (default = 0)	(≥0)
	P23	=	H_{1min}	Minimum value of deviatoric hardening parameter (see Note 7), default = 0.001	(<1)
	P24	=	η_{cs}	Critical state parameter (see Notes)	(≥0, <η_1)
	P25	=	TIPTOL	Apex tolerance (see Notes)	
	P26	=	AXVAL	this refers to the card number in the*AXIS VALUES input module, which defines the transformation angles between the material x_m, y_m (,z_m) and the global axes x_G, y_G (,z_G)., see note 3	
	P27	=	CORTOL	Deviatoric yield and plastic potential surface corner tolerance. Note: 0<CORTOL≤15°. Default value = 1°	

ADDITIONAL PARAMETERS SET BY PROGRAM

P29	=	E_{min}	(Copy of P21)
P30	=	$a_{in} \cdot p_a$	
P31	=	$a_{in} \cdot p_a$-1.1*TIPTOL	
P32	=	-30° (in radians)	
P33	=	$2.c'_{intrc}/\sqrt{3}$	
P34	=	$\sqrt{3}/2$	
P35	=	$0.5/\sqrt{3}$	
P36	=	$2/\sqrt{27}$	
P37	=	$1/(a_{in} \cdot p_a)$	
P38	=	$1/\sqrt{3}$	
P39	=	$6/\sqrt{27}$	
P40	=	η_{cs}/η_1	
P41	=	$1 - \eta_{cs}/\eta_1$	
P46	=	30.0 - CORTOL	
P47	=	-cos(P46 + 120.0)/(cos(3*P46)*CORTOL)	

DEFINITIONS

1. Stress Invariants

Compression positive:

$$I_1 = \sigma'_x + \sigma'_y + \sigma'_z$$
$$I_2 = \tau_{xy}\tau_{yx} + \tau_{yz}\tau_{zy} + \tau_{zx}\tau_{xz} - (\sigma'_x\sigma'_y + \sigma'_y\sigma'_z + \sigma'_z\sigma'_x)$$
$$I_3 = \sigma'_x\sigma'_y\sigma'_z + \tau_{xy}\tau_{yx}\tau_{zx} + \tau_{yx}\tau_{xy}\tau_{xz} - (\sigma'_x\tau_{yz}\tau_{zy} + \sigma'_y\tau_{zx}\tau_{xz} + \sigma'_z\tau_{xy}\tau_{yx})$$

2. Elastic behaviour

Young's modulus (E): 3 alternatives are available, depending on value of YSW

YSW = 0.0

$$E = M p_a \left[\left(\frac{I_1}{p_a} \right)^2 + \frac{6(1+\mu)}{(1-2\mu)} \frac{J^2}{(p_a)^2} \right]^{\lambda}$$

where

$$J^2 = \tau_{xy}^2 + \tau_{zx}^2 + \tau_{yz}^2 + \tfrac{1}{6}[(\sigma'_x - \sigma'_y)^2 + (\sigma'_y - \sigma'_z)^2 + (\sigma'_z - \sigma'_x)^2]$$

YSW = 1.0

$$E = M p_a \left[\frac{I_1}{p_a} \right]^{2\lambda}$$

YSW = 2.0

$$E = M p_a \left[\frac{\sigma'_3}{p_a} \right]^{\lambda}$$

σ_3' = minimum compressive effective stress

Note: in all 3 cases if $E<E_{min}$ then E is reset equal to E_{min}.

Poisson's ratio (μ):

μ is a constant.

3. Deviatoric plasticity

Yield Surface: $$F_1 = \left(\frac{I_1^3}{I_3} - 27\right)\left(\frac{I_1}{p_a}\right)^m - \eta = 0$$

where:

$$\eta = \eta_i [\varepsilon e^{(1-\varepsilon)}]^{\frac{1}{q}} \quad for \ \varepsilon \le 1$$

$$\eta = \eta_i \left[\frac{\eta_{cs}}{\eta_i} + \left(1 - \frac{\eta_{cs}}{\eta_i}\right)\right][\varepsilon e^{(1-\varepsilon)}]^{\frac{1}{q}} \quad for \ \varepsilon > 1$$

$$\varepsilon = W_p / W_{ppeak}$$

$$q = \alpha + \beta[\sigma_3' / p_a] \quad \ge q_{\min} \text{ (see note 4)}$$

$$W_{ppeak} = P p_a \left(\frac{\sigma_3'}{p_a}\right)^l$$

$$W_p = \int \sigma'^T d\varepsilon_p^D \qquad d\varepsilon_p^D \text{ is deviatoric plastic strain}$$

Note: Hardening parameter 1, HARD(1) = $W_p/W_{ppeak.}$

Plastic Potential: $$G_1 = I_1^3 - \left(27 + \eta_2 \left(\frac{p_a}{I_1}\right)^m\right) I_3$$

where: $$\eta_2 = S\eta + R\left(\frac{\sigma_3'}{p_a}\right)^{0.5} + t$$

4. Spherical plasticity

Yield Surface: $$F_2 = I_1^2 + 2I_2 - k = 0$$

where: $$k = p_a^2 \left(\frac{1}{C}\right)^{\frac{1}{p}} \left(\frac{W_c}{p_a}\right)^{\frac{1}{p}}$$

$$W_c = \int \sigma^T d\varepsilon_p^s \qquad d\varepsilon_p^s \text{ is spherical plastic strain}$$

Note: Hardening parameter 2, HARD(2) = W_c

Plastic potential: $$G_2 = I_1^2 + 2I_2$$

5. Effective cohesion and tension

Included by moving origin of stresses

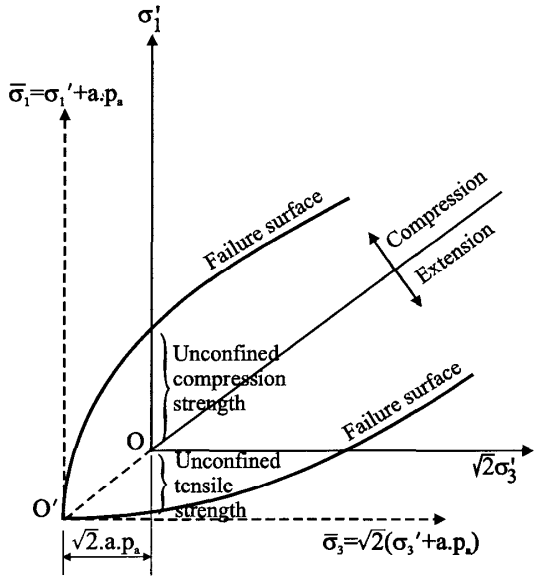

Transformed stresses:

$$\bar{\sigma}_x = \sigma'_x + a\,p_a$$
$$\bar{\sigma}_y = \sigma'_y + a\,p_a$$
$$\bar{\sigma}_z = \sigma'_z + a\,p_a$$
$$\bar{\tau}_{xy} = \tau_{xy} \;;\; \bar{\tau}_{yz} = \tau_{yz} \;;\; \bar{\tau}_{zx} = \tau_{zx}$$

All previous equations are used, but with transformed stresses.

Note: a is dimensionless parameter

NOTES

1. Note 6 explains elastic option.

2. All parameters should be assigned values based on a compression +ve sign convention. The program will make the appropriate conversions necessary for the tension +ve convention that it adopts.

3. If OCRS (P19) = 0.0 $p'_o = OCR \cdot p'$. The hardening parameter for the deviatoric yield surface (HARD(1)) is set to H_{1min} and the hardening parameter for the spherical yield surface (HARD(2)) is calculated by assuming an isotropic stress state with p'=p'$_o$.

   If OCRS (P19) = 1.0 $p'_o = p' - OCR$. The hardening parameter for the deviatoric yield surface (HARD(1)) is set to H_{1min} and the hardening parameter for the spherical yield surface (HARD(2)) is calculated by assuming an isotropic stress state with p'=p'$_o$.

   If OCRS (P19) = 2.0

   If OCR(P20) = 1.0 Material is assumed to be normally consolidated and the hardening parameters for both the deviatoric and spherical yield surfaces, HARD(1) and HARD(2), are calculated assuming the yield surfaces pass through the current state of stress.

   If OCR(P20) >1.0 The OCR (overconsolidation ratio) refers to the conventional definition; $OCR=\sigma'_{vmax}/\sigma'_v$, where σ'_{vmax} is the maximum effective stress experienced by the soil and σ'_v is the current vertical effective stress. The program assumes that $\sigma'_v=\sigma'_{ym}$ and the following procedure is used to determine the initial hardening parameters. The initial stress state (σ_x', σ_y', τ_{xy}, σ_z') is used to calculate $\sin\phi'$ and the direct effective stress σ_{ym}' associated with the material axis x_m, y_m ($,z_m$), defined by AXVAL. For plane stress, plane strain, axi-symmetric and FSAFEM analyses:

$$\sigma'_{ym} = \sigma'_x \sin^2\alpha + \sigma'_y \cos^2\alpha - 2\tau_{xy}\sin\alpha\cos\alpha$$

   For conventional three dimensional analyses:

$$\sigma'_{ym} = \sigma'_x (e_2^x)^2 + \sigma'_y (e_2^y)^2 + 2\tau_{xy}(e_2^x e_2^y) + \sigma'_z (e_2^z)^2 + 2\tau_{xz}(e_2^x e_2^z) + 2\tau_{yz}(e_2^y e_2^z)$$

   The maximum previous stress state is assumed to be given by $\sigma'_{ymo}=OCR.\sigma'_{ym}$, $\sigma'_{xmo}=\sigma'_{zmo}=(1-\sin\phi').\sigma'_{ymo}$, $\tau_{xymo}=0$, where ϕ' is the angle of shearing resistance ϕ' associated with the maximum previous state of stress (this is determined by iteration). The hardening parameters, HARD(1) and HARD(2), are then determined assuming both the deviatoric and spherical yield

surfaces to pass though this maximum previous state of stress.

Note: For this option it is σ_{ym}' that is multiplied by OCR. Therefore the user has to make sure that the axes are in the correct direction, using AXVAL.

If OCRS (P19) = 3.0

If OCR(P20) = 0.0 Material is assumed to be normally consolidated and the hardening parameters for both the deviatoric and spherical yield surfaces, HARD(1) and HARD(2), are calculated assuming the yield surfaces pass through the current state of stress.

If OCR(P20) >0.0 The conventional overconsolidation ratio is defined as $=\sigma'_{vmax}/\sigma'_{v}$, where $\sigma'_{vmax}=\sigma'_{v}$-OCR is the maximum effective stress experienced by the soil and σ'_{v} is the current vertical effective stress. The program assumes that $\sigma'_{v}=\sigma'_{ym}$ and the following procedure is used to determine the initial hardening parameters. The initial stress state (σ_x', σ_y', τ_{xy}, σ_z') is used to calculate $\sin\phi'$ and the direct effective stress σ_{ym}' associated with the material axis x_m, y_m ($,z_m$), defined by AXVAL. For plane stress, plane strain, axi-symmetric and FSAFEM analyses:

$$\sigma'_{ym} = \sigma'_x \sin^2\alpha + \sigma'_y \cos^2\alpha - 2\tau_{xy}\sin\alpha\cos\alpha$$

For conventional three dimensional analyses:

$$\sigma'_{ym} = \sigma'_x (e_2^x)^2 + \sigma'_y (e_2^y)^2 + 2\tau_{xy}(e_2^x e_2^y) + \sigma'_z (e_2^z)^2 + 2\tau_{xz}(e_2^x e_2^z) + 2\tau_{yz}(e_2^y e_2^z)$$

The maximum previous stress state is assumed to be given by $\sigma'_{ymo}=\sigma'_{ym}$-OCR, $\sigma'_{xmo}=\sigma'_{zmo}=(1-\sin\phi').\sigma'_{ymo}$, $\tau_{xymo}=0$, where ϕ' is the angle of shearing resistance ϕ' associated with the maximum previous state of stress (this is determined by iteration). The hardening parameters, HARD(1) and HARD(2), are then determined assuming both the deviatoric and spherical yield surfaces to pass though this maximum previous state of stress.

Note: For this option it is σ_{ym}' that has OCR subtracted from it. Therefore the user has to make sure that the axes are in the correct direction, using AXVAL.

4. $q=\alpha+\beta(\sigma'_3/p_a)$ is not allowed to drop below q_{min}. If this occurs q is reset to q_{min}. q_{min} can be specified on the input cards. If not set a default value of 0 will be adopted.

5. Three options are available for specifying the elastic Young's modulus. In all three cases the modulus can vary with stress level and is controlled by a coefficient (M) and exponent (λ). The equations for each option are given under the 'DEFINITIONS' section for this model. An option is selected by specifying the appropriate value of the Young's modulus switch (YSW). In all cases the Poisson's ratio is assumed constant and equal to μ.

   Alternative elastic parameters and their variation with stress and/or strain level can be specified using the *SMALL STRAIN PROPERTIES module. If a small strain model is specified for the current material type, it takes precedence and controls the elastic behaviour. In such a circumstance the parameters specified on this card are not used.

6. For 'near' isotropic stress states the hardening parameter H_1 associated with the deviatoric yield surface is theoretically very small. In such a situation loading results in -ve changes in plastic work associated with the deviatoric yield surface. This is clearly incorrect but results due to an inconsistency in the theoretical model. It is not a numerical problem. To avoid this shortcoming a small but finite minimum value of the hardening parameter H_1 must be employed. This value must be selected such that loading causes an increase in its value. Unfortunately this critical value is not easily derivable from the model equations and is dependent on the stress magnitude. It is therefore not possible for the program to calculate the value automatically. Consequently the user must input H_{1min}. If this values is not specified a default value of 0.001 will be adopted. If the value specified is to small and the program calculates -ve changes in H_1 such that H_1 reduces below H_{1min}, the program will abort with an error message. If this occurs the user should increase H_{1min}.

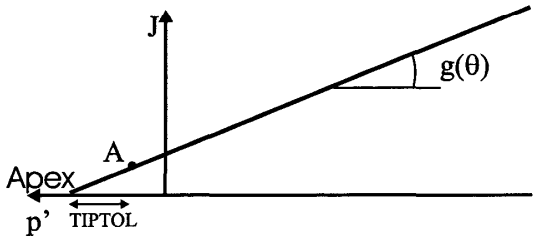

7. If the stress state approaches the apex of the yield surface it will be pushed back to the point A in the diagram above (i.e it will be pushed back a distance of TIPTOL from the apex) . This prevents:
   a) the singularity of the apex causing problems, especially with the flow steps.
   b) the stress state flipping onto the mirror image of the yield surface.

8. In the original form of the model the shear strength decays after reaching a peak value defined by η_1 to zero at large shear strains. This is clearly unrealistic, hence the provision of specifying η_{cs}. In $\eta_{cs}>0$ then once peak has been reached the shear strength will decay to η_{cs} at large strains. Hence this provision essentially provides a limit to the strength at large strains. However, it should not be confused with a true critical state as the model does not ensure that there are zero plastic volumetric strains when η_{cs} is approached.

9. If the material and global axes coincide then set AXVAL=0.0. Otherwise AXVAL refers to the card number in the *AXIS VALUES input module which defines the transformation angle (2D analyses) or the transformation matrix(3D analyses) between the material and global axes. Note a real number (i.e. 3.0) must be set for AXVAL.

10. If the parameters R and/or α are non zero then the contribution of σ_3' to the deviatoric yield and plastic potential surfaces manifests itself in non unique partial derivative contributions at the corners defined by a Lodes angle θ of +30°. At these corners some of the terms of the derivatives of the deviatoric yield and plastic potential functions are not unique. To overcome this problem these partially derivatives at the corners are calculated from a "rounded "corner. The rounded corner is controlled by the value of CORTOL which specifies the angle over which the rounding occurs. For example a value of CORTOL=1.0 indicates that the corners are only rounded over the range $29° \le \theta \le 30°$. If P27 (=CORTOL) is not specified then a default value of 1.0° is assumed for CORTOL.

11. The Factor of Safety, Fs, is applied to the values of c' and tan(ϕ') in triaxial compression. However obtaining these values is not straight forward as the model is not expressed in terms of these parameters or parameters directly related to them. In addition the value of tan(ϕ') in triaxial compression varies with mean effective stress. When a factor of safety is applied the program first calculates the initial angle of shearing resistance in triaxial compression at the current mean effective stress, ϕ'_{in}, using a_{in} and η_1 (this involves solving a cubic equation). This value is then modified by the factor of safety to obtain the active value of $\phi' = \tan^{-1}(\tan(\phi'_{in})/Fs)$. This and the original c'_{in}, calculated from a_{in} and η_1, modified by Fs are then used to calculate the active values of a and η (this involves the solution of a second cubic equation). Initially, at the start of an analysis or when elements are constructed, F_s is set to unity. It can be changed by using the *INCREASE FACTOR OF SAFETY module.

HARDENING PARAMETERS

HARD(1) contains the hardening parameter for the deviatoric yield surface = W_p/W_{ppeak}. It can be modified by the *MODIFY HARDENING PARAMETER module.

HARD(2) contains the hardening parameter for the spherical yield surface = W_c. It can be modified by the *MODIFY HARDENING PARAMETER module.

HARD(3) contains the current factor of safety Fs. At the start of an analysis or when elements are constructed, Fs is set to unity. It can be changed by the *INCREASE FACTOR OF SAFETY module.

APPENDIX II

ICFEP INPUT EXAMPLE: TRIAXIAL TEST

```
      SUBROUTINE INSTRS(   PRPL,  PRPNL,    NEL,  IETYP, MATNOS,     XC,
     S                       YC,     ZC,     S1,     S2,     S3,     S4,
     S                       S5,     S6,     S7,     S8,     PW,     VR)
      INCLUDE 'DP.T'
C****
C****           TEMPLATE FOR THE INITIAL STRESS SUBROUTINE
C****           ==========================================
C****
C**** This is a user defined subroutine for introducing initial
C**** stresses/forces, pore fluid stresses and void ratios into
C**** a nonlinear analysis.
C****
C**** The following parameters are passed to this routine:-
C****
C****   - The arrays PRPL(I) and PRPNL(I) contain the linear and
C****     and nonlinear material properties for the current
C****     integration point.
C****
C****   - NEL is the current element number
C****
C****   - IETYP is the current element type, i.e.
C****         IETYP = 1 for solid elements
C****         IETYP = 2 for joint elements
C****         IETYP = 3 for beam elements
C****         IETYP = 4 for membrane elements
C****         IETYP = 5 for bar elements
C****         IETYP = 6 for shell elements
C****
C****   - MATNOS is the current material property number
C****
C****   - XC and YC are the x and y global coordinates of the
C****     current integration point
C****
C****   - ZC is the global z coordinate of the current integration
C****     point for full 3D analysis, is the THETA coordinate for
C****     Fourier series aided analyses and is set to zero for all
C****     other analyses
C****
C****
C**** The following parameters must be set in this routine:-
C****
C****   - S1, S2, S3, S4, S5, S6, S7 and S8. These are equivalenced
C****     to the element stresses and/or forces and are dependent
C****     on the element type.  See notes for each element type
C****
C****   - PW = The pore fluid stress
C****
C****   - VR = The void ratio. This is used by some of the
C****          nonlinear and variable permeability models.
C****
C****   Note: If values are not set they will default to zero
C****
C****      NOTE: ICFEP USES A TENSION POSITIVE SIGN CONVENTION
C****      ===================================================
C****
      DIMENSION PRPL(*), PRPNL(*), PAR(8)
      EQUIVALENCE (PAR(1),SX,TSP,FA,SA),   (PAR(2),SY,SN,BMA,SOP,SB,FB),
     E       (PAR(3),SXY,TST,S,SAB,FAB),            (PAR(4),SZ,FOP,XMA),
     E            (PAR(5),SXZ,BMOP,XMB),              (PAR(6),SYZ,XMAB),
     E                     (PAR(7),SFA),                    (PAR(8),SFB)
C****
C**** ZERO ARRAY -PAR(I)-
C****
      CALL RZERO(PAR,8)
C****
C**** SET INITIAL STRESSES
C****
C****
```

```
      IF(IETYP.EQ.1) THEN
C****
C****                   SOLID/BRICK ELEMENTS
C****                   ====================
C****
C****     The following parameters must be set here:-
C****
C****      SX   =   SIGX   (or SIGR       for axi-symmetric analyses)
C****      SY   =   SIGY   (or SIGZ       for axi-symmetric analyses)
C****      SXY  =   SIGXY  (or SIGRZ      for axi-symmetric analyses)
C****      SZ   =   SIGZ   (or SIG(THETA) for axi-symmetric analyses)
C****      PW   =   Pore fluid stress
C****      VR   =   Void ratio
C****
C****     In addition for 3D and Fourier series aided analysis the
C****     following stress components must be set:-
C****
C****      SXZ  =   SIGXZ  (or SIGRT      for Fourie aided analyses)
C****      SYZ  =   SIGYZ  (or SIGZT      for Fourie aided analyses)
C****
         SY  = -588.408
         SX  = -588.408
         SXY = 0.0
         SZ  = SX
         SXZ = 0.0
         SYZ = 0.0
         VR  = 0.0
         PW  = 0.0
C****
C****
      ELSE IF(IETYP.EQ.2) THEN
C****
C****                   JOINT/SHELL ELEMENTS
C****                   ====================
C****
C****    The following parameters must be set here:-
C****
C****     TSP  =   Shear stress along joint. For full 3D analyses
C****              it is the shear stress in the direction of nodes
C****              1 to 5 in the parent isoparametric element.
C****     SN   =   Normal stress across joint
C****     PW   =   Pore fluid stress
C****
C****    In addition for 3D and Fourier series aided analysis the
C****    following stress component must be set:-
C****
C****     TST  =   Shear stress in THETA (ZC) direction for Fourier
C****              series aided analyses. For full 3D analysis it is
C****              the shear stress in the plane of the element
C****              perpendicular to TSP (i.e. in the direction of
C****              nodes 1 to 2 in the parent isoparametric element).
C****
C****
      ELSE IF(IETYP.EQ.3) THEN
C****
C****                   BEAM ELEMENTS
C****                   =============
C****
C****    The following parameters must be set here:-
C****
C****     FA   =   Axial force
C****     BMA  =   Moment
C****     S    =   Shear force
C****     FOP  =   Out of plane force
C****     BMOP =   Out of plane moment
C****
C****
      ELSE IF(IETYP.EQ.4) THEN
```

```
C****
C****                    MEMBRANE ELEMENTS
C****                    =================
C****
C****     The following parameters must be set here:-
C****
C****     For axisymmetric, plane stress and plane strain analyses:
C****
C****        SA   =   Axial stress
C****        SOP  =   Out of plane stress
C****
C****     For full 3D analyses:
C****
C****        SA   = In plane direct stress in the direction of maximum
C****               element curvature
C****        SB   = In plane direct stress in the direction of minimum
C****               element curvature
C****        SAB  = In plane shear stress
C****
         SA  = 0.0
         SB  = 0.0
         SAB = 0.0
C****
      ELSE IF(IETYP.EQ.5) THEN
C****
C****                    BAR ELEMENTS
C****                    ============
C****
C****    The following parameters must be set here:-
C****
C****     FA   =   Axial force
C****     FOP  =   Out of plane force
C****
C****
C****
         FA  = 0.0
         FOP = 0.0
C****
C****
      ELSE IF(IETYP.EQ.6) THEN
C****
C****                     SHELL ELEMENTS
C****                     =============
C****
C****    The following parameters must be set here:-
C****
C****     For axisymmetric, plane stress and plane strain analyses:
C****
C****        FA   =   Axial force
C****        BMA  =   Moment
C****        S    =   Shear force
C****        FOP  =   Out of plane force
C****        BMOP =   Out of plane moment
C****
C****     For full 3D analyses:
C****
C****        FA   = In plane direct force in the direction of maximum
C****               element curvature
C****        FB   = In plane direct force in the direction of minimum
C****               element curvature
C****        FAB  = In plane shear force
C****        XMA  = Moment around the direction of maximum curvature
C****        XMB  = Moment around the direction of minimum curvature
C****        XMAB = Twisting moment
C****        SFA  = Transverse shear force acting on planes
C****               perpendicular to the direction of maximum curvature
C****        SFB  = Transverse shear force acting on planes
C****               perpendicular to the direction of minimum curvature
```

```
C****
C****
      END IF
C****
C**** SET RETURN ARGUEMENTS -S1, S2, S3, S4, S5, S6, S7 AND S8-
C****
      S1 = PAR(1)
      S2 = PAR(2)
      S3 = PAR(3)
      S4 = PAR(4)
      S5 = PAR(5)
      S6 = PAR(6)
      S7 = PAR(7)
      S8 = PAR(8)
C****
C****
      RETURN
      END
```

```
*comm DENSE SACRAMENTO RIVER SAND DRAINED TRIAXIAL TEST - 588.408kPa
*PROGRAM CONTROL
START    0, 0
STOP   430, 1
NEWDATA
NONLINEAR
PLANE 3
OUTDISC ~/home3/RUN/CHRISTINA/SACRAMENTO/DENSE/SACR-588/TRIAXIAL.SVE
INITIAL_STRESS ~/home3/DATA/CHRISTINA/SACRAMENTO/DENSE/SACR-588/instr
LTOLERANCE 200, 200, -1
ITERATION 1, 100
ALPHA     1, 100, 5
HPPLOTTER
SAVE
*ENDCONTROL
*DEFINE
*TITLE
1: DRAINED TRIAXIAL TEST
*REFERENCE POINTS
1: 0.0, 0.0
2: 1.0, 0.0
3: 1.0, 1.0
4: 0.0, 1.0
*BLOCK DATA
1: 18, 1, 1, 2, 3, 4, 1, 1
*UPDATE STIFFNESS
1: 1, 1000, 1, 100, 1
*LINEAR MATERIAL PROPERTIES
1: 1.0, 1.0, 1.0, 463.963E3, 0.2
*NONLINEAR MATERIAL PROPERTIES
1:1: 14.0, 101.325, 2.0, 1680.0, 0.57, 0.2, 80.0, 0.23, -2.95, 0.44
1:2: 8.45, 3.0, 0.060, 0.12, 1.16, 0.00023, 0.86, 0.0, 0.0, 1.0,*
*PRESCRIBED DISPLACEMENTS
1: 1, 10000, 1, 4, 1, 0
2: 1, 10000, 2, 1, 2, 0
3: 1, 200,   2, 3, 4, 1
4: 201, 430,   2, 3, 4, 2
*DISPLACEMENT VALUES
1: 2.0, -1.67E-4
2: 2.0, -0.001
*LIST
1: 0, 1000, 1, 343
2: 0, 1000, 1, 342
3: 0, 1000, 1, 391
*XY-GRAPHS
 1:  430, 430, 1, 6159, 1,1,0, 5230, 1,1,0, 0,0,1,0,1
 2:  430, 430, 1, 6159, 1,1,0, 6160, 1,1,0, 0,0,1,0,1
*FRAME SIZE
1: A4L
*SAVE
1:  1,   10,  1
2: 10, 1000, 10
*ENDDATA
```

APPENDIX III

ICFEP INPUT EXAMPLE: HOLLOW CYLINDER TEST

```
      SUBROUTINE INSTRS(   PRPL,  PRPNL,    NEL,  IETYP, MATNOS,     XC,
     S                       YC,     ZC,     S1,     S2,     S3,     S4,
     S                       S5,     S6,     S7,     S8,     PW,     VR)
      INCLUDE 'DP.T'
C****
C****           TEMPLATE FOR THE INITIAL STRESS SUBROUTINE
C****           ==========================================
C****
C**** This is a user defined subroutine for introducing initial
C**** stresses/forces, pore fluid stresses and void ratios into
C**** a nonlinear analysis.
C****
C**** The following parameters are passed to this routine:-
C****
C****   - The arrays PRPL(I) and PRPNL(I) contain the linear and
C****     and nonlinear material properties for the current
C****     integration point.
C****
C****   - NEL is the current element number
C****
C****   - IETYP is the current element type, i.e.
C****         IETYP = 1 for solid elements
C****         IETYP = 2 for joint elements
C****         IETYP = 3 for beam elements
C****         IETYP = 4 for membrane elements
C****         IETYP = 5 for bar elements
C****         IETYP = 6 for shell elements
C****
C****   - MATNOS is the current material property number
C****
C****   - XC and YC are the x and y global coordinates of the
C****     current integration point
C****
C****   - ZC is the global z coordinate of the current integration
C****     point for full 3D analysis, is the THETA coordinate for
C****     Fourier series aided analyses and is set to zero for all
C****     other analyses
C****
C****
C**** The following parameters must be set in this routine:-
C****
C****   - S1, S2, S3, S4, S5, S6, S7 and S8. These are equivalenced
C****     to the element stresses and/or forces and are dependent
C****     on the element type.  See notes for each element type
C****
C****   - PW = The pore fluid stress
C****
C****   - VR = The void ratio. This is used by some of the
C****          nonlinear and variable permeability models.
C****
C****   Note: If values are not set they will default to zero
C****
C****      NOTE: ICFEP USES A TENSION POSITIVE SIGN CONVENTION
C****      ===================================================
C****
      DIMENSION PRPL(*), PRPNL(*), PAR(8)
      EQUIVALENCE (PAR(1),SX,TSP,FA,SA),   (PAR(2),SY,SN,BMA,SOP,SB,FB),
     E       (PAR(3),SXY,TST,S,SAB,FAB),            (PAR(4),SZ,FOP,XMA),
     E            (PAR(5),SXZ,BMOP,XMB),              (PAR(6),SYZ,XMAB),
     E                     (PAR(7),SFA),                    (PAR(8),SFB)
C****
C**** ZERO ARRAY -PAR(I)-
C****
      CALL RZERO(PAR,8)
C****
C**** SET INITIAL STRESSES
C****
C****
```

```
      IF(IETYP.EQ.1) THEN
C****
C****                    SOLID/BRICK ELEMENTS
C****                    ====================
C****
C****     The following parameters must be set here:-
C****
C****      SX   =   SIGX   (or SIGR       for axi-symmetric analyses)
C****      SY   =   SIGY   (or SIGZ       for axi-symmetric analyses)
C****      SXY  =   SIGXY  (or SIGRZ      for axi-symmetric analyses)
C****      SZ   =   SIGZ   (or SIG(THETA) for axi-symmetric analyses)
C****      PW   =   Pore fluid stress
C****      VR   =   Void ratio
C****
C****     In addition for 3D and Fourier series aided analysis the
C****     following stress components must be set:-
C****
C****      SXZ  =   SIGXZ  (or SIGRT      for Fourie aided analyses)
C****      SYZ  =   SIGYZ  (or SIGZT      for Fourie aided analyses)
C****
           PW  =  0.0
           SY  =  -30.0
           SX  =  -30.0
           SXY =  0.0
           SZ  =  SX
           SXZ =  0.0
           SYZ =  0.0
           PW  =  0.0
           VR  =  0.0
C****
C****
      ELSE IF(IETYP.EQ.2) THEN
C****
C****                     JOINT/SHELL ELEMENTS
C****                     ====================
C****
C****    The following parameters must be set here:-
C****
C****     TSP  =   Shear stress along joint. For full 3D analyses
C****              it is the shear stress in the direction of nodes
C****              1 to 5 in the parent isoparametric element.
C****     SN   =   Normal stress across joint
C****     PW   =   Pore fluid stress
C****
C****    In addition for 3D and Fourier series aided analysis the
C****    following stress component must be set:-
C****
C****     TST  =   Shear stress in THETA (ZC) direction for Fourier
C****              series aided analyses. For full 3D analysis it is
C****              the shear stress in the plane of the element
C****              perpendicular to TSP (i.e. in the direction of
C****              nodes 1 to 2 in the parent isoparametric element).
C****
C****
           TSP  = 0.0
           SN   = 0.0
           PW   = 0.0
      ELSE IF(IETYP.EQ.3) THEN
C****
C****                     BEAM ELEMENTS
C****                     =============
C****
C****    The following parameters must be set here:-
C****
C****     FA   =   Axial force
C****     BMA  =   Moment
C****     S    =   Shear force
C****     FOP  =   Out of plane force
```

```
C****     BMOP =   Out of plane moment
C****
C****
      ELSE IF(IETYP.EQ.4) THEN
C****
C****                   MEMBRANE ELEMENTS
C****                   =================
C****
C****     The following parameters must be set here:-
C****
C****     For axisymmetric, plane stress and plane strain analyses:
C****
C****        SA   =   Axial stress
C****        SOP  =   Out of plane stress
C****
C****     For full 3D analyses:
C****
C****        SA   = In plane direct stress in the direction of maximum
C****               element curvature
C****        SB   = In plane direct stress in the direction of minimum
C****               element curvature
C****        SAB  = In plane shear stress
C****
         SA  = 0.0
         SB  = 0.0
         SAB = 0.0
C****
      ELSE IF(IETYP.EQ.5) THEN
C****
C****                   BAR ELEMENTS
C****                   ============
C****
C****    The following parameters must be set here:-
C****
C****     FA   =   Axial force
C****     FOP  =   Out of plane force
C****
C****
C****
         FA  = 0.0
         FOP = 0.0
C****
C****
      ELSE IF(IETYP.EQ.6) THEN
C****
C****                    SHELL ELEMENTS
C****                    ==============
C****
C****    The following parameters must be set here:-
C****
C****     For axisymmetric, plane stress and plane strain analyses:
C****
C****        FA   =   Axial force
C****        BMA  =   Moment
C****        S    =   Shear force
C****        FOP  =   Out of plane force
C****        BMOP =   Out of plane moment
C****
C****     For full 3D analyses:
C****
C****        FA   = In plane direct force in the direction of maximum
C****               element curvature
C****        FB   = In plane direct force in the direction of minimum
C****               element curvature
C****        FAB  = In plane shear force
C****        XMA  = Moment around the direction of maximum curvature
C****        XMB  = Moment around the direction of minimum curvature
C****        XMAB = Twisting moment
```

```
C****         SFA  = Transverse shear force acting on planes
C****                perpendicular to the direction of maximum curvature
C****         SFB  = Transverse shear force acting on planes
C****                perpendicular to the direction of minimum curvature
C****
C****
       END IF
C****
C**** SET RETURN ARGUEMENTS -S1, S2, S3, S4, S5, S6, S7 AND S8-
C****
       S1 = PAR(1)
       S2 = PAR(2)
       S3 = PAR(3)
       S4 = PAR(4)
       S5 = PAR(5)
       S6 = PAR(6)
       S7 = PAR(7)
       S8 = PAR(8)
C****
C****
       RETURN
       END
```

```
*COMM LOOSE SACRAMENTO RIVER SAND DRAINED HOLLOW CYLINDER TEST - 200kPa
*PROGRAM CONTROL
START 1,1
STOP  10,1
NEWDATA
NONLINEAR
PLANE 5
INDISC  /home3/msc3/RUN/CHRISTINA/SACRAMENTO/HC/DENSE/SACR-L-200/MESH3D.SVE
OUTDISC /home3/msc3/RUN/CHRISTINA/SACRAMENTO/HC/DENSE/SACR-L-200/ISOTROPIC.SVE
INITIAL_STRESSES /home3/msc3/DATA/CHRISTINA/SACRAMENTO/HC/DENSE/SACR-200/inst
*comm AUTOMATIC_INCREMENTATION 10000
LTOLERANCE 200, 200, -1
ITERATION 1, 1500
alpha 1, 1500, 5
FLOW 10000, 1000, 10
SAVE
*ENDCONTROL
*DEFINE
*TITLE
1: Single element, isotropic consolidation
*LINEAR MATERIAL PROPERTIES
1: 1.0, 1.0, 1.0, 95.541E3, 0.2
*NONLINEAR MATERIAL PROPERTIES
1:1: 14.0, 101.325, 2.0, 1680.0, 0.57, 0.2, 80.0, 0.23, -2.95, 0.44
1:2: 8.45, 3.0, 0.060, 0.12, 1.16, 0.00023, 0.86, 0.0, 0.0, 1.0,*
*UPDATE STIFFNESS
1: 1, 1000, 1, 120, 1
*PRESCRIBED DISPLACEMENTS
1:    1, 10000, 2, -1, -1, 0
2:    1, 10000, 2, -2, -2, 0
3:    1, 10000, 2, -6, -6, 0
4:    1, 10000, 2, -5, -5, 0
5:    1, 10000, 1, -1, -1, 0
6:    1, 10000, 1, -5, -5, 0
7:    1, 10000, 5, -1, -1, 0
8:    1, 10000, 5, -2, -2, 0
*POINT LOADS
*comm SIGz
1:    1, 10, 2, -3, -3, 1
2:    1, 10, 2, -4, -4, 1
3:    1, 10, 2, -7, -7, 1
4:    1, 10, 2, -8, -8, 1
*comm SIGth
5:    1, 10, 1, -3, -3, 1
6:    1, 10, 1, -2, -2, 1
7:    1, 10, 1, -7, -7, 1
8:    1, 10, 1, -6, -6, 1
9:    1, 10, 1, -1, -1, 2
10:   1, 10, 1, -5, -5, 2
11:   1, 10, 1, -4, -4, 2
12:   1, 10, 1, -8, -8, 2
*comm SIGr
13:   1, 10, 5, -1, -1, 2
14:   1, 10, 5, -2, -2, 2
15:   1, 10, 5, -3, -3, 2
16:   1, 10, 5, -4, -4, 2
17:   1, 10, 5, -5, -5, 1
18:   1, 10, 5, -6, -6, 1
19:   1, 10, 5, -7, -7, 1
20:   1, 10, 5, -8, -8, 1
*load values
1:   1.0,  -4.25
2:   1.0,   4.25
*LIST
1: 0, 2000, 1, 343
2: 0, 2000, 1, 344
3: 0, 2000, 1, 393
4: 0, 2000, 1, 346
```

```
5: 0, 2000, 1, 332
6: 0, 2000, 1, 391
*XY-GRAPH
 1:  10, 10, 1, 5206, 1,1,1, 5211, 1,1,1, 0,0,1,1,1
*FRAME
1:A4L
*SAVE
1: 1, 11000, 1
*ENDDATA
```

```
*PROGRAM CONTROL
START 11,1
STOP  1000,1
NEWDATA
NONLINEAR
PLANE 5
INDISC  /home3/msc3/RUN/CHRISTINA/SACRAMENTO/HC/DENSE/SACR-L-200/ISOTROPIC.SVE
OUTDISC
/home3/msc3/RUN/CHRISTINA/SACRAMENTO/HC/DENSE/SACR-L-200/DRAINED/SHEARING.SVE
INITIAL_STRESSES /home3/msc3/DATA/CHRISTINA/SACRAMENTO/HC/DENSE/SACR-200/inst
*comm AUTOMATIC_INCREMENTATION 10000
LTOLERANCE 200, 200
ITERATION 1, 1500
alpha 1, 1500, 5
FLOW 10000, 1000, 10
SAVE
*ENDCONTROL
*DEFINE
*TITLE
1: Single element, isotropic consolidation
*LINEAR MATERIAL PROPERTIES
1: 1.0, 1.0, 1.0, 95.541E3, 0.2
*NONLINEAR MATERIAL PROPERTIES
1:1: 14.0, 101.325, 2.0, 1680.0, 0.57, 0.2, 80.0, 0.23, -2.95, 0.44
1:2: 8.45, 3.0, 0.060, 0.12, 1.16, 0.00023, 0.86, 0.0, 0.0, 1.0,*
*UPDATE STIFFNESS
1: 1, 1500, 1, 120, 1
*PRESCRIBED DISPLACEMENTS
1:    1, 10000, 2, -1, -1, 0
2:    1, 10000, 2, -2, -2, 0
3:    1, 10000, 2, -6, -6, 0
4:    1, 10000, 2, -5, -5, 0
5:    1, 10000, 1, -1, -1, 0
6:    1, 10000, 1, -5, -5, 0
7:    1, 10000, 5, -1, -1, 0
8:    1, 10000, 5, -2, -2, 0
*POINT LOADS
*comm SIGz
1:    1, 10, 2, -3, -3, 1
2:    1, 10, 2, -4, -4, 1
3:    1, 10, 2, -7, -7, 1
4:    1, 10, 2, -8, -8, 1
*comm SIGth
5:    1, 10, 1, -3, -3, 1
6:    1, 10, 1, -2, -2, 1
7:    1, 10, 1, -7, -7, 1
8:    1, 10, 1, -6, -6, 1
9:    1, 10, 1, -1, -1, 2
10:   1, 10, 1, -5, -5, 2
11:   1, 10, 1, -4, -4, 2
12:   1, 10, 1, -8, -8, 2
*comm SIGr
13:   1, 10, 5, -1, -1, 2
14:   1, 10, 5, -2, -2, 2
15:   1, 10, 5, -3, -3, 2
16:   1, 10, 5, -4, -4, 2
17:   1, 10, 5, -5, -5, 1
18:   1, 10, 5, -6, -6, 1
19:   1, 10, 5, -7, -7, 1
20:   1, 10, 5, -8, -8, 1
*comm monotonic shearing
21:  11,1000, 1, -4, -4, 3
22:  11,1000, 1, -3, -3, 3
23:  11,1000, 1, -7, -7, 3
24:  11,1000, 1, -8, -8, 3
25:  11,1000, 2, -2, -2, 3
26:  11,1000, 2, -6, -6, 3
27:  11,1000, 2, -3, -3, 3
```

```
28:  11,1000, 2, -7, -7, 3
29:  11,1000, 1, -2, -2, 4
30:  11,1000, 1, -6, -6, 4
31:  11,1000, 1, -1, -1, 4
32:  11,1000, 1, -5, -5, 4
33:  11,1000, 2, -4, -4, 4
34:  11,1000, 2, -8, -8, 4
35:  11,1000, 2, -1, -1, 4
36:  11,1000, 2, -5, -5, 4
*load values
1:   1.0,  -4.25
2:   1.0,   4.25
3:   1.0,   -0.1
4:   1.0,  0.1
*LIST
1: 0, 2000, 1, 343
2: 0, 2000, 1, 344
3: 0, 2000, 1, 393
4: 0, 2000, 1, 346
5: 0, 2000, 1, 332
6: 0, 2000, 1, 391
*XY-GRAPH
 1:  10, 10, 1, 5206, 1,1,1, 5211, 1,1,1, 0,0,1,1,1
*FRAME
1:A4L
*SAVE
1: 1, 11000, 1
*ENDDATA
```